Asteroseismic studies of two binary systems containing pulsating components

Valentina S. Schmid

Examination committee:
Prof. Dr. Riccardo Raabe, chair
Prof. Dr. Conny Aerts, supervisor
Dr. Andrew Tkachenko
Prof. Dr. Hugues Sana
Prof. Dr. Rony Keppens
Dr. Eric Michel
(Observatoir de Paris-Meudon)
Prof. Dr. Andrej Prša
(Villanova University)

Dissertation presented in partial
fulfilment of the requirements for
the degree of Doctor in Science:
Astronomy and Astrophysics

August 2016

The research represented in this PhD thesis was made possible thanks to an Aspirant Fellowship offered to the author by the Research Foundation Flanders (FWO), Belgium.

Cover image
Illustration of a binary system with a pulsating component, which is overlaid with a gravity-mode ray path pattern taken from Cunha et al. (2007).
Background: *Kepler* full-frame image. Courtesy of NASA/*Kepler* mission.
Composition and Design: Jonas Debosscher and Steven Bloemen

Uitgegeven in eigen beheer, Valentina S. Schmid, Celestijnenlaan 200D box 2401, B-3001 Leuven (Belgium)

Acknowledgements

A PhD is like a journey. You will venture out to explore new lands and while discovering the path you are treading, you will learn at least as much about yourself. Like on any journey, a good guide, who knows the path, its crooks and turns, is invaluable. Not travelling alone, but in good company, makes the journey easier and a lot more fun. Along this way, which started four years ago, I have had many guides and companions, who shone a light, while I was treading in the dark, who pointed me into the right direction or who simply just handed me a walking stick. Without these people it would not have been possible to reach my final destination, so I would like to take a brief moment to give them due credit.

Conny, thank you for the guidance. Your comprehensive view of the field and your intuition always kept me on track. Thank you for taking time out of your busy schedule and giving priority to your students. But most of all, thank you for believing in me from the start and for keeping believing in me, even though I could not always do so myself. Thank you also for providing me with the next challenge and giving me the opportunity to head into a new direction after my PhD.

Pieter, thank you for your enthusiasm and for being our python encyclopaedia. I will certainly never forget the uncertainties, ever again. Andrew, thank you for your great ideas. Ehsan, thank you for being a great teacher and for being our MESA and GYRE guru. Péter, thanks for all the discussions and advise. It was and still is amazing, to work in an environment, where I can simply jump into the next office, whenever I am stuck or too confused about science.

My jury members, thank you for taking the time to read the manuscript and for giving comments that made it better.

Timothy and Alejandra, it was a pleasure travelling on this road alongside you. Thank you for sharing your insights, for making me feel “not stupid”, the occasional ventilation of frustration about administration or “I don’t know what I’m doing here”. Good luck for your last climb, the end is nigh!

Bram, Wim, and Rik, thank you for solving all technical issues – big or small. Anne and Anita, thank you for the help with administration. Saskia, Jesus, and Florian, thank for you keeping Mercator up and running for us.

My office mates – who are many, because it is the third office I am in right now – Jonas, Alejandra, Andrew, Ward, Robin, Jonathan, and Timothy, thanks for the occasional interruption and the company on long nights. Sorry for all the light, I just can't help it.

Alejandra & Jonas, Judith, Joris & Martina, Paul, Robin, Roy, and Steven; the beginnings. Thanks for the dinners, the schnaps, and the smooth start into PhD life.

Ana, Cole, Dylan, Jels, May, Mike, and Shreeya; the next generation. Thanks for the beers and the chats. I wish you all the best on your journey!

Sara & Wim, Katrijn, Péter, Robin, Michel, Devika, Rajeev, Ehsan & Hoda, Konstanze, Katrien, Wim, Pierre, Bart, Gert, Marie, and all the other IvS coffee room regulars and not-so-regulars. Thank you for the weird, fun, sciency, and nerdy conversations – the type that you can only have in the IvS coffee room. Thank you for making the IvS such an enjoyable place to work at.

Stephie, Katinka & Melissa, Annabelle and Mareike, thanks for new friendships. I hope we can turn them into old friendships.

Johan and Diane, thank you for welcoming me into your family with open arms.

Ulli, Elsa, Laura, Kri, Cory, Helga, Nathalie, Niki, and Sabs; because work isn't everything. Thank you for keeping in touch across the long distance and for making it feel like it was just yesterday, every time.

Mama, Papa, Madlen, and Martin; Sebastian, Lukas, Teresa, and Mariana, thank you for always being there. For giving me a place that I can always return to.

Steven, thank you for always sticking by my side. Here is to the next adventure!

Thank you! Dankeschön! Dank u wel!

Valentina
Leuven, past midnight on the 5th of August, 2016

Abstract

Stellar pulsations propagate throughout the star and carry with them information about the condition within the deep stellar interior. This information is crucial for fine-tuning models of stars and allows us to test if real stars obey the current theory of stellar structure and evolution. Two stars orbiting around a common centre of mass form a binary system. Under certain conditions, these systems allow us to derive masses and radii of their component stars without relying on stellar models. Pulsating stars residing in binary systems thus offer rigorous tests for theoretical models. In this work, we present the detailed studies of a well-known pulsator that turned out to be a member of a spectroscopic binary and a binary system containing two pulsating stars that was recently discovered from data assembled by the NASA *Kepler* satellite.

The first example we studied in this thesis is the δ Sct star 4 CVn. This intermediate-mass sub-giant star is a well studied pulsator. We assembled and analysed a large spectroscopic data set and discovered that this star is the primary of a wide, eccentric binary system. Unfortunately, 4 CVn completely outshines its companion and no constraints could be derived from the binarity. In the line-profile variations of the spectra we detected 20 pulsation modes. We attempted to identify the degree ℓ and the azimuthal order m for the two dominating modes. However, fast rotation hampered the mode identification and made it impossible to derive unique results for any seismic interpretation.

The second example is a double-lined eccentric binary system that contains two g- and p-mode hybrid pulsators. This rich system was discovered from four years of data assembled by the *Kepler* satellite. In addition to the photometric data, we have obtained ground-based follow-up spectroscopy, covering the binary orbit. Underneath the high-amplitude pulsations, we discovered a signal of reflection and ellipsoidal variation in the light curve. From this signal and the radial velocity measurements, we derived masses and radii. In the periodogram of the light curve, we detected six series of equally spaced g-mode periods and rotational splitting in the g and p modes for both stars. We used these stringent observational constraints for seismic modelling. An estimate of the convective-core overshooting and additional internal mixing was derived. These are the first such seismic estimates derived for hybrid intermediate-mass pulsators. However, as the models failed to predict the detailed pattern of the period spacings to the high precision of the data, we concluded that mixing in only the radial direction is insufficient to describe the detailed stellar structure with current state-of-the-art one-dimensional stellar models. We calculated core-to-surface rotation rates for both stars and found slight differential rotation for the secondary and almost uniform rotation for the primary. Our work delivered the first seismic estimates of the level of chemical mixing inside intermediate-mass binary pulsators and paves the way for more such type of studies in the near future.

Contents

Chapter 1

Scientific framework

1.1 Introduction

From the smallest scales of dust grains up to the evolution of galaxies, stars play a key role in many different research fields of astrophysics. Stars are responsible for the production of heavy elements and the enrichment of their environments. They help us detect and characterise exoplanets and allow us to determine the formation and structure of the Milky Way and other galaxies. All these research fields depend on the accuracy of the theories of stellar structure and evolution and shortcomings in theoretical models propagate into the accuracy and precision of any conclusions built upon them. While the general picture of stars is well understood, several details in terms of internal mixing processes, rotation or magnetic fields still need to be resolved.

Asteroseismology opens a new window beyond the photosphere to gauge the inside of stars. The oscillations that we detect as brightness variations here on Earth, carry with them information of the conditions within the deep stellar interior, where they originate. By comparing these observations to the predictions made by theoretical stellar models we can fine tune the physical descriptions that enter these models. Ultimately asteroseismology helps us test our theories of stellar structure and evolution.

Binary stars are yet another way to put these theories to the test. Aside from apsidal motion, i.e. the precession of the orbit within its own plane, which places constraints on the interior structure of the components, certain types of systems, i.e. double-lined eclipsing binaries, have the benefit of enabling precise measurements of their masses and radii. Based only on Kepler's laws and geometry, the interpretation of these measurements becomes independent of stellar model predictions. The input parameters to theoretical evolutionary tracks can then be tweaked, until the observations are matched.

Pulsating binary stars, thus, provide the unique opportunity for a synergy of two different methods.

In what follows, we present an overview of the theories of stellar structure and evolution. We present the basics of asteroseismology and introduce the reader to the subject of binary stars.

1.2 Modelling stars and their evolution

In this section, we briefly discuss the basics of stellar structure and evolution and some complications that arise from the simplifications. For more detailed descriptions, we refer the reader to recent monographs in this field, e.g. the ones by Maeder (2009) or Kippenhahn et al. (2012).

1.2.1 Stellar structure

Stellar modelling codes often approximate stars as spherically symmetric, non-rotating objects without a magnetic field. The variables describing the stellar structure, the radius $r(m)$, pressure $P(m)$, temperature $T(m)$, density $\rho(m)$, luminosity $l(m)$, and the chemical composition $X_i(m)$, where $\sum X_i = 1$, then only vary in the radial direction $r(m)$ at a point in time t. Using the fractional mass m, where $m = 0$ at the centre and $m = M$ at the surface, as an independent variable, a system of basic equations based on the assumptions of the conservation of mass, momentum, and energy, as well as the energy transport equation and the equation of nucleosynthesis, emerges:

$$\frac{\partial r}{\partial m} = \frac{1}{4\pi r^2 \rho}, \tag{1.1}$$

$$\frac{\partial P}{\partial m} = -\frac{Gm}{4\pi r^4}, \tag{1.2}$$

$$\frac{\partial l}{\partial m} = \varepsilon_n - \varepsilon_\nu + \varepsilon_g, \tag{1.3}$$

$$\frac{\partial T}{\partial m} = -\frac{GmT}{4\pi r^4 P}\nabla, \tag{1.4}$$

$$\frac{\partial X_i}{\partial t} = \frac{m_i}{\rho}\left(\sum_j r_{ji} - \sum_k r_{ik}\right),\ i = 1, \ldots, I. \tag{1.5}$$

Equations (1.2) and (1.4), where G is the gravitational constant, assume hydrostatic equilibrium, i.e. only the forces of pressure and gravity act on a mass element. In Eq. (1.3) ε_n is the energy gained from nuclear reactions, ε_ν is the energy loss through neutrino flux, and ε_g is the change of the internal energy through expansion or contraction. Together they produce a net amount of energy $l(m)$ passing outwards through a mass shell of the star. In the energy transport equation (Eq. 1.4) the temperature gradient is defined as $\nabla = d\ln T/d\ln P$ and describes the variation of temperature with depth, where the pressure is a measure of depth. When energy is transported by radiation or conduction only, then $\nabla = \nabla_{\rm rad}$, where

$$\nabla_{\rm rad} = \frac{3\kappa}{16\pi acG}\frac{lP}{mT^4}, \tag{1.6}$$

with κ the Rosseland mean opacity, a the radiation density constant, and c the speed of light. There are two criteria to decide whether a layer is stable against convection: the *Schwarzschild criterion*

$$\nabla_{\rm rad} < \nabla_{\rm ad}, \tag{1.7}$$

and the *Ledoux criterion*

$$\nabla_{\rm rad} < \nabla_{\rm ad} + \nabla_\mu, \tag{1.8}$$

where $\nabla_{\rm ad}$ is the adiabatic temperature gradient, describing the variation of temperature in a blob of matter as it rises or sinks adiabatically, and $\nabla_\mu = d\ln\mu/d\ln P$ is the mean-molecular-weight gradient, which has a stabilising effect. When $\nabla_{\rm rad}$ becomes too large, for example due to a high energy production rate or high opacity, convection becomes a more efficient mechanism to transport the energy. In this case ∇ in Eq. (1.4) can be estimated by, e.g. the *mixing-length theory*. In this theory it is assumed that hot macroscopic blobs rise a certain length before they dissolve into the new environment and dump their excess heat there. This mixing length $\ell_m = \alpha_{\rm MLT} H_P$ is usually treated as a free parameter in stellar models and expressed in terms of the local pressure scale height denoted by H_P. By comparing model calculations to helioseismic observations of the Sun, it was found that $\alpha_{\rm MLT}^{\odot} = 1.99$ (Christensen-Dalsgaard et al. 1996; Christensen-Dalsgaard 2002)[1]. Assuming that other stars have similar values, it is customary to take $\alpha_{\rm MLT}$ between 1.5 and 2.0. It is also assumed to have the same value throughout the stellar interior. In regions that are stable against convection, i.e. where Eq. (1.8) holds, the buoyancy force pushes the displaced mass elements back to their original position. As a mass element overshoots, it can start oscillating around its equilibrium position. This vibrational stability plays an important role for stellar oscillations (see Sect. 1.3). A characteristic frequency for an oscillating mass element is the Brunt-Väisälä frequency N,

$$N^2 \simeq \frac{g^2\rho}{P}(\nabla_{\rm ad} - \nabla + \nabla_\mu)\,, \tag{1.9}$$

with $g = Gm/r^2$, the gravitational acceleration.

---

[1] Data and parameters for Model S can be found at http://astro.phys.au.dk/~jcd/

Equation (1.5) represents the change in the mass fraction X_i of particles of type i and mass m_i with time, due to thermonuclear reactions r_{ji} (which convert particle j into particle i) and r_{ik} (which convert particle i into particle k). When the change in structure is slow compared to the change in composition, Eq. (1.5) can be decoupled from Eqs (1.1)-(1.4) and the stellar structure can be solved separately for a time t and composition X_i. This is the case on the main sequence (see Sect. 1.2.2), where hydrogen is fused into helium.

To solve the system of differential equations (1.1) to (1.5), we need to reduce the number of unknown variables to $4 + I$. With an *equation of state* we can describe the quantities ρ, ε_n, ε_ν, κ, and ∇_{ad} as functions of P and T. For an ideal gas with radiation, the equation of state would be

$$P = \frac{\mathcal{R}}{\bar{\mu}}\rho T + \frac{1}{3}aT^4 \tag{1.10}$$

with $\mathcal{R}$ the gas constant and $\bar{\mu}$ the mean molecular weight. The unknown variables are now r, P, T, l, $X_1, \ldots, X_I$ and the dependent variables are m and t. With the appropriate boundary conditions and initial parameters this system of equations can then be solved to obtain a *stellar model.*

Initial conditions

Several parameters need to be established upfront, such as the stellar mass M and the chemical composition X_i. Usually X_i is divided into three parts: the hydrogen mass fraction X, the helium mass fraction Y, and the "rest" Z. As Z contains all elements heavier than H and He, it is often referred to as the metallicity. It usually makes up $< 2\%$ of the total mass and it is difficult to measure its exact composition, i.e. how much of which element is contained in Z. For the Sun it is possible to derive precise metal mixtures, and considerable effort is put into this (see, e.g. Asplund et al. 2009). The composition for stellar models is then often taken relative to the Sun.

Another parameter that is difficult to define is the opacity κ, as it depends on the composition and the level of ionisation of the different elements. It would be very computationally intensive to compute the opacity on the fly. Hence, stellar modelling codes usually use precomputed opacity tables. These are the focus of several research groups and two examples are OPAL (Iglesias & Rogers 1993, 1996) and the *Opacity Project* (OP, Seaton 2005).

MESA

One example for a one-dimensional stellar modelling code is Modules for Experiments in Stellar Astrophysics, or short MESA[2] (Paxton et al. 2011, 2013, 2015). MESA is an open-source code with a large user base that continuously tests and updates the code thoroughly. It is divided into modules, which treat the physical aspects and numerical methods separately. Each module can be compiled and used on its own and they are all combined in the `star` module, which solves the stellar structure and evolves a stellar model. A MESA model of a star is divided into cells from the surface to the centre. For each cell the structure and composition equations are solved simultaneously. Some parameters are an average over the shell, while others are defined at the cell boundary. Before another time step is taken, the code reevaluates the meshing of the model and adjusts it to the changes in the previous time step, such as mass gain or loss and changes in the composition. Then it finds the next time step, optimised for computational speed and precision. Lastly, it solves for the altered stellar structure. In the following section, we explain the evolution of stars.

1.2.2 Stellar evolution

To determine the evolution of a star with certain input parameters, such as initial mass M and initial composition X_i, the stellar structure equations are solved at discrete time steps Δt. The evolution can be followed on the Hertzsprung-Russell diagram (HRD), where the surface luminosity L is plotted against the effective temperature T_{eff}. Figure 1.1 shows such an HRD with evolutionary tracks for stars with three initial masses 1.3 $M_{\odot}$, 1.6 $M_{\odot}$, and 2 $M_{\odot}$. The models were calculated with MESA and the default initial composition ($X = 0.7$ and $Z = 0.02$) was used.

Stars are born when a large molecular cloud collapses and fragments into several smaller parts. The fragments keep collapsing in free fall at first, which is eventually halted when the dense cores reach hydrostatic equilibrium. An accretion disk forms around the new protostar, which feeds matter to the star and from which new planets can form. In the centre, the protostar keeps contracting and the temperature increases. When the central temperature T_c is high enough to sustain stable hydrogen burning, the contraction of the protostar is stopped. Nuclear reactions are now the main source of energy and completely balance the energy loss through the surface luminosity. The star is in full equilibrium and has reached the zero-age main sequence (ZAMS). For hydrogen to occur via the *proton-proton chain* (*pp* chain), T_c has to be $\sim 5 \times 10^6$ K.

---

[2] http://mesa.sourceforge.net

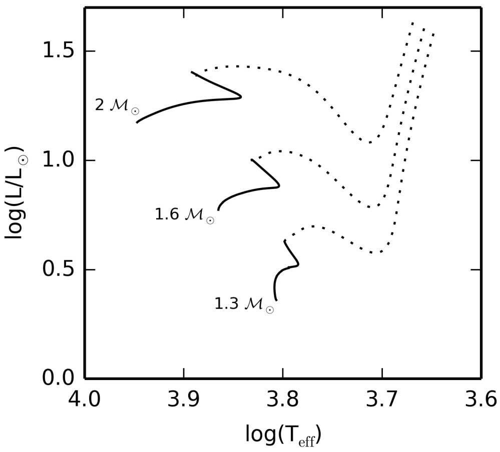

Figure 1.1: Hertzsprung-Russell diagram with evolutionary tracks for three initial masses. The main-sequence phase, where stable core-hydrogen burning takes place is represented by the solid lines. The post-main sequence phase, after the central hydrogen mass fraction, X_c, reaches zero, is displayed as dashed lines.

The reactions of the *pp* chain are:

$$\begin{aligned} {}^1\mathrm{H} + {}^1\mathrm{H} &\rightarrow {}^2\mathrm{H} + e^+ + \nu \\ {}^2\mathrm{H} + {}^1\mathrm{H} &\rightarrow {}^3\mathrm{He} + \gamma \\ {}^3\mathrm{He} + {}^3\mathrm{He} &\rightarrow {}^4\mathrm{He} + 2{}^1\mathrm{H} \end{aligned} \tag{1.11}$$

At higher T_c of about 1.5×10^7 K, the *CNO cycle* sets in:

$$\begin{aligned} {}^{12}\mathrm{C} + {}^1\mathrm{H} &\rightarrow {}^{13}\mathrm{N} + \gamma \\ {}^{13}\mathrm{N} &\rightarrow {}^{13}\mathrm{C} + e^+ + \nu_e \\ {}^{13}\mathrm{C} + {}^1\mathrm{H} &\rightarrow {}^{14}\mathrm{N} + \gamma \\ {}^{14}\mathrm{N} + {}^1\mathrm{H} &\rightarrow {}^{15}\mathrm{O} + \gamma \\ {}^{15}\mathrm{O} &\rightarrow {}^{15}\mathrm{N} + e^+ + \nu_e \\ {}^{15}\mathrm{N} + {}^1\mathrm{H} &\rightarrow {}^{12}\mathrm{C} + {}^4\mathrm{He} \end{aligned} \tag{1.12}$$

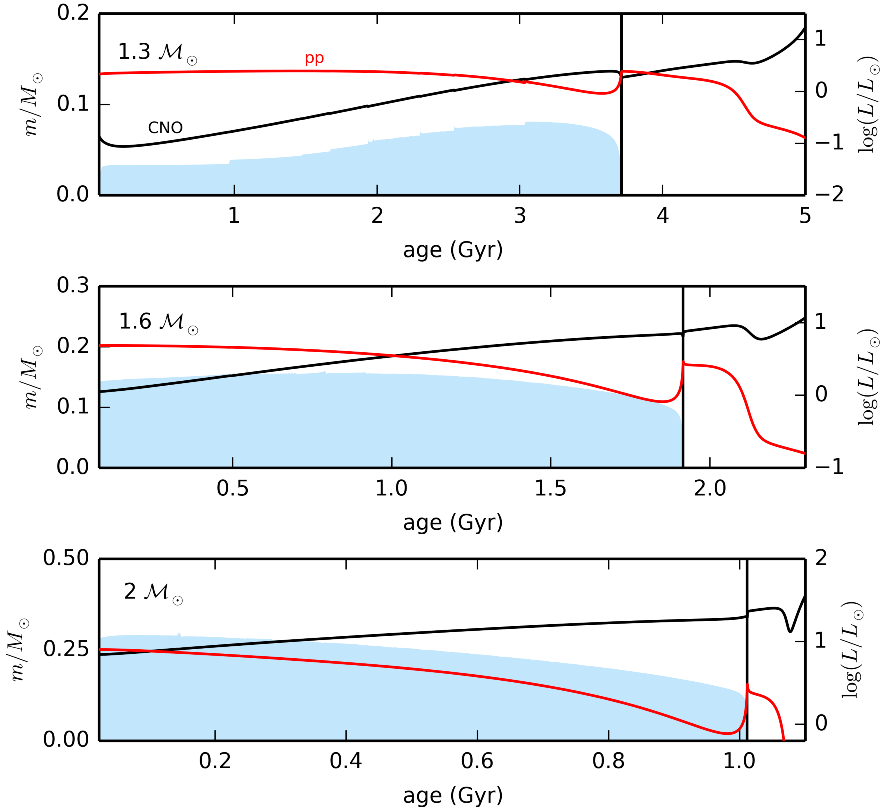

Figure 1.2: Evolution of the convective core (blue shaded region) and the energy production of the *pp* chain (red solid line) and the CNO cycle (black solid line) as a function of age for the tracks of Fig. 1.1. The extent of the convective core is shown as fractional mass and the energy production rates are in solar luminosities. The vertical lines indicate the point where X_c drops to zero. *From top to bottom*, panels display parameters of tracks for initial mass: 1.3 $M_\odot$, 1.6 $M_\odot$, and 2 $M_\odot$.

These nuclear reactions are very temperature sensitive. For the *pp* chain $\varepsilon_{pp} \propto T^6$ at $T = 5 \times 10^6$ K, while for the CNO cycle $\varepsilon_{\mathrm{CNO}} \propto T^{18}$ at $T \approx 20 \times 10^6$ K. The energy production from thermal contraction, on the other hand, is only $\varepsilon_g \propto T$. Thus, as hydrogen burning becomes the prime energy source, replacing thermal contraction, the energy production is more concentrated close to the stellar centre. This strongly influences the stellar structure and reorganises it, according to the dominant nuclear reaction chain. At Sun-like masses or below, T_c is just high enough to ignite the *pp* chain. A radiative core is surrounded by a deep convective envelope, which is caused by the low temperatures and high opacities at the surface. Stars of higher mass reach higher temperatures and the CNO cycle becomes more dominant throughout the main-sequence phase. Due to its higher energy production rate $\varepsilon_{\mathrm{CNO}} > \varepsilon_{pp}$, it causes the convective core to grow. This is the case for the star of $M = 1.3\ M_\odot$ and in the first half of the main sequence for the 1.6 $M_\odot$ star, as can be seen in Fig. 1.2. A growing convective core leads to a sharp increase of the mean-molecular-weight gradient ∇_μ at the edge of the convective region. Inside the core the molecular weight increases due to the conversion from hydrogen to helium, which causes the luminosity to rise. Near the surface, the convective zone becomes shallower the higher the mass and temperature. T_{eff} drops faster in radiative regions and the stars thus move to the right on the HRD (see Fig. 1.1). When the star has reached a minimum T_{eff} the central-hydrogen content is very low. As a consequence it contracts and quickly burns the remaining hydrogen. The contraction is accompanied with a movement to the left in the HRD. When the core is completely devoid of hydrogen, convection in the helium core ceases and hydrogen burning continues in a shell around it. As its outer envelope expands the star becomes a sub giant. In the centre, the helium core keeps growing in mass and starts contracting. The release of gravitational energy causes the envelope to increase tremendously and the star climbs up the red giant branch.

Stars with $M \gtrsim 1.6\ M_\odot$ have a shrinking convective core, as is the case in the second half of the main sequence for the star of $M = 1.6\ M_\odot$ and for the 2 $M_\odot$ star in Figs 1.1 and 1.2. Since $\kappa_e \propto (1 + X)$ in the cores of massive stars, the opacity in the core decreases leading to a decrease in ∇_{rad} and less need for convective motions to transport energy. The increasing dominance of the CNO cycle with growing mass leads to bigger convective cores (compare the two lower panels in Fig. 1.2). On the other hand, the outer convective region of stars becomes shallower until it it is completely radiative for stars $\gtrsim 2.2\ M_\odot$. Moreover, more massive stars have considerably shorter main-sequence life times, owing to the higher energy production rate. This can be illustrated by the nuclear time-scale, on which main-sequence stars evolve

$$\tau_H = E_H/L \sim M/L \sim M^{-2.5}. \tag{1.13}$$

At which masses the transition from a radiative to a convective core happens is influenced by many factors, such as, e.g. the initial composition and opacities, but it typically occurs between 1.3 $M_\odot$ and 2.2 $M_\odot$. In this thesis, we study stars of this mass range with asteroseismology.

The further evolution of the stars discussed above is similar. When the helium core reaches a certain mass and temperature, helium burning starts. They develop a dense CO core, while the outer envelope is large and cool with low densities. At this stage, stars lose a considerable amount of mass in the form of dust-driven winds. When the entire envelope is lost and the hot CO core with a thin helium shell is exposed, the star moves to the left on the HRD with increasing $T_{\rm eff}$. In the meantime, the surrounding shell can be ionised by the light of the remaining core and light up as a planetary nebula. The hot core becomes a degenerate white dwarf with a typical mass between 0.6 $M_\odot$ and 1.1 $M_\odot$, cooling and contracting as it loses gravitational energy.

1.2.3 Complications

Even though the structure and evolution of intermediate-mass main-sequence stars seems to be fairly well understood, there are still several complications left in the current theories. One of these is convection. Since there is still no complete theory on the turbulent motions of convective eddies, basic approximations, such as the mixing-length theory, are currently used in stellar modelling codes. It is applied to the regions inside the star, where the stability criterion from Eq. (1.7) does not hold. Consequently there is a strict border to the convective core, where $\nabla_{\rm rad} = \nabla_{\rm ad}$. However, a mass element, which experiences an acceleration by the buoyancy force, does not stop at this border and, owing to its inertia, penetrates into the radiative zone. As the radiative zone is stable against convection, the mass element is stopped after a short distance and pushed back by the buoyancy force, which causes mixing of the stellar material. This phenomenon is called convective-core overshooting. It strongly influences the stellar evolution, as fresh hydrogen from the radiative zone is mixed into the convective core. This not only creates a more massive helium core at the end of the main sequence, but it also prolongs the time the star spends burning hydrogen in the core. The distance the convective blobs travel inside the radiative zone is not well known. It is assumed to be only a fraction of the local pressure scale height H_P and is usually treated as a free parameter in stellar modelling codes. Fitting isochrones to observations of eclipsing binary stars (e.g. Claret 2007; Stancliffe et al. 2015) or comparing theoretically predicted pulsations of stellar models to observed mode frequencies (e.g. Moravveji et al. 2015, 2016) are two methods to deduce the overshooting parameter $\alpha_{\rm ov}$. We demonstrate these methods in Chapter 4 with the pulsating binary KIC 10080943.

Another complication in stellar modelling is rotation. Due to the complicated hydrodynamical processes it induces, rotation is often ignored in one-dimensional stellar modelling codes. Nonetheless, it has several significant effects on the structure and evolution of stars (for an extensive review, see Maeder & Meynet 2012). For example, the spherical symmetry is broken as the centrifugal force causes stars to be flatter at the poles and rotation can alter the later stages of evolution (i.e. stellar winds or supernova explosions). Furthermore, rotation can induce mixing, which is often approximated by a diffusion process in the radiative parts of the model. However, this neglects shear layers and differential rotation in the radial direction. Essentially, the internal rotation of a star is invisible to us. Through most observing techniques, such as rotational modulation due to surface spots or Doppler-broadened spectral lines, we can only measure the surface rotation rate. Asteroseismology is the only method that allows us to place observational constraints on physical processes, deep inside the star. This has raised new questions to be answered: angular momentum transport seems to be more efficient than initially assumed, leading to too fast rotation of red giant cores (e.g. Beck et al. 2012; Tayar & Pinsonneault 2013; Deheuvels et al. 2015; Fuller et al. 2015) or counter-rotating layers seem to be possible inside stars (e.g. Triana et al. 2015; Rogers 2015). In Chapters 3 and 4 we will present a measurement of the internal rotation for the stars KIC 10080943A and KIC 10080943B.

1.3 Asteroseismology

The theories that were introduced in the first section have to be tested and for this we rely on observations. Classical spectroscopic or photometric observations are confined to the stellar surfaces. So, every inference that is made on the interior conditions is subject to uncertainty and degeneracies. Asteroseismology, on the other hand, allows a unique view into the deep interiors of stars. Stellar pulsation modes propagate inside the star and are sensitive to different regions, depending on where their amplitudes are the highest. On the surface, they cause brightness or radial velocity variations, which can be seen in time-resolved observations. During the data analysis process, the aim is to gather as many observational constraints from the observed pulsations as possible. How many constraints can be derived and their quality is strongly dependent on the quality of the seismic data. A long time base and a high duty cycle is needed to resolve the pulsation frequencies and a low noise level is necessary to detect numerous low-amplitude modes. From the ground, extensive observing campaigns are difficult to organise. Large telescopes, which provide high precision for faint stars, are oversubscribed and the night-day rhythm leads to gaps in the data. In Chapter 2 we show the challenges of ground-based observations for seismic applications and present the analysis of an extensive spectroscopic dataset of the bright F-type star 4 CVn. Great breakthroughs have been achieved in the recent years by space-bourne missions, such as CoRoT (Auvergne et al. 2009) and *Kepler* (Borucki et al. 2010). An introduction to *Kepler* and some of its major discoveries is given in Sect. 1.5.1. In Chapter 3 we present the analysis of a *Kepler* target.

In this section we introduce the basics of how and why stars pulsate. A more comprehensive review is provided by Aerts et al. (2010). Updates, including new insights, are given by Chaplin & Miglio (2013) and Aerts (2015).

1.3.1 Stellar oscillations

Stellar oscillations are described as perturbations to the equilibrium structure and appear in the form of *pressure modes* or *gravity modes*. For pressure modes, or in short p modes, the pressure force acts as the dominant restoring force and the gas motions are predominantly in the radial direction. They have their highest amplitudes in the acoustic cavity in the outer regions of the star. For gravity modes, or g modes, the dominant restoring force is buoyancy. They propagate in the interior radiative parts of the star, so are either trapped underneath the convective envelope or are confined to the regions near the convective core. The g modes primarily cause displacement in the horizontal direction. This means that the spherical symmetry of the equilibrium structure is not preserved in a pulsating star. Thus, we describe the displacements due to the perturbations in three directions; radius r, co-latitude θ, and longitude ϕ. The co-latitude is measured from the pulsation axis, which is, except in some special cases, assumed to be the axis of rotation. The three components of the displacement vector of one mode are then given by

$$\xi_r(r,\theta,\phi,t) = a_n(r) Y_\ell^m(\theta,\phi) e^{-\mathrm{i}2\pi\nu t}, \tag{1.14}$$

$$\xi_\theta(r,\theta,\phi,t) = b_n(r) \frac{\partial Y_\ell^m(\theta,\phi)}{\partial\theta} e^{-\mathrm{i}2\pi\nu t}, \tag{1.15}$$

$$\xi_\phi(r,\theta,\phi,t) = \frac{b_n(r)}{\sin\theta} \frac{\partial Y_\ell^m(\theta,\phi)}{\partial\phi} e^{-\mathrm{i}2\pi\nu t}, \tag{1.16}$$

where $a_n(r)$ and $b_n(r)$ are the radial and horizontal amplitudes, respectively, ν is the frequency, and Y_ℓ^m denotes the spherical harmonic representing the angular dependence of the mode. This gives rise to three quantum numbers: n, ℓ, and m. The *radial order* n gives the number of nodes in the radial direction. The higher the number of radial nodes, the higher the frequencies of p modes, while for g modes there is an increase in period. The number of surface nodal lines is given by the *spherical degree* ℓ and the *azimuthal order* m denotes how many of these surface nodes are lines of longitude. There are thus $|m| = 2\ell + 1$ possible values for m.

When $\ell = 0$, the star only oscillates in the radial direction and thus preserves its spherical symmetry. These modes are always p modes. The simplest mode is the radial fundamental, where $n = 1$ and the centre of the star is the only node in radial direction. A characteristic period for the radial fundamental mode can be estimated from the

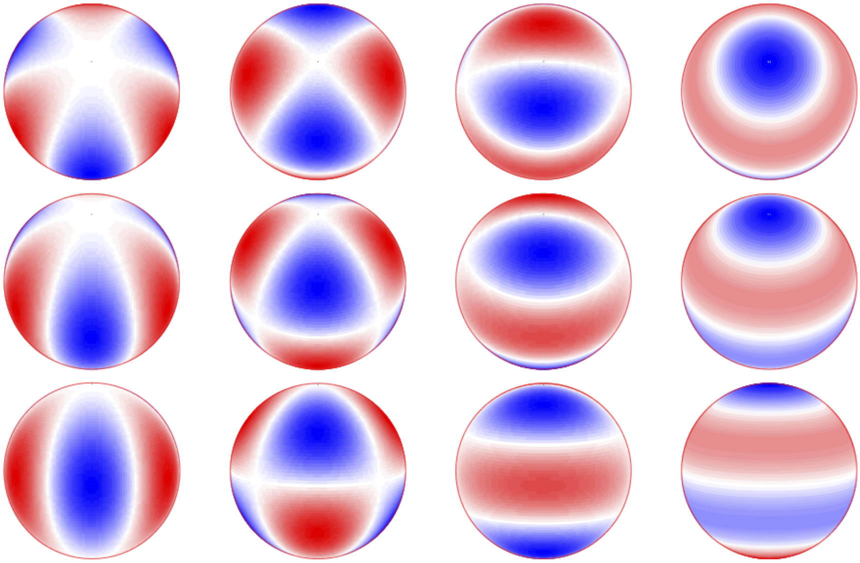

Figure 1.3: Snapshots of non-radial *octupole* modes ($\ell = 3$) as seen under an inclination angle $i = 30°$ *(top row)*, $i = 60°$ *(middle row)*, and $i = 90°$ *(bottom row)*. The white lines are the surface nodes, which are at rest with respect to other surface elements. The red parts are moving inwards while they heat and the blue parts are moving outward while they cool. The azimuthal order m is decreasing from left to right. On the left side are the *sectoral* octupole modes, where $\ell = |m|$ and $(\ell, m) = (3, \pm 3)$, and on the right are the *axisymmetric* modes, where $(\ell, m) = (3, 0)$. In the middle, the two *tesseral* modes with $(\ell, m) = (3, \pm 2)$ and $(\ell, m) = (3, \pm 1)$, are shown. Figure courtesy of C. Aerts.

dynamical time scale $\tau_{\text{dyn}} = \sqrt{R^3/GM}$, which is the time it takes a star in hydrostatic equilibrium to recover from a slight perturbation.

The more complicated case of $\ell \neq 0$ gives rise to non-radial modes, which also cause displacements in the horizontal direction. The $\ell = 1$ modes are referred to as *dipole* modes, $\ell = 2$ modes are *quadrupole* modes, $\ell = 3$ modes are *octupole* modes, and so on. Dipole modes have one nodal line on the surface, which is either a line of co-latitude for the axisymmetric mode, where $m = 0$ or of longitude for the sectoral mode, where $m = \pm 1$. Figure 1.3 shows how the surface elements of an octupole mode are displaced. Adjacent surface elements always move in the opposite direction and cool while they expand or heat while they contract. The stationary lines in between are the surface nodes, which are given by the degree. For the Sun, we are able to resolve the surface and map the variations in the surface velocity field. For distant stars, however, this is not yet possible and we can only measure the integrated brightness or velocity in the line-of-sight over the surface. As a consequence the intensity variations of the surface elements of high-degree modes cancel each other out and result in lower apparent amplitudes when the intrinsic amplitudes are equal. In practice, only low-degree modes can be observed in photometry. This effect is called *partial cancellation*.

In Fig. 1.4 examples of *eigenfunctions*, i.e. the displacement vectors of the modes, as well as the *mode inertia* (see Eq. (3.139) in Aerts et al. 2010) are shown. The radial fundamental mode, a low radial-order dipole p mode, and a high radial-order dipole g mode were computed with GYRE (see below) for the three models of Fig. 1.1 at $X_c = 0.33$. It can be seen that the g mode causes much larger displacements in the horizontal direction than in the radial direction and that its inertia is much larger in the stellar interior than the one of the p modes. Furthermore, its oscillation is offset from the centre of the star and starts at the edge of the convective core.

In the non-rotating case all $2\ell + 1$ modes of a certain ℓ and different m have the same frequency. This degeneracy is lifted when a star is rotating. As the rotation axis is assumed to coincide with the pulsation axis, modes of $m \neq 0$ are travelling waves. *Prograde* modes with positive m are travelling in the direction of rotation, while *retrograde* modes with negative m travel in the opposite direction. The Coriolis force causes a shift in the frequencies, slightly reducing those of prograde modes and increasing retrograde mode frequencies. In an inertial frame of reference, the rotation frequency Ω is added to the mode frequencies and, hence, has the opposite effect. The combined effect of the Coriolis force and the rotation frequency can be described to first order as

$$\nu_{n\ell m} = \nu_{n\ell 0} + m(1 - C_{n\ell})\Omega/2\pi \tag{1.17}$$

(Ledoux 1951), where $C_{n\ell}$ is the Ledoux constant and $\nu_{n\ell 0}$ is the axisymmetric mode, which is unaffected by rotation. The observation of rotationally split multiplets greatly aids mode identification, i.e. the practice of assigning an ℓ and m value to observed frequencies. Knowing which mode gives rise to which frequency is essential when comparing observations to theoretical frequency spectra. It allows us to gain insight into which parameters and physical descriptions have to be changed in the stellar models to give the best prediction of the observed pulsation modes. Another method of mode identification, based on line-profile variations is presented and applied to a δ Scuti pulsator (see Sect. 1.3.3) in Chapter 2.

GYRE

GYRE[3] (Townsend & Teitler 2013) is a stellar pulsation code that solves the linearised pulsation equations and computes the eigenfunctions and eigenfrequencies of a stellar model. An already computed stellar model, e.g. a MESA model, can be provided as

---

[3] https://bitbucket.org/rhdtownsend/gyre/wiki/Home

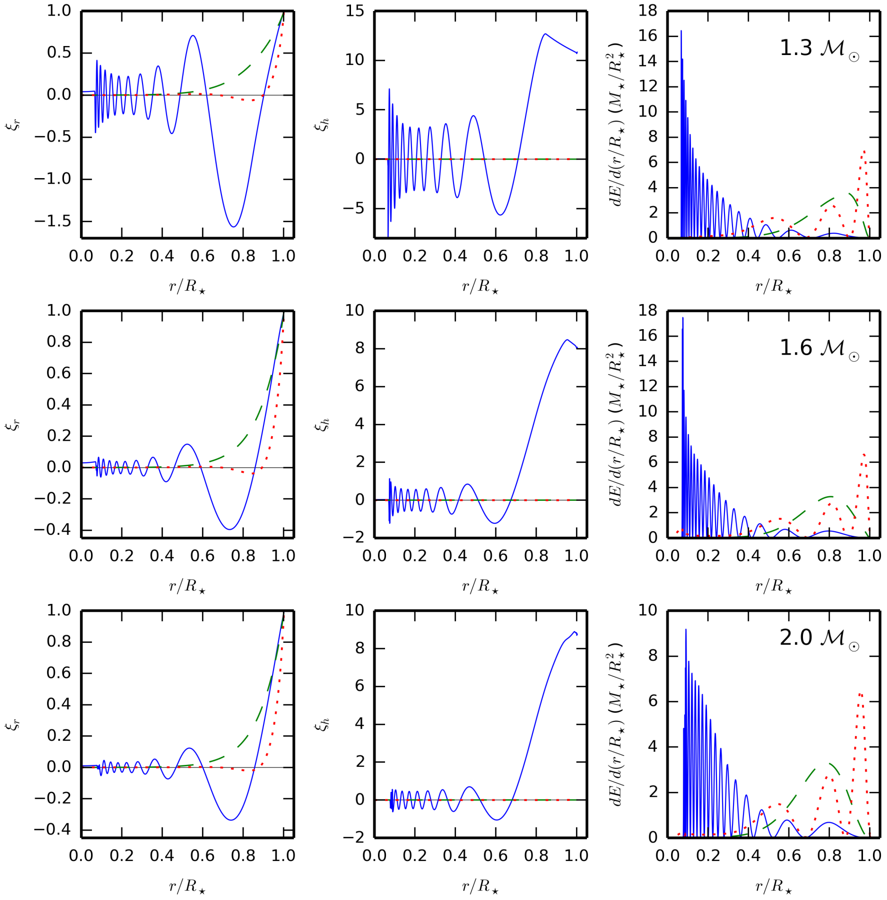

Figure 1.4: Eigenfunctions and mode inertia of the radial fundamental mode (green dashed line), the dipole p mode of $n = 3$ (red dotted line), and the dipole g mode of $n = -20$ (blue solid line) for the three models of Fig. 1.1 at $X_c = 0.33$ as a function of the fractional radius of the star. The radial and horizontal components of the displacement vector are shown in the *left* and *centre panels*, respectively. They are normalised such that the radial components attain value 1.0 at the stellar surface. The horizontal black line indicates zero displacement. In the *right panels* the differential mode inertia is shown for each mode.

input to the code. Alternatively, GYRE provides the possibility to generate polytropic models. After the input stellar model is read, the radial grid is reconstructed and the code starts the search for the eigenfrequencies. This is based on a user defined frequency interval and step size. GYRE can perform adiabatic as well as non-adiabatic computations. Rotation can be considered, either by providing a rotating stellar model, or by perturbing the eigenfrequencies. The perturbations can be computed according to Eq. (1.17) or through the Traditional Approximation of Rotation (TAR, e.g. Townsend 2003), which is based on the inclusion of the Coriolis force in the equation of motion while neglecting the horizontal component of the rotation vector. GYRE is, as MESA, an open-source code, which provides the possibility to use these two codes together.

1.3.2 Driving mechanisms

Most of the energy of the perturbations is lost throughout the volume of the star. As the star aims to return to its equilibrium state, it damps the oscillations. In order for oscillations to become stable and reach observable amplitudes, there has to be a mechanism to feed energy into the initial perturbation. This mechanism has to be efficient enough to overcome the damping caused by the rest of the stellar interior.

There are different mechanisms driving perturbations to become stable pulsations. Here we will discuss two, which are at work in the stars discussed in this thesis.

The κ mechanism

One way how energy can be fed into perturbations is by transferring thermal energy into kinetic energy, following the principle of a heat engine. For this mechanism to work, a layer inside the star must be able to trap heat upon compression. Under normal circumstances, the temperature of a compressing layer will increase and cause a drop in opacity, according to Kramers' law

$$\kappa \propto \rho T^{-7/2}. \tag{1.18}$$

This is not necessarily the case for partial ionisation zones, however. There, part of the energy gained upon compression will be used to ionise the matter. Consequently, the temperature does not rise as much and the density increase will lead to an increase in opacity. The radiation below this opaque layer is trapped and pressure builds up, causing the layer to expand again. During the expansion the matter recombines and emits extra energy to the surroundings. The layer therefore does not cool as much as without recombination, which means that the opacity drops. The radiation, trapped below the partial ionisation zone, is free to flow through and transport the energy past this layer. This is accompanied by a drop in pressure, which causes the layer to contract, starting the cycle all over again. Due to the role opacity plays in this cycle this mechanism is also called the κ mechanism. This mechanism can only operate if there is a region of partial ionisation in the correct position inside the star. If this layer is too close to the surface, its density is too low to support the pulsations. If it is too deep inside the star, the enclosing matter will damp the oscillations. This mechanism is responsible for the excitation of low-order pressure modes in intermediate-mass stars (Chapter 2).

The convective-flux blocking mechanism

In stars with sufficiently deep outer convective zones, radiation can be blocked and transferred into mechanical energy that drives oscillations. This is because at the bottom of these zones, the radiative flux drops suddenly and energy is transported by convective motions. Additional flux coming from a perturbation below, thus cannot be transported inside the convective zone by radiation. When this layer is at a certain depth inside the star, the period of this oscillation is similar to the time it takes a mass element to release excess heat to its surroundings, i.e. the thermal relaxation time. The convective flux thus has no time to adapt to the variations induced by the oscillations and periodically blocks the radiative flux coming from below, transferring it into kinetic energy and driving the pulsation. This mechanism is responsible for the excitation of high-order gravity modes in intermediate-mass stars (Chapters 3 and 4).

1.3.3 Pulsating stars across the HRD

Across the HRD, from young pre-main-sequence stars to old white dwarfs, stars pulsate. In Fig. 1.5, we can identify regions with a cumulation of pulsating stars and for each region there is one dominating mode type. This reflects the interior conditions, which are necessary for stars to become unstable against perturbations and to start oscillating.

We can follow the main sequence to see how the interior changes and where it is favourable of pulsations. On the low-mass end of the ZAMS we can find our Sun and other *solar-like pulsators*. For these stars the convective envelope is deep enough that turbulent motions can stochastically excite oscillations. The p modes are constantly damped and re-excited and lead to frequency spectra with a Gaussian-like envelope peaking at a frequency of maximum power. It is expected that all stars with deep convective envelopes show these types of oscillations. Indeed, De Ridder et al. (2009) could show, based on CoRoT data, that also red giant stars have stochastically excited p modes. If we move up in mass along the ZAMS, the convective envelope gradually becomes shallower. In γ Dor stars it can excite g modes through the convective-flux blocking mechanism. More details on γ Dor stars are given below and in Chapters 3 and 4. When the convective envelope becomes even shallower, the second partial

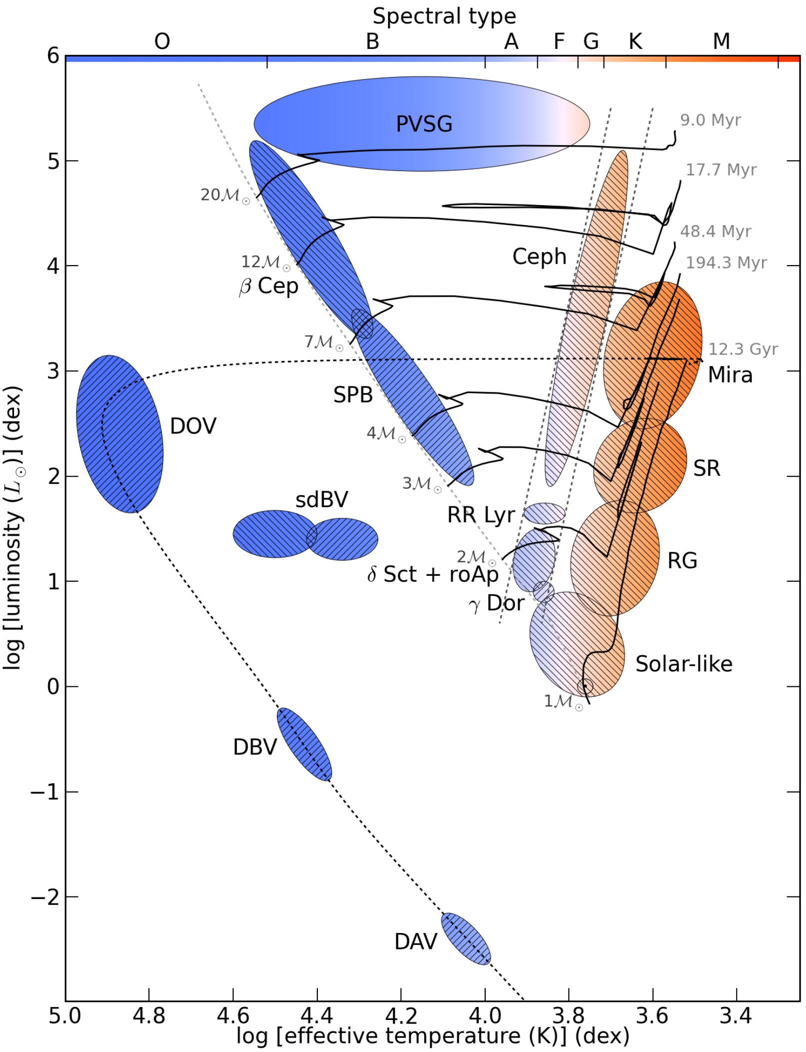

Figure 1.5: Hertzsprung-Russell diagram with the classes of pulsating stars indicated by the coloured patches. The colour corresponds to the spectral type, which is given on the top axis, and the hatching marks the mode type (\\ is for p modes and // is for g modes). Evolutionary tracks are taken from Schaller et al. (1992) and Driebe et al. (1998) and initial masses and evolutionary time scales are added in grey. The two parallel vertical dashed lines mark the classical instability strip, while the light-grey dashed line is the ZAMS. Figure courtesy of P. I. Pápics, inspired by a similar figure made by J. Chirstensen-Dalsgaard.

ionisation zone of helium is situated in a good position to drive p modes through the κ mechanism. This is the case within the *classical instability strip* (the two parallel lines in Fig. 1.5), where the δ Sct stars (for more details see below and Chapter 2), and the evolved RR Lyrae and Cepheid pulsators can be found. Young contracting stars also cross the instability strip on their way to the main sequence and pulsate as δ Sct stars (e.g. Zwintz et al. 2014). On the red edge of the classical instability strip, the partial ionisation zone of hydrogen is responsible for the Mira and semi-regular (SR) variables. On the more-massive end of the ZAMS, the interior is hot enough for the partial ionisation zone of the iron-group elements to excite pulsations via the κ mechanism. First, we find the slowly-pulsating B-type (SPB) stars, which have low-frequency g-mode oscillations. In even more massive and hotter stars, the κ mechanism excites p modes in the β Cep stars.

On the left side of the main sequence, we find compact pulsators; white dwarfs and sub-dwarf B (sdB) stars. The former are end-products of stellar evolution of stars born with a mass $< 9\ M_\odot$. Their g modes are driven by the heat mechanism in the partial ionisation zones of C and O. The sdB stars are exposed He-burning cores of evolved stars that have lost their H envelopes, likely due to binary interaction. These stars exhibit both g and p modes, which are excited in the partial ionisation zone of iron-like elements.

In Fig. 1.5 we find that some g mode and p mode instability regions overlap. In these regions, stars are expected that show both types of modes simultaneously. These are called hybrid pulsators. This is the case for the γ Dor and δ Sct stars, the SPB and the β Cep stars, as well as the sdB variable stars. Hybrid stars are especially rich objects to study, as the g modes allow us to probe the core regions, while the p modes have high amplitudes in the outer layers of the star. Another type of hybrid pulsators are stars which show heat-driven and stochastically excited modes simultaneously. Cool δ Sct or γ Dor stars with a substantial convective envelope could exhibit such a hybrid behaviour. We will now go into more detail of the γ Dor and δ Sct stars, and hybrids thereof.

γ Dor stars

Cousins et al. (1989) first reported the variability of the star γ Doradus and Cousins (1992) found two sinusoidal periods in the light curves. Spot models by Balona et al. (1994) failed to explain the variability and it was suspected that γ Dor might belong to a newly discovered class of pulsating stars. Several other stars showed a similar type of variability, for example 9 Aurigae (Krisciunas et al. 1995). This led Kaye et al. (1999) to define the γ Dor-type variables as a class of pulsating stars. They are multi-periodic A7-F5 stars with $T_{\rm eff} = 6500 - 7500$ K, oscillating in high-order low-degree g modes with periods between 0.4 d and 3 d. However, the physical mechanism behind their pulsations was not yet understood. Guzik et al. (2000) first proposed the convective-flux blocking mechanism to be responsible for the pulsations in this class. They used the mixing-length theory or "frozen" convection approximation, which assumes that the convective motion is time-independent and mixing is instantaneous. Using a more realistic treatment of time-dependent convection, Grigahcène et al. (2005) and Dupret et al. (2005) could confirm this theory. Furthermore, they excluded a contribution from the κ mechanism to the driving of γ Dor pulsations but predicted the existence of γ Dor/δ Sct hybrid stars.

Due to their periods of the order of one day, these stars are difficult to detect from the ground. Aerts et al. (1998), Handler (1999), and Henry et al. (2007) reported some 100 bona fide γ Dor stars that were found by ground-based observations and in Hipparcos data. On the other hand, Cuypers et al. (2009) made a thorough analysis of the high-precision g-mode frequencies found in a large sample of γ Dor stars studied from ground-based multi-colour photometry. Only a handful of γ Dor/δ Sct hybrids were known. This picture was overturned by the nearly uninterrupted data by CoRoT and *Kepler*. These new observations revealed several hundred new γ Dor stars, of which about a third were hybrid stars (e.g. Grigahcène et al. 2010; Uytterhoeven et al. 2011; Hareter 2012; Bradley et al. 2015).

δ Sct stars

The δ Sct pulsators are already known for more than a century, when it was first discovered that the star δ Scuti has variable radial velocities. A detailed review, including some historical remarks, is given by Breger (2000a). The stars of this pulsating class are slightly more massive and hotter (T_{eff} between 7000 and 8000 K) than the γ Dor stars and have shorter pulsation periods of 18 min to 8 hr. However, as mentioned above, the instability regions for these two types of stars overlap and γ Dor/δ Sct stars with long and short periods exist. The δ Sct stars lie in the classical instability strip and are main-sequence or sub-giant stars. In early studies it was assumed that δ Sct stars pulsate in radial modes, but it is meanwhile well known that most have many non-radial modes. Extensive ground-based observing campaigns have revealed more than 75 frequencies for FG Vir (Breger et al. 2005; Zima 2006) and more than 30 frequencies for 4 CVn (Breger et al. 1999; Breger 2000b; Schmid et al. 2014, and Chapter 2 in this thesis).

The high-precision photometry assembled by space missions was also beneficial for the research on δ Sct stars, revealing many low-amplitude modes (of the order of μmag). This led to the discovery of many δ Sct, but also γ Dor stars outside the theoretical instability strips (Balona & Dziembowski 2011; Balona et al. 2011; Uytterhoeven et al. 2011; Bradley et al. 2015) and calls for a revision of the theory of mode excitation.

1.4 Binary stars

Stellar multiplicity and binary stars are interesting and rewarding research fields. Binaries are abundant, about 50 % of intermediate-mass stars are estimated to reside inside binary or multiple systems (Duchêne & Kraus 2013); they are responsible for phenomena that cannot be explained without multiplicity, such as some stars with peculiar abundances and the existence of sdB stars, among others; they are a crucial source for precise and accurate stellar parameters without the need to rely on stellar models (Torres et al. 2010). In this thesis we mainly use the binarity of our targets as an asset for obtaining precise stellar masses and radii. We will now introduce the basics of binary stars, modelling their observations, and their evolution. More details are provided by Hilditch (2001) and Aerts et al. (2010).

For the purpose of obtaining precise stellar parameters, the most interesting binary systems are those with two members of similar brightness and in a slow evolutionary phase without mass exchange. Here, we focus on unevolved stars. In this case, a spectrum of the system is a composite of both components. From this double-lined spectrum we can obtain two radial-velocity curves with their *semi-amplitudes*

$$K_{1,2} = \frac{2\pi a_{1,2} \sin i}{P(1-e^2)^{1/2}}, \tag{1.19}$$

where P is the orbital period, e is the eccentricity, and $a_{1,2}$ are the semi-major axes of the elliptical orbits of each component. Since these velocity amplitudes relate to each other in the way $K_1/K_2 = M_2/M_1 = q$, the ratio of the component masses can be obtained by relying only on Kepler's laws and geometry. However, the observed radial-velocity curves are only a projection of the real orbits as they are seen under an inclination angle i. Thus, we can only derive a minimum value for the masses from double-lined spectroscopic binaries. Under certain circumstances, the inclination can be derived from light curves. If i is close to $90°$, then the stars periodically move in front and eclipse each other, causing a dip in the overall brightness. Furthermore, the width of the eclipses is related to the relative sizes of the stars $r = R/a$, where R is the stellar radius. Another way to derive the inclination angle was proposed by Welsh et al. (2011) for the eccentric ellipsoidal variable KOI-54. Due to the extreme eccentricity of the system, the stars approach so closely in periastron that they become deformed. This leads to an increase in brightness as the visible cross sections of the component stars change. From the precise shape of the peak in brightness and thanks to *Kepler's* high-precision photometry the authors concluded that the inclination has to be $i = 5.5° \pm 0.1°$. In Chapter 3 we apply this method to the system KIC 10080943. The absolute masses and radii can then be combined with effective temperatures, e.g. from spectroscopic analysis, to derive the luminosities and place both components on the HRD. In the best cases the relative uncertainties for these values are just a few percent. In the future, precise distances from the ESA mission Gaia[4] (Perryman et al. 2001) offer another opportunity to derive luminosities for binary systems, which can be used to compare results from different methods.

1.4.1 Pulsations in binary stars

Binary systems containing pulsating stars allow us to combine two complementing methods to test and improve stellar models. Ideally, we managed to perform mode identification for the pulsating component star, to know which modes give rise to the observed frequencies. We can then use the model-independent measurements of the masses and luminosities to eliminate free parameters in the modelling process. However, in close binaries the oscillations of a star can be influenced by the tidal effects exerted by the companion. For example, the frequencies of free oscillations that are excited by the κ mechanism, or other intrinsic driving mechanisms, may be shifted. Very strong tidal effects, such as in close binaries with high eccentricity, may also excite modes that are otherwise damped. This happens when a forcing frequency of the tidal force comes close to an eigenfrequency of a component star. The tidal forces usually drive modes of $\ell = 2$ that are a multiple of the orbital frequency (Aerts 2007).

Aside from the benefit binarity can bring to seismic modelling, the data analysis can be quite challenging. In double-lined systems the two stars are usually very similar in terms of mass and T_{eff}. As both of these stars might be pulsating, it can be difficult to tell which frequency belongs to which star or if they only originate in one star. In Chapter 3 we demonstrate how we unravelled the dense frequency spectrum of the γ Dor/δ Sct hybrid binary KIC 10080943 and assign a majority of the high-amplitude modes to either of the components. Another complication that can arise, especially for eclipsing binary stars, is the disentangling of the binary and the pulsation signal in the light curve. This is usually done in an iterative approach (see, e.g. Debosscher et al. 2013; Maceroni et al. 2014). The analysis of pulsating binary stars is, therefore, a time consuming, yet rewarding procedure.

1.4.2 The Roche model

If two members of a binary system are sufficiently close, they are deformed by the gravitational pull of their companion. This deformation can be described by the *Roche model*, which describes the gravitational potential around two point masses revolving about their centre of mass. Around each point mass, there are surfaces of constant potential and on these *equipotential surfaces* the surface of a star can be located. This is illustrated in Fig. 1.6. Close to the centre of the star, the equipotential surface is

---

[4] http://sci.esa.int/gaia/

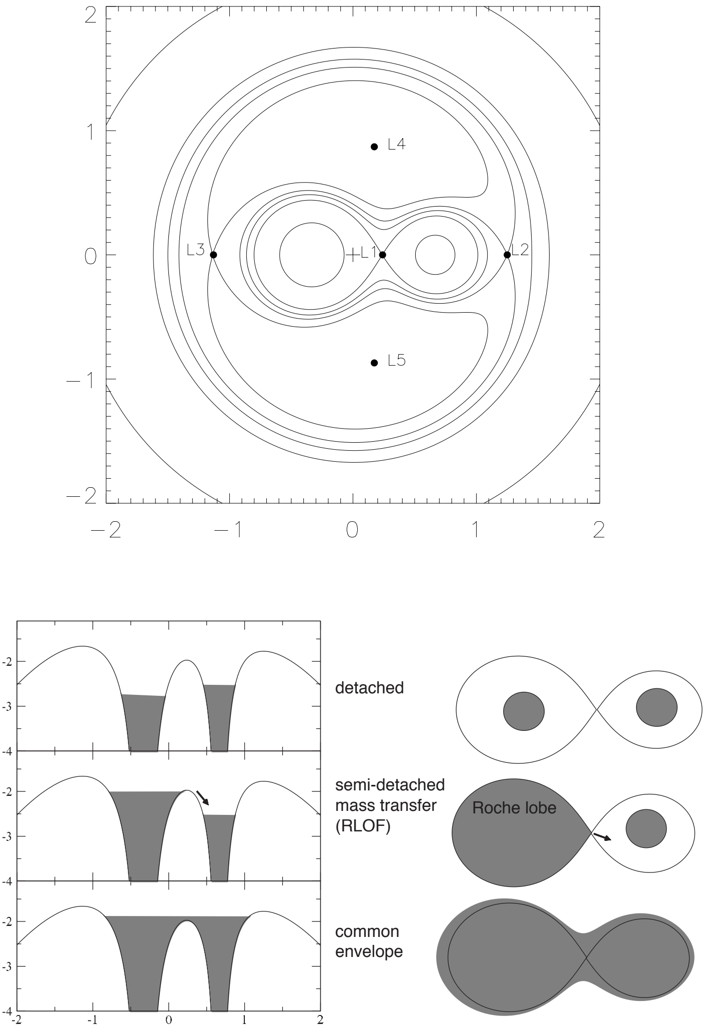

Figure 1.6: *Top panel:* Equipotential surfaces in the (x, y) plane for a binary system with mass ratio $q = M_2/M_1 = 0.5$. The origin of the coordinate system is situated at the centre of mass, marked by the cross. All five Lagrangian points are indicated by black dots and labelled. The Roche lobe is the "eight-shaped" curve passing through L_1. *Bottom panel:* A schematic representation of the potential well and the Roche lobes for a binary system of the same mass ratio in three scenarios: detached (top), semi-detached (middle), and common envelope (bottom). Figure taken from Jorissen (2003).

spherical and separate from the equipotential surface around the other star. As we move further away from the point mass in the centre, the surfaces become more deformed until they touch at the *inner Lagrangian point* L_1. This is the limiting surface within which all matter is bound to a star. It is called the *Roche lobe*. The absolute sizes of the Roche lobes depend primarily on the separation a between the two stars, while the mass ratio q influences their relative size. For $q = 1$ the Roche lobes of both components have equal size, while for $q < 1$ the Roche lobe of the more massive star is bigger than that of the less massive star. One limitation of the Roche model is that it is only defined for tidally-locked binaries in a circular orbit. It can be generalised to asynchronous rotation and eccentric orbits under the assumption that both stars rotate as rigid bodies and conserve their volume. In this case, the Roche lobes are dependent on the orbital phase. During the evolution of the binary the Roche lobes play an important role, as will be explained in more detail in the following section.

PHOEBE

PHysics Of Eclipsing BinariEs (PHOEBE[5]) (Prša & Zwitter 2005) is a modelling tool based on the Wilson-Devinney code (Wilson & Devinney 1971; Wilson 1979). It was designed to model light curves and radial-velocity curves of eclipsing binary stars. A Roche model of the binary system, described by the input parameters, is computed for a discrete number of points. At each point the model is evaluated to construct the synthetic light and radial-velocity curves. In this process the variation of the surface brightness due to local variation in the gravitational acceleration or mutual irradiation of the components is computed. To match the synthetic data to observations, two optimisation algorithms are included into the package; the differential corrections method (Wilson 1993) and the Nelder-Mead simplex (Nelder & Mead 1965). The increasing precision of photometric and spectroscopic data allowed new discoveries such as, e.g. Doppler beaming (Bloemen et al. 2013) and called for an improvement of the current methods. A new version, PHOEBE 2.0, is currently being developed (Prša et al. 2013; Degroote et al. 2013). It will include new optimisation routines and allow the use of different types of observations, e.g. interferometry, in addition to photometry and radial velocities. This new version is still in its development and validation phase. For this reason, we used the original PHOEBE version in this thesis.

1.4.3 Evolution of binary stars

Most binary systems start out as a *detached* system, where both components are confined within their Roche lobe. In this phase their evolution is often assumed to be like that of a single star. Yet, each star is subject to the tidal torque exerted by the

---

[5] http://phoebe-project.org

companion, which causes a slight deformation and, hence, a departure from spherical symmetry. The tidal force is strongest along the line connecting the centres of both stars in the orbital plane. For a rotating star the axis of symmetry, therefore, quickly aligns with the axis of orbital motion. If the star rotates more quickly about its own axis than it orbits its companion, the tidal bulge runs "ahead" of the tide-generating potential, which pulls it back. If the rotation is slower than the orbital period, the bulge lags behind and is pulled up by the tidal force. The tidal force thus slows down or speeds up the rotation of the stars, while simultaneously decreasing or increasing the separation a between them. This leads to an exchange of angular momentum between the components and the orbit as the system *synchronises* and *circularises*. The former happens when the rotational angular frequency of the components converges to the orbital angular frequency and the system becomes tidally locked. Synchronisation is expected to happen on shorter time scales than circularisation (e.g. Zahn 1992). In low-mass stars with a convective envelope the tide is dissipated more efficiently, owing to friction of the turbulent motions. It is the fastest mechanism and can be estimated by the friction time scale $t_f \sim (MR^2/L)^{1/3}$. Zahn (1977) derived the time scales for synchronisation $t_{\rm sync}$ and circularisation $t_{\rm circ}$ for these types of stars to be

$$t_{\rm sync} = \frac{1}{6q^2k_2}\left(\frac{MR^2}{L}\right)^{1/3} \frac{I}{MR^2}\left(\frac{a}{R}\right)^6 \approx 10^4\left(\frac{1+q}{2q}\right)^2 P^4 \text{ years} \tag{1.20}$$

$$t_{\rm circ} = \frac{1}{84q(1+q)k_2}\left(\frac{MR^2}{L}\right)^{1/3}\left(\frac{a}{R}\right)^8 \approx 10^6 q^{-1}\left(\frac{1+q}{2}\right)^{5/3} P^{16/3} \text{ years,} \tag{1.21}$$

where M, R, and L are the stellar mass, radius, and luminosity, respectively, I is the moment of inertia of the star, and k_2 is the apsidal constant, which can be derived from stellar structure models. In this approximation, the period P is in days. Analogously, Zahn (1977) gives time scales for high-mass stars with a radiative envelope:

$$t_{\rm sync} = \frac{1}{5 \cdot 2^{5/3}}\left(\frac{R^3}{GM}\right)^{1/2} \frac{I}{MR^2} \frac{1}{q^2(1+q)^{5/6}} \frac{1}{E_2}\left(\frac{a}{R}\right)^{17/2} \tag{1.22}$$

$$t_{\rm circ} = \frac{2}{21}\left(\frac{R^3}{GM}\right)^{1/2} \frac{1}{q(1+q)^{11/6}} \frac{1}{E_2}\left(\frac{a}{R}\right)^{21/2}, \tag{1.23}$$

where E_2 is the tidal-torque constant, which is dependent on the stellar structure. In a radiative envelope the tide is dissipated by radiative damping, which is a less efficient mechanism than turbulent friction. Therefore, the time scales are shorter for low-mass stars than for high-mass stars. A short-period system of stars with a convective envelope typically synchronises while the stars are still on the main sequence. For stars with a radiative envelope, on the other hand, the synchronisation and circularisation time scales are usually longer than their evolutionary time scales. For these, one only expects to see synchronous rotation and circularisation in very close systems.

Apart from tidal interaction, stars in a binary system can interact directly in the form of mass exchange or mass loss from the system, which dramatically influences their evolution. Stars expand in the course of stellar evolution. In some phases, like the red-giant stage, they can increase their radius by roughly a factor 50. For single stars this is unproblematic, but for binary stars there is a limit to how large a star can become. This limit is set by the Roche lobe. The more massive member evolves faster and, for close enough binaries, eventually reaches the limit and fills its Roche lobe. The binary is now a *semi-detached* system. At this point mass transfer sets in from the more massive donor to the less massive gainer through the inner Lagrangian point L_1. This is causing a change in the mass ratio of the system, which in turn affects the Roche lobes. When the gainer star cannot accrete all material at once or when it expands faster than its Roche lobe, it can overfill its Roche lobe. The system is now in *over-contact* and has a *common envelope* that engulfs both stars. In this phase, mass can be lost from the system through the outer Lagrangian point L_2. As the stars move through their common envelope, friction can cause a loss of angular momentum and the system will spiral in. Figure 1.6 illustrates binary systems in a detached, semi-detached, and over-contact configuration. The scenario that was just laid out is just one possibility. It is obvious that, depending on the initial separation of the two binary components, Roche lobe overflow can occur at different evolutionary stages with many different outcomes. When it happens on a nuclear time scale, the system has enough time to adjust and the mass transfer is stable. In this situation, the gainer star can also become the more massive one. The common-envelope phase, explained above, is one possible formation channel for sdB stars (Heber 2009). If mass transfer occurs in later stages of evolution, e.g. on the asymptotic giant branch, the donor can pollute the gainer. In this way main sequence stars in binaries can show peculiar abundances of elements, which are only created in late stages of evolution (Jorissen 2003; van Winckel 2003).

Detached binary systems allow the accurate determination of masses and radii of both components. For short period binaries both components are unevolved main-sequence stars. If we want to derive stellar parameters for more evolved stars, such as red giants, we need to observe long-period systems. For the separation between the two members to be large enough for the stars to expand as red giants, the period has be to be of the order of a hundred days. From the ground it is difficult to detect or follow such systems, as they require dedicated long-term observing campaigns. However, thanks to the long temporal baseline of the *Kepler* data, samples of detached eclipsing red-giant binaries that exhibit solar-like pulsations were found by Gaulme et al. (2013) and Beck et al. (2014), making detailed modelling possible. Compact objects, such as white dwarfs or sdB stars, also form detached binaries with a large distribution of orbital periods. These systems have usually experienced interaction in the past. As discussed in Sect. 1.3.3, they can have pulsations as well, making them interesting objects to study.

1.5 Observing techniques

The predictions made by the theories introduced above have to withstand comparisons to observations. New advances in instrumentation and observing techniques make such tests ever more adamant. In the observational studies presented in this thesis we make use of state-of-the-art techniques: space-based white-light photometry and ground-based high-resolution spectroscopy. To study the phenomena of pulsating stars and binary systems, the targets have to be monitored over an extended period of time. This requires dedicated instruments. In the past decade there have been three main space missions that continuously observed fields in the sky, obtaining light curves of several stars: MOST (Walker et al. 2003), CoRoT (Auvergne et al. 2009), and *Kepler* (Borucki et al. 2010). We used data obtained by the *Kepler* satellite, which was the most recent of these three missions. For time-series spectroscopy we needed to have long-term access to telescopes, equipped with high-resolution spectrographs. This was possible at the 2.1-m Otto-Struve telescope in Texas, USA and the 1.2-m Mercator telescope in La Palma, Spain. In the following subsections, we introduce the utilised observing techniques and instruments.

1.5.1 Space photometry: The *Kepler* mission

The NASA space mission *Kepler* was designed to find Earth-sized terrestrial planets around other stars through the transit method. From its launch on 6 March 2009 until the end of its nominal mission on 11 May 2013 it observed a dedicated field-of-view (FOV) of 105 sq. deg in the Cygnus and Lyra constellations (see Fig. 1.7). This FOV was chosen to lie $> 55^\circ$ above the ecliptic plane to avoid stray light of the Sun from entering the 0.95-m aperture. It should also contain a large number of stars in the photometer's dynamical range from *Kepler* magnitude $Kp = 7$ to $Kp = 17$ (Koch et al. 2010). More than 150 000 stars were monitored almost continuously during these four years. White-light photometric measurements of 6 seconds were stacked onboard to 29.4 min integrations in long cadence (LC) mode, reaching a precision of 30 parts per million for stars with $11.5 \leq Kp \leq 12.5$ (Jenkins et al. 2010). For 512 carefully selected stars, 58.8 s integrations were provided in short cadence (SC) mode (Gilliland et al. 2010). The four-year light curves were divided into 18 quarters (Q0-Q17). After each quarter, the satellite rolled by 90° to realign its solar arrays with the Sun and the targets fell onto a different module. By 11 May 2013 two of the four reaction wheels, which maintain stable pointing to the FOV, have failed. As the necessary stability for the original FOV could no longer be achieved, the satellite was repurposed as the K2 mission. K2 monitors the ecliptic plane, where the solar photon pressure is minimised allowing the most stable pointing based on the two still functional reaction wheels (Howell et al. 2014). Various FOVs in the ecliptic are observed during some three

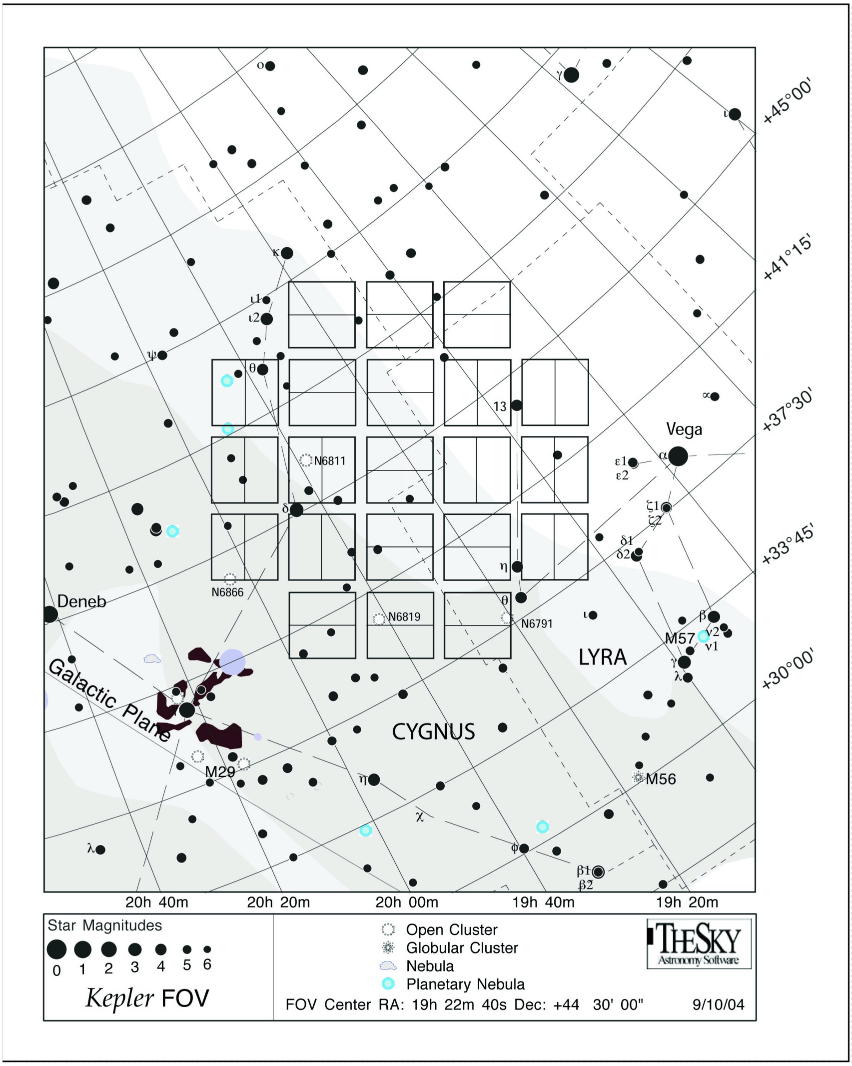

Figure 1.7: The field-of-view of the *Kepler* satellite. The 21 CCD detector modules were aligned such that the brightest objects in the field would fall into the gaps in between. Figure courtesy of NASA/*Kepler* mission.

months, bringing different types of stars within reach that were inaccessible by the nominal *Kepler* mission, such as high-mass and pre-main sequence stars.

To date, the nominal *Kepler* mission has discovered more than 4000 planet candidates and follow-up studies confirmed 1041 exoplanets (at the time of writing). However, the unprecedented precision of the almost continuous observations not only revolutionised exoplanet research, it also brought huge successes to the fields of asteroseismology and binary stars.

With roughly 16 000 red-giant stars observed, it opened the possibility for ensemble asteroseismology, providing masses and ages for numerous objects. *Kepler* saw the discovery of mixed modes in red-giants (Beck et al. 2011), leading to a measurement of the rotation rate of the He-core (Beck et al. 2012; Deheuvels et al. 2012). Thanks to the nearly uninterrupted observations over a long temporal baseline of four years, low-frequency g modes were detected in both SPB and γ Dor pulsators (see Sect. 1.3.3). This led to the discovery of g-mode period spacings for both types of pulsators, providing the opportunity for detailed modelling of the stellar interior (see, e.g. Pápics et al. 2014; Bedding et al. 2015; Moravveji et al. 2015; Schmid et al. 2015; Van Reeth et al. 2015a,b, and Chapters 3 and 4 in this thesis).

The *Kepler* Eclipsing Binary Catalogue now counts 2772 identified objects (Prša et al. 2011; Slawson et al. 2011; Kirk et al. 2016; Abdul-Masih et al. 2016) and delivered interesting detections and discoveries, such as, e.g. circumbinary planets (Doyle et al. 2011) and Doppler beaming (van Kerkwijk et al. 2010; Bloemen et al. 2012). Measurements of eclipse-timing variations, furthermore, allow the detection of triple systems (Conroy et al. 2014). The satellite also observed numerous pulsating stars in binaries, among them highly-eccentric systems with ellipsoidal variations and tidally-induced pulsations, dubbed heartbeat stars following the shape of their light curves (Welsh et al. 2011; Thompson et al. 2012; Hambleton et al. 2013).

1.5.2 High resolution spectroscopy

Spectroscopy and especially high-resolution spectroscopy is useful for different research questions. For example, the perturbations in the surface-velocity field of stars, caused by pulsations, are visible as Doppler shifts in absorption lines. The higher the spectral resolution $R = \lambda/\Delta\lambda$ at wavelength λ, the smaller the variations that can be observed. Additionally, a low noise level or high signal-to-noise ratio S/N is necessary to study these line-profile variations. More details on this technique are presented in Chapter 2, where we apply it to the bright δ Sct star 4 CVn. Our observations of 4 CVn were obtained at the 2.1-m Otto-Struve telescope, which is located at McDonald observatory in the Davis Mountains in West Texas, USA. The Sandiford Cassegrain-Échelle spectrograph, described in detail by McCarthy et al. (1993), produces spectra of $R = 60\,000$ through a slit of one arc sec. It provides continuous wavelength coverage from 3 700 Å to 8 500 Å. Due to the Cassegrain mount, the instrument is subject to temperature and pressure variations throughout the night and calibration data has to be taken after every science exposure. The raw spectra are then reduced and calibrated manually using the IRAF software package. In Sect. 2.2 we describe our observing strategy for 4 CVn.

Another application of high-resolution spectroscopy is spectral fitting. Observed spectra are compared to synthetic ones to find the effective temperature T_{eff}, the surface gravity $\log g$, the metallicity [M/H], and the projected rotational velocity $v \sin i$ of the stellar atmosphere. This method is more reliable the more absorption lines a spectrum contains. A high resolution and a high S/N are also beneficial for precise results. We use spectra obtained from the HERMES spectrograph to perform spectral fitting for 4 CVn and KIC 10080943 in Chapters 2 and 3, respectively.

Furthermore, the entire spectrum is shifted by the radial velocity of the star. This shift can be extracted by cross-correlating line masks with the data. The mask is moved across the spectrum to find a match between the features of the two, which occurs at the radial velocity of the observed star. If the star is in a binary system, radial velocity curves of a series of spectra reveal the star's motion in orbit about its companion and are used to characterise the system. We derived the radial velocities of KIC 10080943 from HERMES spectra in Chapter 3 and of several more binaries discovered from the *Kepler* mission in Chapter 5.

HERMES is an échelle spectrograph mounted on the Coudé focus of the 1.2-m Mercator telescope at the Roque de los Muchachos observatory in La Palma, Spain. It provides a high spectral resolution of 85 000 with the high-resolution fibre and covers a wavelength range of 377 – 900 nm. The instrument is situated in a temperature-controlled room and fed by an optical fibre. More information on the technical details of the instrument are provided by Raskin et al. (2011). The location of the telescope is ideal for follow-up programmes of *Kepler* targets, as the *Kepler* FOV is visible during the summer months on La Palma. A reduction pipeline and cross-correlation tool, designed specifically for HERMES, facilitate the use of the data and execute all steps prior to continuum normalisation. All further steps are explained in Sects 2.4 and 3.2.

1.6 Outline of this thesis

Asteroseismic studies have been carried out for decades but have delivered only a few well-studied objects from ground-based observations. Recent improvements in computational power and particularly new data of unseen precision and quality make this subject extremely timely and more relevant than ever before. In this thesis, we present detailed analyses of two case studies of pulsating stars in binary systems, employing different methods.

In Chapter 2 we present a new extensive spectroscopic data set of the δ Sct star 4 CVn. This star has been well studied photometrically. More than 30 oscillation modes are known and strong variability of the mode amplitudes has been detected. However, detailed and accurate seismic modelling can only be achieved when the degree ℓ and azimuthal order m of these pulsations are known. The variability of the profiles of absorption lines in the spectrum in principle holds more information on the mode geometry than photometric data do. We use a new time series of high-resolution spectra of 4 CVn, spanning over four years, to find the pulsation modes and attempt mode identification. In the course of this analysis we have discovered that 4 CVn is a wide eccentric binary system. Unfortunately, as the primary is a sub-giant star, it outshines its companion. Hence, we cannot derive accurate masses and radii for the two stars. We present our analysis of the ground-based data of this star in Chapter 2.

In Chapter 3 we discuss the *Kepler* light curve and the spectra of the double-lined binary system KIC 10080943. The variable light curve shows pulsations of high and low frequencies, which means that the system could contain one or two hybrid pulsators. Hidden beneath these high-amplitude pulsations, we find a periodic brightening signal that can be attributed to the binary nature of this target. We derive the component's masses and radii, by modelling this brightening signal and the radial velocities, which we obtained from the spectra. In the g-mode pulsations, we find six series of quasi-equidistantly spaced periods. From rotational splittings detected in the g and p modes and the phase modulations of the pulsations, which are caused by the binary motion, we show that both stars pulsate as γ Dor/δ Sct hybrids.

We use these results from combined space and ground-based data analysis for seismic modelling of KIC 10080943A and KIC 10080943B in Chapter 4. The period spacing series allow us to derive convective-core overshooting parameters and to constrain the extra mixing necessary to explain the oscillation properties of both stars. We use the p modes of the stars to compute their core-to-surface rotation rates, which are in line with the few reported similar measurements for other F-type main-sequence stars. The masses derived from binary modelling turned out to be slightly overestimated, owing to the observed mean period spacing, which is below 3000 s. Nevertheless, we find that the binarity presents other important constraints for the modelling. The requirement for equal age and initial composition of both components, as well as the mass ratio, allow us to highlight shortcomings in the one-dimensional stellar models. This is relevant input for future improvements of the input physics of such models.

We end this thesis with general conclusions and provide a prospect of future projects including our preliminary study of a sample of five eclipsing binary systems containing pulsating components in Chapter 5.

Chapter 2

Time series spectroscopy of the δ Scuti star 4 CVn

This chapter was originally published as

Discovery of binarity, spectroscopic frequency analysis, and mode identification of the δ Sct star 4 CVn

V. S. Schmid, N. Themeßl, M. Breger, P. Degroote, C. Aerts, P. G. Beck, A. Tkachenko, T. Van Reeth, S. Bloemen, J. Debosscher, B. G. Castanheira, B. E. McArthur, P. I. Pápics, V. Fritz, and R. E. Falcon

Astronomy & Astrophysics, vol. 570, A33, 18 pages (2014)

Abstract

More than 40 years of ground-based photometric observations of the δ Sct star 4 CVn has revealed 18 independent oscillation frequencies, including radial as well as non-radial p-modes of low spherical degree $\ell \leq 2$. From 2008 to 2011, more than 2000 spectra were obtained at the 2.1 m Otto-Struve telescope at the McDonald Observatory. We present the analysis of the line-profile variations, based on the Fourier-parameter fit method, detected in the absorption lines of 4 CVn, which carry clear signatures of the pulsations. From a non-sinusoidal, periodic variation of the radial velocities, we discover that 4 CVn is an eccentric binary system with an orbital period $P_{orb} = 124.44 \pm 0.03$ d and an eccentricity $e = 0.311 \pm 0.003$. We detect 20 oscillation frequencies, 9 of which previously unseen in photometric data; attempt mode identification for the two dominant modes, $f_1 = 7.3764$ d^{-1} and $f_2 = 5.8496$ d^{-1}; and determine the prograde or retrograde nature of 7 of the modes. The projected rotational velocity of the star, $v_{eq} \sin i \simeq 106.7$ km s^{-1}, translates to a rotation rate of $v_{eq}/v_{crit} \geq 33\%$. This relatively high rotation rate hampers unique mode identification, since higher order effects of rotation are not included in the current methodology. We conclude that, in order to achieve unambiguous mode identification for 4 CVn, a complete description of rotation and the use of blended lines have to be included in mode-identification techniques.

2.1 Introduction

As shown in the Hertzsprung-Russell diagram in Fig. 1.5 the group of δ Sct pulsators is located in the classical instability strip. They are on or slightly above the main sequence moving toward the giant branch after the hydrogen in their cores is depleted. This evolutionary stage makes them interesting from an astrophysical point of view and important objects for asteroseismic studies, since their interior structures undergo large changes.

New advances in the field of A- and F-type stars were achieved by space-based telescopes, such as MOST (Walker et al. 2003), CoRoT (Auvergne et al. 2009), and most recently *Kepler* (Borucki et al. 2010), which provide high-precision time series photometry. For example, Murphy et al. (2013) presented a detailed asteroseismic study of an SX Phe star in a binary and also derived masses for both components. Grigahcène et al. (2010) and Uytterhoeven et al. (2011, and references therein) found that γ Dor/δ Sct hybrids are a much more common phenomenon than expected from ground-based observations. Nevertheless, extensive ground-based observing campaigns are still necessary. Differences between different passbands and variations occurring on very long timescales of years and decades are hidden in the white-light photometric data of space missions that are comparatively short-lived. High-precision spectroscopic observations allow us to study the features of stellar oscillations in line-profile variations (LPVs) and give important information on the abundances of stellar photospheres. In this chapter we present the results of long-term spectroscopic observations of 4 CVn, one of the best studied δ Sct stars.

The star 4 CVn ($V = 6.04$ mag, $T_{\rm eff} = 6800 \pm 150$ K, $\log g = 3.34 \pm 0.20$, $\log L/L_\odot = 1.550 \pm 0.070$, $v_{eq} \sin i \geq 120$ km s^{-1}; Lenz et al. 2010; Castanheira et al. 2008) has been observed photometrically for more than 40 years. The analysis of the extensive data set by Breger et al. (1999), Breger (2000b), and Breger et al. (2008) led to the discovery of a complex pulsation pattern consisting of 18 independent pulsation modes (Table 2.1). The main range of pulsation frequencies lies between 4 d^{-1} and 10 d^{-1}.

Table 2.1: Photometric frequencies and amplitudes, and preliminary mode identification of 4 CVn.

	Frequency d^{-1}	Amplitude y filter mmag	ℓ	m
ν_1	8.595	15.3	1	1
ν_2	7.375	11.6	1	-1
ν_3	5.048	10.7	1	-1
ν_4	6.117	9.2		
ν_5	5.851	10.1	2	1
ν_6	5.532	6.4	2	
ν_7	6.190	5.7		
ν_8	6.976	5.0	0	0
ν_9	4.749	3.2		
ν_{10}	7.552	3.3	1	
ν_{11}	6.750	0.9		
ν_{12}	6.440	1.6		
ν_{13}	5.986	0.8		
ν_{14}	7.896	0.8		
ν_{15}	5.134	0.8		
ν_{16}	5.314	0.8		
ν_{17}	6.404	0.4		
ν_{18}	6.680	0.2		

Notes. Frequencies and amplitudes taken from Breger et al. (1999). The ℓ values are based on multicolour photometry by Lenz et al. (2010) and the m values are the preliminary results of the spectroscopic mode identification of the 2008 data set by Castanheira et al. (2008), ignoring the binarity of the pulsator.

Additional combination frequencies have been detected in lower and higher frequency ranges. Almost all modes show variations in amplitude and frequency that occur over several years and decades. Amplitude variations have been observed in many δ Sct stars. With sufficient frequency resolution, modes with varying amplitude and phase can be resolved as two close frequencies that produce a beating pattern (Breger & Bischof 2002; Breger & Pamyatnykh 2006). Correlations between the amplitude and phase shifts can confirm a beating of two close, intrinsic modes as opposed to true amplitude variability of a single mode. For 4 CVn the frequencies 6.1170 d^{-1} and 6.1077 d^{-1} are confirmed to be intrinsic modes producing amplitude variations and phase shifts through beating (Breger 2010). However, for frequencies with amplitude and phase variability on timescales longer than one year, the coverage of the beating cycle is incomplete. Thus, it cannot be ruled out that they are single modes with true amplitude variability.

Mode identification can be achieved by interpretation of spectroscopic LPVs. The expansion and contraction of the star and displacements of stellar-surface elements caused by the oscillations lead to periodic Doppler shifts in the profiles of absorption lines. By comparing the observed properties of LPVs to theoretical predictions, the harmonic degree ℓ and the azimuthal order m of the mode can be derived. Moreover, fitting with synthetic line profiles allows the determination of other stellar parameters and line-profile parameters, such as the projected rotational velocity $v_{eq} \sin i$, and the inclination i (the angle between the pulsation axis and the line of sight; we assume that the pulsation axis coincides with the rotation axis). Unlike brightness or radial velocity, which are values integrated over the stellar surface, LPVs are less prone to partial cancelation effects and therefore allow for the detection of high-degree modes (for details see Aerts et al. 2010, Chapter 6).

Spectroscopic data was gathered at the McDonald Observatory in Texas, USA, from January 2008 until June 2011 (see Sect. 2.2). Preliminary results of the frequency analysis and mode identification of the season of 2008 were published by Castanheira et al. (2008). They assigned ℓ and m values to five different modes previously detected in photometry, summarised in Table 2.1. No high-degree modes were found. Furthermore, they measured $v_{eq} \sin i \geq 120\ \mathrm{km\,s^{-1}}$ for 4 CVn.

A subsequent analysis by Breger (2010) revealed correlations between the frequency variations and the azimuthal orders of the modes. While the prograde modes of 4 CVn show an increasing frequency followed by a decline after the year 1991, its retrograde modes have a decrease in frequency with a rising value after 1991. Radial modes, on the other hand, show very little or no frequency variations. Breger (2010) interpreted this different behaviour of prograde and retrograde modes as a change in rotational splitting.

For this chapter we analysed the complete data set of spectroscopic observations. First of all, **we discovered the star to be a spectroscopic binary**. After orbital subtraction, we performed mode identification by applying the Fourier-parameter fit method (Zima 2006) to the LPVs present in metal absorption lines in the 4 CVn spectrum (see Fig. 2.1). Additionally, we present an abundance analysis and confirm the solar-like metallicity of the star.

2.2 Data and observations

The Sandiford Échelle Spectrograph (McCarthy et al. 1993) is an instrument mounted on the 2.1 m Otto-Struve Cassegrain reflector telescope at the McDonald Observatory, Texas, USA. It has a resolving power of $R = 60\,000$ and is therefore ideally suited to

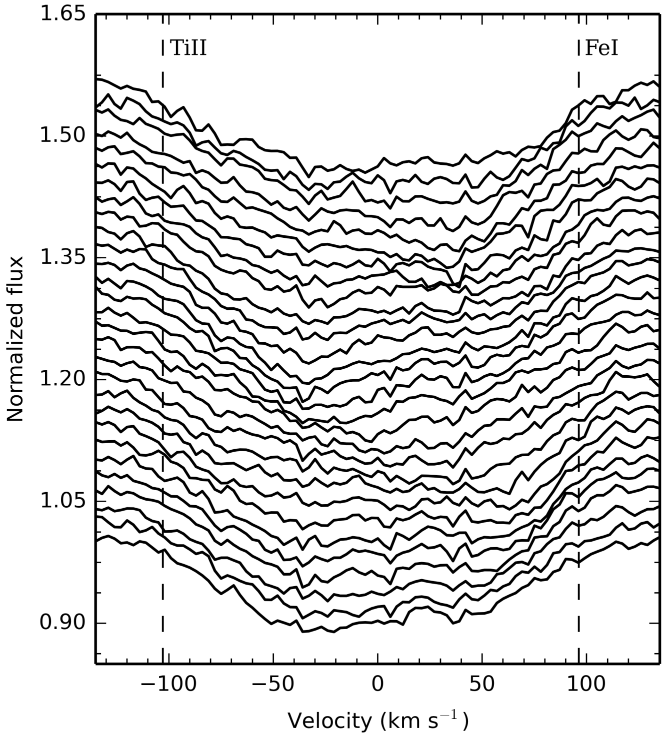

Figure 2.1: Line-profile variations in the Fe II line at 4508.288 Å. The flux is normalised to 1 and is displayed with an offset. Shown are 29 spectra from the night of 31 March 2010. The vertical, dashed lines mark the metal lines Ti II at 4506.743 Å (-102.81 km s^{-1}) and Fe II at 4509.735 Å (96.29 km s^{-1}), respectively.

observe the relatively bright star 4 CVn (V = 6.04 mag) with a high signal-to-noise ratio (S/N) and a high spectral resolution. Depending on the atmospheric conditions we chose an integration time of 600–900 s, leading to a mean S/N of ~ 200 at a temporal resolution of 4% and 10% for the two main modes present in the photometric data, ν_1 = 8.594 d^{-1} and ν_2 = 5.048 d^{-1}, respectively (see Table 2.1). The instrument provides a continuous wavelength coverage in the observed range of 4200 Å to 4700 Å. In total, 2129 spectra were obtained throughout 86 nights in the period from January 2008 until June 2011 (see Table 2.2) leading to a time span of ΔT = 1248 d and thus to a frequency resolution of $1/\Delta T$ = 0.0008 d^{-1}. For precise wavelength calibration, comparison frames of a Th-Ar lamp were obtained after each exposure.

Standard IRAF routines for the reduction of échelle spectra were used to carry out the data reduction and wavelength calibration. Subsequently, the spectra were normalised

Table 2.2: Observation log of obtained spectroscopy of 4 CVn.

Season	Start date	End date	nights	N
2008	2008-Jan-19	2008-May-20	33	874
2010	2010-Feb-18	2010-May-26	33	767
2011	2010-Dec-14	2011-Jun-21	20	488
Total	2008-Jan-19	2011-Jun-21	86	2129

Notes. Nights denotes the number of nights observed in each specific year; N is the number of scientific spectra taken of 4 CVn. Not all spectra were used in the analysis because of cosmic-ray hits or very low S/N.

in a similar manner to that described by Pápics et al. (2012), i.e. by fitting a cubic spline to manually chosen continuum points. They were then cut around a suitable line for further analysis. This line, an absorption feature of Fe II at 4508.288 Å, was carefully chosen from the available spectral range, as explained below.

2.2.1 Line selection

Certain criteria have to be fulfilled for the selection of an absorption line for the analysis of the LPVs, such as a sufficient depth and sharpness. For sharp lines, the pulsational broadening is dominant over other line-broadening mechanisms across the whole profile. It is also important that the line is unblended and does not overlap with any other atomic line. Metal lines are therefore better suited for mode identification from LPVs than hydrogen or helium lines (for more details see Aerts et al. 2010, Chapter 6). Different spectral lines originate from different layers in the atmosphere and thus probe different pulsation modes. Therefore, the signatures of the oscillations might be smeared out in the line profiles of blended lines. Moreover, the displacement of the line-forming regions by the pulsations leads to slight variations of the local temperature, which in turn lead to equivalent width (EW) variations. This will affect the outcome of the mode identification and has to be taken into account.

Castanheira et al. (2008) found $v_{eq} \sin i \geq 120$ km s^{-1} for 4 CVn, which means that the star is a moderately fast rotator. This aggravates the situation of dense blue spectra of F stars with only very small continuum regions, as each absorption line is rotationally broadened. To select suitable lines for our study, we calculated an atmospheric model with effective temperature $T_{\text{eff}} = 6800$ K, surface gravity $\log g = 3.32$, and solar metallicity (Breger & Pamyatnykh 2002; Lenz et al. 2010) using the LLMODEL code (Shulyak et al. 2004). With the SYNTHV (Tsymbal 1996) code we computed a synthetic spectrum and checked each line separately. The Fe II line around 4508.288 Å is the only line that is unblended except for two contributions in the line wings of Ti II at

Table 2.3: Orbital Parameters of 4 CVn.

P_{orb} (days)	124.44 ± 0.03
T (JD)	2 454 605 ± 10.3
e	0.311 ± 0.003
ω (deg)	70.2 ± 0.7
K_1 (km s^{-1})	13.24 ± 0.05
γ (km s^{-1})	-10.44 ± 0.03
RMS (km s^{-1})	2.8

4506.743 Å (27.2% of the line depth of Fe II) and Fe I at 4509.735 Å (39.8%). The positions of the two blending features are marked by vertical, dashed lines in Fig. 2.1.

Additionally, Castanheira et al. (2008) used another Fe II line around 4549.474 Å for mode identification of the 2008 data set of 4 CVn in their analysis. We refrained from using this line because it turned out to be heavily blended by at least five other absorption features, of which Fe I at 4549.466 Å and Ti II at 4549.617 Å give the strongest contribution to this line blend.

2.3 Binarity and radial velocity variations

After the spectra were corrected for the barycentric velocity shift, a dominant non-sinusoidal variation was visible in the first moment of the line, which represents the radial velocity (for a definition, see Aerts et al. 1992). This periodicity can be explained by a binary component and the movement of the primary around the centre of mass of the system. No spectral features of the secondary could be detected in the data. This is further discussed in Sect. 2.4.

Since the first moment of the line depends somewhat on the wavelength range within which it is calculated, we created five different data sets with different dispersion ranges. We then fitted a Keplerian orbit to each data set. The best solution and errors of the parameters were estimated with a Markov chain Monte Carlo (MCMC) method implemented in the package `emcee` (Foreman-Mackey et al. 2013). To account for the scatter due to pulsations, we assumed an uncertainty of $\sigma_{\mathrm{RV}} = 2.8$ km s^{-1} (the RMS value of the residuals after subtraction of the binary model, see Table 2.3) for each radial velocity measurement. To account for the dependence of the radial velocities on the dispersion range, we fitted all five data sets combined. All five models are consistent within the uncertainties of each solution. Figure 2.2 shows the orbital model fitted to the radial velocities obtained from the dispersion range -128.0 km s^{-1} to 106.0 km s^{-1} and the residuals after subtraction of the mean orbit. The results are listed in Table 2.3.

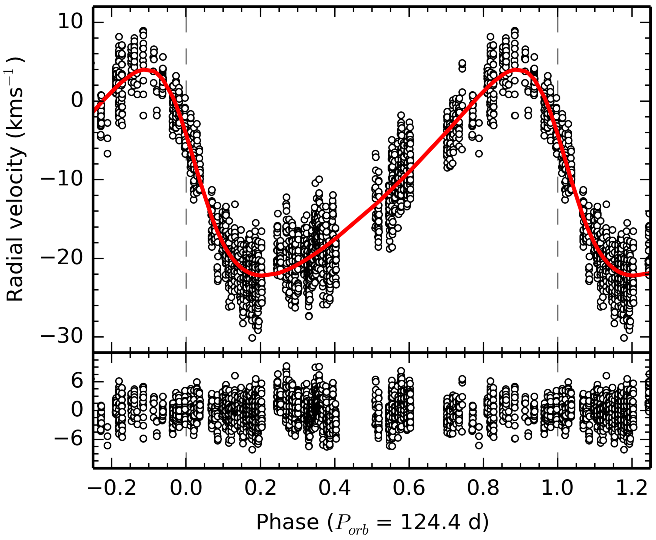

Figure 2.2: *Top panel:* Observed radial velocities (open circles) fitted with the orbital model (solid line) with the parameters displayed in Table 2.3 and phased with the orbital period P_{orb} = 124.4 d. *Bottom panel:* Residuals after subtracting the binary model with an RMS of 2.8 km s^{-1}. The pulsation signal (see Table 2.6) is visible on top of the variation due to binarity and remains present in the residuals. The vertical, dashed lines mark the beginning and the end of one phase.

Because of the binary motion of the pulsating star we expect the frequencies to show a periodic shift at the base of the orbital period (for an explanation of the Doppler shift of oscillation frequencies, see Shibahashi & Kurtz 2012). For the observed photometric frequencies a shift of ~ 0.0002 d^{-1} to ~ 0.0004 d^{-1} can be estimated. Since the analysed data set has a frequency resolution of 0.0008 d^{-1}, we cannot resolve the expected frequency shifts caused by the binary motion. We also did not detect a variation based on the orbital period of the times of maxima in an (O – C) diagram of the first moment.

From the mean binary orbit, a correction value was calculated for each spectrum to shift the data to the reference frame of the primary. The frequency analysis and mode identification of the pulsations was subsequently performed on the data corrected for the binary motion.

2.4 Revision of fundamental parameters

Since the data gathered at McDonald Observatory are limited in wavelength range, we obtained additional observations with the HERMES spectrograph (Raskin et al. 2011). We obtained three spectra equally spread over the night of 3 February 2013. The reduction was performed by the HERMES pipeline and normalisation was done in the same way as for the McDonald spectra, i.e. by fitting a cubic spline to the continuum region (Pápics et al. 2012). We extracted a wavelength range of 4500 Å to 6000 Å from the data.

For the analysis of the average spectrum of 4 CVn, we used the GSSP programme package (Tkachenko et al. 2012; Lehmann et al. 2011). The code relies on a comparison between observed and synthetic spectra computed in a grid of T_{eff}, $\log g$, microturbulence ξ, metallicity [M/H], and $v_{eq} \sin i$, and finds the optimum values of these parameters from a minimum in χ^2. Individual abundances of chemical elements are adjusted in the second step by fixing the metallicity to the above determined value but keeping the other atmospheric parameters free. The errors of measurement (1-σ confidence level) are calculated from the χ^2 statistics using the projections of the hypersurface of the χ^2 from all grid points of all parameters onto the parameter in question. For a more detailed discussion on the estimation of the uncertainties, see Tkachenko et al. (2013b). Strong LPVs detected in the spectrum of 4 CVn, as well as possible contributions from the secondary component, are an additional source of uncertainties which are not taken into account in the spectral analysis. Our analysis is based on the grid of atmosphere models computed using the most recent version of the LLMODELS code (Shulyak et al. 2004). For the calculation of the synthetic spectra, we used the SYNTHV code (Tsymbal 1996), and information on atomic lines has been extracted from the Vienna Atomic Line Database (VALD, Kupka et al. 2000).

Table 2.4 lists the atmospheric parameters of 4 CVn we derived. The individual abundances of some chemical elements are given in Table 2.5. The spectral type and the luminosity class have been computed using an interpolation in the tables published by Schmidt-Kaler (1982). Figure 2.3 compares the observations with the best fit synthetic spectrum in a 300 Å wide wavelength range including the H_β spectral line.

Moreover, we used the Hipparcos parallax of 10.51 mas (van Leeuwen 2007) in combination with 2MASS and Geneva photometry to compute the luminosity and the radius of the star. We used a grid-based method, which also includes interstellar reddening as a free parameter, as described by Degroote et al. (2011). By using the radius and the spectroscopic $\log g$ we are able to estimate the mass. We find an extinction $E(B-V) = 0.02$ mag. Although this value is close to zero, adding extinction to the calculations is important for the consistency of our estimated parameters, mass and radius. The results of the photometric analysis are summarised in Table 2.4.

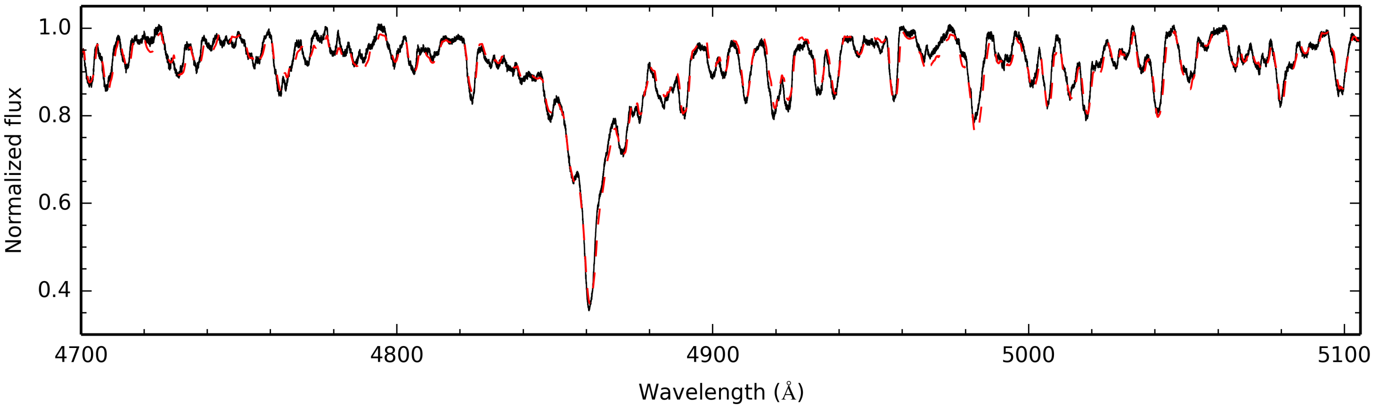

Figure 2.3: Fit of the observed spectrum (solid) with a synthetic spectrum (dashed) computed using our optimised parameters (see Table 2.4).

Table 2.4: Fundamental and atmospheric parameters of 4 CVn.

$T_{\rm eff}$(K)	6875 ± 120^{a}
$\log g$ (dex)	3.30 ± 0.35^{a}
[m/H] (dex)	-0.05 ± 0.15^{a}
$v_{eq} \sin i$ (km s^{-1})	109 ± 3^{a}
ξ (km s^{-1})	4.00 ± 0.45^{a}
ST	F2 III-IV^{a}
π (mas)	10.51 ± 0.40
$\log L/L_{\odot}$	1.47 ± 0.05^{b}
Radius ($R_{\odot}$)	3.7–4.1^{b}
Mass ($M_{\odot}$)	1.0–2.0^{b}

Notes. $^{(a)}$ Parameters derived via spectral analysis.
$^{(b)}$ Parameters based on combined photometric and spectroscopic observations.

Table 2.5: Abundances of individual chemical elements of 4 CVn.

Element	Value dex	Sun dex	Element	Value dex	Sun dex
Fe	-4.69(15)	-4.59	Cr	-6.47(20)	-6.40
Mg	-4.41(25)	-4.51	Mn	-6.65(40)	-6.65
Ti	-7.24(30)	-7.14	Si	-4.41(40)	-4.53
Ni	-5.82(20)	-5.73	C	-3.64(40)	-3.65
Ca	-5.84(25)	-5.73	Ba	-9.52(50)	-9.87
			Sc	-8.57(50)	-8.99

Notes. Error bars are given in parentheses in terms of last digits. Solar values are those derived by Grevesse et al. (2007).

We also used the above analysed observed spectrum to compute a mean profile with a high S/N by means of the least-squares deconvolution technique (LSD) (Donati et al. 1997; Kochukhov et al. 2010). Figure 2.4 shows the LSD profile of 4 CVn, the line mask was pre-computed based on the parameters listed in Table 2.4. Besides clear bumps in the centre of the profile (dip) of the star, there is also an indication of another broad spectral line at $RV \sim 280$ km s^{-1}. Whereas the former is connected to the intrinsic variability of the star in terms of low- and high-degree non-radial pulsations, the latter might be a signature of a (very) faint stellar companion.

Given the measured semi-amplitude of the primary $K_1 = 13.24$ km s^{-1} and the measured systemic velocity $\gamma = -10.44$ km s^{-1}, a radial velocity of $\sim$ 280 km s^{-1} of the secondary at orbital phase $\phi = 0.64$ would lead to a mass ratio of $q \leq 0.05$. The line strength of the spectral feature around $RV \sim 280$ km s^{-1} in the LSD profile is

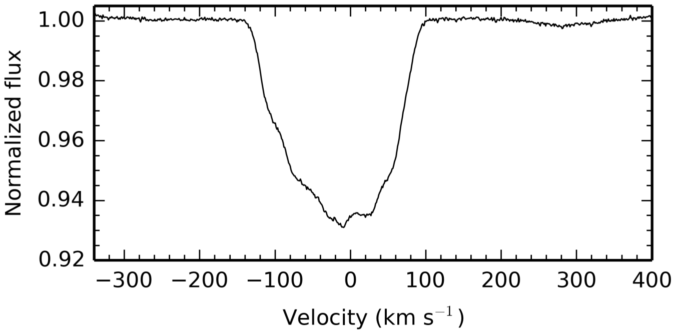

Figure 2.4: Average line profile of 4 CVn computed by means of the LSD technique.

$\sim$ 0.2%. If we assume a minimum contribution of $\sim$ 0.2% of the secondary to the system luminosity $\log L/L_\odot = 1.47$, we estimate $L_2 \sim 0.06\ L_\odot$, which corresponds to an early M-type main-sequence star of $\sim 0.6\ M_\odot$ (Carroll & Ostlie 2006, Appendix G). A mass ratio of $q \leq 0.05$ would then give a primary mass of $\sim 12\ M_\odot$, which is too massive given the observed spectral type F2III-IV.

The additional spectral contribution is so faint that it could also be an effect of continuum normalisation. As the spectral lines of 4 CVn are broadened by fast rotation ($v_{eq} \sin i$ = 109 km s^{-1}), a continuum is not present everywhere in the wavelength range. Thus, inaccurate continuum normalisation rather than a secondary signal is a more likely explanation for the spectral feature at $RV \sim 280$ km s^{-1}.

2.5 Frequency analysis

Before starting the analysis of the data we inspected each spectrum by eye. We rejected 93 observations, owing to weak cosmic-ray hits within the line or poor S/N, leaving 2036 good spectra (797 in 2008, 758 in 2010, and 481 in 2011). Since the periodogram of 4 CVn is characterised by amplitude variations on short and long timescales, we split the whole data set into three parts, and studied each season separately, otherwise the variability of the oscillation pattern would lead to disturbing side peaks in the Fourier spectra and to uncertainties between real frequency peaks and aliasing.

To search for significant periodicities in the LPVs we employed the Fourier-parameter fit method (FPF), which was developed by Zima (2006) as an advancement of the pixel-by-pixel method (Mantegazza 2000). It is implemented in the software package FAMIAS (Zima 2008). For each bin in the dispersion range of the line a Fourier transform is performed and a Lomb-Scargle periodogram (Lomb 1976; Scargle 1982) is calculated. An optimisation of the mode parameters is done by applying a least-squares fitting algorithm to the original spectra, again, for each bin separately and thereby computing zero point, amplitude, and phase across the line profile. Subsequently, these parameters are used for mode identification (see Sect. 2.6). A Monte Carlo perturbation approach has been used to calculate the errors on the amplitudes, assuming a Gaussian distribution of the noise of the amplitude profiles. The S/N of each frequency is calculated from the mean periodogram, prewhitened with the significant frequency peaks. Thereby, the noise (σ_{res}) is calculated as the mean amplitude in a range of 10 d^{-1} (covering most of the frequency spectrum) around the frequency peak in the periodogram. We have adopted a significance criterion of $A > 4\sigma_{\mathrm{res}}$ (Breger et al. 1993). The results of our analysis are summarised in Table 2.6, where the amplitudes are obtained by integrating the amplitude profile across the line in the given dispersion range.

2.5.1 The Fe II line at 4508.288 Å

The increase in noise towards low frequencies in the periodograms (see Figs. 2.5–2.7) can be explained by instrumental effects or imperfect subtraction of the binary orbit. Given that the spectrograph is mounted at the telescope and not placed in a remote room where pressure and temperature could be kept constant to avoid spectral drift, some long-term variations are unavoidably present in the data. The high noise level can also be caused by instrumental noise and correlations of different noise sources. Residual variability on the basis of the binary orbit would cause frequency peaks around 0.008 d^{-1}. For these reasons, we discarded all low-frequency peaks below 2 d^{-1} as being not trustworthy. Furthermore, the daily gaps due to the night-day rhythm led to significant one-day aliasing, which is visible in the spectral window of each season (see inset in the top panels of Figs. 2.5, 2.6, and 2.7 for seasons 2008, 2010, and 2011, respectively). To overcome these obstacles a prewhitening of each frequency was performed before carrying out another Fourier transform.

Figures 2.5, 2.6, and 2.7 display the mean of the periodograms that were computed for each bin and for the seasons 2008, 2010, and 2011, respectively. Different stages of prewhitening are shown and the seven dominant frequencies are marked. We found six frequencies that are confirmed by photometric studies and are present in the periodograms of the whole data set and in all three seasons separately as well. These are $f_1 = 7.3764\ \mathrm{d}^{-1}$, $f_2 = 5.8496\ \mathrm{d}^{-1}$, $f_3 = 5.0481\ \mathrm{d}^{-1}$, $f_4 = 8.5942\ \mathrm{d}^{-1}$, $f_5 = 5.5315\ \mathrm{d}^{-1}$, and $f_6 = 8.6552\ \mathrm{d}^{-1}$ (Breger 2016). Other photometrically significant frequencies could be detected in some seasons, while their amplitude was below the detection limit in other subsets. The frequency $f_{11} = 6.975\ \mathrm{d}^{-1}$, for example, could only be detected in 2008. Breger (2016) confirm a rapid, steady decrease in amplitude for this frequency from 2008 to 2012. The frequencies $f_8 = 6.6801\ \mathrm{d}^{-1}$, $f_{10} = 6.1171\ \mathrm{d}^{-1}$, and $f_{13} = 6.1910\ \mathrm{d}^{-1}$ also appear to be varying in amplitude, since they have only

Table 2.6: Spectroscopic frequencies and amplitudes of 4 CVn.

	Frequency	$A_{\text{whole set}}$	A_{2008}	A_{2010}	A_{2011}
	d^{-1}	km s^{-1}	km s^{-1}	km s^{-1}	km s^{-1}
	±0.0008	±0.009	±0.015	±0.014	±0.016
f_1	7.3764	0.953	0.95	0.98	1.00
f_2	5.8496	0.869	0.87	0.90	0.88
f_3	5.0481	0.550	0.48	0.53	0.59
f_4	8.5942	0.444	0.48	0.51	0.33
f_5	5.5315	0.389	0.38	0.39	0.44
f_6	8.6552	0.389	0.31	0.40	0.51
f_7	8.1687[a]	0.379	0.33	0.41	0.48
f_8	6.6801	whole set, 2010, 2011			
f_9	4.0743[a]	whole set, 2010, 2011[c]			
f_{10}	6.1171	whole set, 2010			
f_{11}	6.975[b]	2008			
f_{12}	10.1702[a]	whole set, 2010, 2011			
f_{13}	6.1910	whole set, 2011			
f_{14}	12.4244[a]	whole set, 2010, 2011			
f_{15}	9.4113[a]	whole set, 2008, 2010, 2011			
f_{16}	9.7684[a]	whole set, 2008, 2010			
f_{17}	10.0372[a]	whole set, 2008			
f_{18}	6.4030	whole set			
f_{19}	13.388[a]	2008			
f_{20}	10.016[a]	2011			

Notes. Amplitudes $A_{\text{whole set}}$ from the frequency analysis of the whole data set compared to the amplitudes of the different seasons A_{2008}, A_{2010}, and A_{2011}. The amplitudes have an average error of 0.009 km s^{-1} for the whole data set, and of 0.015 km s^{-1}, 0.014 km s^{-1}, and 0.016 km s^{-1} for the seasons 2008, 2010, and 2011, respectively. The frequency resolution $1/\Delta T$ is 0.0008 d^{-1} for the whole data set and 0.009 d^{-1}, 0.01 d^{-1}, and 0.005 d^{-1} for the seasons 2008, 2010, and 2011, respectively.

(a) Frequencies not detected in previous photometric studies.

(b) Photometric radial mode (Lenz et al. 2010).

(c) Alias peak of frequency detected.

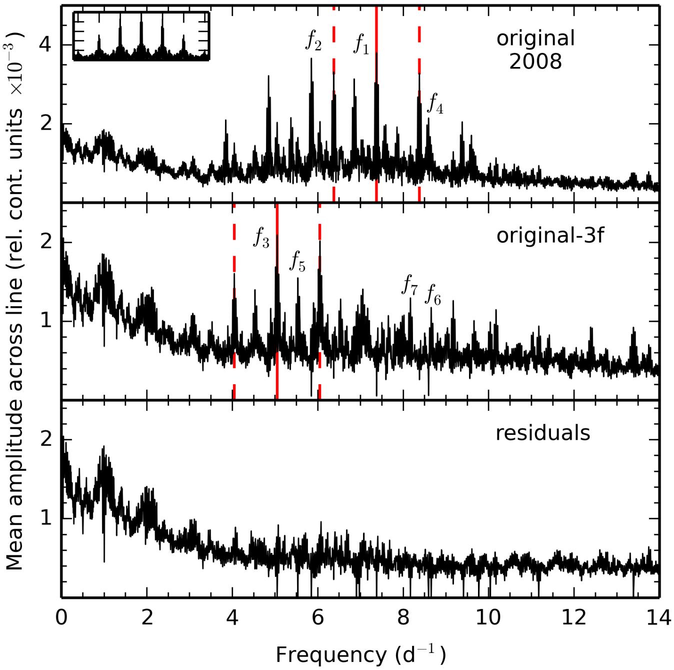

Figure 2.5: Mean of the Lomb-Scargle periodograms per bin of the season of 2008. *From top to bottom*: mean Fourier spectra of the original data set, and after prewhitening of 3 and 14 frequencies, respectively. The red solid lines mark the highest peak in each periodogram, while the red dashed lines mark the respective one-day aliases. Highest peaks are f_1 = 7.3764 d^{-1} *(top panel)* and f_3 = 5.0481 d^{-1} *(middle panel)*. The inset in the *top panel* displays the spectral window for the 2008 data set.

been detected in either the season of 2010 or 2011, or in both. However, the amplitude variabilities we detected for f_8, f_{10}, and f_{13} do not agree with the amplitudes derived from the photometric data set. Since these frequencies have a low S/N, their amplitude could also be below the detection limit in other seasons.

Additionally, we found several frequencies that were not detected in previous photometric studies by Breger et al. (1999), Breger (2000b), and Breger et al. (2008), among them f_7 = 8.1688 d^{-1}, f_9 = 4.0743 d^{-1}, f_{15} = 9.4113 d^{-1}, and f_{16} = 9.7684 d^{-1}. The frequency f_7 can be detected with a comparatively high amplitude ($A > 0.3$ km s^{-1}) in all sets and subsets. Frequencies f_9, f_{15}, and f_{16} have much lower amplitudes, and the amplitudes of f_9 and f_{16} even lie below the detection limit of seasons 2008 and 2011, respectively. The consistency of the detection in the separate seasons and the sufficient S/N for these frequencies in the merged data of the three seasons led us to

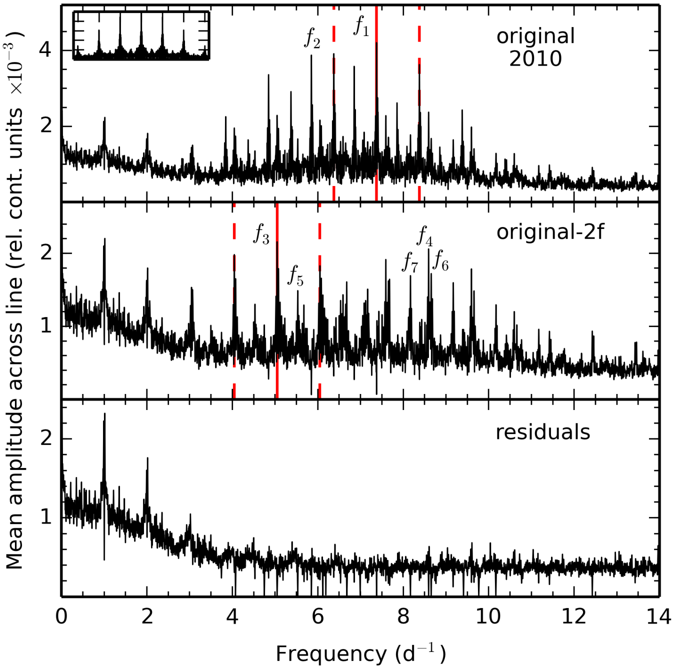

Figure 2.6: Same as Fig. 2.5 for the season of 2010. *From top to bottom*: mean Fourier spectra of the original data set, and after prewhitening of 2 and 17 frequencies, respectively. The highest peaks marked by the red solid lines are f_1 = 7.3764 d^{-1} *(top panel)* and f_3 = 5.0481 d^{-1} *(middle panel).*

the conclusion that they correspond to real oscillation frequencies. The fact that these frequencies were not detected in photometry suggests that they are either high-degree modes with $\ell \geq 2$ or are varying in amplitude and have reached detectable amplitudes in the last five years.

Breger et al. (1999) could identify peaks above 10 d^{-1} as combination frequencies of the main modes between 4 d^{-1} and 10 d^{-1}. The frequencies f_{12} = 10.1702 d^{-1}, f_{14} = 12.4244 d^{-1}, f_{17} = 10.0372 d^{-1}, f_{19} = 13.388 d^{-1}, and f_{20} = 10.016 d^{-1} lie in this high frequency range, but could not be confirmed to be combinations of any of the detected frequency peaks with $4 \leq f \leq 10$ d^{-1}. The amplitude and the phase profiles across the line of a mode offer an additional diagnostic to distinguish between noise peaks and real frequencies. If these profiles show a significant trend and not just random scatter, the frequency is likely to be a real pulsation mode. In Appendix A the amplitude and phase profiles across the line are displayed for the frequencies f_8 to f_{20}. While the amplitude profiles of f_{12}, f_{14}, f_{17}, f_{19}, and f_{20} are rather noisy, the phase

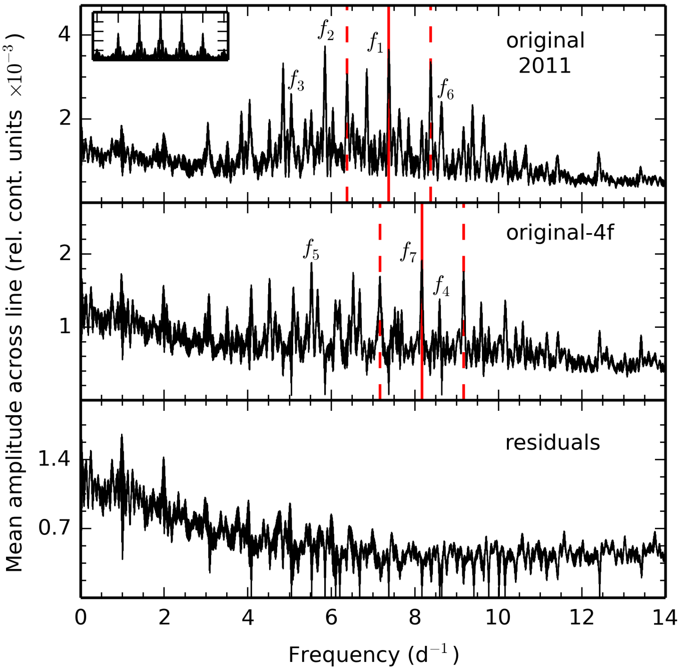

Figure 2.7: Same as Figs. 2.5 for the season of 2011. *From top to bottom*: Fourier spectra of the original data set, and after prewhitening of 4 and 16 frequencies, respectively. The highest peaks marked by the red solid lines are f_1 = 7.3764 d^{-1} *(top panel)* and f_7 = 8.1687 d^{-1} *(middle panel)*.

profiles of these peaks do resemble those of real mode frequencies, i.e. increasing or decreasing from the blue to the red edge of the line. They were thus added to Table 2.6.

In order to test the influence of the line-cutting limits, we did a frequency analysis using different dispersion ranges for the Fe II line 4508.288 Å, as explained in Sect. 2.3. All different values of frequency and amplitude for all five dispersion ranges are consistent within the 1σ error bars.

2.5.2 Analysis of LSD profiles

As a result of the high rotation rate of the star, we only found one absorption line to be suitable for performing mode identification. In order to test the potential of using more information from the other spectral lines, we calculated LSD profiles for the McDonald spectra obtained in 2010 with the method by Kochukhov et al. (2010) and Tkachenko

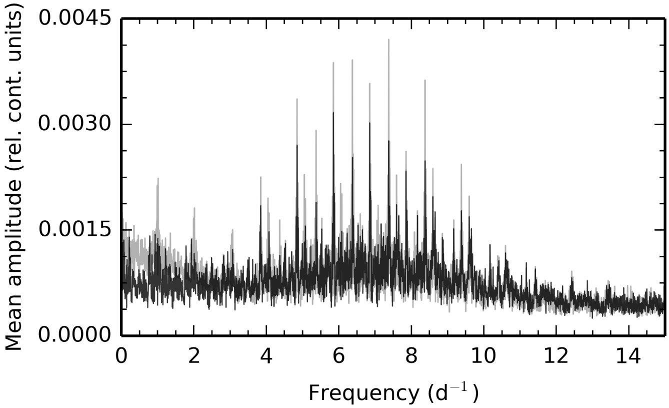

Figure 2.8: Mean of the Lomb-Scargle periodogram per bin in the season of 2010 for the Fe II line 4508.288 Å (grey) and the standard LSD profiles for all lines in the line mask, rescaled to the depth of the Fe II line (black).

et al. (2013c). We made use of the line mask, which was computed as discussed in Sect. 2.4, to calculate a standard LSD profile from all the lines in the line mask, as well as an LSD profile of the Fe lines only, using the multi-profile technique, in order to take the blending of Fe-lines into account. Figures 2.25, 2.26, and 2.27 in Appendix B show the mean profile, the standard deviation, and a 2D colour image of the LPVs, phase folded onto the frequency $f_1 = 7.3764$ d^{-1}, for the Fe II line at 4508.288 Å, the standard LSD profiles, and the Fe-LSD profiles, respectively.

The shape and depth of an LSD profile depends on the line mask used for the computation. As it can be considered an average of several lines (weak and strong lines of different elements), the depth will typically be less than that of a strong single line, such as Fe II at 4508.288 Å. In addition, the overall shape of the LSD profile can differ from that of a single line. All these effects can be seen in the figures in Appendix B. We note that the amplitude scales in Fig. 2.25 (single Fe II line) are different from the amplitude scales in Fig. 2.26 (standard LSD profiles) and Fig. 2.27 (Fe-LSD profiles). The uneven structure in the continuum region in the bottom panels of Figs. 2.26 and 2.27 is a consequence of the continuum normalisation, which is complicated by the high $v_{eq} \sin i = 109$ km s^{-1} of 4 CVn. We did not detect any feature in the LSD profiles that is moving according to the orbital period and could be connected to the companion of 4 CVn.

As already explained in Sect. 2.2.1, different lines can be more or less sensitive to stellar pulsations. It is therefore possible that the pulsation signal is smeared out in an LSD profile. This can affect the phase, but also the amplitude of the pulsation modes. Figure 2.8 depicts the mean amplitude spectra for the Fe II line 4508.288 Å (grey) and for the standard LSD profiles (black). In order to compare the two periodograms, we had to rescale the LSD profiles to match the amplitude of the Fe II line, as the pulsation amplitudes are expressed in units relative to the continuum of the line. The noise level in the periodogram of the rescaled LSD profiles is only lower in the low-frequency range and it contains less pulsation signal than the periodogram of the single line. This is reflected in the number of detected frequencies. While we were able to detect 14 significant ($A > 4\sigma_{\rm res}$) frequencies in the LPVs of Fe II (Table 2.6), we could only find 8 of them in the LPVs of the LSD profile. The frequencies detected in the LSD profiles had a lower S/N, and the amplitudes dropped by almost 30% for f_1 and by $\sim 7\%$ for f_2.

The results are similar for the LSD profiles based only on the Fe lines. The noise level in the mean periodogram of the Fe-LSD profiles is slightly higher than in the mean periodogram of the standard LSD profiles, since fewer lines were used for the computation of the profiles. Consequently, the amplitudes and S/N of the detected frequencies are even lower than the values found from the analysis of the standard LSD profiles.

As the LSD profiles do not yield any improvement to the single line, we conducted the further analysis on the Fe II line 4508.288 Å. It was already stressed by Aerts et al. (2010, Chapter 4) that line-profile analysis works best on one carefully selected, isolated line, if available.

2.6 Mode identification

2.6.1 Fourier-parameter fit method

During the frequency analysis (see Sect. 2.5) the observed Fourier parameters zero point Z_λ, amplitude A_λ, and phase ϕ_λ across the line were obtained for each oscillation frequency. For mode identification the observed profiles are compared to theoretical profiles. The most probable solutions can be compared by calculating a reduced χ^2. The theoretical values are computed from synthetic line profiles, which result from an integration over a surface grid divided into 10 000 segments. The intrinsic profile of each surface element is assumed to be Gaussian, and the local variations of flux arise from variations of temperature and surface gravity. Temperature variations, which lead to a varying EW, are neglected in a first approximation. Thus, we can also neglect the dependence of EW on temperature and assume a constant EW. The method is described in detail by Zima (2006, 2008, and references therein).

The FPF method requires the input of the stellar parameters: the mass and radius are used to estimate the ratio of horizontal to vertical amplitude of the velocity field, while the metallicity, effective temperature, and surface gravity are used to interpolate

Table 2.7: Line-profile parameters used for the mode identification of 4 CVn.

Central wavelength (Å)	4508.288
$v_{eq} \sin i$ (km s^{-1})	106.0 – 107.3
EW (km s^{-1})	15.0 – 15.25
σ (km s^{-1})	8.0 – 9.5
dZ (km s^{-1})	–0.05 – 0.5

Notes. The ranges of the line-profile parameters contain the best fits of the different sets of stellar parameters and the frequencies f_1 and f_2.

on a grid of limb-darkening coefficients. Besides giving a solution for (ℓ, m), it also allows us to derive parameters of the line that are independent of pulsation, like, EW (only in first approximation), the width of the intrinsic Gaussian profile σ, and the velocity offset of the line centre at 0 km s^{-1} dZ, which is a measure of radial velocity. Additionally, the inclination angle between pulsation axis and line of sight as well as $v_{eq} \sin i$ can be derived.

We note that the method is most powerful when determining the m-values and not as powerful for the ℓ-values (Zima 2008).

2.6.2 Mode identification of f_1 = 7.3764 d^{-1} and f_2 = 5.8496 d^{-1}

Mode identification was carried out for the two dominant frequencies f_1 = 7.3764 d^{-1} and f_2 = 5.8496 d^{-1}. We folded the series of spectra according to the phase of f_1 and f_2, respectively, and smoothed the LPVs in 50 phase bins. In this way we removed the signal of the several other p-modes which are excited to very low amplitudes and whose frequencies are hard to distinguish from noise and can therefore not be extracted from the data. Hence, we are able to treat the star as a mono-periodic pulsator during the mode identification. The zero point, amplitude, and phase profiles across the line obtained from the phase folded data set are displayed in Figs. 2.9 and 2.10 for f_1 and f_2, respectively.

We found the solution $(\ell_1, m_1) = (3, -2)$ for f_1. For f_2, mode identification was ambiguous; $(\ell_2, m_2) = (3, 3)$ and $(\ell_2, m_2) = (2, 2)$ are the best fits to f_2 depending on the stellar input parameters. However, other solutions cannot be excluded for both f_1 and f_2, since the χ^2 differs by only a few percent. Furthermore, we obtain a high χ^2 ($\chi^2 > 28$) for all ℓ and m combinations, which means that no solution provides a good fit to the observations. This will be discussed in Sect. 2.7. All results are summarised in Appendix C, in Tables 2.10, 2.11, and 2.12. Figures 2.28, 2.29, 2.30, 2.31, 2.32, and 2.33 show the observed amplitude and phase profile of f_1 fitted with the modes $(3, -2)$, $(3, -3)$, $(3, -1)$, $(2, -2)$, $(2, -1)$, and $(1, -1)$, respectively. The fits to the observed

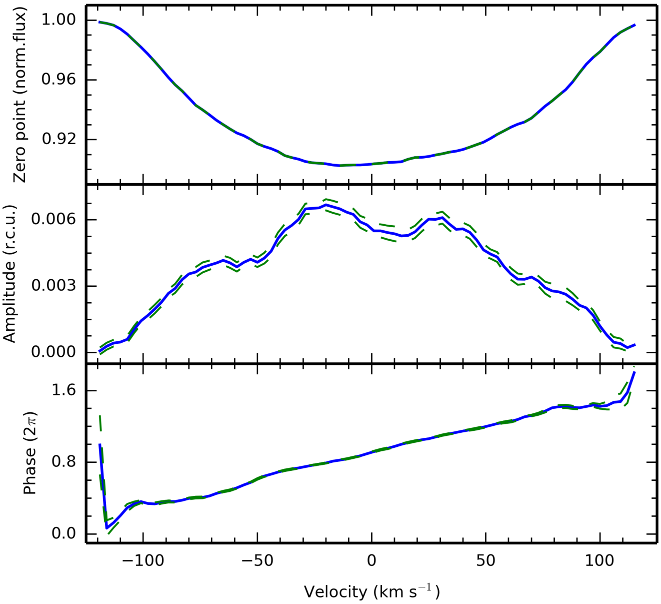

Figure 2.9: Zero point *(top panel)*, amplitude *(middle panel)*, and phase *(bottom panel)* across the line of the frequency f_1, calculated with the phase folded data set. Observations are shown as the blue solid line, while the errors of the observations are the green dashed lines.

amplitude and phase profile of f_2 with the modes $(3,3)$, $(3,2)$, $(3,1)$, $(2,2)$, $(2,1)$, and $(1,1)$ are shown in Figs. 2.34, 2.35, 2.36, 2.37, 2.38, and 2.39, respectively.

Line-profile parameters

Before fitting amplitude and phase across the line to identify the modes, the pulsation-independent line-profile parameters, $v_{eq} \sin i$, EW, σ, and dZ are constrained by fitting the zero-point profile with a non-pulsating model. However, these parameters varied when fitting the pulsation modes and were therefore left as free parameters during the mode identification. The ranges within which the fits were computed are summarised in Table 2.7. With the FPF method we derive a slightly lower $v_{eq} \sin i$ value than in Sect. 2.4, because the GSSP package does not take pulsational line broadening into account.

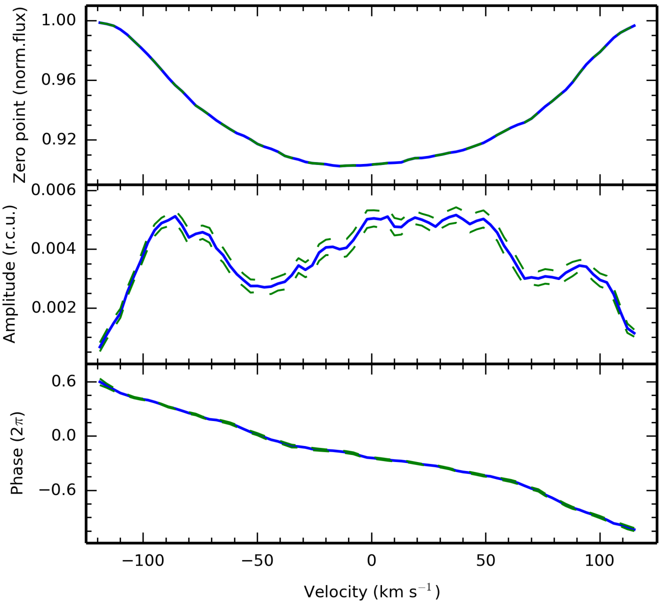

Figure 2.10: Zero point *(top panel)*, amplitude *(middle panel)*, and phase *(bottom panel)* across the line of the frequency f_2, calculated with the phase folded data set. The colours and lines have the same meaning as in Fig. 2.9.

Three sets of stellar input parameters

The photometric and spectroscopic analysis, presented in Sect. 2.4, suggests that the mass of 4 CVn lies between 1 $M_\odot$ and 2 $M_\odot$, while the radius is between 3.7 $R_\odot$ and 4.1 $R_\odot$. The effective temperature of the star $T_{\rm eff}$ = 6875 ± 120 K, the surface gravity $\log g$ = 3.3 ± 0.35 dex, and the metallicity is near solar.

Breger & Pamyatnykh (2002) computed a model with the 18 photometrically observed frequencies of 4 CVn, assuming the star to be single and of $M = 2.4\ M_\odot$, $\log L/L_\odot = 1.76$, $T_{\rm eff} = 6800\ K$, $\log g = 3.32$, $V_{\rm rot} = 82$ km s^{-1}, and solar metallicity. The luminosity of this model is a factor of 2 higher than our deduced value $\log L/L_\odot = 1.47 \pm 0.05$.

Since the stellar parameters are not well constrained, we calculated the mode identification for three different sets of parameters, which are summarised in Table 2.8. The values of set 1 and set 2 lie within the ranges of the results of our spectroscopic and photometric analysis, while the values for set 3 are based on the model by Breger & Pamyatnykh (2002). The inclination angle, i, was fitted within the range 23° ≤ i ≤ 90°.

Table 2.8: Stellar input parameters for the mode identification of 4 CVn.

	Set 1^a	Set 2^a	Set 3^b
Mass ($M_\odot$)	2.0	1.5	2.4
Radius ($R_\odot$)	3.72	3.75	5.6
T_{eff} (K)	7050	6950	6800
$\log g$ (dex)	3.6	3.45	3.32
[m/H] (dex)	0	0	0
v_{crit} (km s^{-1})^c	320.3	276.3	286.0
Inclination (deg)	23 – 90		

Notes. $^{(a)}$ Values based on our spectroscopic and photometric analysis (see Sect. 2.4).
$^{(b)}$ Values based on Breger & Pamyatnykh (2002).
$^{(c)}$ The critical velocity is given by $v_{crit} = \sqrt{GM_*/R_e}$.

We adopted a lower limit $i \sim 23°$ as it is the critical value where the star rotates at the break-up velocity ($v_{crit} = \sqrt{GM_*/R_e}$, where R_e is the equatorial radius; Townsend et al. 2004). The critical velocity v_{crit}, which depends on the stellar mass and radius, is also given for each set in Table 2.8.

It is not possible to distinguish between the three sets of stellar parameters. The best solutions of all three sets lie within 10% of χ^2 and are therefore equally possible. For f_1, the best fitting (ℓ_1, m_1) combination is always a (3, −2) mode. The solution for f_2, however, shows a dependence on the stellar input parameters and differs for the three different sets (see Tables 2.10, 2.11, 2.12).

Inclination angle

For our computations, we assume that the pulsation axis coincides with the rotation axis. The inclination angle i is then the angle between this axis and the line of sight. It is thus not physically possible that f_1 and f_2 are observed at a different i. However, in Tables 2.10–2.12 it can be seen that the value of i varies between the solutions for the different sets of stellar parameters and the two frequencies. This is also illustrated in Fig. 2.11 where (from top to bottom) the χ^2 distribution of i for sets 1, 2, and 3 of the stellar parameters are displayed. The minimum χ^2 value is shown for each 3° bin in inclination for f_1 and f_2 in each panel. For set 3 the frequencies f_1 and f_2 show an opposite behaviour. While f_1 favors higher inclination values around $\sim 60°$ to $\sim 90°$, mode identification for f_2 yields $i < 50°$. Set 1 and set 2 give a more consistent result for i, where f_1 and f_2 follow the same trend. On the other hand, there is also no clear minimum visible in χ^2, neither for f_1 nor for f_2 in any of the three sets. The inclination is highly degenerate with the degree ℓ and the order $|m|$ of the oscillation mode, as it

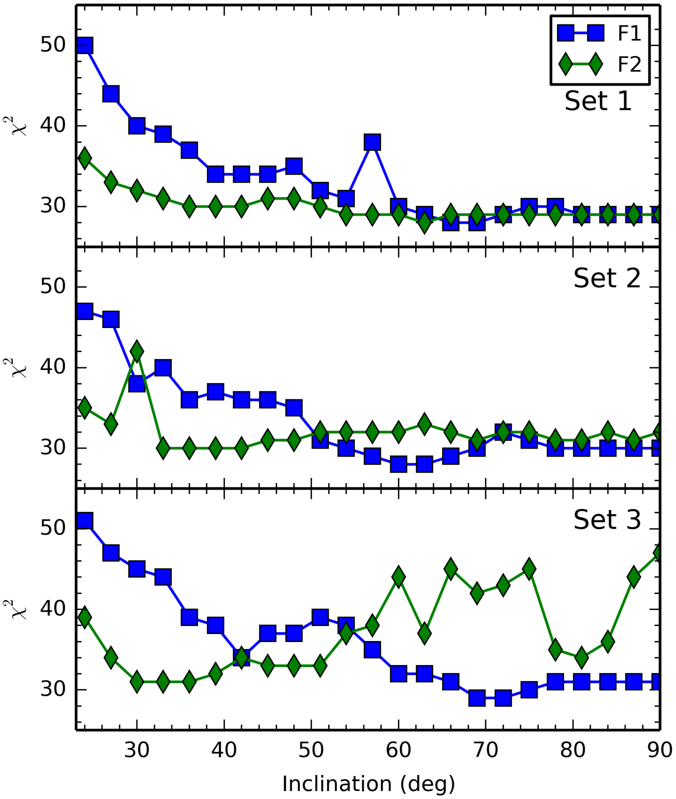

Figure 2.11: The χ^2 distribution of the inclination angle i for f_1 (blue squares) and f_2 (green diamonds) and for set 1 *(top panel)*, set 2 *(middle panel)*, and set 3 *(bottom panel)* of the stellar parameters.

determines the visibility of a certain mode. Mode identification was ambiguous for f_1 and f_2 and certain effects hamper us from drawing clear conclusions, as will be discussed in Sect. 2.7. Thus, we can also not find a consistent inclination for 4 CVn.

Temperature and equivalent-width variations

So far we have ignored variations of temperature in a first approximation and assumed a constant EW; thus, $d(EW)/d(T_{\mathrm{eff}}) = 0$. To improve the fits of the amplitude and phase profiles we varied the parameter $d(EW)/d(T_{\mathrm{eff}})$ and other parameters related to the temperature dependence of the flux variation; at first within a very broad range,

Table 2.9: Identification of the azimuthal order for the seven dominant frequencies.

Frequency d^{-1}		
f_1	7.3764	retrograde
f_2	5.8496	prograde
f_3	5.0481	retrograde or axisymmetric
f_4	5.5315	prograde
f_5	8.5942	prograde
f_6	8.6552	prograde
f_7	8.1688	high-degree, prograde

and gradually narrowing down the range. However, the parameters did not converge and the minimum in χ^2 varied with each iteration, without improving the overall χ^2 significantly. The final solution therefore had to be calculated with $d(EW)/d(T_{\text{eff}}) = 0$, neglecting temperature variations.

2.6.3 Azimuthal order of the seven most-dominant frequencies

Mode identification has also been attempted for the frequencies f_3, f_4, f_5, f_6, and f_7. However, the amplitude of f_3 decreases by almost 40% compared to f_2 and the amplitudes of the other frequencies are even lower. Therefore, phase folding of the spectra on the respective frequencies and smoothing the LPVs in phase bins did not remove the signal of the two most-dominant frequencies sufficiently. Thus, a consistent mode identification cannot be achieved. However, as the FPF method is sensitive to phase, the slope of the phase profile across the line allows us to distinguish between *prograde* (i.e. a wave travelling in the direction of rotation; positive m, following the definition by Zima 2008), *retrograde* (negative m), and *axisymmetric* ($m = 0$) modes. Our results are given in Table 2.9. We also attempted mode identification for $f_{12} = 6.975$ d^{-1}. Our results do not contradict the solution presented in Lenz et al. (2010), who reported that it is a radial mode.

The very complex amplitude and phase profiles of f_7, i.e. containing many bumps, suggests that it is a high-degree mode, with $\ell \geq 3$. For modes with a high ℓ value, partial cancelation would lead to very low amplitudes in photometric observations, where the brightness variation integrated over the stellar disk is measured. This mode has not been detected in photometric data before, which supports our hypothesis of a high ℓ for f_7.

2.7 Discussion

2.7.1 Mode visibility and rotational splitting

The mode identification we attempted for the star 4 CVn yielded ambiguous results. The χ^2 statistics give several possible solutions for f_1 and f_2, depending on the stellar input parameters. For frequency $f_1 = 7.3764$ d^{-1} the best solution yields $\ell_1 = 3$ and for frequency $f_2 = 5.8496$ d^{-1}, $\ell_2 = 2$ or $\ell_2 = 3$. Theory predicts that modes with degree $\ell = 3$ cancel out almost completely in photometric observations (Aerts et al. 2010, Chapter 6). However, both f_1 and f_2 were detected with significant amplitudes in photometric data (see Table 2.1), which contradicts the results of our mode identification. The solutions $(\ell_1, m_1) = (2, -2)$ and $(\ell_2, m_2) = (2, 2)$ would agree most closely with the current theory and our results.

We therefore tested the hypothesis that f_1 and f_2 are the outer parts of a rotationally split quintuplet. Rotational splitting (Ledoux 1951) describes the shift of frequencies of modes of same degree ℓ and different order $|m|$ $(0 \leq |m| \leq \ell)$ due to the Coriolis force. It is dependent on $|m|$ and the rotational period of the star. With set 3 of the stellar parameters and $i > 80°$ it would be possible that we are observing rotational splitting in 4 CVn (see Table 2.12 and Fig. 2.11).

2.7.2 Rotation rate

We conclude that 4 CVn rotates at a significant fraction of its critical velocity. We measured $v_{eq} \sin i \simeq 106.7$ km s^{-1} for the star. Thus, its equatorial velocity v_{eq} is at least $\sim 33\%$ of its critical velocity v_{crit}. Since i and the stellar mass and radius are poorly constrained, it is possible that it rotates at up to almost $\sim 70\%$ of v_{crit}. Tables 2.10–2.12 provide the possible ranges of i and v_{eq}/v_{crit}.

Reese et al. (2013) showed that even a moderate rotation rate $v_{eq}/v_{crit} = 0.3$ has a large effect on the visibility of oscillation modes. While partial cancelation makes $\ell = 3$ modes almost not detectable in photometric data for slow rotation ($v_{eq}/v_{crit} \leq 0.2$), their amplitudes are as high as the amplitudes of modes with $\ell \leq 2$ if $v_{eq}/v_{crit} = 0.3$ (see Fig. 7 of Reese et al. 2013). This would mean that our results of $\ell = 3$ for f_1 and f_2 do not contradict the mode amplitudes observed in photometric light curves. However, fast rotation also alters the geometry of the modes (Reese et al. 2009). Since higher order effects of rotation are not yet included in the methodology for mode identification, this could be an explanation for the poor fits we obtained. If this is the case, the amplitude and phase profiles across the line, as well as the amplitude ratios of multicolour photometry would have to be revisited, with a methodology that includes the effects of rotation on the pulsation modes.

2.8 Summary

In this chapter, we analysed the line-profile variations of the δ Sct star 4 CVn based on the spectroscopic observations obtained between January 2008 and June 2011 at McDonald Observatory, Texas, USA. We discovered that the star is the primary component of an eccentric binary system with an orbital period $P_{orb} = 124.44 \pm 0.03$ d and eccentricity $e = 0.311 \pm 0.003$. No signal of the secondary could be detected in our data. The frequency analysis revealed 20 oscillation modes, 11 of which had already been detected in photometric data sets by Breger et al. (1999), Breger (2000b), and Breger et al. (2008).

By phase folding the series of spectra onto the two dominant frequencies f_1 and f_2 and smoothing the LPVs in phase bins, we removed the signal of other periodicities to prepare the data for mode identification. The best solution for frequency f_1 is an $(\ell_1, m_1) = (3, -2)$ mode, while the best solution for f_2 was either $(\ell_2, m_2) = (3, 3)$ or $(\ell_2, m_2) = (2, 2)$ depending on the stellar input parameters. For the calculations of the synthetic LPVs we used three different sets of stellar parameters:

1. $M = 2.0\,M_\odot$, $R = 3.72\,R_\odot$, $T_{\rm eff} = 7050$ K, $\log g = 3.6$, and [M/H]=0.
2. $M = 1.5\,M_\odot$, $R = 3.75\,R_\odot$, $T_{\rm eff} = 6950$ K, $\log g = 3.45$, and [M/H]=0.
3. $M = 2.4\,M_\odot$, $R = 5.6\,R_\odot$, $T_{\rm eff} = 6800$ K, $\log g = 3.32$, and [M/H]=0.

Sets 1 and 2 are based on the spectroscopic and photometric analysis we performed to revise the stellar parameters. Set 3 is based on a model calculated by Breger & Pamyatnykh (2002). No set of stellar parameters can be excluded, based on the χ^2 statistics.

Relying on previous results by Castanheira et al. (2008), Breger (2010) claimed a relationship between the frequency variations of 4 CVn and the azimuthal order m of the modes, and especially the direction of the running wave (*retrograde*, *prograde*, or *axisymmetric*/*radial* modes). The FPF method is the most sensitive to the sign of m. Our results in Table 2.9 are in agreement with the directions of the waves used by Breger (2010).

The star is a fast rotator with $v_{eq} \sin i \simeq 106.7\,\mathrm{km\,s^{-1}}$. Depending on the stellar input parameters and i (which could not be constrained), the star is rotating at $> 33\%$ of the critical velocity v_{crit}. The higher order effects of rotation were not taken into account in our analysis, since they are not yet included in the methodology for mode identification.

A further limitation from the methodology is that unblended metal lines have to be used for mode identification. However, our observed spectral range (4500 Å to 4700 Å) is a very dense spectral region with many absorption lines and very little continuum for

F stars, and almost all absorption lines are (heavily) blended. In an attempt to solve this problem, we calculated LSD profiles from the McDonald spectra obtained in the season 2010. We found that the pulsation signal is smeared out in the LSD profiles, as the number of significant oscillation modes detected in the LPVs of the LSD profiles is less than for the single Fe II line. The amplitudes and the S/N levels of these modes are also reduced significantly. To improve our analysis a method for identifying the modes in blended lines would have to be developed. In addition, observations in a wider spectral range could help solve the problem of blended lines. The lines that Zima et al. (2006) used for their analysis of the δ Sct star FG Vir lie outside the observed spectral range of the McDonald data. Observing a wider spectral range with a stable, high-resolution spectrograph would allow us to follow up on the additional spectral feature detected in the LSD profile of 4 CVn (see Fig. 2.4), and could possibly lead to identification of the origin of the latter.

Accurate mode identification of many observed frequencies is a crucial input for successful modelling of stellar oscillations. Analyses of LPVs are important as they can constrain the azimuthal order *m* of the pulsation modes. However, current shortcomings in the methodology prevent an unambiguous and accurate mode identification for 4 CVn. Including a complete description of rotation and the use of blended lines into mode-identification techniques will make this possible in the future.

Appendix A: Amplitude and phase profiles

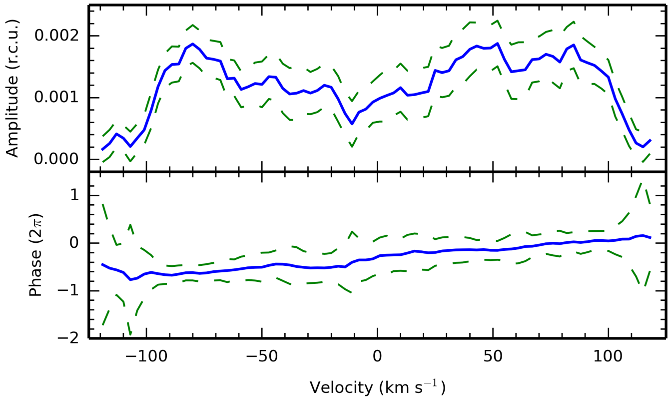

Figure 2.12: Amplitude *(top panel)* and phase *(bottom panel)* across the line for frequency f_8 = 6.6801 d^{-1}. Observations are shown as the blue solid line and errors of the observations are shown as the green dashed line.

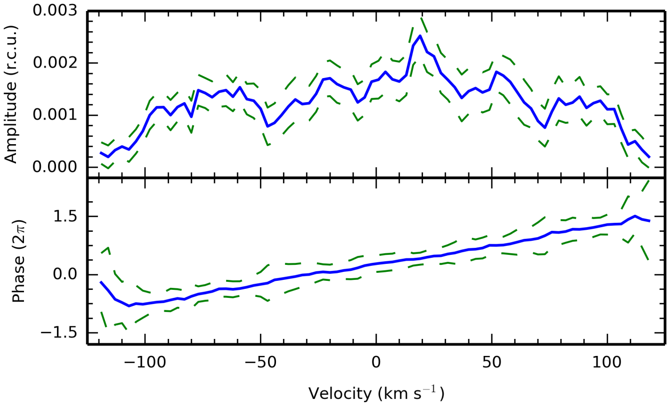

Figure 2.13: Same as Fig. 2.12, but for frequency f_9 = 4.0743 d^{-1}.

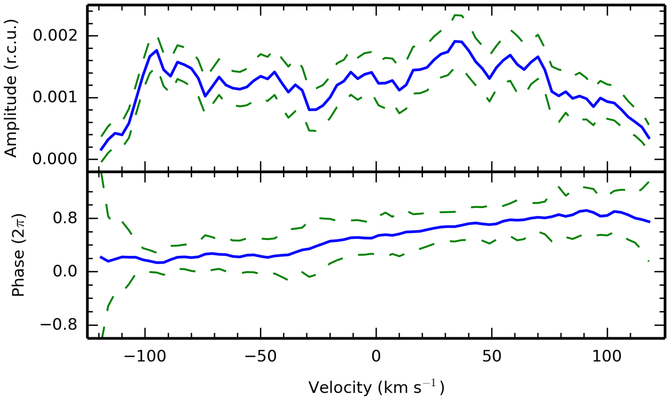

Figure 2.14: Same as Fig. 2.12, but for frequency f_{10} = 6.1171 d^{-1}.

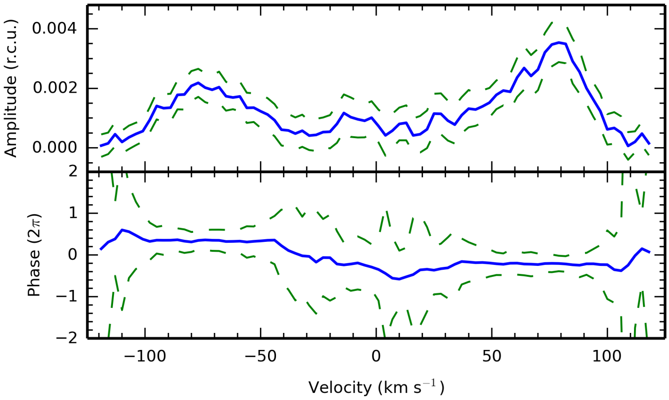

Figure 2.15: Same as Fig. 2.12, but for frequency f_{11} = 6.975 d^{-1}.

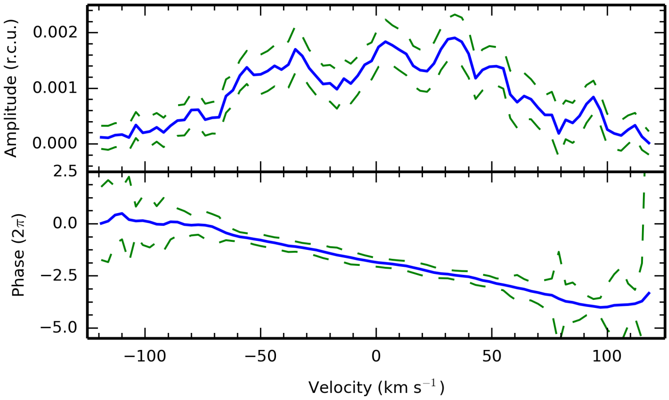

Figure 2.16: Same as Fig. 2.12, but for frequency f_{12} = 10.1702 d^{-1}.

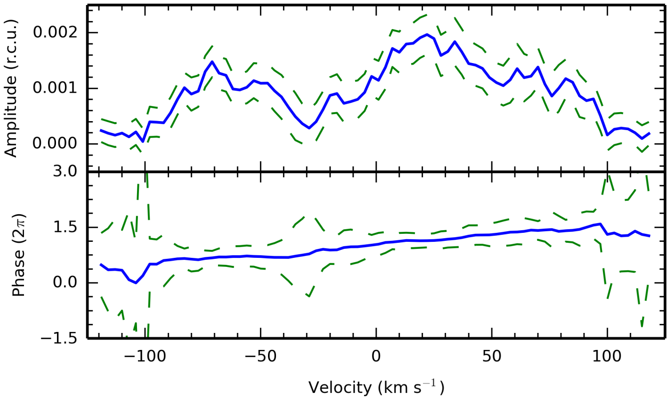

Figure 2.17: Same as Fig. 2.12, but for frequency f_{13} = 6.1910 d^{-1}.

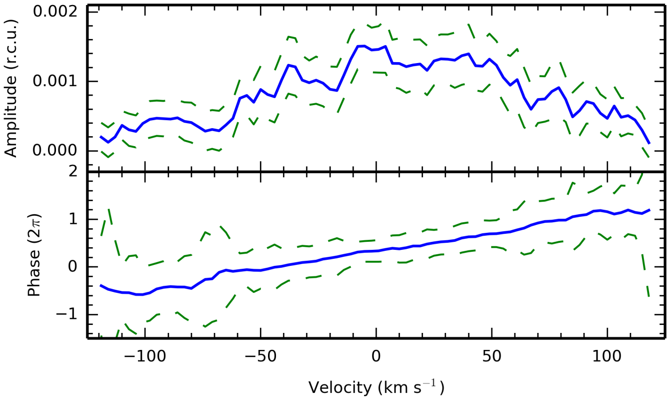

Figure 2.18: Same as Fig. 2.12, but for frequency f_{14} = 12.4244 d^{-1}.

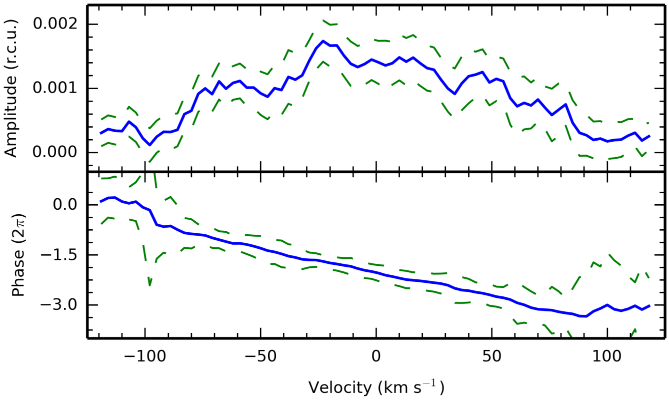

Figure 2.19: Same as Fig. 2.12, but for frequency f_{15} = 9.4113 d^{-1}.

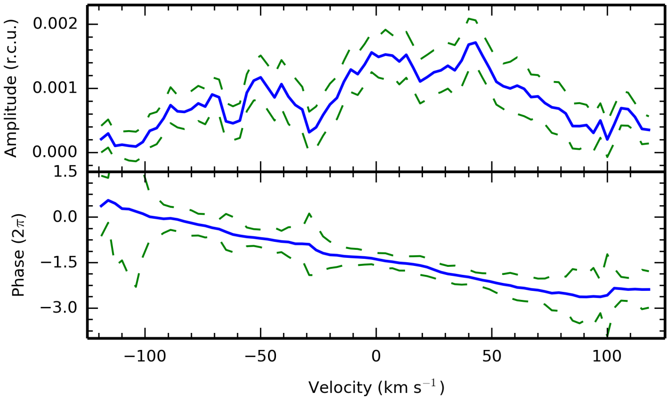

Figure 2.20: Same as Fig. 2.12, but for frequency f_{16} = 9.7684 d^{-1}.

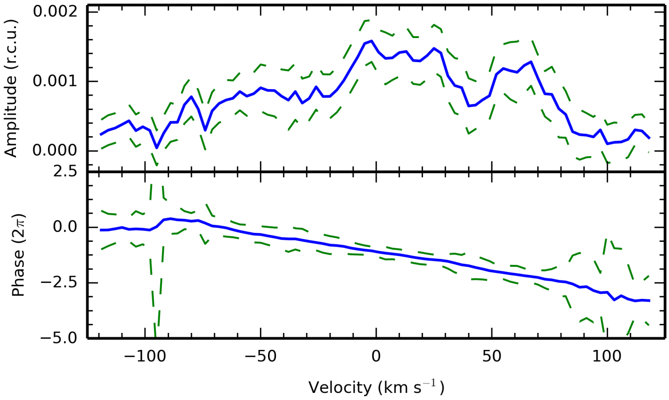

Figure 2.21: Same as Fig. 2.12, but for frequency f_{17} = 10.0372 d^{-1}.

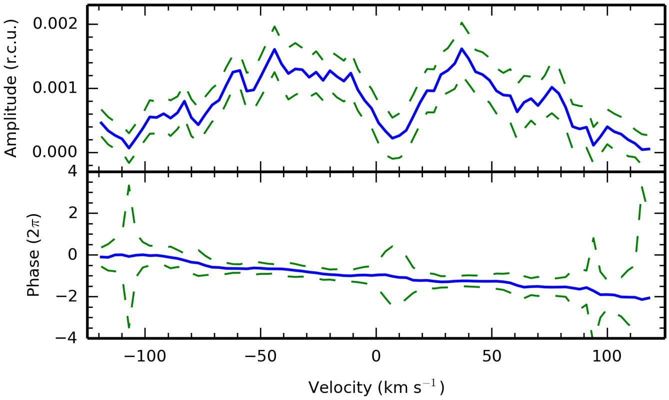

Figure 2.22: Same as Fig. 2.12, but for frequency f_{18} = 6.4030 d^{-1}.

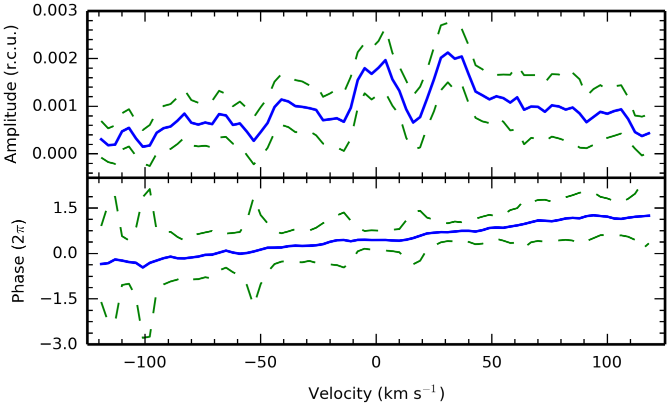

Figure 2.23: Same as Fig. 2.12, but for frequency f_{19} = 13.388 d^{-1}.

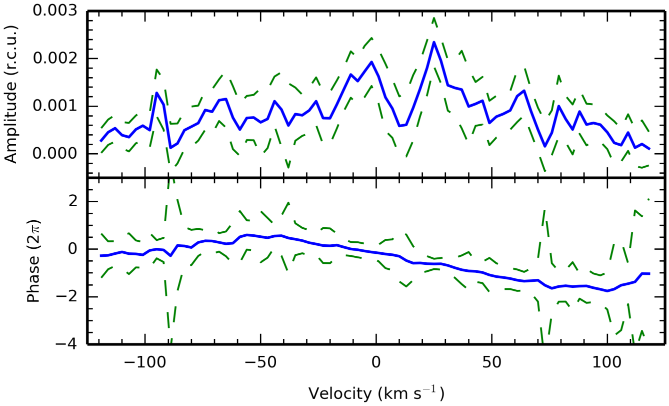

Figure 2.24: Same as Fig. 2.12, but for frequency f_{20} = 10.016 d^{-1}.

Appendix B: Comparison of LSD profiles and single-line profiles

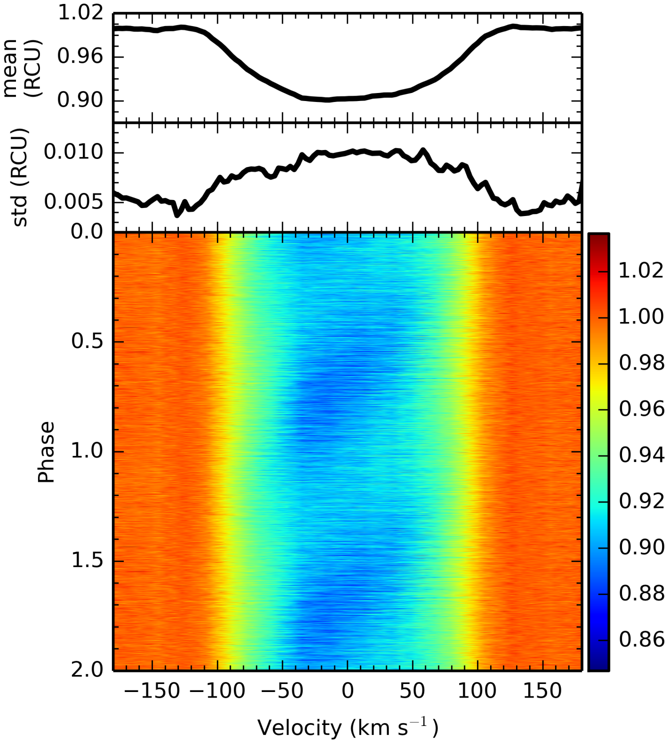

Figure 2.25: *Top panel:* Mean profile of the Fe II line at 4508.288 Å in the season 2010. *Middle panel:* Standard deviation of the Fe II line. *Bottom panel:* Colour image of the LPVs of the Fe II line, phase folded on the frequency f_1 = 7.3764 d^{-1}. The amplitude is colour coded and can be read from the colour bar.

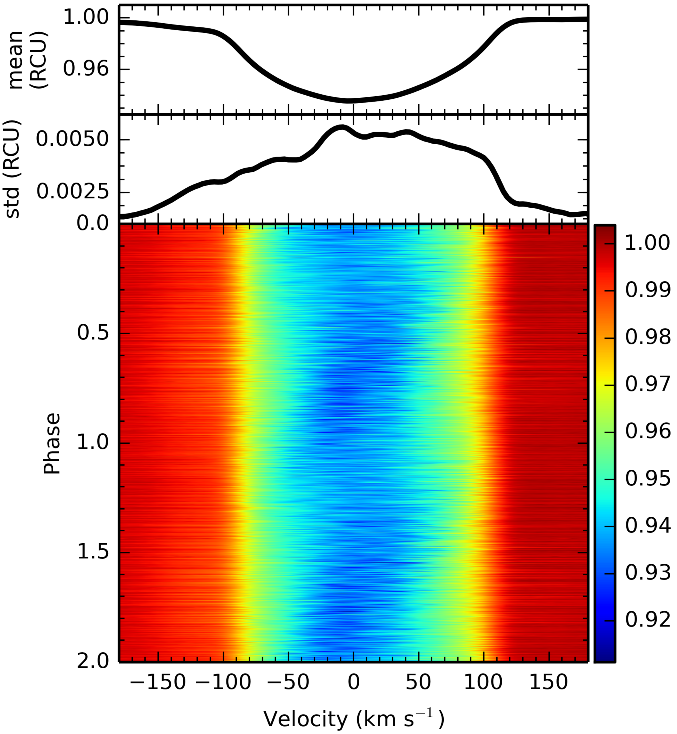

Figure 2.26: Same as Fig. 2.25 for the standard LSD profiles calculated from all lines in the line mask.

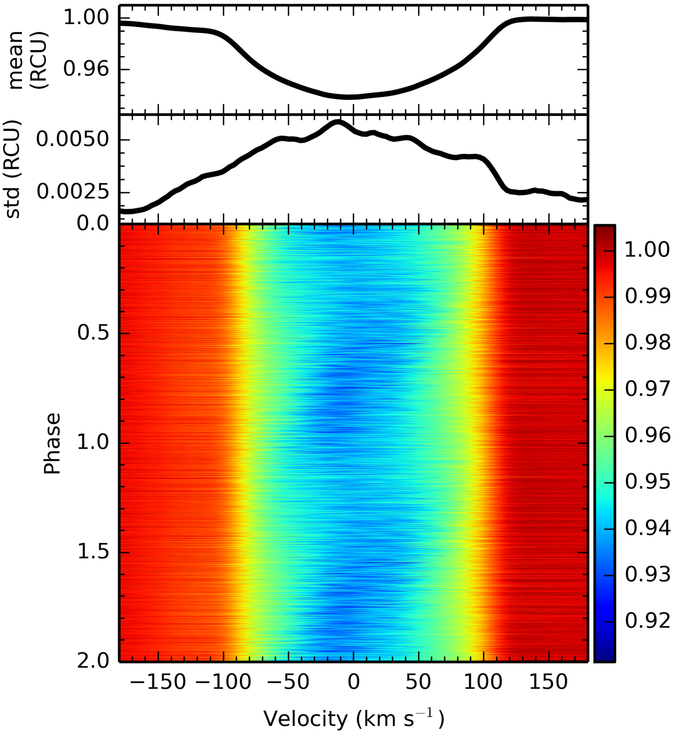

Figure 2.27: Same as Fig. 2.25 for the LSD profiles calculated from all Fe lines in the line mask only.

Appendix C: Results of the mode identification of $f_1 = 7.3764\ \mathrm{d}^{-1}$ and $f_2 = 5.8496\ \mathrm{d}^{-1}$

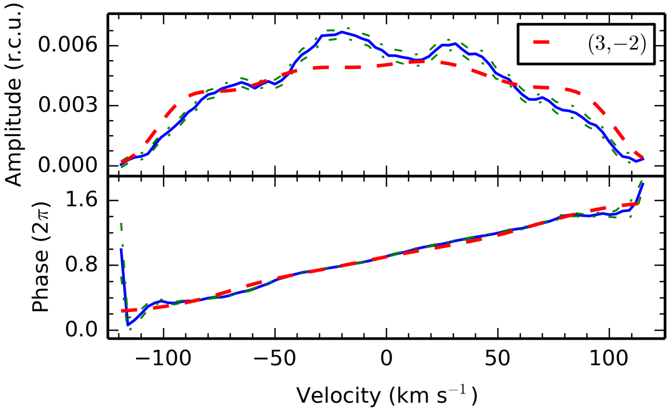

Figure 2.28: Fit of the amplitude *(top panel)* and phase *(bottom panel)* across the line of the frequency f_1 with a $(\ell, m) = (3, -2)$ mode. The observed profiles are calculated from the phase folded data set. Observations are shown as the blue solid line, the errors of the observations are shown as the green dash-dotted line, and the fit is shown as the red dashed line. The fit has a χ^2 of 28.6.

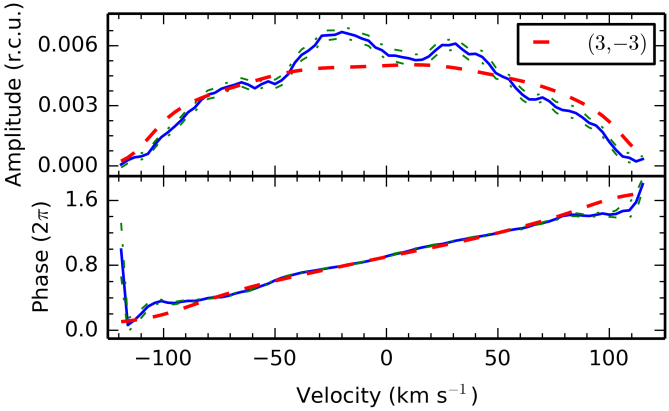

Figure 2.29: Same as Fig. 2.28, but with a $(\ell, m) = (3, -3)$ mode. The fit has a χ^2 of 29.7.

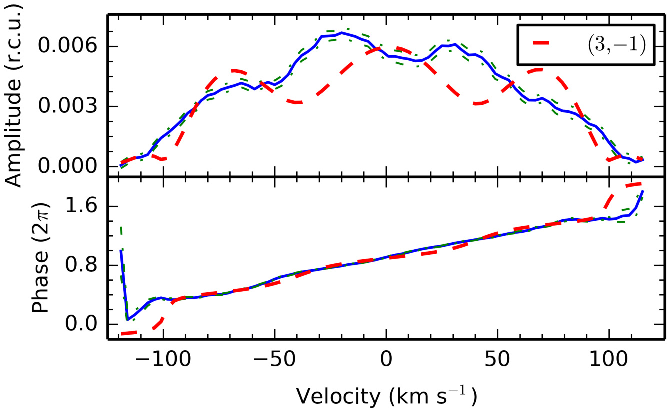

Figure 2.30: Same as Fig. 2.28, but with a $(\ell, m) = (3, -1)$ mode. The fit has a χ^2 of 34.6.

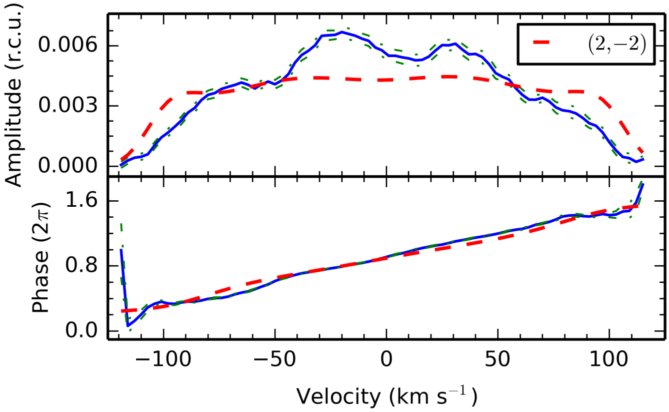

Figure 2.31: Same as Fig. 2.28, but with a $(\ell, m) = (2, -2)$ mode. The fit has a χ^2 of 38.3.

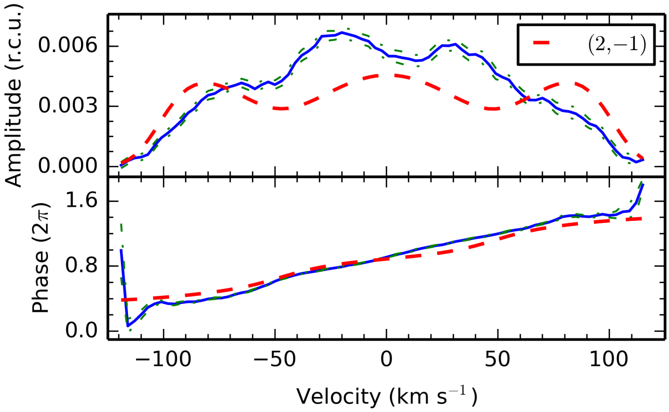

Figure 2.32: Same as Fig. 2.28, but with a $(\ell, m) = (2, -1)$ mode. The fit has a χ^2 of 47.7.

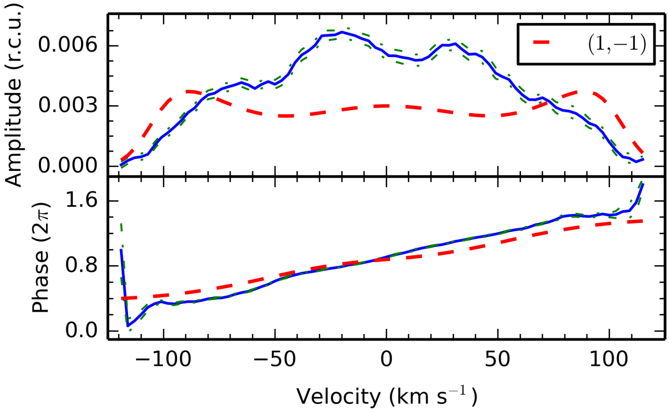

Figure 2.33: Same as Fig. 2.28, but with a $(\ell, m) = (1, -1)$ mode. The fit has a χ^2 of 68.7.

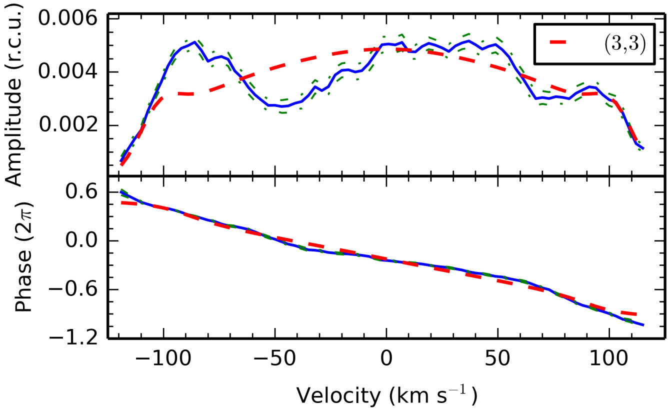

Figure 2.34: Fit of the amplitude *(top panel)* and phase *(bottom panel)* across the line of the frequency f_2 with a $(\ell, m) = (3, 3)$ mode. The observed profiles are calculated from the phase folded data set. Observations are shown as the blue solid line, the errors of the observations are shown as the green dash-dotted line, and the fit is shown as the red dashed line. The fit has a χ^2 of 29.

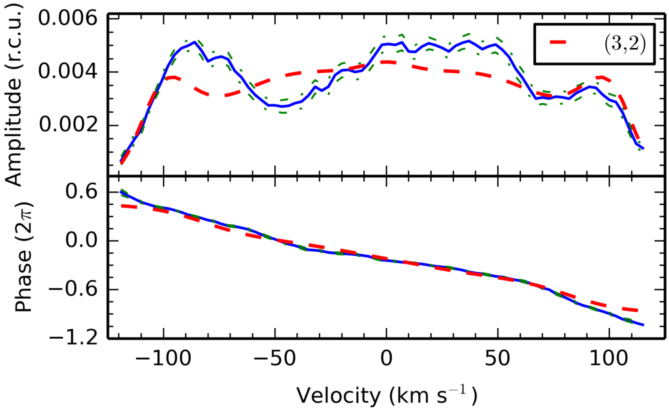

Figure 2.35: Same as Fig. 2.34, but with a $(\ell, m) = (3, 2)$ mode. The fit has a χ^2 of 30.8.

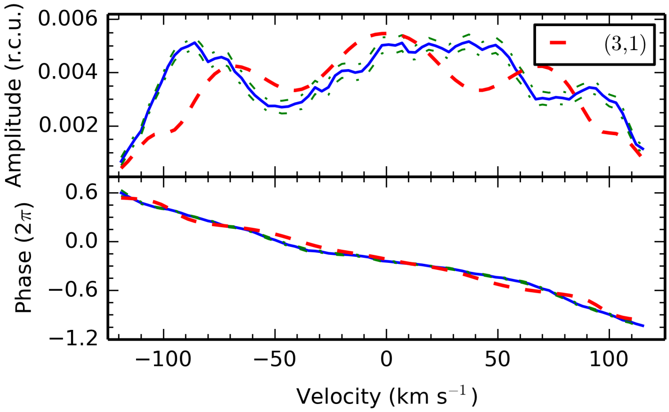

Figure 2.36: Same as Fig. 2.34, but with a $(\ell, m) = (3, 1)$ mode. The fit has a χ^2 of 35.3.

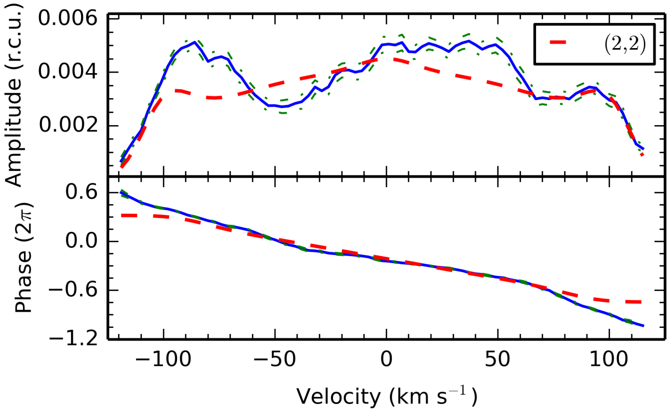

Figure 2.37: Same as Fig. 2.34, but with a $(\ell, m) = (2, 2)$ mode. The fit has a χ^2 of 39.6.

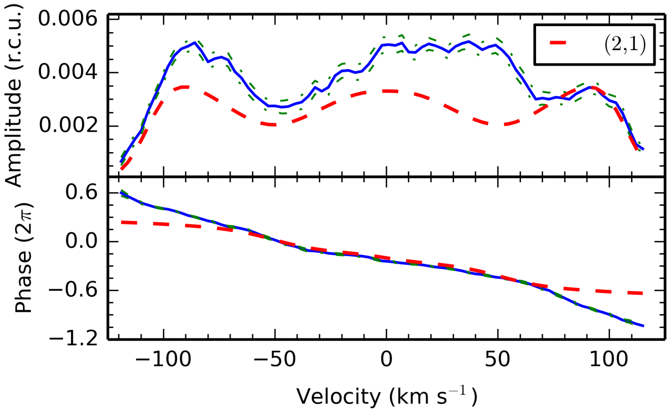

Figure 2.38: Same as Fig. 2.34, but with a $(\ell, m) = (2, 1)$ mode. The fit has a χ^2 of 65.6.

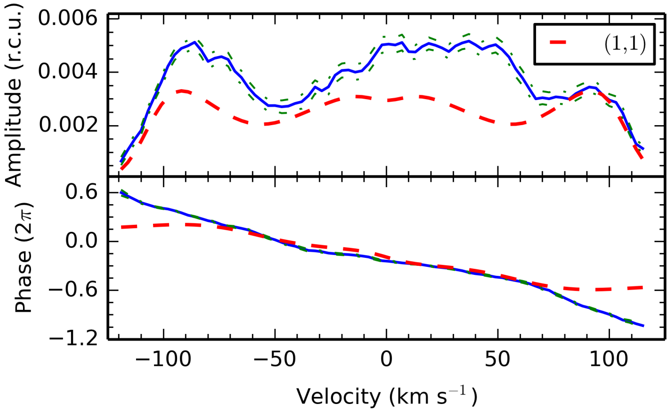

Figure 2.39: Same as Fig. 2.34, but with a $(\ell, m) = (1, 1)$ mode. The fit has a χ^2 of 68.3.

Table 2.10: Results of the mode identification using set 1 of the stellar parameters ($M = 2.0\ M_\odot$, $R = 3.72\ R_\odot$, $\log g = 3.6$, and $T_{\rm eff} = 7050$ K).

$f_1 = 7.3764\ {\rm d}^{-1}$						$f_2 = 5.8496\ {\rm d}^{-1}$					
(ℓ_1, m_1)	i (deg)	$v_{eq} \sin i$ (km s^{-1})	v_{eq} (km s^{-1})	v_{eq}/v_{crit}	χ^2	(ℓ_2, m_2)	i (deg)	$v_{eq} \sin i$ (km s^{-1})	v_{eq} (km s^{-1})	v_{eq}/v_{crit}	χ^2
(3, −2)	66.3	106.5	116.3	0.36	28.6	(3, 3)	61.0	106.9	122.2	0.38	29.0
(3, −3)	88.9	106.7	106.7	0.33	29.7	(3, 2)	36.2	106.8	180.8	0.56	30.8
(3, −1)	41.5	106.6	160.9	0.50	34.6	(3, 1)	51.5	106.6	136.2	0.43	35.3
(2, −2)	51.5	106.6	136.2	0.43	38.3	(2, 2)	44.1	106.8	153.5	0.48	39.6
(2, −1)	38.3	106.5	171.8	0.54	47.7	(2, 1)	35.1	106.7	185.6	0.58	65.6
(1, −1)	43.6	106.6	154.6	0.48	68.7	(1, 1)	24.6	106.7	256.3	0.80	68.3

Notes. The results are ordered by increasing χ^2. The critical velocity $v_{crit} = 320.3$ km s^{-1}.

Table 2.11: Results of the mode identification using set 2 of the stellar parameters ($M = 1.5\ M_\odot$, $R = 3.75\ R_\odot$, $\log g = 3.45$, and $T_{\rm eff} = 6950$ K).

$f_1 = 7.3764\ \mathrm{d}^{-1}$						$f_2 = 5.8496\ \mathrm{d}^{-1}$					
(ℓ_1, m_1)	i (deg)	$v_{eq} \sin i$ (km s^{-1})	v_{eq} (km s^{-1})	v_{eq}/v_{crit}	χ^2	(ℓ_2, m_2)	i (deg)	$v_{eq} \sin i$ (km s^{-1})	v_{eq} (km s^{-1})	v_{eq}/v_{crit}	χ^2
(3, −2)	61.5	106.7	121.4	0.44	28.7	(3, 3)	38.3	106.9	172.5	0.62	30.4
(3, −3)	90.0	106.8	106.8	0.39	30.5	(3, 2)	34.1	107.0	190.9	0.69	30.8
(3, −1)	43.0	106.7	156.5	0.57	36.0	(2, 2)	36.7	106.9	178.9	0.65	36.8
(2, −2)	58.3	106.8	125.5	0.45	38.5	(3, 1)	48.9	106.6	141.5	0.51	39.1
(2, −1)	43.0	106.6	156.3	0.57	47.7	(2, 1)	34.1	106.8	190.5	0.69	64.0
(1, −1)	43.6	106.7	154.7	0.56	69.1	(1, 1)	23.0	106.7	273.1	0.99	66.9

Notes. The results are ordered by increasing χ^2. The critical velocity $v_{crit} = 276.3$ km s^{-1}.

Table 2.12: Results of the mode identification using set 3 of the stellar parameters (M = 2.4 $M_\odot$, R = 5.6 $R_\odot$, $\log g$ = 3.32, and T_{eff} = 6800 K).

$f_1 = 7.3764$ d^{-1}						$f_2 = 5.8496$ d^{-1}					
(ℓ_1, m_1)	i (deg)	$v_{eq} \sin i$ (km s^{-1})	v_{eq} (km s^{-1})	v_{eq}/v_{crit}	χ^2	(ℓ_2, m_2)	i (deg)	$v_{eq} \sin i$ (km s^{-1})	v_{eq} (km s^{-1})	v_{eq}/v_{crit}	χ^2
(3, −2)	69.4	106.8	114.1	0.40	29.7	(2, 2)	31.5	107.0	204.8	0.72	31.6
(3, −3)	87.9	107.0	107.1	0.37	31.6	(3, 2)	79.4	106.5	108.3	0.38	34.0
(3, −1)	42.0	106.8	159.6	0.56	37.4	(3, 3)	23.0	107.2	274.4	0.96	43.8
(2, −2)	57.8	106.9	126.3	0.44	38.7	(3, 1)	40.9	107.0	163.4	0.57	44.3
(2, −1)	44.1	106.8	153.5	0.54	48.5	(2, 1)	30.9	107.0	208.4	0.73	57.4
(1, −1)	43.6	106.9	155.0	0.54	69.1	(1, 1)	23.0	107.0	273.8	0.96	61.7

Notes. The results are ordered by increasing χ^2. The critical velocity v_{crit} = 286.0 km s^{-1}.

Chapter 3

KIC 10080943: a binary hybrid pulsator

This chapter was originally published as

KIC 10080943: An eccentric binary system containing two pressure- and gravity-mode hybrid pulsators

V. S. Schmid, A. Tkachenko, C. Aerts, P. Degroote, S. Bloemen, S. J. Murphy, T. Van Reeth, P. I. Pápics, T. R. Bedding, M. A. Keen, A. Prša, J. Menu, J. Debosscher, M. Hrudková, K. De Smedt, R. Lombaert, and P. Németh

Astronomy & Astrophysics, vol. 584, A35, 22 pages (2015)

Abstract

Context. Gamma Doradus and delta Scuti pulsators cover the transition region between low mass and massive main-sequence stars, and as such, are critical for testing stellar models. When they reside in binary systems, we can combine two independent methods to derive critical information, such as precise fundamental parameters to aid asteroseismic modelling. In the *Kepler* light curve of KIC 10080943, clear signatures of gravity- and pressure-mode pulsations have been found. Ground-based spectroscopy revealed this target to be a double-lined binary system.
Aims. We present the analysis of four years of *Kepler* photometry and high-resolution spectroscopy to derive observational constraints with which to evaluate theoretical

predictions of the stellar structure and evolution for intermediate-mass stars.
Methods. We used the method of spectral disentangling to determine atmospheric parameters for both components and derive the orbital elements. With PHOEBE, we modelled the ellipsoidal variation and reflection signal of the binary in the light curve and used classical Fourier techniques to analyse the pulsation modes.
Results. We show that the eccentric binary system KIC 10080943 contains two hybrid pulsators with masses $M_1 = 2.0 \pm 0.1\ M_\odot$ and $M_2 = 1.9 \pm 0.1\ M_\odot$, with radii $R_1 = 2.9 \pm 0.1\ R_\odot$ and $R_2 = 2.1 \pm 0.2\ R_\odot$. We detect rotational splitting in the g and p modes for both stars and use them to determine a first rough estimate of the core-to-surface rotation rates for the two components, which will be improved by future detailed seismic modelling.

3.1 Introduction

The stellar interior was one of the most inaccessible parts of the Universe until the advent of asteroseismology. Nowadays we can use stellar pulsations to inspect the conditions deep beneath the stellar photosphere and to calibrate theoretical stellar models (e.g. Chaplin & Miglio 2013; Aerts 2015). A particularly interesting group of stars for this type of analysis are the γ Doradus (hereafter γ Dor) and δ Scuti (hereafter δ Sct) pulsators. They are found on and slightly above the main sequence, near the classical instability strip of the Hertzsprung-Russell diagram, ranging between 1.5 $M_\odot$ and 2.5 $M_\odot$ in mass (see Fig. 1.5). In this transition region, the outer convective envelope becomes shallower with increasing mass until it is negligible, and energy is mainly transported radiatively, while in the centre, the core becomes increasingly convective.

The γ Dor stars are somewhat cooler and less massive than δ Sct stars, having masses from 1.5 $M_\odot$ to 1.8 $M_\odot$ and spectral type A7-F5 (Kaye et al. 1999, and references therein). Their typical pulsation periods between 0.3 d and 3 d are consistent with non-radial, high-order, low-degree gravity (g) modes, which are driven by the convective flux blocking mechanism at the base of the convective envelope (Guzik et al. 2000; Dupret et al. 2005). The δ Sct stars, on the other hand, have been studied for almost a century and have masses up to 2.5 $M_\odot$. They pulsate in radial as well as non-radial, low-order, low-degree pressure (p) modes at shorter periods between 18 min and 8 hr, which are driven by the κ mechanism (e.g. Breger 2000a). Besides main-sequence stars and more evolved sub-giants, δ Sct pulsations have also been detected in pre-main sequence stars, providing an important tracer for early stellar evolution (Zwintz et al. 2014). Where the γ Dor and δ Sct instability strips overlap, stars are expected to show both types of pulsations (Dupret et al. 2005). These so-called hybrid pulsators are especially useful for asteroseismic studies to test stellar models, since the g-mode cavity is located close to the core and p modes have higher amplitudes in the outer envelope.

For a non-rotating star, it is theoretically predicted that high radial-order (n) g modes of the same degree ℓ and of consecutive radial orders n are equidistantly spaced in period if $n \gg \ell$ (Tassoul 1980). Miglio et al. (2008) demonstrate that these period spacings can depart from their equidistant behaviour as the star evolves from the start to the end of its core hydrogen-burning phase. These departures from regularity carry crucial information on the conditions near the core where g modes have their largest amplitudes. A gradient in chemical composition can cause mode trapping and can lead to an oscillatory behaviour of period spacings, while additional mixing processes, such as diffusion, convective-core overshooting, and rotation can reduce this gradient. Additional mixing mechanisms can significantly influence the time a star spends on the main sequence by supplying the core with additional hydrogen for fusion (Miglio et al. 2008).

Rotation can furthermore introduce rotational splitting, which facilitates identification of the modes' azimuthal order m and can shift g modes to shorter periods, which has been studied extensively by Bouabid et al. (2013). Rotational splitting, as first described by Ledoux (1951), also occurs for p modes. If it is detected in hybrid pulsators in both the g and p modes, additional constraints can be derived on the radial rotation profile in a largely model-independent way. This has recently been achieved by Kurtz et al. (2014) and Saio et al. (2015), who found nearly rigid rotation in two hybrid F-type pulsators, requiring a much more efficient angular momentum transport mechanism than previously assumed. This has also been concluded from surface-to-core rotation rates detected for red giant stars through rotationally split mixed modes (Beck et al. 2012; Mosser et al. 2012; Deheuvels et al. 2014, 2015), which are two orders of magnitudes below the theoretically predicted value (Cantiello et al. 2014; Fuller et al. 2015). For the Sun, on the other hand, it has not yet been possible to measure the rotation of the core, as until now, no g-mode pulsations with rotational splitting have been observed .

These and other recent breakthroughs in asteroseismology have been achieved by exploiting the nearly uninterrupted, high precision photometry of space missions, such as MOST (Walker et al. 2003), CoRoT (Auvergne et al. 2009), and *Kepler* (Borucki et al. 2010). In particular, the detection and analysis of γ Dor stars and hybrid pulsators have benefited from these observations, since they have been studied in extensive samples of A-F type stars observed with *Kepler* (e.g. Grigahcène et al. 2010; Uytterhoeven et al. 2011; Balona 2014; Bradley et al. 2015). In addition, Tkachenko et al. (2013a) selected 69 candidate γ Dor stars, which have been followed up spectroscopically and analysed in more detail by Van Reeth et al. (2015a,b). Facilitated by the high frequency resolution possible from four years of *Kepler* photometry, they found period spacing patterns in 50 stars. Four more g-mode pulsators have been presented by Bedding et al. (2015), who detect period spacings and rotational multiplets from period échelle diagrams. These excellent observational results confirm the theoretical predictions of period dips, which are the result of a chemical gradient, and slopes, which are the result of rotation, by Bouabid et al. (2013).

Despite the immense potential of asteroseismic modelling for stellar astrophysics, a unique solution is hampered by degeneracies among the free parameters (e.g. mass, age, initial metallicity, chemical mixture, and mixing processes; see, e.g. Moravveji et al. 2015). Additional observational constraints to help lift these degeneracies can be provided by binary stars that contain at least one pulsating component. In particular, eclipsing binaries provide the opportunity to derive masses and radii to very high precision (up to 1%), as they rely purely on geometry (Southworth 2012) and, therefore, aid conclusions derived from modelling. Furthermore, eccentric binaries can tidally excite eigenmodes or alter the frequencies or amplitudes of free pulsations (Maceroni et al. 2009; Welsh et al. 2011; Hambleton et al. 2013), which provide additional opportunities for stellar modelling (Fuller & Lai 2012). In addition, Welsh et al. (2011) were able to determine the orbital inclination, and therefore the absolute masses of the non-eclipsing binary KOI-54 by modelling ellipsoidal variation (the deformation of stellar surface models as Roche potentials) and reflection (mutual heating of irradiated stellar surfaces; Wilson 1990). However, despite their obvious benefits, pulsating binaries also present a challenging analysis, in which signals of two different origins must be disentangled. A common approach has been to treat the asteroseismic and binary signals separately to solve the system iteratively, which has been applied, for example, by Maceroni et al. (2013, 2014) and Debosscher et al. (2013).

In this chapter, we analyse the eccentric, non-eclipsing binary star KIC 10080943 (effective temperature $T_{\rm eff} \sim 7400$ K; surface gravity $\log g \sim 4.0$; Huber et al. 2014), observed during all four years of the nominal *Kepler* mission. Tkachenko et al. (2013a) discovered pulsations of γ Dor and δ Sct type, indicating that the system might contain a hybrid pulsator. From ground-based follow-up observations, they further discovered that it is a double-lined spectroscopic binary.

In Sect. 3.2 we describe the acquisition, characteristics, and reduction of the *Kepler* photometry and ground-based spectroscopy, which we use to derive atmospheric parameters in Sect. 3.3. We describe the modelling of the binary light curve (Sect. 3.4), as well as the frequency analysis (Sect. 3.5), before discussing our findings in Sect. 3.6 and ending with a brief summary.

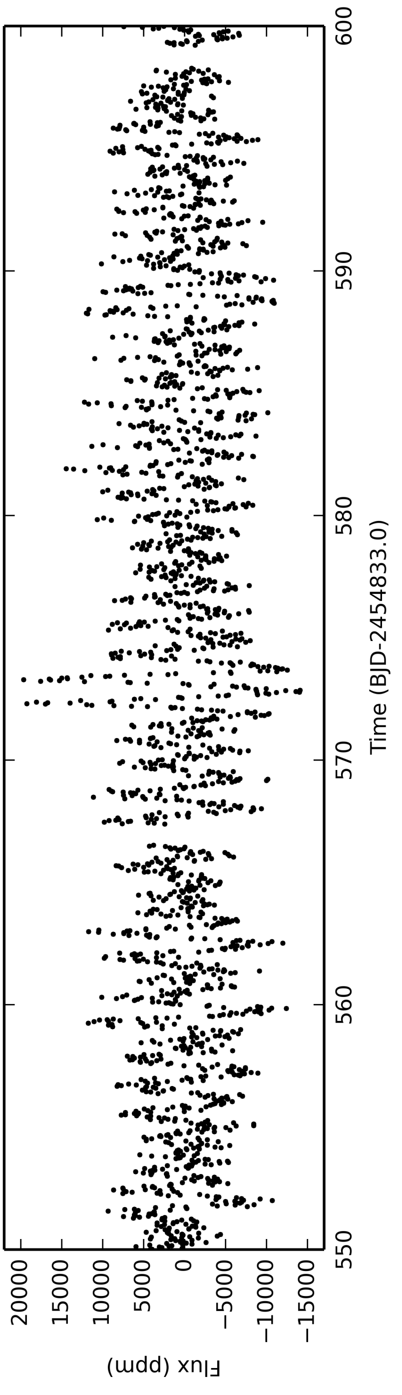

Figure 3.1: Zoom of 50 days of the *Kepler* light curve of KIC 10080943.

3.2 Observations

3.2.1 *Kepler* photometry

The *Kepler* satellite was launched on 6 March 2009 and ended its nominal mission on 11 May 2013, after a second reaction wheel failed and pointing it to its chosen field could no longer be kept stable. During the course of its operation, *Kepler* collected data in eighteen quarters, employing a sampling rate of 29.4244 min in long cadence (LC) mode. For KIC10080943, there are LC observations available from Q0 to Q17, amounting to a time span of 1470.5 days, which contain 65 959 data points after deleting 22 outliers. We extracted the light curve from the public pixel data files using a custom aperture mask, which contained more pixels than the original mask to minimise long term trends (Tkachenko et al. 2013a). After each quarter, the satellite rolled to adjust the position of the solar panels. This caused short gaps in the light curve and made the stars fall on different CCD modules, which deviate in sensitivity and lead to varying observed flux. By fitting a second order polynomial to the light curve in each quarter, we rectify any spurious trends to safely concatenate the data (for more details see Debosscher et al. 2013). A close-up of the final light curve is shown in Fig. 3.1, where time is given as Barycentric *Kepler* Julian Date (BKJD), which is Barycentric Julian Date (BJD), using a zero point of 2454833.0.

3.2.2 HERMES spectroscopy

In addition to the photometric observations, we monitored the star with the HERMES spectrograph (Raskin et al. 2011), mounted on the 1.2-m Mercator telescope in La Palma, Spain. We obtained 26 spectra between August 2011 and October 2014. The raw spectra were reduced using the HERMES pipeline. Since the target is faint for a high-resolution spectrograph on a 1.2-m telescope (*Kepler* magnitude $Kp = 11.8$ mag), most spectra that were obtained have a signal-to-noise ratio (S/N) below 30. We prepared the spectra for normalisation by removing the spectrograph's response function and then dividing this by a synthetic composite spectrum of two identical stars, given the component's similarity and their mass ratio close to unity ($T_{\rm eff,1,2} = 7000$ K, $\log g_{1,2} = 4.0$, metallicity $Z_{1,2} = 0$, projected rotational velocity of the primary $v \sin i_1 = 13\,{\rm km\,s^{-1}}$, and of the secondary $v \sin i_2 = 10\,{\rm km\,s^{-1}}$). Subsequently, we fitted the result with a third-order polynomial, avoiding regions of hydrogen and telluric lines, and used it to normalise the spectra. Given that double-lined F-type binary spectra contain a large number of lines and the observations have a low S/N, we found this method to be the most reliable. Our tests showed that fitting a second-order spline to continuum points resulted in a wavy continuum, varying between spectra.

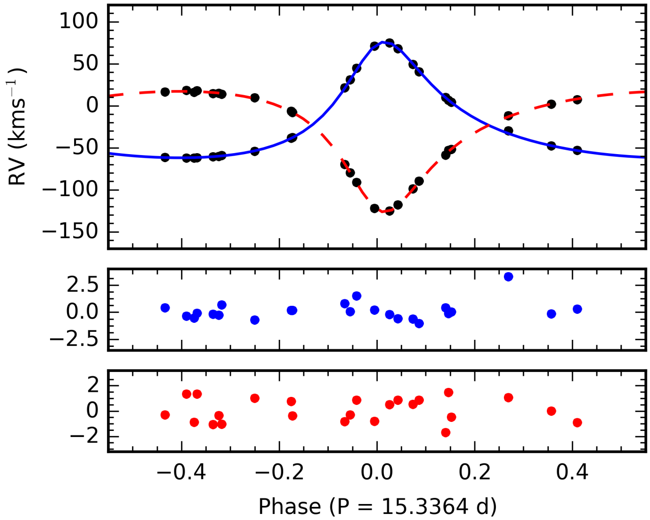

Figure 3.2: *Top panel:* Radial velocities (black dots) of both components with the best fitting model for the primary (solid blue line) and the secondary (dashed red line). The residuals after subtracting the best fit are displayed for the primary in the *middle panel* and the secondary in the *bottom panel.* The error bars on each RV measurement are typically smaller than the symbol size.

We used the normalised spectra to perform spectral disentangling and to obtain fundamental parameters for both components (see Sect. 3.3). In addition, we extracted the radial velocities (RVs) of both components from the spectra's échelle orders prior to normalisation by cross-correlating with a mask of an F0 star and fitting a double Gaussian to the resulting function.

3.3 Spectral disentangling, binary orbit and atmospheric parameters

We used the Fourier method of spectral disentangling (Hadrava 1995), as implemented in the FDBinary code (Ilijic et al. 2004), to extract the spectral contributions of both binary components from the observed composite spectra of the system. The method (originally introduced by Simon & Sturm 1994) allows for simultaneous separation of the spectra of the two binary components and optimisation of the system's orbital elements. Before determining the orbit, we used the RVs to derive the orbital period, which was then fixed in FDBinary to simplify the optimisation problem. The following five spectral regions were used to calculate the orbital parameters: 4530 – 4590 Å, 4600 – 4650 Å, 5164 – 5174 Å, 5250 – 5295 Å, and 5350 – 5380 Å. Table 3.1 lists the mean and standard deviation of the parameters: time of periastron passage t_0, eccentricity e, longitude of periastron ω, and the RV semi-amplitudes K_1 and K_2. The mass ratio $q = M_2/M_1 = K_1/K_2$, the systemic velocity γ, and the semi-major axis as a function of orbital inclination $i_{\rm orb}$, $a \sin i_{\rm orb}$, are also listed. All values are in agreement with those derived from fitting the RVs. The orbital fit to the RVs is shown in Fig. 3.2.

In the next step, we fixed the orbital elements to the mean values and performed spectral disentangling in the range between 4200 Å and 5650 Å. The violet part of the spectrum was ignored because of large uncertainties in the continuum normalisation, while the red part was skipped because of large telluric contamination and an increasing level of noise. The quality of the continuum normalisation of the original data suffered significantly from the low S/N of the data. This naturally propagated into the quality of the disentangled spectra, particularly in the regions of the Balmer lines. We found that the normalisation of the H_β profile was not accurate enough to provide reliable Fourier spectral disentangling in the corresponding wavelength region. Our attempt to perform disentangling in the wavelength domain, using the original method of Simon & Sturm (1994), also failed. The disentangling went reasonably well for the entire red part of the H_γ profile, whereas its blue wing suffered significantly from the zero-frequency component in the Fourier domain. The blue wing was corrected by fitting a low-degree polynomial, to restore the symmetry of the entire profile with respect to its red wing. The reliability of such an approach was later tested by means of the spectrum analysis based on the entire wavelength range and the one excluding the H_γ profile. The metal line spectrum was disentangled in small segments (~30 – 50 Å each), where low-amplitude continuum undulations were corrected by fitting a low-degree polynomial to each of the wavelength regions. The final disentangled spectra were obtained by merging all segments.

We used the GSSP_BINARY software package (Tkachenko 2015) to fit the disentangled spectra. The spectrum analysis relies on a grid search in the fundamental parameters: $T_{\rm eff}$, $\log g$, micro-turbulence ξ, metallicity [M/H], projected rotational velocities $v \sin i_{1,2}$, and the ratio of the radii R_1/R_2; the 1-σ uncertainties are calculated from χ^2 statistics, taking into account all possible correlations between parameters (Lehmann et al. 2011). Due to the low S/N of the data, micro-turbulence is hard to constrain and we derived another solution with micro-turbulence fixed at 2.0 km s^{-1}. The code allows for constrained fitting of the two spectra simultaneously and takes into account the wavelength dependence of the light ratio of the two stars, by replacing it with the ratio of their radii. We found that the final solution was very sensitive to whether the H_γ spectral line was included in the fit, particularly influencing $T_{\rm eff}$ and $\log g$ of the primary component. Given the level of uncertainty in the disentangling of this line and the corrections applied to its blue wing afterwards, we decided to exclude it from the final fit and focused on the metal line spectrum for each of the components. This

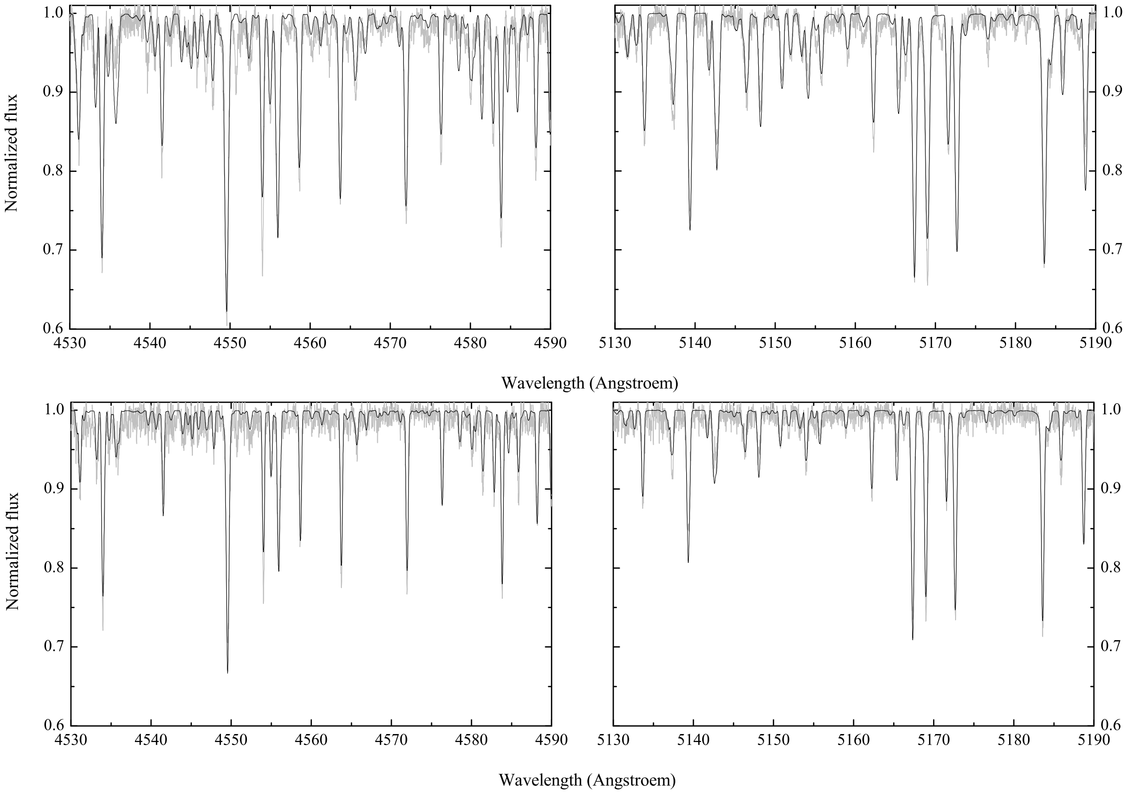

Figure 3.3: Fit to the disentangled spectra of both components of the KIC 10080943 system (*top panels* – primary, *bottom panels* – secondary) with the GSSP_BINARY software package. The observations are shown as the light grey line and the best fit synthetic spectra are illustrated with the black line.

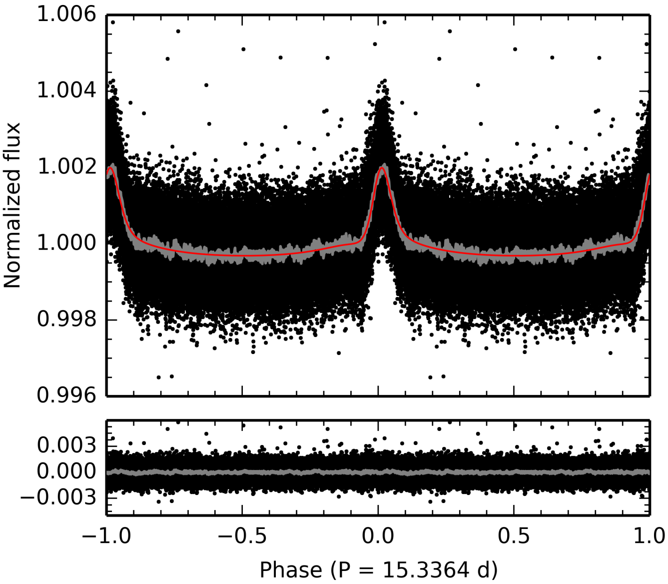

Figure 3.4: Phased binary signal in the observed light curve with oscillations removed (black), and the best fitting model (red) with the residuals shown below. The 1-σ area of the phase-binned light curve is shown in grey.

approach is justified by the large number of metal lines present in the spectra of both stars, which contain sufficient information for $T_{\rm eff}$ and $\log g$ to be constrained from the excitation and ionisation balance, respectively. The finally adopted fundamental parameters are listed in Table 3.1. The quality of the fit for both stars in two different wavelength regions is illustrated in Fig 3.3. The more-massive primary component is found to have a $v \sin i$ about 1.35 times greater than the secondary, which is in turn slightly hotter and less evolved with a smaller radius. We find that the components' metallicities are consistent with each other and may be slightly sub-solar (the solar composition was adopted from Grevesse et al. 2007).

3.4 Binary light curve modelling

The binary signal also appears in the *Kepler* light curve. The orbit is seen in the Fourier transform as the first ten harmonics of the orbital frequency, $f_{\rm orb}$ = 0.0652 d^{-1}, with amplitudes well below most pulsation modes (Fig. 3.9; panel a). Ellipsoidal variation and reflection are non-sinusoidal signals at high eccentricity and cause harmonic peaks

Table 3.1: Parameters of the binary orbit and the component stars of KIC 10080943.

	Primary	**Secondary**
P_{orb} (d)	15.3364 ± 0.0003	
f_{orb} (d^{-1})	0.06520 ± 0.00004	
FDBinary		
t_0 (JD)	$2\,455\,782.23 \pm 0.02$	
e	0.449 ± 0.005	
ω (deg)	344.7 ± 0.7	
$a \sin i_{\mathrm{orb}}$ ($R_\odot$)	37.8 ± 0.3	
q	0.96 ± 0.01	
K ($\mathrm{km\,s^{-1}}$)	68.2 ± 0.7	71.3 ± 0.7
γ ($\mathrm{km\,s^{-1}}$)	-22.8 ± 0.2	
Phoebe		
i_{orb} (deg)	68 ± 3	
$\Delta\phi$	0.2928 ± 0.0001	
e	0.4535 ± 0.0004	
ω (deg)	345.309 ± 0.001	
a ($R_\odot$)	41.1 ± 0.8	
q	$0.9598^{+0.0007}_{-0.0008}$	
γ ($\mathrm{km\,s^{-1}}$)	-22.99 ± 0.02	
T_{eff} (K)	7100 ± 200	7480^{+180}_{-200}
Ω	15.2 ± 0.2	$23.6^{+0.9}_{-1.0}$
α	0.8 ± 0.1	0.95 ± 0.05
β	$0.04^{+0.06}_{-0.03}$	$0.27^{+0.34}_{-0.21}$
M ($M_\odot$)	2.0 ± 0.1	1.9 ± 0.1
R ($R_\odot$)	2.9 ± 0.1	2.1 ± 0.2
$\log g$ (cgs)	3.81 ± 0.03	4.1 ± 0.1
R_1/R_2	1.4 ± 0.1	
GSSP (excluding H_γ)		
T_{eff} (K)	7150 ± 250	7640 ± 240
$\log g$ (cgs)	4.07 ± 0.46	4.13 ± 0.46
ξ ($\mathrm{km\,s^{-1}}$)	3.85 ± 0.90	2.35 ± 0.85
[M/H]	-0.06 ± 0.18	-0.23 ± 0.20
$v \sin i_{\mathrm{rot}}$ ($\mathrm{km\,s^{-1}}$)	19.0 ± 1.3	14.4 ± 1.4
R_1/R_2	1.16 ± 0.19	
Micro-turbulence fixed at 2.0 km s^{-1}		
T_{eff} (K)	7100 ± 220	7450 ± 400
$\log g$ (cgs)	3.7 ± 0.4	4.15 ± 0.85
[M/H]	-0.05 ± 0.17	-0.09 ± 0.30
$v \sin i_{\mathrm{rot}}$ ($\mathrm{km\,s^{-1}}$)	18.7 ± 1.2	13.8 ± 1.6
R_1/R_2	1.41 ± 0.20	

at integer multiples of the orbital frequency. Subtracting the g- and p-mode pulsations using classical iterative prewhitening (see Sect. 3.5) from the original light curve reveals a periodic brightening occurring at orbital phase zero, which we associate with ellipsoidal variation and reflection (Fig. 3.4). To complete the iterative approach of studying pulsating binary light curves, we modelled this signal and subsequently subtracted it from the original light curve, to extract the pure pulsation signal. This procedure was only repeated once, as the difference in subsequent frequency and binary fits was negligible.

3.4.1 MCMC setup

Since KIC 10080943 does not show eclipses, the modelling is not well constrained and degeneracies occur among parameters, such as effective temperatures and stellar surface potentials, Ω, which define the stars' shapes in Roche geometry and can be used to derive the stellar radii. The shape of the ellipsoidal variation signal is, in principle, a function of the temperature ratio, stellar radii, eccentricity, and inclination. At higher orbital inclination, we expect to see a double-humped feature, while for low values of inclination, only one hump appears. Before modelling, we concluded that $i_{\rm orb}$ probably lies between 60° and 82.5°, since a lower value would yield masses that are too high, given an early-F spectral type, and a higher value would result in eclipses. The fact that we only see one peak in the light curve means that reflection is the dominating effect, which constrains the sizes of the stars and their temperatures. Furthermore, this brightening signal has a small amplitude and, thus, a low S/N. Small variations in the light curve are therefore hidden in the noise and interfere with remaining unresolved pulsation frequencies. In this case, the parameter hyper-surface has many dips and troughs, and minimisation algorithms might get stuck in local minima.

We perform a Markov Chain Monte Carlo (MCMC) simulation (implemented in `emcee` by Foreman-Mackey et al. 2013), which allows several chains of models to explore the parameter space and build up a posterior probability density function of the parameter space Θ, given the data set D. If we assume that our parameters follow a Gaussian distribution, we can write the posterior probability as

$$P(\Theta|D) = P(\Theta)e^{-\chi^2/2}, \tag{3.1}$$

where χ^2 is a simple goodness-of-fit measurement. The χ^2 values were calculated at each step of each chain using binary models computed with PHOEBE (Prša & Zwitter 2005), which is based on the Wilson-Devinney code (Wilson & Devinney 1971; Wilson 1979). In this way, an MCMC simulation also improves the model fit to the data by maximising the posterior. Gaussian priors of the effective temperatures and the orbital parameters (e, ω, q, and γ), which are based on the spectral analysis and spectral disentangling, respectively, were used to write the posterior probability as

$$\ln P(\Theta|D) = -0.5 * \left(\chi^2_{LC} + \chi^2_{RV1} + \chi^2_{RV2} + \left(\frac{T_1 - 7150\,\mathrm{K}}{250\,\mathrm{K}}\right)^2 + \left(\frac{T_2 - 7640\,\mathrm{K}}{240\,\mathrm{K}}\right)^2 + \left(\frac{e - 0.449}{0.005}\right)^2 + \left(\frac{\omega - 344.7^\circ}{0.7^\circ}\right)^2 + \left(\frac{q - 0.96}{0.01}\right)^2 + \left(\frac{\gamma + 22.8\,\mathrm{km\,s^{-1}}}{0.2\,\mathrm{km\,s^{-1}}}\right)^2 \right), \tag{3.2}$$

where χ^2_{LC}, χ^2_{RV1}, and χ^2_{RV2} are the respective goodness-of-fit measurements of the light curve, and the primary and secondary RVs, while T_1, T_2, e, ω, q, and γ are the currently inspected values of the model's primary and secondary effective temperature, eccentricity, longitude of periastron, mass ratio, and systemic velocity, respectively.

At each step the algorithm draws the chains' positions in the parameter space from a uniform, non-informative prior distribution, where we chose 3-σ ranges as limits for the parameters that can be constrained from spectroscopy. The limits for the other parameters were chosen by optimising the fit by eye before starting the MCMC computations. Furthermore, we had to introduce a phase shift $\Delta\phi$, to define the zero point in time (t_0) as time of periastron passage, since PHOEBE was designed to model eclipsing binary stars. In a first step, we assumed synchronous rotation for both components and set the synchronicity parameter $F = \omega_{\mathrm{rot}}/\omega_{\mathrm{orb}} = 1$. Subsequently, we introduced a 2:1 resonance with the orbital period for the primary's rotation period ($F_1 = 2$), based on our asteroseismic analysis (Sect. 3.5), while F_2 was allowed to vary. All adjusted parameters and their limits are listed in Table 3.2. Before calculating the χ^2 values, the *Kepler* passband luminosity levels and the bolometric limb-darkening coefficients were computed for the current positions of the chains. The passband limb-darkening coefficients were fixed to values taken from Claret & Bloemen (2011) for models close to our spectroscopic solution.

One drawback of current binary modelling techniques is that they are computationally intensive and are thus unable to deal with datasets as large as produced by the nominal *Kepler* mission. Therefore, we phase-binned the light curve into 658 bins, reducing the number of data points by a factor of 100. This means fixing the orbital period and time of periastron passage.

The algorithm converged after 2000 iterations of 64 chains and was then reiterated 128 000 times to explore the parameter space and determine the uncertainties of each parameter. Figure 3.5 shows the posterior distributions of the following parameters: inclination i_{orb}, effective temperature $T_{\mathrm{eff},1,2}$, and surface potential $\Omega_{1,2}$ of the primary

Table 3.2: Adjusted parameters and non-informative priors for the MCMC simulation.

	Orbital parameters	
i_{orb} (deg)	60.0 – 82.5	
$\Delta\phi$	0.29252 – 0.29285	
e	0.434 – 0.464	
ω (deg)	342.6 – 346.8	
a ($R_\odot$)	37.2 – 44.7	
q	0.93 – 0.99	
γ (km s^{-1})	–23.4 – –22.2	
	Primary	Secondary
T_{eff} (K)	6400 – 7900	6920 – 8360
Ω	13.9 – 19.5	15 – 27
F	2 (fixed)	1.77 – 1.95
α	0.4 – 1.0	
β	0.0 – 1.0	

and secondary component[1]. It can be seen that the orbital inclination is not distributed normally, hence the reported uncertainties should be interpreted as a range of possible values. Furthermore, we find no obvious correlations with other parameters. All orbital parameters defined by the RVs are well within the error bars determined from spectral disentangling, while F_2 could not be constrained. The result is summarised in Table 3.1 and the best model fit to the binary light curve is shown in Fig. 3.4, and to the radial velocity curves in Fig. 3.2.

3.4.2 Bolometric albedos and gravity darkening

Other parameters that influence the shape of the light curve are the bolometric albedo α and the gravity darkening exponent β. The former is linked to reflection and determines the flux fraction that is used to heat the irradiated star, while the latter determines the difference in flux that results from varying surface gravity across the distorted stellar surfaces. The values of these parameters depend on the main energy transport mechanism in the stellar envelope. For predominantly convective envelopes, the theoretically predicted values are $\alpha = 0.5$ (Rucinski 1989) and $\beta = 0.32$ (Lucy 1967; Claret 2003), while for radiative envelopes, the commonly used values are $\alpha = \beta = 1$ (Rucinski 1989; Claret 2003). Both components of KIC 10080943 lie within in a range of mass and temperature for which convective envelopes are expected, but these are

---

[1] This figure was created using `triangle.py v0.1.1` (Foreman-Mackey et al. 2014, http://dx.doi.org/10.5281/zenodo.11020).

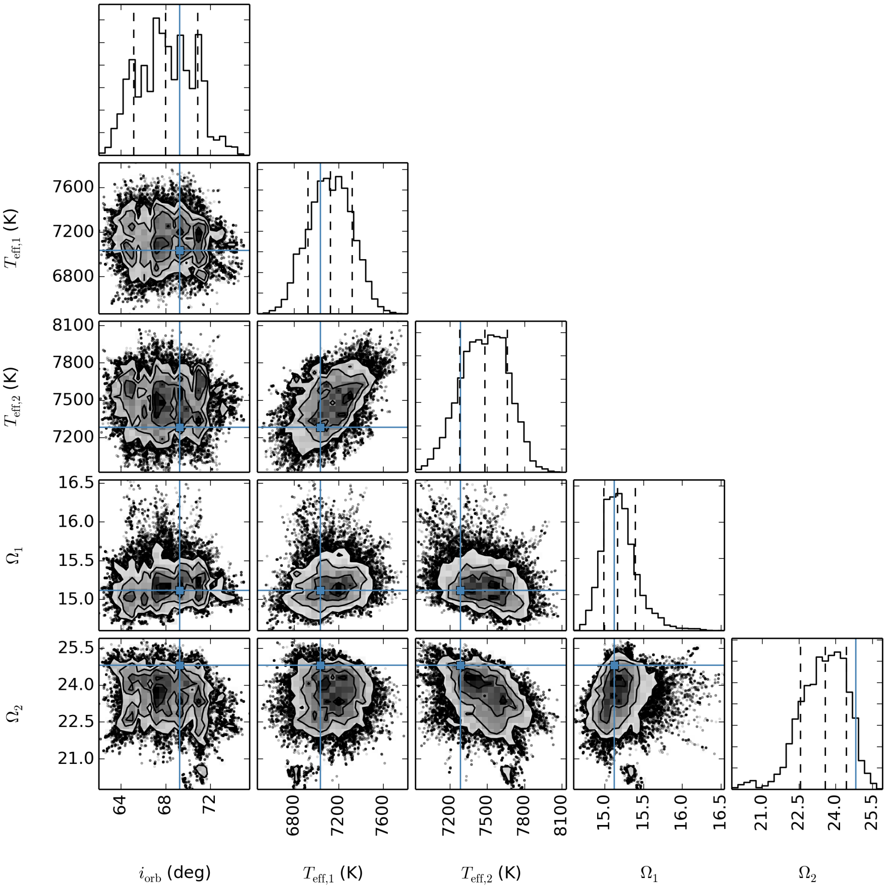

Figure 3.5: Results of fitting the binary light curve, showing the one- and two-dimensional projections of the posterior probability functions of the parameters inclination i, primary and secondary effective temperature $T_{\mathrm{eff},1,2}$, and primary and secondary surface potential $\Omega_{1,2}$. The blue squares are the values of the model with the lowest χ^2. In the 1-d distributions, the 16th, 50th, and 84th percentile are marked by the vertical dashed lines.

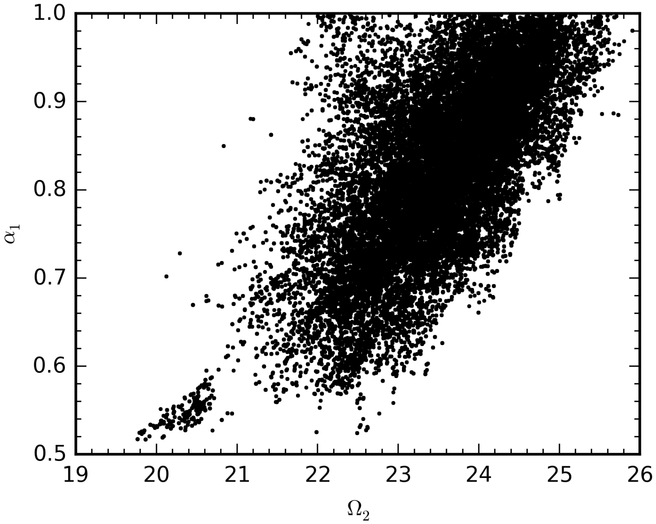

Figure 3.6: Correlation between the secondary surface potential Ω_2 and the primary bolometric albedo α_1.

thin and the radiative zone extends almost to the photosphere. We therefore decided not to fix $\alpha_{1,2}$ and $\beta_{1,2}$ for the modelling (Table 3.2).

We found a weak positive correlation for α and T_{eff} for the primary and the secondary and $\alpha_1 = 0.8 \pm 0.1$, $\alpha_2 = 0.95 \pm 0.05$. Between Ω_2 and α_2, as well as α_1, there is a stronger correlation (Fig. 3.6), which means that for a smaller secondary radius, a higher albedo is required to fit the observed height of the peak associated with reflection.

The gravity-darkening exponents, on the other hand, tend to lower values. In particular for the primary $\beta_1 = 0.035^{+0.06}_{-0.026}$, while showing a strong correlation with Ω_1 (Fig. 3.7). A similar degeneracy between surface potential and gravity darkening has been reported before by Beck et al. (2014).

From these degeneracies, we derive the expected surface potentials for the theoretical albedos and gravity-darkening exponents for convective envelopes. Since any kind of degeneracies represent an uncertainty, we report the surface potentials and radii in Table 3.1 for the full range of possible values, including the MCMC solution. The corresponding ratio R_1/R_2 is then in excellent agreement with the spectroscopic value with fixed micro-turbulence.

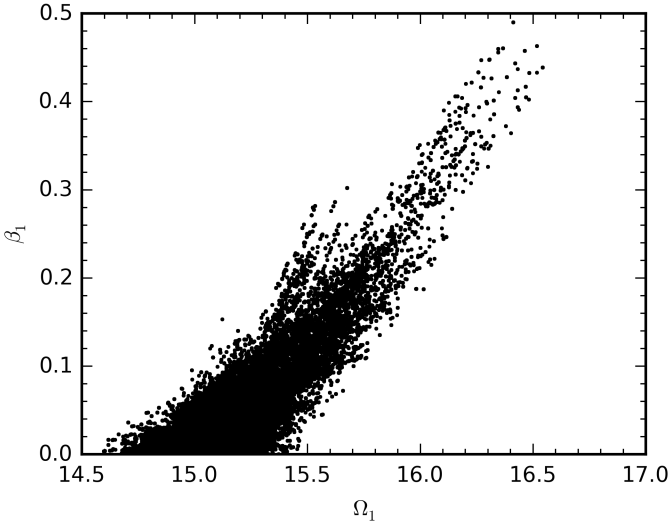

Figure 3.7: Correlation between surface potential Ω_1 and gravity darkening exponent β_1 of the primary.

3.5 Pulsation frequency analysis

In the *Kepler* light curve, the periodic flux variations caused by stellar pulsations are far more prominent than the binary signal. We extracted this oscillatory behaviour with a Fourier transform (for a detailed description of the method, we refer to Degroote et al. 2009). There are two variability regions clearly distinguishable in the periodogram, displayed in Fig. 3.8. Zooms onto the different regions are shown in Fig. 3.9. Below a frequency of 5 d^{-1}, we find pulsation modes of γ Dor type, while in the high frequency range, above 8 d^{-1}, we find typical δ Sct pulsation modes. Both regions are highly structured.

As a stop criterion for the iterative prewhitening, we chose a p value below 0.001, meaning there is a 0.1 % chance that a frequency peak is due to noise. Of all detected peaks, we only considered those with $S/N \geq 4$ (Breger et al. 1993), where the noise level was calculated as the mean amplitude of the residual periodogram in a 1 d^{-1} frequency range around each peak. Since the noise level is not uniform across the frequency spectrum, and is higher in the low-frequency regime and in regions where many peaks cluster, an ordinary prewhitening does not reach the high-frequency peaks with low amplitudes ($A < 20$ ppm). Hence we applied a Gaussian filter with $\sigma = 0.02$ d to the light curve and subtracted the result from the original light curve to treat the high-frequency regime. This method lowers the signal below 9 d^{-1} considerably; the

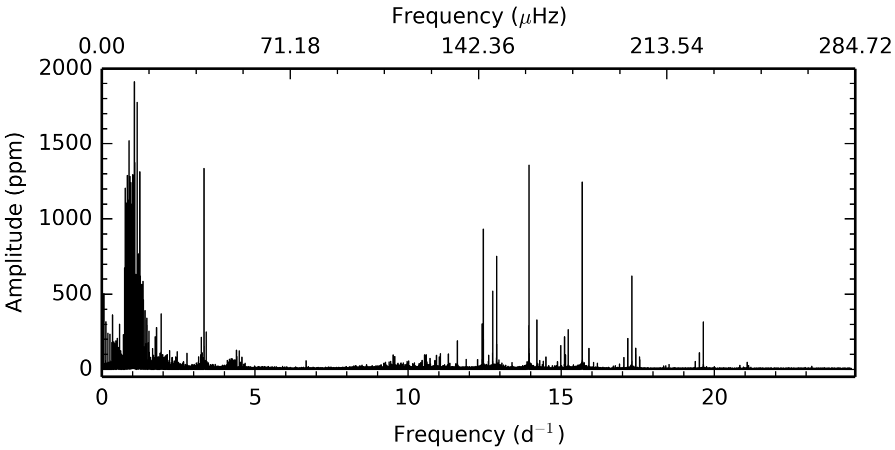

Figure 3.8: Periodogram of the original light curve of four years of *Kepler* data.

highest peak in this region has $A < 110$ ppm. When merging the two sets of the two frequency searches, we therefore selected all peaks ≤ 9 d^{-1} from the original light curve and all peaks > 9 d^{-1} from the filtered light curve. We then fitted a harmonic model with these frequencies to the original light curve.

The width of one frequency peak is connected with the *Rayleigh limit* $1/T = 0.00068$ d^{-1}, with $T = 1470.4624$ d being the length of the data set. Loumos & Deeming (1978) found that two peaks with a separation smaller than $2.5/T$ influence each other during the prewhitening process. There are several low-amplitude, yet significant frequencies that are found in the vicinity of high-amplitude peaks with a separation smaller than the Rayleigh limit, which we excluded from the final frequency list. Figure 3.10 shows the periodogram of the residual light curve, after subtracting the binary model calculated in Sect. 3.4 and 522 significant frequencies.

We calculated the errors on the frequency, amplitude, and phase, following the description of Montgomery & O'Donoghue (1999). These errors rely on the assumption of white noise in the data and therefore underestimate the real error, in this current study by a factor ~ 2 owing to correlation effects (Schwarzenberg-Czerny 2003). We applied this correction factor to the errors, following Degroote et al. (2009). All parameters, their correlation-corrected uncertainties, and S/N values are listed in Table 3.9.

As already mentioned in Sect. 3.4, we also detect the binary ellipsoidal variation and reflection signal as orbital harmonics in the periodogram (see Fig. 3.9, panel a). To disentangle both signals, we have to perform an iterative analysis. After subtracting the binary model, we only found minimal changes in the determined pulsation frequencies, in comparison with the solution derived from the original light curve with the orbital

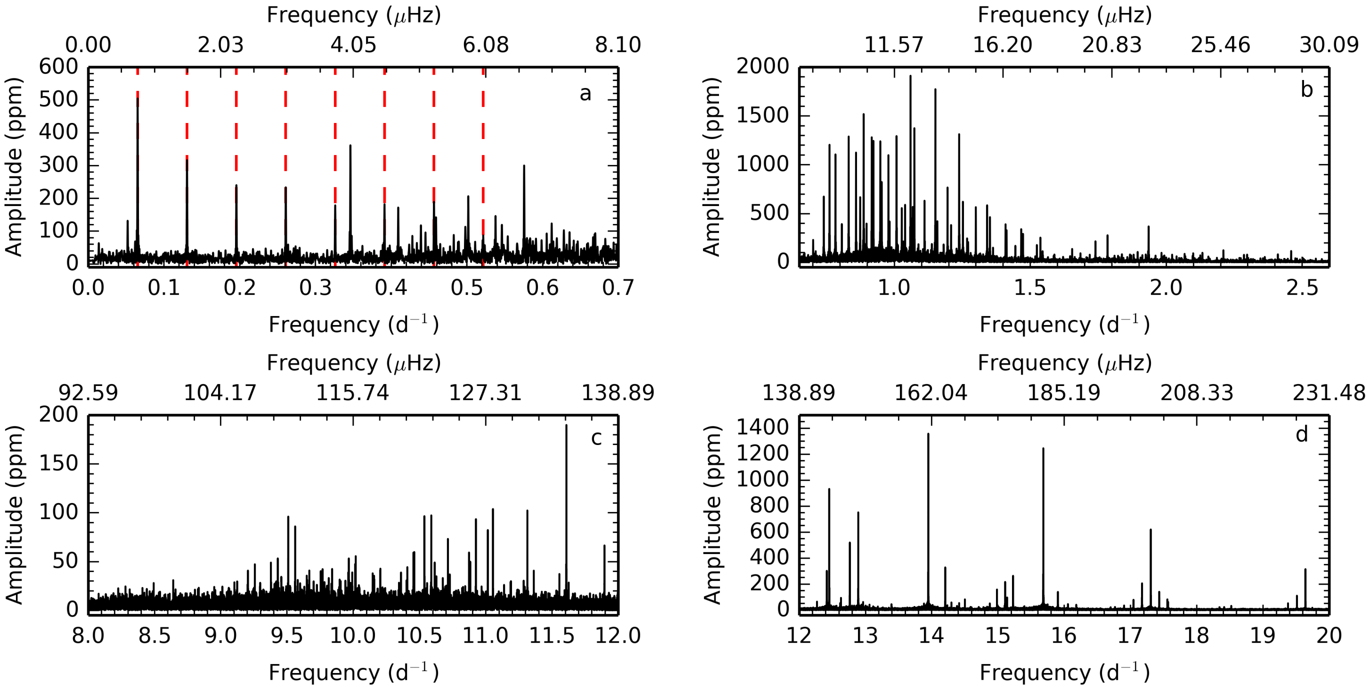

Figure 3.9: *Panel a:* Zoom into the long period range, where the orbital harmonics are indicated by the vertical dashed lines. *Panel b:* Zoom into the g-mode pulsations. *Panel c:* Zoom into the low-amplitude p modes and into the high-amplitude p modes (*panel d*).

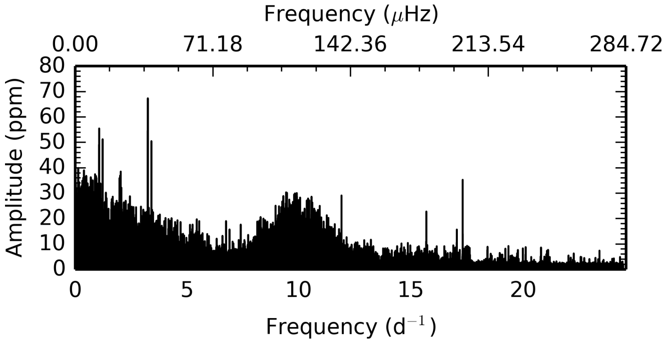

Figure 3.10: Periodogram of the residual light curve after subtracting the binary model and 522 significant frequencies (see text).

harmonics prewhitened in Fourier space rather than the binary light curve in the time domain. The frequency 2.2940 d^{-1} with $S/N = 4.01$ is not detected anymore when working with the residual light curve after orbital subtraction. Six additional frequencies were detected: f_{255}, f_{256}, f_{265}, f_{268}, f_{276}, and f_{512}.

3.5.1 Tidally influenced pulsations

Another source for frequencies at multiples of the binary orbit are tidally induced or influenced pulsations. Examples of pulsating stars in eccentric binaries exhibiting tidally excited modes are given by Welsh et al. (2011) and Hambleton et al. (2013), where almost all g modes could be attributed to this driving mechanism. In the case of KIC 10080943, we only see weak tidal influence on the pulsations. Altogether we found four frequencies that are in the vicinity of integer multiples of the orbital frequency, listed in Table 3.3, where the relative frequency $f_r = f_{obs} - nf_{orb} > 1/T$.

The frequency $f_{128} = 0.45663 \approx 7f_{orb}$ coincides with the orbital harmonics caused by the non-sinusoidal binary signal. Consequently, it was prewhitened together with the orbital harmonics to study the pulsations alone in the first iteration of the binary-pulsation analysis. By cutting the brightening from the pulsation-residual light curve and fitting a polynomial to the phases outside the brightening, we manually separated the two signals. All non-sinusoidal signals at the orbital period are removed, while oscillations at orbital harmonics remain, creating a peak in the frequency spectrum. When a binary model was subtracted in subsequent iterations, as opposed to orbital harmonics, this confusion no longer arose.

Table 3.3: Frequencies and amplitudes close to multiples of the orbital frequency are given, as well as the frequency ratio f/f_{orb}.

	f d^{-1}	A ppm	f/f_{orb}
f_{16}	0.978056	1131.2	15.00084
f_{128}	0.45663	75.2	7.00353
f_{147}	1.56487	71.9	24.00107
f_{388}	2.6734	28.9	41.00307

3.5.2 The g modes

In the g mode regime (Fig. 3.9, panel b), we find six period spacing series, located in the frequency range with the highest mode amplitudes (0.7 d^{-1} $\leq f \leq$ 1.7 d^{-1} and 0.6 d $\leq p \leq$ 1.4 d). The frequencies of those series are listed in Table 3.4 and displayed in Fig. 3.11. Miglio et al. (2008) predict a mean spacing value for dipole ($\ell = 1$) modes of a 1.6 $M_{\odot}$ star to be slightly higher than 3000 s. The values we detect are in good agreement with this mass range, typical for γ Dor stars.

Table 3.4: Degree ℓ, azimuthal order m, frequencies (f), amplitudes (A), and periods (p) of the six period spacing series in the high amplitude g mode region. The 1-σ uncertainties on p and Δp are denoted by ϵp and $\epsilon\Delta p$, respectively. We use the convention that $m > 0$ represents prograde and $m < 0$ retrograde modes.

ℓ	m	f d^{-1}	A ppm	p d	ϵp d	Δp s	$\epsilon\Delta p$ s
1	−1	1.059380	1977.9	0.943948	0.000008		
1	−1	0.982312	459.6	1.018006	0.000012	6398.6	1.2
1	−1	0.948204	1340.8	1.054625	0.000009	3163.9	1.3
1	−1	0.916666	1279.3	1.090910	0.000012	3135.0	1.3
1	−1	0.886920	1531.3	1.127497	0.000013	3161.1	1.5
1	−1	0.858848	1144.9	1.164350	0.000011	3184.1	1.5
1	−1	0.831820	1280.5	1.202183	0.000014	3268.8	1.5
1	−1	0.806569	402.2	1.239820	0.000019	3251.8	2.0
1	−1	0.783175	1052.3	1.276853	0.000013	3199.7	2.0
1	−1	0.761386	1200.0	1.313394	0.000014	3157.1	1.6
1	−1	0.740340	661.8	1.350731	0.000019	3225.9	2.0
1	1	1.341113	606.0	0.745650	0.000006		
1	1	1.238142	1324.1	0.807662	0.000007	5357.8	0.8
1	1	1.195443	744.2	0.836510	0.000007	2492.5	0.9
1	1	1.150808	1772.7	0.868955	0.000007	2803.2	0.9

Table 3.4: continued.

ℓ	m	f	A	p	ϵp	Δp	$\epsilon\Delta p$
		d^{-1}	ppm	d	d	s	s
1	1	1.073577	1358.9	0.931466	0.000010	5400.9	1.0
1	1	1.039427	661.0	0.962068	0.000009	2644.1	1.2
1	1	1.007861	1261.2	0.992200	0.000009	2603.4	1.1
1	1	0.978056	1131.2	1.022437	0.000008	2612.4	1.1
1	1	0.949885	882.5	1.052759	0.000010	2619.8	1.1
1	1	0.922897	1314.2	1.083545	0.000009	2659.9	1.2
1	1	0.897600	380.9	1.114083	0.000016	2638.5	1.6
1	1	0.874150	695.3	1.143968	0.000013	2582.1	1.8
1	1	0.852334	65.9	1.173249	0.000085	2529.9	7.4
1	−1	1.267385	191.6	0.789026	0.000014		
1	−1	1.210145	138.4	0.826347	0.000021	3224.6	2.1
1	−1	1.158164	433.8	0.863436	0.000009	3204.4	1.9
1	−1	1.110739	646.9	0.900301	0.000008	3185.2	1.0
1	−1	1.067345	602.5	0.936905	0.000009	3162.5	1.0
1	−1	1.027043	465.3	0.973669	0.000011	3176.4	1.2
1	−1	0.989183	160.8	1.010936	0.000027	3219.9	2.5
1	−1	0.953435	836.7	1.048840	0.000010	3274.9	2.5
1	−1	0.920187	254.7	1.086736	0.000021	3274.2	2.0
1	0	1.280641	75.7	0.780859	0.000033		
1	0	1.228631	139.8	0.813914	0.000020	2855.9	3.3
1	0	1.181151	182.2	0.846632	0.000017	2826.9	2.2
1	0	1.137729	130.7	0.878944	0.000025	2791.7	2.6
1	0	1.097340	71.8	0.911294	0.000047	2795.1	4.6
1	1	1.545015	140.0	0.647243	0.000013		
1	1	1.473044	282.0	0.678866	0.000007	2732.3	1.3
1	1	1.408823	365.4	0.709812	0.000007	2673.7	0.9
1	1	1.351542	466.8	0.739896	0.000007	2599.2	0.8
1	1	1.299530	570.4	0.769509	0.000006	2558.6	0.8
1	1	1.251994	598.2	0.798726	0.000006	2524.3	0.7
1	1	1.208481	435.2	0.827485	0.000008	2484.8	0.9
2		1.653748	156.4	0.604687	0.000010		
2		1.585806	49.7	0.630594	0.000032	2238.4	2.9
2		1.524030	192.0	0.656155	0.000010	2208.4	2.9
2		1.466409	343.6	0.681938	0.000006	2227.7	1.0
2		1.412779	339.2	0.707825	0.000007	2236.6	0.8

Table 3.4: continued.

ℓ	m	f d^{-1}	A ppm	p d	ϵp d	Δp s	$\epsilon\Delta p$ s
2		1.362748	161.1	0.733811	0.000014	2245.2	1.4
2		1.315677	46.9	0.760065	0.000049	2268.3	4.4
2		1.271250	234.8	0.786627	0.000011	2295.0	4.4

Some of the period spacing series are slightly tilted in the Δp vs. p diagram, which could be due to rotation. Bouabid et al. (2013) found that under the influence of rotation, the periods are not equally spaced anymore, but rather that spacing increases with period for retrograde modes, resulting in an upward slope, while the opposite is true for prograde and zonal modes. This slope is steeper with higher rotation. These theoretical predictions were confirmed observationally for numerous g-mode pulsators by Van Reeth et al. (2015b).

To detect rotational splitting among the frequencies, we created a histogram of all differences in frequency. Two values stick out in this histogram: $\Delta f_{g_1} \approx 0.091$ d^{-1} and $\Delta f_{g_2} \approx 0.07$ d^{-1}. This is indicative of rotational splitting. We find that two series are split in frequency by the former value (Table 3.5). Based on their period spacing values we identify them as dipole modes and assume that these are a series of prograde and a series of retrograde modes. Since the central $m = 0$ modes cannot be detected, the frequency splitting is twice the actual rotational splitting. Approximating the Ledoux constant for dipole g modes by $C_{n,\ell} \approx 0.5$ then leads to a rotational period $P_{\mathrm{rot,g_1}} \approx 11$ d. The second frequency splitting value of $\Delta f_{g_2} \approx 0.07$ d^{-1} can be associated with three other series (Table 3.6). Their period spacing values point towards dipole modes as well and we conclude that we observe prograde, zonal, and retrograde modes. For the triplets we find a rotational period $P_{\mathrm{rot,g_2}} \approx 7$ d. The rotationally split g-mode doublets and triplets likely originate in the two different binary components. They are illustrated in Fig. 3.12.

The modes of the series that could not be associated with either frequency splitting value presumably have $\ell = 2$, since their period spacing values are below those of the other series. In an independent analysis of the g modes of KIC 10080943, Keen et al. (2015) confirmed the results presented here.

3.5.3 The p modes

In the highly structured p-mode regime ($f > 8$ d^{-1}; Fig. 3.9, panels c and d) we detected four multiplets caused by rotational splitting, which are displayed in Fig. 3.13 and listed in Table 3.7. The most prominent feature is the quintuplet around 17.3 d^{-1}, which has a mean frequency splitting of $\Delta f_{\mathrm{p_1}} = 0.1304 \pm 0.0013$ d^{-1} $= 2 f_{\mathrm{orb}}$. In the triplet around

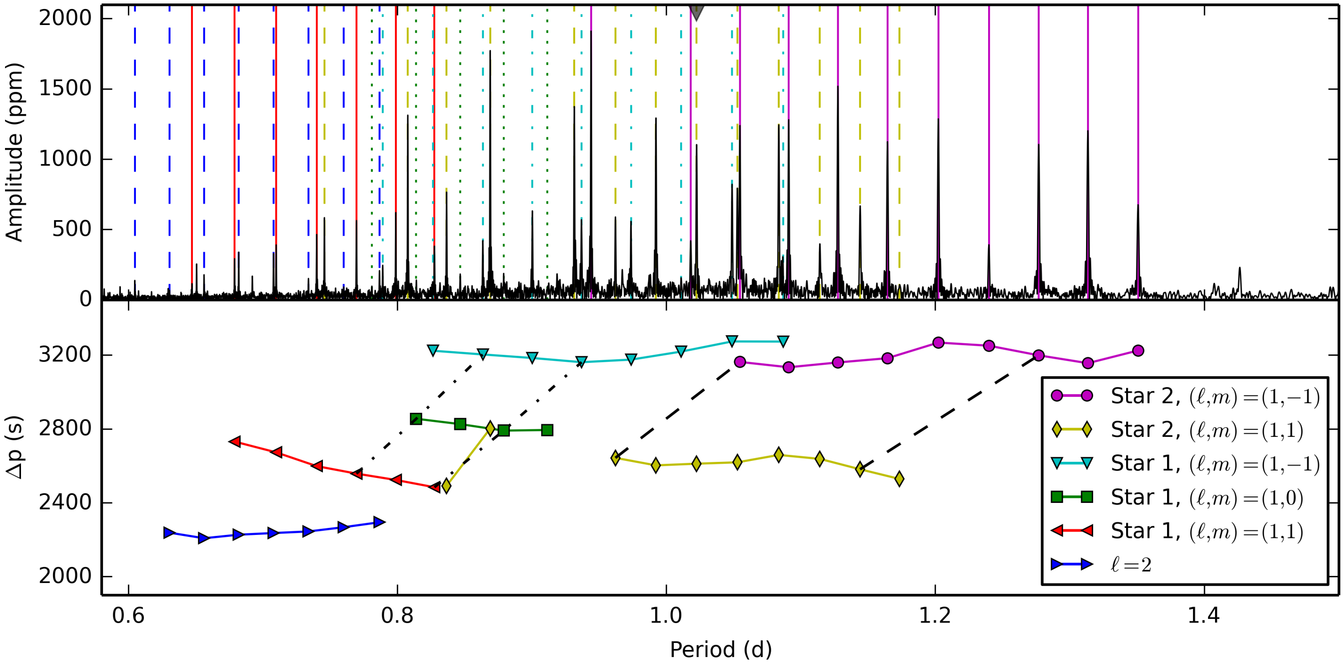

Figure 3.11: Series of equidistantly spaced periods in the g mode regime. The exact values of frequencies, periods, amplitudes of the modes, as well as the period spacings and their uncertainties are given in Table 3.4. *Top panel:* Period spectrum, zoomed into the region of highest amplitudes. Marked by the black triangle is the frequency at $15 \cdot f_{\mathrm{orb}}$. The vertical lines indicate the modes of the period spacing series. *Bottom panel:* Period spacing Δp vs. period p of all six identified period spacing series. The dashed line connects the rotationally-split doublets ($\Delta f_2 \approx 0.091$ d^{-1}) and the dash-dotted line connects the rotationally-split triplets ($\Delta f_1 \approx 0.091$ d^{-1}). For clarity only the outer most pairs and triplets are marked.

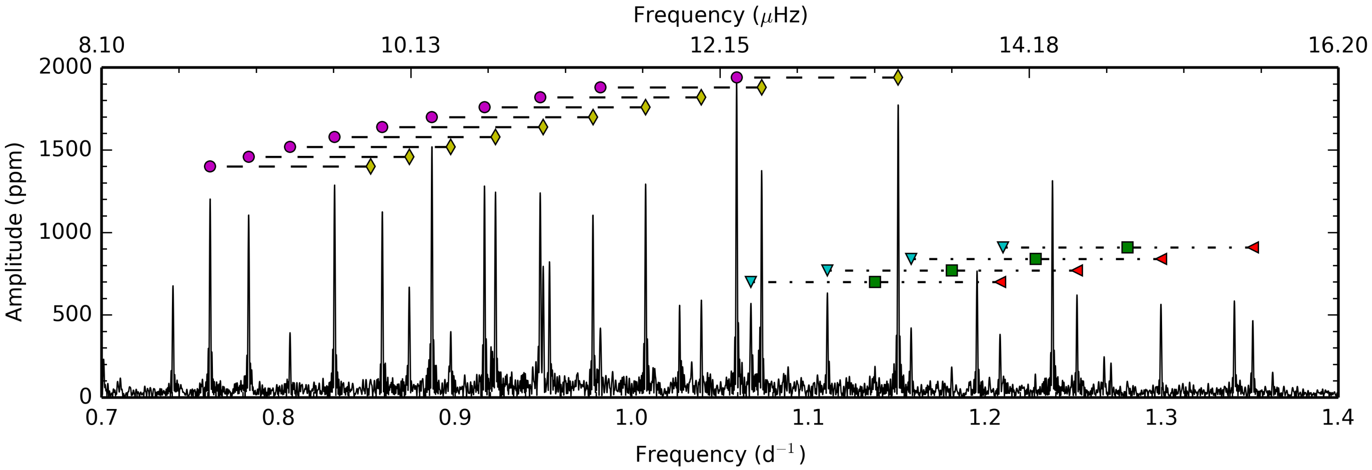

Figure 3.12: Rotationally split multiplets in the g mode region as reported in Tables 3.5 and 3.6. The symbols have the same meaning as in Fig. 3.11.

Table 3.5: Frequency splittings of the modes occurring in the period spacing series of doublets. The identification of the azimuthal order m is given.

m	f d^{-1}	Δf d^{-1}	$\epsilon\Delta f$ d^{-1}
−1	0.761386		
1	0.852334	0.09095	0.00006
−1	0.783175		
1	0.874150	0.09098	0.00001
−1	0.806569		
1	0.897600	0.09103	0.00002
−1	0.831820		
1	0.922897	0.09108	0.00001
−1	0.858848		
1	0.949885	0.09104	0.00001
−1	0.886920		
1	0.978056	0.09114	0.00001
−1	0.916666		
1	1.007861	0.09119	0.00001
−1	0.948204		
1	1.039427	0.09122	0.00001
−1	0.982312		
1	1.073577	0.09126	0.00002
−1	1.059380		
1	1.150808	0.09143	0.00001

Table 3.6: Frequency splittings of the modes occurring in the period spacing of triplets.

m	f d^{-1}	Δf d^{-1}	$\epsilon\Delta f$ d^{-1}
−1	1.027043		
0	1.097340	0.07030	0.00006
−1	1.067345		
0	1.137729	0.07038	0.00003
1	1.208481	0.07075	0.00003
−1	1.110739		
0	1.181151	0.07041	0.00003
1	1.251994	0.07084	0.00003
−1	1.158164		
0	1.228631	0.07047	0.00003
1	1.299530	0.07090	0.00003
−1	1.210145		
0	1.280641	0.07050	0.00006
1	1.351542	0.07090	0.00006

15 d^{-1}, we found a smaller splitting value of $\Delta f_{\mathrm{p}_2} = 0.1213 \pm 0.0019$ d^{-1}. Furthermore, none of the multiplets are symmetric about their centre frequency, which could be indicative of second-order rotational effects (e.g. Saio 1981) or magnetic splitting, in addition to rotational splitting (e.g. Goode & Thompson 1992). This is most noticeable for the triplet at 19.5 d^{-1} , where the mean splitting value ($\Delta f = 0.1315 \pm 0.0029$ d^{-1}) is also larger, although within the error bars of Δf_{p_1}. We note that the rotational splitting values that occur in the p modes are different from the ones found in the g modes, which will be further discussed in Sect. 3.6.

Furthermore, we find that the two highest-amplitude peaks $f_4 = 13.94759$ d^{-1} and $f_{13} = 15.683330$ d^{-1} are singlets, and hence likely to be radial modes, although their degree as well as radial order remain unidentified at this stage. In Sect. 3.5.5 we present evidence that these two frequencies originate in the two different stars.

Another spacing, which occurs several times among frequency pairs, is $\Delta f = 0.052$ d^{-1}. It is most striking in the frequency range 8 d^{-1} $< f <$ 12 d^{-1} (Fig. 3.9, panel c) and is connected to the difference of two high-amplitude g modes $f_1 - f_{12} = 0.05152 \pm 0.000013$ d^{-1}. We interpret these p-mode frequency pairs as due to non-linear resonant mode coupling. The spacing also appears in the periodogram as

Table 3.7: Frequency splittings in the p mode regime.

f d^{-1}	A ppm	Δf d^{-1}
12.62972	95.1	
12.763339	533.5	0.133619 ± 0.000020
12.890541	758.4	0.127202 ± 0.000005
14.98412	160.9	
15.10724	220.1	0.12312 ± 0.000014
15.226646	257.2	0.119406 ± 0.000013
17.04422	83.0	
17.17332	201.9	0.12910 ± 0.000032
17.305043	616.1	0.131723 ± 0.000011
17.43413	108.4	0.129087 ± 0.000020
17.56586	64.4	0.13173 ± 0.000045
19.37580	57.3	
19.51028	115.4	0.13448 ± 0.000045
19.638879	315.5	0.1285994 ± 0.000021

$f_{87} = 0.05208$ d^{-1}. A similar effect has been observed in the slowly pulsating B-type (SPB) binary KIC 6352430 by Pápics et al. (2013), who gave a similar interpretation.

3.5.4 Combination frequencies

Non-linear pulsation effects can manifest themselves in the Fourier spectrum as combination frequencies and harmonics of a few parent frequencies. Pápics et al. (2015) and Kurtz et al. (2015) have recently used them to explain the skewed, non-sinusoidal light curves of many γ Dor and SPB stars. We also identify non-linearity in the light curve of KIC 10080943 from the detection of several low-order combination frequencies of the form $nf_i \pm mf_j = f_k$, where n and m are small integers, f_i and f_j are called the parent frequencies, and f_k the combination frequency. To keep the number of combinations manageable, we limit the search for combinations to $(n + m) \leq 2$ and to parent frequencies among the 40 highest amplitude modes. We note that from those 40 modes, only five are not identified to be part of a period spacing series or rotational multiplet. Owing to the dense frequency spectrum, there are several combinations that can be made by pure chance (Pápics 2012), and several different parents can combine to the same combination frequency. Nevertheless, we found clear and obvious patterns.

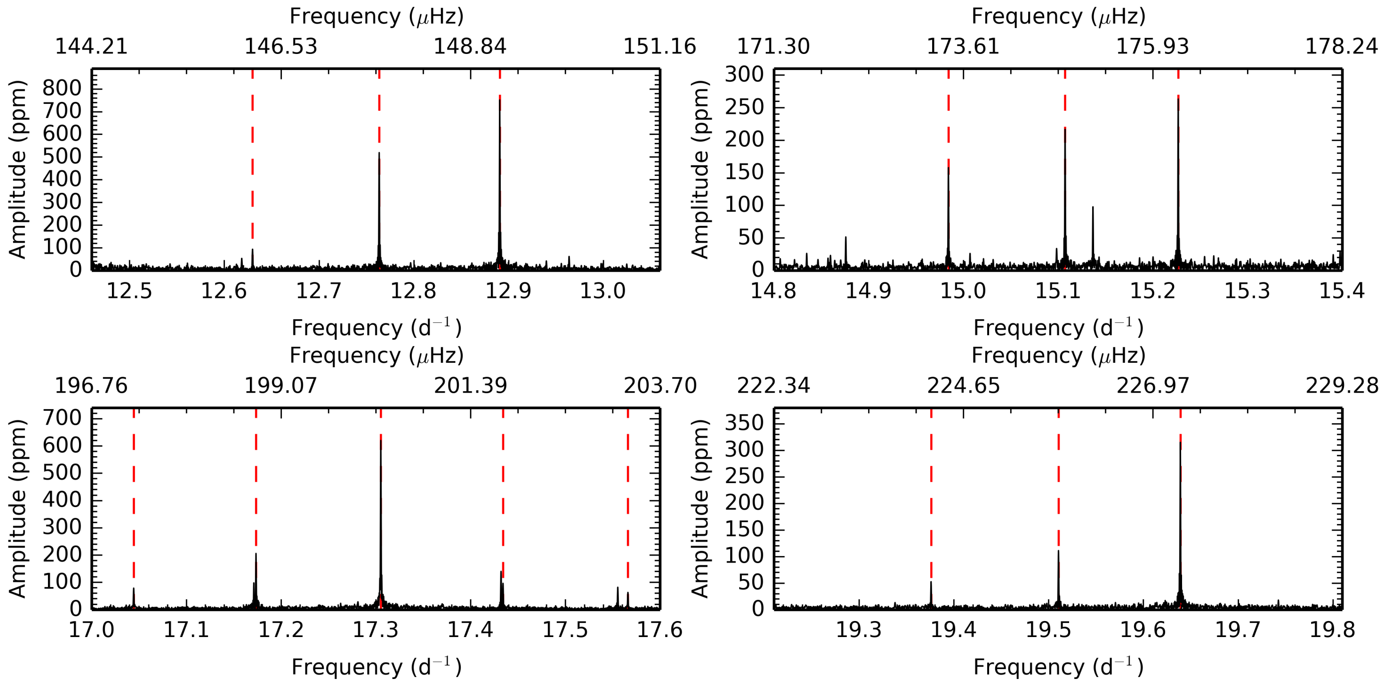

Figure 3.13: Frequency splittings in the p-mode regime of the periodogram. The vertical dashed lines indicate the modes, composing the multiplets. The frequencies, amplitudes, and frequency differences are listed in Table 3.7. *Top left:* Triplet with mean separation $\Delta f_1 = 0.1304 \pm 0.0032$ d^{-1}. *Top right:* Triplet with a mean separation $\Delta f_2 = 0.1213 \pm 0.0019$ d^{-1}. *Bottom left:* Quintuplet with mean separation $\Delta f_1 = 0.1304 \pm 0.0013$ d^{-1}. *Bottom right:* Triplet with mean separation $\Delta f = 0.1315 \pm 0.0029$ d^{-1}.

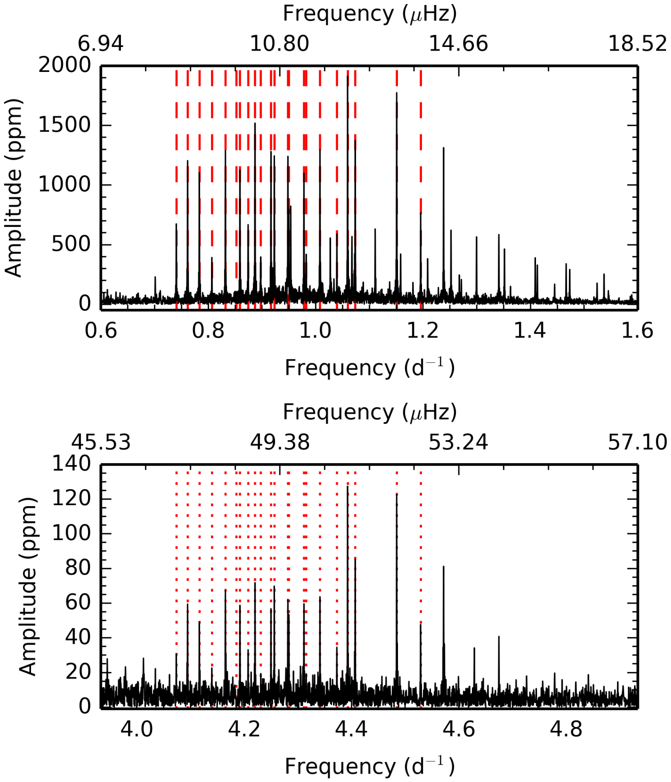

Figure 3.14: All the marked frequencies (dotted lines) in the *bottom panel* result from linear combinations of parent frequencies (dashed lines) depicted in the *top panel* and the parent frequency f_8 = 3.333499 d^{-1}.

Frequencies f_4 = 13.94759 d^{-1} and f_8 = 3.33350 d^{-1} create combinations (sums and differences) with almost all mode frequencies of the rotationally split doublets in the g modes. The frequency group between 4 d^{-1} and 4.7 d^{-1} is fully explained through resonances with f_8, which is illustrated in Fig. 3.14. Moreover, the single peak between the g- and p-mode regions can be related to $2f_8$ = 6.66697 d^{-1} (see Fig. 3.8).

Nonlinear mode coupling also happens among the high-amplitude g modes, which (almost exclusively) explain the frequencies between 1.6 d^{-1} and 2.6 d^{-1}. Although some combinations are created by modes of the frequency triplets, by far the majority of combinations are caused by the frequency doublets, due to their higher amplitudes.

3.5.5 Phase modulation

The motion of the stars in the binary orbit causes a periodic variation in the path length travelled by the light from the stars to the Earth, which results in a phase change of the observed pulsation over the orbital period (Murphy et al. 2014). Since these changes should be in anti-phase for the two components, we used this method to determine which pulsation frequencies originate in which star.

The entire *Kepler* light curve was divided into 5-day segments to retrieve the phase variations, and the phases of the pulsations were determined with the frequencies fixed to the values in Table 3.9. These phase variations were then converted into light arrival time delays. A Fourier transform of these time delays gives the orbital period, the projected light travel time across the orbit, and the eccentricity (a full description is provided by Murphy et al. 2014; Murphy & Shibahashi 2015). For a period as short as 15.3364 d, the segment size is a trade off between the frequency resolution for each segment and the sampling rate of the orbit. This is easier to achieve the higher the amplitude of the p modes. Despite the obvious limitation of this method for short-period binaries, we were able to determine the phases of the orbital variations of seven modes (excluding f_{18}, which has strong beating with a close frequency), given in Table 3.8. For f_4 and f_{13} the phases are 2.06 ± 0.08 and 5.31 ± 0.17, respectively, which are π rad out of phase within the errors. They have time delays of 44.0 ± 3.5 s and 36.2 ± 4.8 s, respectively, where the smallest time delay belongs to the star with the smaller $a \sin i_{\rm orb}$ and larger mass. Consequently, the peaks whose orbital variation has a phase near 5.0 belong to the primary, while those with phases near 2.0 belong to the secondary.

This method can also be used to derive orbital parameters, without the use of ground-based spectroscopy. For KIC 10080943 they are in good agreement with our results derived from RVs and spectral disentangling, but the results from phase modulation (PM) have much larger error bars, due to the short orbital period and a segment size of only 5 days.

Another effect caused by the light travel time delay is modulation of frequencies, which creates side lobes at the orbital frequency in the periodogram. We detected these side lobes for the high-amplitude p modes. These can also be used to study an orbit photometrically (e.g. Shibahashi & Kurtz 2012; Telting et al. 2014; Shibahashi et al. 2015), but once again, our spectroscopy is far superior for deducing orbital properties in the case of KIC 10080943.

Table 3.8: The frequencies and orbital variation phases for 7 of the 8 highest amplitude p modes.

	Frequency d^{-1}	Orbital phase rad	Star
f_4	13.947586	2.06 ± 0.08	2
f_{13}	15.683330	5.31 ± 0.17	1
f_{21}	12.890541	5.75 ± 0.19	1
f_{27}	17.305043	3.64 ± 0.26	?
f_{32}	12.763339	0.87 ± 0.24	?
f_{45}	14.203334	2.03 ± 0.34	2
f_{46}	19.638879	4.75 ± 0.28	1

3.6 Discussion

3.6.1 Core-to-surface rotation

We detect two different frequency splitting values in the g modes, as well as another two different values in the p modes. This is strong evidence that both stars pulsate as p- and g-mode hybrids. Our binary analysis yields similar masses for both stars, which supports this hypothesis. By detecting rotational splitting in the g modes, which are sensitive to the region close to the stellar core, as well as in the p modes, which have their highest amplitudes in the stellar envelope, we can constrain the internal rotation profile of a star in a largely model-independent way, as explained in detail in Kurtz et al. (2014) and in Saio et al. (2015) for two previously analysed single stars with similar mass. Here, we achieve this via the detected frequency patterns and combination frequencies. The p-mode frequency f_4 only creates combinations with the frequencies of the g-mode doublets, while the frequency $f_{13} = 15.68333\ \mathrm{d}^{-1}$ does not create combination frequencies in this way and also does not originate in the same star as f_4 (Table 3.8). The PM results further show that $f_{21} = 12.890541\ \mathrm{d}^{-1}$, which is part of a triplet with rotational splitting $\Delta f_{\mathrm{p}_1} = 0.1304\ \mathrm{d}^{-1}$, does not stem from the same star as f_4 either. We therefore conclude that the p-mode splitting that corresponds to the rotational period $P_{\mathrm{rot,g}_1} \approx 11$ d of the g-mode doublet has to be $\Delta f_{\mathrm{p}_2} = 0.1213\ \mathrm{d}^{-1}$. For pure p modes, the Ledoux constant $C_{n,\ell} \approx 0$ and $\beta_{n,\ell} = 1 - C_{n,\ell} \approx 1$, resulting in a rotational period $P_{\mathrm{rot,p}_2} \approx 8.2$ d. Thus, we conclude a core-to-surface rotation rate for the secondary of approximately $P_{\mathrm{core},2}/P_{\mathrm{surface},2} \approx 1.3$. Similarly for the primary, $P_{\mathrm{rot,p}_1} \approx 7.7$ d and $P_{\mathrm{core},1}/P_{\mathrm{surface},1} \approx 0.9$.

The core-to-surface rotation rates derived here are rough first estimates, as the proper computation of the p-mode Ledoux constant requires seismic modelling of the zonal modes, taking into account a possible influence by the g-mode cavity, as well as the observed departure from equidistance in the p-mode splittings (Table 3.7). Also, the g-mode splittings vary with frequency. Triana et al. (2015) deduced the internal rotation profile of the SPB KIC 10526294 from g-mode frequency inversion, after detailed seismic modelling of the zonal modes by Moravveji et al. (2015). We plan to follow a similar methodology, if feasible for KIC 10080943, with the aim of determining the interior rotation profiles of its components with better precision than the first rough estimates we present here. We come back to this issue in the next chapter.

3.6.2 Spin-orbit alignment

It is usually assumed that the rotational axis of binary components are aligned with the axis of the orbital plane. The low amplitudes of the zonal g modes suggest that the stars are seen under a high inclination angle, whereas the configuration of the p-mode multiplets seem to indicate a low inclination angle. Since heat-driven pulsations might not be excited to similar intrinsic amplitudes, the splitting geometry only provides weak evidence for the inclination of the stellar pulsation axis. The orbital inclination angle has to be below 82.5°, given that no eclipses are observed. We can further test the assumption $i_{\rm orb} \simeq i_{\rm rot}$ by deriving a radius with the rotational splitting and $v \sin i_{\rm rot}$ for $i_{\rm orb} = 68 \pm 3^{\circ}$. For the primary ($f_{\rm surface,1} = 0.1304 \pm 0.0013$ d^{-1}, $v_1 \sin i_{\rm rot,1} = 18.7 \pm 1.2$ km s^{-1}), we find a radius of $3.06 \pm 0.22\, R_{\odot}$, and for the secondary ($f_{\rm surface,2} = 0.1213 \pm 0.0019$ d^{-1}, $v_2 \sin i_{\rm rot,2} = 13.8 \pm 1.6$ km s^{-1}) $2.43 \pm 0.29\, R_{\odot}$, giving a ratio $R_1/R_2 = 1.26 \pm 0.18$. Using the $v \sin i_{\rm rot}$ values from the spectroscopic solution with micro-turbulence as a free parameter makes marginal difference and gives a ratio $R_1/R_2 = 1.24 \pm 0.17$. The values derived here are in agreement with the radii derived from binary modelling and spectroscopic analysis, given the 1-σ uncertainties in Table 3.1, as well as the assumed spin-orbit alignment.

3.7 Summary

From the extraordinarily rich frequency spectrum of the four-year *Kepler* light curve of KIC 10080943, we have shown that this eccentric binary system contains two γ Dor/δ Sct hybrids. In the clearly separated g mode range, we discover six period spacing series, which form rotationally split triplets of prograde, zonal, and retrograde modes for one star and doublets of prograde and retrograde modes for the other star. We also find rotationally split multiplets with two distinct spacings in the p-mode range, where one star seems to have a 2:1 resonance with the orbital period. Using combination frequencies we manage to link period spacing in the g modes with rotational splitting in the p modes for both components. We derive that the primary has almost uniform rotation or a slightly more rapid core than surface, while the secondary's core rotates more slowly than its surface. Similar results have been obtained by Kurtz et al. (2014) and Saio et al. (2015) for two single hybrid g- and p-mode pulsators. The phase modulation detected for the high-amplitude p modes of KIC 10080943, which is caused by the light travel time effect in the binary orbit, suggests that the secondary is the stronger pulsator.

Buried beneath the high amplitude pulsations, we discover ellipsoidal variation and reflection with an amplitude of only 0.2%. The effects are not dominating the light curve, which is not surprising since the 15.3364-d orbit with $e = 0.449$ results in a separation of $\sim 22.6\ R_\odot$ at periastron. We derived the orbital solution from 26 ground-based spectra, showing lines of both components with a mass ratio close to unity. From the disentangled spectra, we confirmed the early F spectral type for both stars, with temperatures $T_{\mathrm{eff},1} = 7100 \pm 220$ K and $T_{\mathrm{eff},2} = 7450 \pm 400$ K. The surface gravities can only be moderately constrained with spectroscopy. A high-precision estimate was, however, achieved by the binary fit obtained for the light curve. We used PHOEBE to compute the models and an MCMC simulation to improve the fit, as well as derive the posterior probability distribution for each parameter. The inclination angle is not normally distributed and a range of possible values is $i_{\mathrm{orb}} = 68^\circ \pm 3^\circ$. For this range, we derive absolute masses $M_1 = 2.0 \pm 0.1\ M_\odot$ and $M_2 = 1.9 \pm 0.1\ M_\odot$. From the fitted surface potentials, corrected for degeneracies with albedo and gravity darkening, we find the radii $R_1 = 2.9 \pm 0.1\ R_\odot$ and $R_2 = 2.1 \pm 0.2\ R_\odot$. From these values we derive surface gravities $\log g_1 = 3.81 \pm 0.03$ and $\log g_2 = 4.1 \pm 0.1$. Since the brightening signal in the light curve of KIC 10080943 has very low amplitude, it was necessary to combine spectroscopic, photometric, and asteroseismic analyses to obtain a good characterisation of the system. More precise parameters can be obtained for binaries, where the brightening signal is more significant and the tidal distortion has a larger contribution than the reflection effect. Double-lined, eclipsing binaries, however, offer the most reliable method to derive high-precision fundamental parameters in a largely model-independent way, and without suffering from degeneracies in the same way as the example presented in this chapter.

As stars evolve along the main sequence, they develop a chemical composition gradient near the core, which creates a periodic signal in the period spacing in the Δp vs. p diagram (Van Reeth et al. 2015b). We can use the period spacing series detected for KIC 10080943 to derive the properties of the mixing mechanisms taking place in the deep stellar interior. Further crucial constraints on the stellar structure of both components of KIC 10080943, keeping in mind its close binary nature and accompanying tidal forces, can be derived from the rotation rates that are detected for the region near the cores and the surfaces. Tight asteroseismic constraints on the interior rotation profile of both stars can only be drawn from the detailed comparison to stellar models, which we present in the following chapter.

Appendix A: Frequency analysis results

Table 3.9 lists the Fourier parameters, their uncertainties, and S/N values of the frequencies found after removing the binary orbit.

Table 3.9: Results of the pulsation frequency analysis for KIC 10080943. Values listed are: Frequency f, amplitude A, and phase ϕ, their respective uncertainties ϵ_f, ϵ_A, and ϵ_ϕ, as well as the S/N calculated in a frequency range of 1 d^{-1}, 3 d^{-1}, and the complete range up to the Nyquist frequency. Period spacing doublets (PS d) and triplets (PS t), frequency splittings (FS) and combination frequencies are identified by comments.

	f	ϵ_f	A	ϵ_A	ϕ	ϵ_ϕ		S/N		Comment
	d^{-1}	d^{-1}	ppm	ppm	2π/rad	2π/rad	1 d^{-1}	3 d^{-1}	Full	
f_1	1.059380	0.000009	1977.8	47.3	−0.060	0.024	220.0	244.1	552.9	PS d; $m = -1$
f_2	1.150808	0.000009	1772.4	44.4	0.486	0.025	204.9	218.7	495.5	PS d; $m = 1$
f_3	0.88692	0.00001	1532.7	42.0	−0.198	0.027	158.3	189.1	428.5	PS d; $m = -1$
f_4	13.947586	0.000002	1360.9	7.7	0.140	0.006	861.7	788.8	380.5	
f_5	1.07358	0.00001	1358.9	40.5	−0.244	0.030	152.4	167.7	379.9	PS d; $m = 1$
f_6	0.948204	0.000008	1340.3	29.4	−0.477	0.022	142.5	165.4	374.7	PS d; $m = -1$
f_7	1.23814	0.00001	1324.2	37.1	−0.459	0.028	157.9	163.4	370.2	PS d; $m = 1$
f_8	3.33350	0.00001	1321.8	38.6	0.400	0.029	213.9	227.2	369.5	
f_9	0.922896	0.000008	1313.4	27.7	0.250	0.021	138.4	162.1	367.2	PS d; $m = 1$
f_{10}	0.831821	0.000010	1280.7	32.8	0.147	0.026	131.0	158.0	358.0	PS d; $m = -1$
f_{11}	0.91667	0.00001	1280.0	34.7	−0.170	0.027	134.8	158.0	357.9	PS d; $m = -1$
f_{12}	1.007861	0.000009	1261.0	31.3	0.234	0.025	136.4	155.6	352.5	PS d; $m = 1$
f_{13}	15.683330	0.000003	1241.7	9.4	−0.450	0.008	815.8	858.6	347.1	
f_{14}	0.761387	0.000008	1200.0	26.1	0.446	0.022	120.2	148.1	335.5	PS d; $m = -1$
f_{15}	0.858847	0.000008	1145.8	24.8	−0.091	0.022	117.8	141.4	320.3	PS d; $m = -1$
f_{16}	0.978055	0.000008	1130.6	23.3	0.213	0.021	121.3	139.5	316.1	PS d; $m = 1$; $15f_{\mathrm{orb}}$
f_{17}	0.783176	0.000008	1052.3	21.8	0.345	0.021	106.3	129.9	294.2	PS d; $m = -1$
f_{18}	12.452578	0.000003	931.5	6.8	0.021	0.007	351.2	294.1	260.4	
f_{19}	0.949885	0.000009	881.7	20.8	0.408	0.024	93.9	108.8	246.5	PS d; $m = 1$
f_{20}	0.953435	0.000009	836.8	19.9	−0.092	0.024	89.3	103.3	233.9	PS t; $m = -1$
f_{21}	12.890541	0.000003	758.4	6.2	0.226	0.008	348.4	295.1	212.0	FS 1

Table 3.9: continued.

	f	ϵ_f	A	ϵ_A	ϕ	ϵ_ϕ		S/N		Comment
	d^{-1}	d^{-1}	ppm	ppm	2π/rad	2π/rad	1 d^{-1}	3 d^{-1}	Full	
f_{22}	1.195443	0.000010	744.5	19.2	0.026	0.026	87.4	91.9	208.1	PS d; $m = 1$
f_{23}	0.87415	0.00001	695.2	18.6	0.286	0.027	71.6	85.8	194.4	PS d; $m = 1$
f_{24}	0.74034	0.00001	661.6	18.1	0.229	0.027	66.2	81.6	185.0	PS d; $m = -1$
f_{25}	1.039427	0.000010	660.6	17.5	0.379	0.026	72.3	81.5	184.7	PS d; $m = 1$
f_{26}	1.110740	0.000010	647.0	16.9	−0.074	0.026	73.9	79.8	180.9	PS t; $m = -1$
f_{27}	17.305043	0.000004	616.1	6.8	0.426	0.011	420.0	461.8	172.2	FS 3
f_{28}	1.341113	0.000010	605.8	15.9	0.195	0.026	74.6	74.8	169.4	PS d; $m = 1$
f_{29}	1.06734	0.00001	602.6	16.5	0.103	0.027	67.3	74.4	168.5	PS t; $m = -1$
f_{30}	1.251994	0.000010	598.5	15.5	−0.313	0.026	71.6	73.9	167.3	PS t; $m = 1$
f_{31}	1.299530	0.000010	570.4	15.1	0.487	0.027	69.2	70.4	159.5	PS t; $m = 1$
f_{32}	12.763339	0.000004	533.5	5.9	0.460	0.011	233.0	195.7	149.1	FS 1
f_{33}	1.35154	0.00001	466.6	14.8	−0.459	0.032	57.5	57.6	130.5	PS t; $m = 1$
f_{34}	1.02704	0.00001	464.9	14.5	0.063	0.031	50.7	57.4	130.0	PS t; $m = -1$
f_{35}	0.98231	0.00001	459.4	14.2	0.163	0.031	49.3	56.7	128.4	PS d; $m = -1$
f_{36}	1.20848	0.00001	435.3	13.6	0.347	0.031	51.6	53.7	121.7	PS t; $m = 1$
f_{37}	1.15816	0.00001	434.1	13.9	0.414	0.032	50.4	53.6	121.4	PS t; $m = -1$
f_{38}	0.80657	0.00001	401.9	13.4	−0.038	0.033	40.7	49.6	112.4	PS d; $m = -1$
f_{39}	0.89760	0.00001	380.9	13.2	−0.359	0.035	39.8	47.0	106.5	PS d; $m = 1$
f_{40}	1.93517	0.00001	370.1	13.0	−0.486	0.035	51.7	48.6	103.5	
f_{41}	1.40882	0.00001	365.4	12.8	−0.045	0.035	46.4	45.1	102.2	PS t; $m = 1$
f_{42}	1.46641	0.00001	343.6	12.7	0.458	0.037	45.0	42.4	96.0	PS $\ell = 2$?
f_{43}	0.34619	0.00001	341.4	12.5	−0.171	0.037	33.4	42.1	95.5	
f_{44}	1.41278	0.00001	339.5	12.3	−0.098	0.036	43.2	41.9	94.9	PS $\ell = 2$?
f_{45}	14.203334	0.000007	332.7	5.9	0.061	0.018	215.5	202.3	93.0	

Table 3.9: continued.

	f	ϵ_f	A	ϵ_A	ϕ	ϵ_ϕ		S/N		Comment
	d^{-1}	d^{-1}	ppm	ppm	2π/rad	2π/rad	1 d^{-1}	3 d^{-1}	Full	
f_{46}	19.638879	0.000007	315.5	6.0	−0.232	0.019	271.2	268.8	88.2	FS 4
f_{47}	12.415537	0.000007	299.8	5.8	−0.471	0.020	110.5	93.0	83.8	
f_{48}	0.57559	0.00002	285.8	12.2	−0.270	0.043	28.8	35.3	79.9	
f_{49}	1.47304	0.00002	282.1	12.1	0.361	0.043	37.1	34.8	78.9	PS t; $m = 1$
f_{50}	1.78406	0.00002	272.0	12.0	0.267	0.044	37.6	34.9	76.0	
f_{51}	0.94422	0.00002	267.8	11.9	−0.139	0.044	28.4	33.0	74.9	
f_{52}	15.226646	0.000009	257.2	5.9	−0.051	0.023	173.2	175.8	71.9	FS 2
f_{53}	0.92019	0.00002	253.8	11.8	0.231	0.046	26.8	31.3	71.0	PS t; $m = -1$
f_{54}	1.53695	0.00002	240.3	11.7	−0.049	0.049	32.0	30.0	67.2	
f_{55}	3.40515	0.00002	235.3	11.6	0.367	0.049	38.7	41.0	65.8	
f_{56}	1.27125	0.00002	234.7	11.6	0.365	0.049	28.3	29.0	65.6	PS $\ell = 2$?
f_{57}	0.50177	0.00002	228.9	11.5	−0.070	0.050	22.5	28.2	64.0	
f_{58}	15.10724	0.00001	220.1	5.9	0.459	0.027	152.3	148.7	61.5	FS 2
f_{59}	0.70108	0.00002	214.1	11.5	−0.488	0.054	21.4	26.4	59.9	PS d; $m = -1$
f_{60}	3.24598	0.00002	206.3	11.4	0.464	0.055	33.3	34.7	57.7	
f_{61}	17.17332	0.00001	201.9	5.9	−0.085	0.029	136.6	148.8	56.4	FS 3
f_{62}	1.73953	0.00002	200.3	11.4	0.283	0.057	27.6	25.6	56.0	$f_{14} + f_{16}$
f_{63}	11.60773	0.00001	194.7	5.9	0.205	0.030	41.8	40.6	54.4	
f_{64}	1.52403	0.00002	192.1	11.4	0.344	0.059	25.4	23.9	53.7	PS $\ell = 2$?
f_{65}	1.26738	0.00002	191.7	11.3	0.429	0.059	23.0	23.7	53.6	PS t; $m = -1$
f_{66}	0.40927	0.00002	191.5	11.3	−0.248	0.059	18.8	23.6	53.5	
f_{67}	1.18115	0.00002	182.2	11.3	−0.149	0.062	21.3	22.5	50.9	PS t; $m = 0$
f_{68}	1.44497	0.00002	179.8	11.3	−0.059	0.063	23.3	22.2	50.3	
f_{69}	0.98918	0.00003	161.5	11.2	0.332	0.070	17.4	19.9	45.1	PS t; $m = -1$

Table 3.9: continued.

	f	ϵ_f	A	ϵ_A	ϕ	ϵ_ϕ	S/N			Comment
	d^{-1}	d^{-1}	ppm	ppm	2π/rad	2π/rad	1 d^{-1}	3 d^{-1}	Full	
f_{70}	14.98412	0.00001	160.9	5.9	0.212	0.037	112.2	108.6	45.0	FS 2
f_{71}	1.36275	0.00003	160.8	11.2	0.245	0.070	19.9	19.8	45.0	PS $\ell = 2$?
f_{72}	1.65375	0.00003	156.4	11.2	0.201	0.072	21.5	19.8	43.7	PS $\ell = 2$?
f_{73}	0.45927	0.00003	148.7	11.2	0.177	0.075	14.6	18.3	41.6	
f_{74}	17.43194	0.00002	146.9	5.9	0.186	0.040	103.1	111.4	41.1	
f_{75}	1.03385	0.00003	143.7	11.2	−0.020	0.078	15.7	17.7	40.2	
f_{76}	1.22863	0.00003	139.8	11.2	−0.331	0.080	16.7	17.3	39.1	PS t; $m = 0$
f_{77}	1.54502	0.00003	139.8	11.2	0.203	0.080	18.5	17.5	39.1	PS t; $m = 1$
f_{78}	1.21014	0.00003	138.3	11.1	0.413	0.081	16.4	17.1	38.7	PS t; $m = -1$
f_{79}	15.90340	0.00002	131.3	5.9	0.014	0.045	90.3	90.7	36.7	
f_{80}	1.13773	0.00003	130.7	11.1	0.130	0.085	15.0	16.1	36.5	PS t; $m = 0$
f_{81}	4.39286	0.00003	130.4	11.1	0.172	0.085	28.8	27.5	36.5	$f_1 + f_8$
f_{82}	0.49791	0.00003	127.9	11.1	0.458	0.087	12.5	15.8	35.8	
f_{83}	0.53779	0.00003	125.7	11.1	−0.426	0.088	12.6	15.5	35.2	
f_{84}	2.45933	0.00003	124.4	11.1	−0.028	0.089	18.9	18.5	34.8	$f_8 - f_{23}$
f_{85}	17.30454	0.00002	121.9	6.1	−0.378	0.050	83.1	91.4	34.1	
f_{86}	4.48430	0.00003	120.5	11.1	−0.321	0.092	27.5	26.1	33.7	$f_2 + f_8$
f_{87}	0.05208	0.00003	120.5	11.1	0.266	0.092	11.8	14.9	33.7	$f_1 - f_{12}$
f_{88}	2.21019	0.00004	117.7	11.1	0.189	0.094	17.1	16.4	32.9	$f_1 + f_2$
f_{89}	0.71065	0.00004	116.1	11.0	−0.318	0.095	11.6	14.3	32.5	
f_{90}	19.51028	0.00002	115.4	6.0	0.049	0.052	98.4	99.8	32.3	FS 4
f_{91}	0.43931	0.00004	111.6	11.0	−0.171	0.099	10.9	13.8	31.2	
f_{92}	17.43413	0.00002	108.4	6.0	0.252	0.055	76.1	82.3	30.3	FS 3
f_{93}	11.05360	0.00002	107.6	6.0	−0.223	0.056	17.3	18.4	30.1	

Table 3.9: continued.

	f d^{-1}	ϵ_f d^{-1}	A ppm	ϵ_A ppm	ϕ 2π/rad	ϵ_ϕ 2π/rad	S/N 1 d^{-1}	S/N 3 d^{-1}	Full	Comment
f_{94}	2.77695	0.00004	106.2	11.0	−0.204	0.104	16.9	16.8	29.7	
f_{95}	1.09549	0.00004	103.1	11.0	−0.352	0.107	11.7	12.7	28.8	
f_{96}	1.02790	0.00004	102.6	11.0	−0.212	0.107	11.2	12.7	28.7	
f_{97}	2.13299	0.00004	102.5	11.0	0.462	0.107	14.6	14.0	28.6	$f_1 + f_5$
f_{98}	1.89480	0.00004	101.6	11.0	−0.223	0.109	14.1	13.2	28.4	$f_3 + f_{12}$
f_{99}	2.09895	0.00004	101.6	11.0	−0.120	0.108	14.4	13.8	28.4	$f_1 + f_{25}$
f_{100}	11.31330	0.00002	100.5	6.0	−0.076	0.060	18.3	18.8	28.1	
f_{101}	3.27179	0.00004	100.3	11.0	0.440	0.109	16.2	17.0	28.0	
f_{102}	15.13665	0.00002	99.9	6.0	−0.076	0.060	69.1	67.6	27.9	
f_{103}	0.62811	0.00004	99.1	11.0	−0.080	0.111	9.9	12.2	27.7	
f_{104}	10.53635	0.00002	96.4	6.0	−0.046	0.062	13.0	14.3	26.9	
f_{105}	0.63559	0.00004	95.2	10.9	−0.036	0.115	9.5	11.7	26.6	
f_{106}	12.62972	0.00002	95.1	6.0	−0.102	0.064	39.2	32.7	26.6	FS 1
f_{107}	10.92536	0.00002	94.8	6.0	0.236	0.063	14.4	15.5	26.5	
f_{108}	1.98244	0.00004	94.6	11.0	−0.302	0.116	13.3	12.5	26.5	$f_1 + f_9$
f_{109}	10.58834	0.00002	94.0	6.0	−0.448	0.064	12.9	14.1	26.3	
f_{110}	1.93377	0.00004	93.5	10.9	−0.207	0.117	13.1	12.3	26.2	$f_1 + f_{23}$
f_{111}	1.24936	0.00004	93.4	10.9	0.009	0.117	11.2	11.5	26.1	
f_{112}	0.54623	0.00004	92.8	11.0	0.479	0.118	9.4	11.5	25.9	
f_{113}	3.23050	0.00004	91.8	10.9	0.282	0.119	14.8	15.4	25.7	
f_{114}	9.50927	0.00002	90.5	6.0	0.247	0.066	11.3	12.7	25.3	
f_{115}	9.56125	0.00003	89.6	6.0	−0.136	0.067	11.2	12.5	25.0	
f_{116}	0.61196	0.00005	88.8	10.9	0.121	0.123	8.9	11.0	24.8	
f_{117}	0.96207	0.00005	88.5	10.9	−0.290	0.123	9.4	10.9	24.7	

Table 3.9: continued.

	f d^{-1}	ϵ_f d^{-1}	A ppm	ϵ_A ppm	ϕ 2π/rad	ϵ_ϕ 2π/rad	1 d^{-1}	S/N 3 d^{-1}	Full	Comment
f_{118}	1.86648	0.00005	87.5	10.9	0.100	0.124	12.2	11.3	24.5	$f_1 + f_{38}$
f_{119}	1.83685	0.00005	86.6	10.9	−0.068	0.126	12.0	11.2	24.2	$f_3 + f_{19}$
f_{120}	2.29750	0.00005	85.7	10.9	0.266	0.127	12.7	12.1	24.0	$f_1 + f_7$
f_{121}	2.06737	0.00005	85.1	10.9	−0.000	0.128	12.0	11.4	23.8	$f_1 + f_{12}$
f_{122}	0.48268	0.00005	84.9	10.9	0.221	0.128	8.3	10.5	23.7	
f_{123}	11.01498	0.00003	84.6	6.0	−0.398	0.071	13.3	14.3	23.7	
f_{124}	15.68426	0.00003	84.4	6.0	0.399	0.071	55.4	58.3	23.6	
f_{125}	14.49976	0.00003	83.9	6.1	−0.047	0.072	57.6	53.4	23.5	
f_{126}	0.68314	0.00005	83.1	10.9	−0.319	0.131	8.3	10.3	23.2	
f_{127}	17.04422	0.00003	83.0	6.0	0.093	0.072	57.2	60.7	23.2	FS 3
f_{128}	0.45663	0.00005	83.0	10.9	−0.353	0.131	8.1	10.2	23.2	$\sim 7 f_{\mathrm{orb}}$
f_{129}	4.57165	0.00005	82.9	10.9	0.417	0.131	19.7	18.4	23.2	$f_7 + f_8$
f_{130}	2.41065	0.00005	82.6	10.9	−0.400	0.132	12.5	12.0	23.1	$f_8 - f_9$; $f_{26} + f_{31}$
f_{131}	4.40705	0.00005	82.2	10.9	−0.046	0.133	18.3	17.4	23.0	$f_5 + f_84$
f_{132}	0.66954	0.00005	81.9	11.0	0.104	0.134	8.2	10.1	22.9	
f_{133}	17.17108	0.00003	81.1	6.0	0.398	0.074	54.9	59.8	22.7	
f_{134}	1.87113	0.00005	78.4	10.9	0.484	0.138	10.9	10.2	21.9	$f_6 + f_9$
f_{135}	3.16095	0.00005	77.0	10.9	0.381	0.141	12.2	12.8	21.5	
f_{136}	2.02164	0.00005	76.5	10.9	0.267	0.142	10.8	10.2	21.4	$f_5 + f_6$
f_{137}	0.66871	0.00005	76.2	10.9	0.428	0.143	7.6	9.4	21.3	
f_{138}	1.28064	0.00005	76.1	10.8	0.294	0.143	9.2	9.4	21.3	PS t; $m = 0$
f_{139}	17.55513	0.00003	75.6	6.0	0.263	0.080	55.8	57.7	21.1	
f_{140}	1.09333	0.00005	74.7	10.8	−0.257	0.145	8.5	9.2	20.9	
f_{141}	10.71370	0.00003	73.9	6.0	0.322	0.081	10.5	11.4	20.7	

Table 3.9: continued.

	f	ϵ_f	A	ϵ_A	ϕ	ϵ_ϕ		S/N		Comment
	d^{-1}	d^{-1}	ppm	ppm	2π/rad	2π/rad	1 d^{-1}	3 d^{-1}	Full	
f_{142}	1.91219	0.00006	73.7	10.9	−0.294	0.147	10.3	9.6	20.6	$f_2 + f_{14}$
f_{143}	0.44517	0.00006	73.4	10.8	0.284	0.148	7.2	9.1	20.5	
f_{144}	1.68439	0.00006	72.6	10.8	0.416	0.149	10.0	9.2	20.3	$f_9 + f_{14}$
f_{145}	1.09734	0.00006	72.2	10.8	−0.286	0.150	8.2	8.9	20.2	PS t; $m = 0$
f_{146}	0.58229	0.00006	72.1	10.8	0.361	0.150	7.2	8.9	20.2	
f_{147}	1.56487	0.00006	71.5	10.8	0.224	0.151	9.5	9.0	20.0	$\sim 24 f_{\mathrm{orb}}$
f_{148}	1.58868	0.00006	71.2	10.8	−0.225	0.152	9.6	9.0	19.9	
f_{149}	1.16815	0.00006	70.8	10.9	−0.132	0.153	8.3	8.7	19.8	PS t; $m = 1$
f_{150}	4.16531	0.00006	70.5	10.8	0.317	0.153	14.5	14.2	19.7	$f_8 + f_{10}$
f_{151}	4.28171	0.00006	70.0	10.8	−0.304	0.154	15.0	14.4	19.6	$f_6 + f_8$
f_{152}	1.75472	0.00006	69.1	10.8	0.201	0.156	9.6	8.8	19.3	$f_9 + f_{10}$
f_{153}	0.59108	0.00006	68.8	10.8	0.122	0.157	6.9	8.5	19.2	
f_{154}	0.66657	0.00006	68.7	10.8	−0.443	0.157	6.9	8.5	19.2	
f_{155}	1.99032	0.00006	68.6	10.8	0.237	0.158	9.6	9.1	19.2	$f_5 + f_{11}$
f_{156}	2.28587	0.00006	68.5	10.8	−0.163	0.158	10.1	9.7	19.1	
f_{157}	2.12514	0.00006	67.8	10.8	0.066	0.159	9.7	9.3	19.0	$f_3 + f_7$
f_{158}	1.99293	0.00006	67.6	10.8	−0.345	0.159	9.5	8.9	18.9	$f_8 - f_{28}$
f_{159}	4.22042	0.00006	67.5	10.8	−0.042	0.160	14.0	13.8	18.9	$f_3 + f_8$
f_{160}	11.89501	0.00003	66.8	6.0	−0.115	0.090	17.1	15.8	18.7	
f_{161}	0.85233	0.00006	66.5	10.8	0.440	0.162	6.8	8.2	18.6	PS d; $m = 1$
f_{162}	12.26797	0.00003	66.4	6.0	0.394	0.090	22.0	19.0	18.6	
f_{163}	0.42355	0.00006	66.2	10.8	−0.064	0.163	6.5	8.2	18.5	
f_{164}	4.25635	0.00006	66.1	10.8	0.460	0.163	14.0	13.6	18.5	$f_8 + f_9$
f_{165}	0.65111	0.00006	65.9	10.8	−0.385	0.164	6.6	8.1	18.4	

Table 3.9: continued.

	f	ϵ_f	A	ϵ_A	ϕ	ϵ_ϕ		S/N		Comment
	d^{-1}	d^{-1}	ppm	ppm	2π/rad	2π/rad	$1\ \mathrm{d}^{-1}$	$3\ \mathrm{d}^{-1}$	Full	
f_{166}	0.27133	0.00006	65.9	10.8	−0.313	0.164	6.5	8.1	18.4	
f_{167}	1.87998	0.00006	65.7	10.8	0.429	0.164	9.2	8.5	18.4	
f_{168}	14.29636	0.00003	65.4	6.0	0.141	0.092	43.3	40.3	18.3	
f_{169}	0.58352	0.00006	65.3	10.8	0.394	0.165	6.6	8.1	18.3	
f_{170}	1.04128	0.00006	64.7	10.8	0.469	0.166	7.1	8.0	18.1	
f_{171}	17.56586	0.00004	64.4	6.0	−0.259	0.094	47.4	49.1	18.0	FS 3
f_{172}	2.03782	0.00006	64.1	10.8	−0.101	0.168	9.0	8.5	17.9	$f_2 + f_3$; $f_1 + f_{16}$
f_{173}	4.34135	0.00006	63.6	10.8	0.416	0.169	13.9	13.3	17.8	$f_8 + f_{12}$
f_{174}	0.60537	0.00006	63.2	10.8	0.247	0.170	6.4	7.8	17.7	
f_{175}	1.96058	0.00006	63.1	10.7	0.224	0.170	8.8	8.3	17.6	$f_3 + f_5$
f_{176}	1.82254	0.00006	62.4	10.8	−0.497	0.172	8.6	8.0	17.5	$f_6 + f_{23}$
f_{177}	4.09487	0.00006	62.4	10.8	−0.334	0.172	12.5	12.4	17.4	$f_8 + f_{14}$
f_{178}	1.80983	0.00007	60.8	10.7	−0.061	0.177	8.4	7.8	17.0	$f_3 + f_9$
f_{179}	1.86490	0.00007	60.7	10.7	−0.086	0.177	8.5	7.9	17.0	$f_3 + f_{16}$
f_{180}	1.64629	0.00007	60.7	10.7	−0.211	0.177	8.3	7.7	17.0	
f_{181}	14.41275	0.00004	60.3	6.0	−0.413	0.100	40.7	37.9	16.9	
f_{182}	4.19234	0.00007	59.6	10.7	0.099	0.180	12.3	12.1	16.7	$f_8 - f_{15}$
f_{183}	4.31159	0.00007	59.3	10.7	0.366	0.181	12.9	12.3	16.6	$f_8 - f_{16}$
f_{184}	0.48924	0.00007	58.8	10.7	−0.486	0.182	5.8	7.3	16.4	
f_{185}	4.25017	0.00007	58.4	10.7	0.034	0.184	12.3	12.0	16.3	$f_8 + f_{11}$
f_{186}	10.46011	0.00004	58.3	6.0	0.424	0.103	7.7	8.5	16.3	
f_{187}	10.01821	0.00004	58.3	6.0	0.052	0.103	7.5	8.2	16.3	
f_{188}	2.06998	0.00007	58.0	10.7	0.479	0.185	8.2	7.8	16.2	$f_7 + f_{10}$
f_{189}	1.85672	0.00007	57.9	10.7	−0.061	0.185	8.1	7.5	16.2	$f_5 + f_{17}$

Table 3.9: continued.

	f	ϵ_f	A	ϵ_A	ϕ	ϵ_ϕ		S/N		Comment
	d^{-1}	d^{-1}	ppm	ppm	2π/rad	2π/rad	1 d^{-1}	3 d^{-1}	Full	
f_{190}	10.45394	0.00004	57.8	6.0	0.201	0.104	7.7	8.5	16.2	
f_{191}	12.96381	0.00004	57.8	6.0	0.062	0.104	27.0	23.3	16.1	
f_{192}	19.37580	0.00004	57.3	6.0	−0.475	0.105	48.1	49.6	16.0	FS 4
f_{193}	12.61831	0.00004	57.2	6.0	−0.052	0.105	23.4	19.6	16.0	
f_{194}	9.96619	0.00004	56.7	6.0	−0.458	0.105	7.2	8.0	15.8	
f_{195}	0.64132	0.00007	56.5	10.7	0.490	0.190	5.7	7.0	15.8	
f_{196}	3.33477	0.00007	55.9	10.7	−0.060	0.191	9.0	9.6	15.6	
f_{197}	1.99958	0.00007	55.8	10.7	−0.286	0.192	7.8	7.4	15.6	$f_7 + f_{14}$
f_{198}	1.83497	0.00007	55.4	10.7	0.029	0.193	7.7	7.2	15.5	$f_3 + f_6$
f_{199}	10.87306	0.00004	55.1	6.0	−0.117	0.109	8.3	8.9	15.4	
f_{200}	0.45392	0.00007	54.8	10.7	0.086	0.195	5.4	6.8	15.3	
f_{201}	1.70610	0.00007	54.5	10.7	0.280	0.196	7.5	6.9	15.2	$f_{10} + f_{23}$
f_{202}	6.66697	0.00007	54.5	10.7	−0.368	0.197	19.8	16.7	15.2	$2f_8$
f_{203}	0.57938	0.00007	54.2	10.7	−0.005	0.198	5.4	6.7	15.2	
f_{204}	1.02580	0.00007	54.2	10.7	0.377	0.198	5.9	6.7	15.1	
f_{205}	1.90545	0.00007	54.1	10.7	−0.332	0.198	7.6	7.1	15.1	$f_5 + f_{10}$
f_{206}	1.08844	0.00007	53.8	10.7	0.191	0.199	6.1	6.6	15.1	
f_{207}	1.93237	0.00008	52.9	10.7	0.462	0.203	7.4	6.9	14.8	$f_5 + f_{15}$
f_{208}	2.15488	0.00008	52.8	10.7	0.083	0.203	7.6	7.2	14.8	$f_7 + f_{11}$
f_{209}	1.92456	0.00008	52.6	10.7	−0.193	0.203	7.3	6.9	14.7	$f_{11} + f_{12}$
f_{210}	2.36240	0.00008	52.6	10.7	−0.404	0.204	7.9	7.6	14.7	$f_{26} + f_{30}$
f_{211}	2.09692	0.00008	51.5	10.7	0.293	0.208	7.3	7.0	14.4	$f_7 + f_{15}$
f_{212}	0.42793	0.00008	51.4	10.7	−0.399	0.208	5.0	6.3	14.4	
f_{213}	9.37824	0.00004	51.3	6.0	−0.158	0.117	6.6	7.3	14.4	

Table 3.9: continued.

	f	ϵ_f	A	ϵ_A	ϕ	ϵ_ϕ	S/N			Comment
	d^{-1}	d^{-1}	ppm	ppm	2π/rad	2π/rad	1 d^{-1}	3 d^{-1}	Full	
f_{214}	2.66484	0.00008	51.3	10.7	0.379	0.208	8.1	8.0	14.3	
f_{215}	9.43012	0.00004	51.3	6.0	−0.494	0.117	6.5	7.3	14.3	
f_{216}	4.28342	0.00008	51.2	10.7	−0.444	0.209	10.9	10.6	14.3	$f_8 - f_{19}$
f_{217}	0.68246	0.00008	50.5	10.7	0.464	0.211	5.1	6.2	14.1	
f_{218}	4.11667	0.00008	50.0	10.7	−0.471	0.214	10.0	10.0	14.0	$f_8 + f_{17}$
f_{219}	1.58580	0.00008	49.7	10.7	−0.195	0.215	6.7	6.3	13.9	PS $\ell = 2$?
f_{220}	14.87583	0.00005	49.4	6.0	−0.397	0.121	33.9	32.9	13.8	
f_{221}	2.05497	0.00008	48.9	10.7	−0.356	0.219	6.9	6.5	13.7	$f_{15} + f_{22}$
f_{222}	0.43379	0.00008	48.8	10.7	−0.246	0.219	4.8	6.0	13.7	
f_{223}	0.62954	0.00008	48.8	10.7	0.046	0.219	4.9	6.0	13.6	
f_{224}	0.53683	0.00008	48.5	10.7	−0.175	0.220	4.9	6.0	13.6	
f_{225}	0.01391	0.00008	48.0	10.7	0.255	0.222	4.7	5.9	13.4	
f_{226}	1.88147	0.00008	47.8	10.7	−0.024	0.223	6.7	6.2	13.4	$f_{12} + f_{23}$
f_{227}	1.02881	0.00008	47.8	10.7	−0.358	0.223	5.2	5.9	13.4	
f_{228}	3.28658	0.00008	47.8	10.7	−0.038	0.224	7.7	8.1	13.4	
f_{229}	2.18633	0.00008	47.6	10.7	−0.145	0.224	6.9	6.6	13.3	$f_6 + f_7$
f_{230}	10.88242	0.00005	47.4	6.0	−0.470	0.126	7.1	7.7	13.3	
f_{231}	1.31568	0.00008	47.4	10.7	0.242	0.225	5.8	5.8	13.2	PS $\ell = 2$?
f_{232}	3.42078	0.00009	46.9	10.7	−0.491	0.227	7.7	8.2	13.1	
f_{233}	0.51082	0.00009	46.7	10.7	−0.261	0.228	4.6	5.8	13.0	
f_{234}	21.06992	0.00005	46.4	6.0	−0.372	0.129	41.5	43.3	13.0	
f_{235}	2.11852	0.00009	46.2	10.6	−0.140	0.230	6.6	6.3	12.9	$2f_1$
f_{236}	10.01384	0.00005	45.9	6.0	−0.365	0.130	5.9	6.5	12.8	
f_{237}	9.25703	0.00005	45.8	6.0	−0.318	0.131	6.0	6.7	12.8	

Table 3.9: continued.

	f	ϵ_f	A	ϵ_A	ϕ	ϵ_ϕ		S/N		Comment
	d^{-1}	d^{-1}	ppm	ppm	2π/rad	2π/rad	$1\ \mathrm{d}^{-1}$	$3\ \mathrm{d}^{-1}$	Full	
f_{238}	2.05736	0.00009	45.8	10.6	−0.071	0.233	6.5	6.1	12.8	
f_{239}	0.87703	0.00009	45.0	10.7	−0.188	0.237	4.6	5.6	12.6	
f_{240}	2.34630	0.00009	45.0	10.7	0.240	0.237	6.7	6.4	12.6	$f_2 + f_{22}$
f_{241}	4.52889	0.00009	44.9	10.7	0.252	0.237	10.5	9.9	12.6	$f_8 + f_{22}$
f_{242}	2.00985	0.00009	44.9	10.6	−0.020	0.237	6.3	6.0	12.5	$f_1 + f_{19}$
f_{243}	10.61408	0.00005	44.9	6.0	−0.114	0.133	6.2	6.8	12.5	$f_4 - f_8$
f_{244}	16.18006	0.00005	44.7	6.0	0.453	0.134	31.3	30.9	12.5	
f_{245}	1.37671	0.00009	44.5	10.7	0.015	0.239	5.6	5.5	12.5	
f_{246}	1.94632	0.00009	43.7	10.7	−0.466	0.244	6.1	5.7	12.2	$f_1 + f_3$
f_{247}	2.27410	0.00009	43.3	10.6	0.017	0.246	6.4	6.1	12.1	
f_{248}	1.71854	0.00009	43.2	10.6	−0.019	0.246	6.0	5.5	12.1	$f_3 + f_{10}$
f_{249}	0.55412	0.00009	42.8	10.7	0.169	0.249	4.3	5.3	12.0	
f_{250}	16.05491	0.00005	42.7	6.0	0.340	0.140	29.3	29.5	11.9	
f_{251}	1.32102	0.00009	42.5	10.7	0.114	0.251	5.2	5.2	11.9	
f_{252}	1.08332	0.00009	42.3	10.6	−0.021	0.251	4.8	5.2	11.8	
f_{253}	12.56088	0.00005	42.3	6.0	−0.139	0.141	16.6	14.1	11.8	
f_{254}	2.35539	0.00009	42.2	10.7	−0.155	0.252	6.3	6.1	11.8	$f_8 - f_{16}$
f_{255}	0.06173	0.00010	42.0	10.6	0.496	0.253	4.1	5.2	11.7	
f_{256}	0.53098	0.00010	41.8	10.6	0.431	0.254	4.2	5.2	11.7	
f_{257}	0.49131	0.00010	41.7	10.6	−0.186	0.256	4.1	5.1	11.6	
f_{258}	3.30970	0.00010	41.6	10.6	−0.103	0.256	6.7	7.1	11.6	
f_{259}	0.71633	0.00010	41.4	10.6	0.451	0.257	4.1	5.1	11.6	
f_{260}	2.50619	0.00010	41.3	10.6	−0.467	0.257	6.3	6.2	11.5	
f_{261}	3.38128	0.00010	41.3	10.6	0.182	0.258	6.8	7.2	11.5	

Table 3.9: continued.

	f	ϵ_f	A	ϵ_A	ϕ	ϵ_ϕ		S/N		Comment
	d^{-1}	d^{-1}	ppm	ppm	2π/rad	2π/rad	1 d^{-1}	3 d^{-1}	Full	
f_{262}	2.50168	0.00010	41.2	10.6	−0.137	0.258	6.3	6.2	11.5	$f_8 - f_{10}$
f_{263}	2.26902	0.00010	41.2	10.6	0.486	0.259	6.0	5.8	11.5	$f_5 + f_{22}$; $f_{26} + f_{37}$
f_{264}	3.22229	0.00010	41.1	10.6	0.428	0.259	6.6	6.9	11.5	
f_{265}	0.52134	0.00010	41.0	10.6	0.056	0.259	4.1	5.1	11.5	
f_{266}	2.12069	0.00010	41.0	10.6	0.183	0.260	5.9	5.6	11.5	
f_{267}	1.79117	0.00010	40.9	10.6	0.284	0.260	5.7	5.2	11.4	$f_{11} + f_{23}$
f_{268}	0.13958	0.00010	40.9	10.6	0.443	0.260	4.0	5.0	11.4	
f_{269}	12.88824	0.00005	40.8	6.0	0.342	0.146	18.7	15.9	11.4	
f_{270}	2.40044	0.00010	40.6	10.6	−0.048	0.261	6.1	5.9	11.4	$f_1 + f_{28}$
f_{271}	1.76921	0.00010	40.6	10.6	−0.474	0.262	5.6	5.2	11.3	$f_{12} - f_{14}$
f_{272}	9.96196	0.00006	40.6	6.0	0.467	0.148	5.2	5.7	11.3	
f_{273}	1.10506	0.00010	40.4	10.6	−0.145	0.263	4.6	5.0	11.3	
f_{274}	1.11757	0.00010	40.4	10.6	0.245	0.264	4.6	5.0	11.3	
f_{275}	1.66328	0.00010	40.2	10.6	0.230	0.264	5.5	5.1	11.2	$2f_{10}$
f_{276}	0.59613	0.00010	40.1	10.6	0.408	0.265	4.0	4.9	11.2	
f_{277}	4.67465	0.00010	39.9	10.6	0.400	0.267	9.7	9.1	11.1	$f_8 + f_{28}$
f_{278}	2.6325	0.0001	39.8	10.6	−0.403	0.267	6.2	6.1	11.1	
f_{279}	9.76823	0.00006	39.6	6.0	0.440	0.151	5.0	5.5	11.1	
f_{280}	9.84033	0.00006	39.4	6.0	−0.343	0.152	5.0	5.5	11.0	
f_{281}	1.8144	0.0001	39.3	10.6	0.066	0.270	5.4	5.0	11.0	$f_5 + f_{24}$
f_{282}	2.4470	0.0001	39.3	10.6	0.430	0.271	5.9	5.8	11.0	
f_{283}	9.75396	0.00006	39.2	6.0	−0.346	0.153	4.9	5.5	11.0	
f_{284}	9.99194	0.00006	39.2	6.0	0.095	0.153	5.0	5.5	11.0	
f_{285}	4.3729	0.0001	39.0	10.6	−0.377	0.272	8.6	8.2	10.9	$f_8 + f_{25}$

Table 3.9: continued.

	f d^{-1}	ϵ_f d^{-1}	A ppm	ϵ_A ppm	ϕ 2π/rad	ϵ_ϕ 2π/rad	S/N 1 d^{-1}	S/N 3 d^{-1}	S/N Full	Comment
f_{286}	10.40783	0.00006	39.0	6.0	−0.177	0.153	5.1	5.7	10.9	
f_{287}	10.72778	0.00006	38.9	6.0	0.276	0.154	5.6	6.0	10.9	
f_{288}	1.6572	0.0001	38.8	10.6	−0.419	0.273	5.4	4.9	10.9	$f_{11} + f_{24}$
f_{289}	11.36186	0.00006	38.6	6.0	−0.205	0.155	7.3	7.4	10.8	
f_{290}	1.8263	0.0001	38.4	10.6	−0.318	0.276	5.3	5.0	10.7	
f_{291}	11.55488	0.00006	38.4	6.0	0.332	0.156	8.0	7.9	10.7	
f_{292}	10.14600	0.00006	38.3	6.0	0.006	0.157	4.9	5.4	10.7	
f_{293}	9.20496	0.00006	38.0	6.0	0.178	0.158	5.0	5.6	10.6	
f_{294}	1.2200	0.0001	38.0	10.6	0.420	0.280	4.5	4.7	10.6	
f_{295}	1.1666	0.0001	38.0	10.6	0.228	0.279	4.4	4.7	10.6	
f_{296}	9.66821	0.00006	37.9	6.0	0.094	0.158	4.7	5.3	10.6	
f_{297}	1.2312	0.0001	37.9	10.6	−0.241	0.279	4.5	4.7	10.6	
f_{298}	13.39179	0.00006	37.8	6.0	−0.216	0.158	20.9	18.7	10.6	
f_{299}	3.4590	0.0001	37.8	10.6	0.322	0.281	6.3	6.7	10.6	
f_{300}	10.35998	0.00006	37.7	6.0	0.215	0.158	5.0	5.5	10.6	
f_{301}	2.4809	0.0001	37.6	10.6	−0.341	0.282	5.7	5.6	10.5	
f_{302}	1.4009	0.0001	37.3	10.6	0.205	0.284	4.7	4.6	10.4	
f_{303}	1.6184	0.0001	36.9	10.6	−0.002	0.288	5.0	4.7	10.3	
f_{304}	2.1587	0.0001	36.7	10.6	0.471	0.289	5.3	5.0	10.3	$f_2 + f_{12}$
f_{305}	1.8207	0.0001	36.7	10.6	0.318	0.289	5.1	4.7	10.3	$f_1 + f_{14}$
f_{306}	9.50839	0.00006	36.6	6.0	0.430	0.164	4.6	5.1	10.2	
f_{307}	2.3016	0.0001	36.5	10.6	−0.203	0.290	5.4	5.2	10.2	$2f_2$
f_{308}	2.2244	0.0001	36.5	10.6	−0.005	0.291	5.3	5.1	10.2	$f_2 + f_5$
f_{309}	18.51928	0.00006	36.3	6.0	−0.463	0.165	30.4	28.9	10.2	

Table 3.9: continued.

	f	ϵ_f	A	ϵ_A	ϕ	ϵ_ϕ	S/N			Comment
	d^{-1}	d^{-1}	ppm	ppm	2π/rad	2π/rad	$1\ \mathrm{d}^{-1}$	$3\ \mathrm{d}^{-1}$	Full	
f_{310}	17.30397	0.00006	36.1	6.0	−0.454	0.165	24.6	27.1	10.1	
f_{311}	2.5503	0.0001	36.1	10.6	−0.358	0.293	5.6	5.5	10.1	$f_8 - f_{17}$
f_{312}	10.20335	0.00006	36.1	6.0	0.004	0.166	4.7	5.1	10.1	
f_{313}	1.3314	0.0001	35.9	10.6	0.348	0.295	4.4	4.4	10.0	
f_{314}	4.2077	0.0001	35.9	10.6	0.402	0.295	7.4	7.3	10.0	$f_8 - f_{23}$
f_{315}	1.1078	0.0001	35.8	10.6	−0.067	0.296	4.1	4.4	10.0	
f_{316}	10.62709	0.00006	35.7	6.0	0.321	0.168	4.9	5.4	10.0	
f_{317}	1.8008	0.0001	35.5	10.6	−0.372	0.298	4.9	4.6	9.9	$f_{14} + f_{25}$
f_{318}	12.79675	0.00006	35.5	6.0	−0.151	0.169	15.7	13.2	9.9	
f_{319}	2.0738	0.0001	35.1	10.6	0.479	0.302	5.0	4.7	9.8	$f_2 + f_9$
f_{320}	1.5487	0.0001	35.0	10.6	0.209	0.303	4.6	4.4	9.8	
f_{321}	3.1476	0.0001	34.9	10.6	−0.039	0.303	5.6	5.8	9.8	
f_{322}	1.9559	0.0001	34.7	10.6	−0.387	0.305	4.8	4.6	9.7	$2f_{16}$
f_{323}	2.1024	0.0001	34.7	10.6	0.480	0.305	4.9	4.7	9.7	$f_{14} + f_{28}$
f_{324}	2.4337	0.0001	34.7	10.6	0.293	0.306	5.3	5.1	9.7	$f_7 + f_{22}$
f_{325}	9.45663	0.00006	34.6	6.0	0.393	0.172	4.4	4.9	9.7	
f_{326}	14.01277	0.00006	34.6	6.0	0.228	0.173	21.9	20.4	9.7	
f_{327}	2.3117	0.0001	34.3	10.6	0.085	0.309	5.1	4.9	9.6	$f_5 + f_7$
f_{328}	9.64858	0.00007	34.2	6.0	0.178	0.175	4.3	4.8	9.6	
f_{329}	15.39018	0.00007	33.8	6.0	0.059	0.177	22.6	23.4	9.5	
f_{330}	2.4746	0.0001	33.8	10.6	−0.004	0.313	5.1	5.0	9.5	$f_8 - f_{15}$
f_{331}	10.20426	0.00007	33.8	6.0	−0.400	0.176	4.4	4.8	9.5	
f_{332}	14.38098	0.00007	33.8	6.0	−0.469	0.177	22.7	21.1	9.4	
f_{333}	1.7113	0.0001	33.8	10.6	−0.429	0.314	4.7	4.3	9.4	$f_{14} + f_{19}$

Table 3.9: continued.

	f	ϵ_f	A	ϵ_A	ϕ	ϵ_ϕ		S/N		Comment
	d^{-1}	d^{-1}	ppm	ppm	2π/rad	2π/rad	1 d^{-1}	3 d^{-1}	Full	
f_{334}	2.4918	0.0001	33.8	10.6	−0.499	0.314	5.2	5.0	9.4	$f_2 + f_{28}$
f_{335}	2.1053	0.0001	33.7	10.6	0.159	0.315	4.8	4.6	9.4	
f_{336}	3.3177	0.0001	33.6	10.6	0.393	0.315	5.4	5.8	9.4	
f_{337}	2.3256	0.0001	33.6	10.6	−0.353	0.315	5.0	4.8	9.4	$f_8 - f_{12}$
f_{338}	1.7751	0.0001	33.6	10.6	−0.023	0.316	4.7	4.3	9.4	$f_{11} + f_{15}$
f_{339}	14.23463	0.00007	33.5	6.0	0.338	0.178	21.8	20.4	9.4	
f_{340}	15.89620	0.00007	33.3	6.0	−0.392	0.180	23.0	23.0	9.3	
f_{341}	9.94001	0.00007	33.2	6.0	0.428	0.181	4.2	4.7	9.3	
f_{342}	4.5729	0.0001	33.1	10.6	0.345	0.319	7.9	7.4	9.3	
f_{343}	3.4302	0.0001	32.9	10.6	0.210	0.322	5.4	5.8	9.2	
f_{344}	3.0143	0.0001	32.8	10.6	−0.215	0.323	5.2	5.3	9.2	
f_{345}	1.8396	0.0001	32.8	10.6	0.019	0.323	4.5	4.2	9.2	$f_9 + f_{11}$
f_{346}	1.7818	0.0001	32.7	10.6	0.011	0.324	4.5	4.2	9.1	$f_9 + f_{15}$
f_{347}	2.2033	0.0001	32.6	10.6	0.080	0.325	4.7	4.5	9.1	$f_{12} + f_{22}$
f_{348}	9.70058	0.00007	32.3	6.0	−0.216	0.185	4.0	4.5	9.0	
f_{349}	10.15667	0.00007	32.1	6.0	0.428	0.186	4.1	4.6	9.0	
f_{350}	16.90244	0.00007	32.0	6.0	−0.084	0.187	22.1	23.5	9.0	
f_{351}	2.5723	0.0001	31.5	10.6	0.366	0.335	4.9	4.8	8.8	$f_8 - f_{14}$
f_{352}	2.1288	0.0001	31.5	10.6	0.498	0.336	4.5	4.3	8.8	$f_2 + f_{16}$
f_{353}	9.41419	0.00007	31.4	6.0	0.103	0.190	4.0	4.5	8.8	
f_{354}	1.7483	0.0001	31.1	10.6	0.049	0.340	4.3	4.0	8.7	$2f_{23}$
f_{355}	3.1771	0.0001	31.0	10.6	−0.144	0.341	4.9	5.1	8.7	
f_{356}	3.6999	0.0001	30.9	10.6	−0.198	0.342	5.4	5.8	8.6	
f_{357}	1.9572	0.0001	30.8	10.6	0.246	0.344	4.3	4.1	8.6	$f_1 + f_{39}$

Table 3.9: continued.

	f	ϵ_f	A	ϵ_A	ϕ	ϵ_ϕ		S/N		Comment
	d^{-1}	d^{-1}	ppm	ppm	2π/rad	2π/rad	1 d^{-1}	3 d^{-1}	Full	
f_{358}	4.1401	0.0001	30.5	10.6	0.153	0.346	6.2	6.1	8.5	$f_8 + f_{38}$
f_{359}	2.3852	0.0001	30.5	10.6	0.492	0.347	4.6	4.4	8.5	
f_{360}	11.18933	0.00007	30.4	6.0	0.418	0.197	5.3	5.5	8.5	
f_{361}	1.7500	0.0001	30.4	10.6	−0.052	0.348	4.2	3.9	8.5	
f_{362}	1.9877	0.0001	30.3	10.6	−0.351	0.349	4.2	4.0	8.5	$f_6 + f_{25}$
f_{363}	4.6289	0.0001	30.2	10.6	−0.081	0.350	7.3	6.8	8.5	
f_{364}	2.4168	0.0001	30.1	10.6	0.154	0.351	4.5	4.4	8.4	$2f_{36}$; $f_8 - f_{11}$
f_{365}	1.9307	0.0001	29.9	10.6	0.308	0.353	4.2	3.9	8.4	$f_9 + f_{12}$
f_{366}	4.0738	0.0001	29.6	10.6	0.430	0.357	5.9	5.9	8.3	$f_8 + f_{24}$
f_{367}	3.3084	0.0001	29.5	10.6	0.077	0.359	4.8	5.0	8.2	
f_{368}	2.3192	0.0001	29.4	10.6	−0.061	0.359	4.4	4.2	8.2	$f_{16} + f_{28}$; $f_{26} + f_{36}$
f_{369}	1.6483	0.0001	29.4	10.6	0.054	0.360	4.0	3.7	8.2	$f_3 + f_{14}$
f_{370}	3.5509	0.0001	29.4	10.6	0.319	0.360	5.0	5.3	8.2	
f_{371}	10.67501	0.00008	29.3	6.0	0.067	0.204	4.1	4.5	8.2	
f_{372}	3.2266	0.0001	29.2	10.6	0.254	0.361	4.7	4.9	8.2	$3f_{38}$
f_{373}	1.9787	0.0001	29.1	10.6	0.230	0.363	4.1	3.8	8.1	$f_7 + f_{24}$
f_{374}	15.00698	0.00008	28.9	6.0	−0.230	0.208	20.1	19.5	8.1	$f_1 + f_4$
f_{375}	3.6053	0.0001	28.7	10.6	−0.473	0.368	5.0	5.3	8.0	
f_{376}	13.06067	0.00008	28.5	6.0	−0.479	0.210	14.0	12.0	8.0	
f_{377}	8.6411	0.0001	28.2	10.6	−0.487	0.374	4.4	4.7	7.9	
f_{378}	3.1292	0.0001	28.2	10.6	0.440	0.374	4.5	4.6	7.9	
f_{379}	8.4938	0.0001	28.2	10.6	0.198	0.375	4.8	4.9	7.9	
f_{380}	11.18669	0.00008	28.1	6.0	0.446	0.213	4.8	5.0	7.9	
f_{381}	3.2665	0.0001	27.8	10.6	0.098	0.380	4.5	4.7	7.8	

Table 3.9: continued.

	f	ϵ_f	A	ϵ_A	ϕ	ϵ_ϕ		S/N		Comment
	d^{-1}	d^{-1}	ppm	ppm	2π/rad	2π/rad	1 d^{-1}	3 d^{-1}	Full	
f_{382}	12.87401	0.00008	27.7	6.0	−0.467	0.216	12.7	10.7	7.7	$f_4 - f_5$
f_{383}	15.26414	0.00008	27.6	6.0	0.298	0.217	18.5	18.9	7.7	
f_{384}	2.4357	0.0001	27.6	10.6	−0.352	0.383	4.2	4.1	7.7	$f_8 - f_{39}$
f_{385}	3.2031	0.0001	27.1	10.6	0.118	0.389	4.3	4.5	7.6	
f_{386}	15.61814	0.00008	26.9	6.0	0.487	0.223	17.8	18.6	7.5	
f_{387}	12.70941	0.00008	26.7	6.0	−0.215	0.225	11.4	9.5	7.5	$f_4 - f_7$
f_{388}	2.6734	0.0001	26.4	10.6	−0.048	0.399	4.2	4.1	7.4	$\sim 41 f_{\mathrm{orb}}$
f_{389}	4.3159	0.0001	26.4	10.6	0.253	0.400	5.7	5.5	7.4	$f_8 + f_{35}$
f_{390}	3.1378	0.0001	26.4	10.6	0.067	0.400	4.2	4.4	7.4	
f_{391}	15.74857	0.00009	26.4	6.0	0.078	0.227	17.5	18.4	7.4	
f_{392}	3.0832	0.0002	26.4	10.6	−0.085	0.400	4.2	4.3	7.4	
f_{393}	2.6082	0.0002	26.4	10.6	−0.140	0.401	4.1	4.0	7.4	
f_{394}	3.0671	0.0002	26.2	10.6	−0.100	0.404	4.2	4.3	7.3	
f_{395}	3.1869	0.0002	26.1	10.6	−0.255	0.404	4.2	4.3	7.3	
f_{396}	20.83211	0.00009	26.0	6.0	0.298	0.231	22.8	23.9	7.3	
f_{397}	3.0789	0.0002	25.8	10.6	0.361	0.410	4.1	4.2	7.2	
f_{398}	3.3580	0.0002	25.7	10.6	0.130	0.411	4.2	4.4	7.2	
f_{399}	15.89268	0.00009	25.5	6.0	−0.141	0.234	17.6	17.6	7.1	
f_{400}	13.88239	0.00009	25.5	6.0	−0.383	0.235	15.9	14.6	7.1	
f_{401}	3.6216	0.0002	25.4	10.6	0.434	0.416	4.4	4.7	7.1	
f_{402}	12.99941	0.00009	25.2	6.0	−0.231	0.238	12.0	10.3	7.0	$f_4 - f_6$
f_{403}	15.09838	0.00009	25.1	6.0	0.327	0.240	17.4	16.9	7.0	$f_2 + f_4$
f_{404}	11.28554	0.00009	25.0	6.0	−0.274	0.239	4.5	4.6	7.0	
f_{405}	3.3988	0.0002	24.8	10.6	−0.416	0.426	4.1	4.3	6.9	

Table 3.9: continued.

	f	ϵ_f	A	ϵ_A	ϕ	ϵ_ϕ	S/N			Comment
	d^{-1}	d^{-1}	ppm	ppm	2π/rad	2π/rad	1 d^{-1}	3 d^{-1}	Full	
f_{406}	15.51415	0.00009	24.7	6.0	−0.281	0.243	16.4	17.2	6.9	
f_{407}	11.13741	0.00009	24.7	6.0	−0.114	0.243	4.1	4.3	6.9	
f_{408}	8.4419	0.0002	23.8	10.6	−0.416	0.444	4.1	4.2	6.6	
f_{409}	11.44662	0.00009	23.7	6.0	0.340	0.253	4.7	4.6	6.6	
f_{410}	13.11575	0.00010	23.6	6.0	0.179	0.254	11.9	10.3	6.6	$f_4 - f_{10}$
f_{411}	13.02469	0.00010	23.6	6.0	0.086	0.254	11.4	9.8	6.6	$f_4 - f_9$
f_{412}	4.2779	0.0002	23.5	10.6	−0.089	0.449	5.0	4.8	6.6	
f_{413}	4.7785	0.0002	23.5	10.6	−0.131	0.450	5.8	5.5	6.6	
f_{414}	12.93973	0.00010	23.3	6.0	0.082	0.257	10.8	9.3	6.5	$f_4 - f_{12}$
f_{415}	8.3129	0.0002	23.3	10.6	−0.280	0.454	4.3	4.3	6.5	
f_{416}	11.24917	0.00010	23.1	6.0	−0.269	0.260	4.1	4.2	6.4	
f_{417}	14.83452	0.00010	23.1	6.0	−0.380	0.260	16.0	15.3	6.4	$f_3 + f_4$
f_{418}	11.62548	0.00010	23.0	6.0	−0.397	0.261	5.0	4.8	6.4	
f_{419}	16.76466	0.00010	22.9	6.0	0.280	0.261	17.0	16.6	6.4	
f_{420}	15.02118	0.00010	22.7	6.0	−0.435	0.264	15.8	15.3	6.3	$f_4 + f_5$
f_{421}	13.18621	0.00010	22.7	6.0	−0.130	0.264	11.7	10.2	6.3	$f_4 - f_{14}$
f_{422}	12.34206	0.00010	22.7	6.0	−0.227	0.264	8.0	6.7	6.3	
f_{423}	21.11610	0.00010	22.6	6.0	−0.107	0.265	20.1	21.1	6.3	
f_{424}	4.0138	0.0002	22.5	10.6	−0.336	0.468	4.4	4.4	6.3	
f_{425}	14.5854	0.0001	22.3	6.0	−0.191	0.269	15.4	14.4	6.2	
f_{426}	18.4122	0.0001	22.2	6.0	0.328	0.269	18.9	17.6	6.2	
f_{427}	3.8506	0.0002	22.2	10.6	0.095	0.475	4.1	4.3	6.2	
f_{428}	13.3975	0.0001	22.2	6.0	−0.146	0.269	12.3	11.1	6.2	
f_{429}	13.0309	0.0001	22.2	6.0	−0.482	0.270	10.8	9.2	6.2	$f_4 - f_{11}$

Table 3.9: continued.

	f	ϵ_f	A	ϵ_A	ϕ	ϵ_ϕ		S/N		Comment
	d^{-1}	d^{-1}	ppm	ppm	2π/rad	2π/rad	$1\ \mathrm{d}^{-1}$	$3\ \mathrm{d}^{-1}$	Full	
f_{430}	4.9878	0.0002	22.1	10.6	0.262	0.477	5.7	5.6	6.2	
f_{431}	4.3095	0.0002	22.1	10.6	−0.013	0.478	4.8	4.6	6.2	
f_{432}	3.9278	0.0002	21.8	10.6	0.005	0.484	4.1	4.2	6.1	
f_{433}	14.7795	0.0001	21.7	6.0	−0.063	0.276	15.0	14.2	6.1	$f_4 + f_{10}$
f_{434}	13.0887	0.0001	21.5	6.0	0.456	0.279	10.6	9.2	6.0	$f_4 - f_{15}$
f_{435}	13.1291	0.0001	20.8	6.0	−0.061	0.288	10.5	9.1	5.8	
f_{436}	16.6999	0.0001	20.6	6.0	−0.244	0.291	15.0	14.7	5.7	
f_{437}	14.8596	0.0001	20.0	6.0	0.045	0.299	13.8	13.3	5.6	
f_{438}	14.8958	0.0001	19.8	6.0	0.372	0.303	13.7	13.2	5.5	$f_4 + f_6$
f_{439}	18.3432	0.0001	19.8	6.0	−0.470	0.303	16.8	15.5	5.5	
f_{440}	11.9959	0.0001	19.8	6.0	−0.409	0.303	5.4	4.9	5.5	
f_{441}	14.3990	0.0001	19.7	6.0	0.272	0.304	13.2	12.3	5.5	
f_{442}	12.9695	0.0001	19.6	6.0	0.115	0.305	9.2	7.9	5.5	$f_4 - f_{16}$
f_{443}	13.1644	0.0001	19.6	6.0	−0.024	0.306	10.1	8.7	5.5	$f_4 - f_{17}$
f_{444}	15.1857	0.0001	19.1	6.0	0.365	0.312	13.1	13.0	5.4	$f_4 + f_7$
f_{445}	17.2811	0.0001	19.0	6.0	0.227	0.315	12.9	14.2	5.3	$f_4 + f_8$
f_{446}	18.3406	0.0001	19.0	6.0	−0.490	0.315	16.2	14.9	5.3	
f_{447}	14.5997	0.0001	18.9	6.0	0.175	0.316	13.0	12.2	5.3	
f_{448}	11.8614	0.0001	18.9	6.0	0.351	0.318	4.7	4.4	5.3	
f_{449}	12.3874	0.0001	18.8	6.0	−0.053	0.319	6.8	5.8	5.3	
f_{450}	15.8389	0.0001	18.8	6.0	−0.224	0.318	12.7	13.0	5.3	
f_{451}	11.7135	0.0001	18.2	6.0	0.298	0.330	4.1	4.0	5.1	
f_{452}	11.8369	0.0001	18.2	6.0	0.161	0.330	4.5	4.2	5.1	
f_{453}	14.8064	0.0001	18.1	6.0	−0.275	0.332	12.5	11.9	5.0	$f_4 + f_{15}$

Table 3.9: continued.

	f	ϵ_f	A	ϵ_A	ϕ	ϵ_ϕ	S/N			Comment
	d^{-1}	d^{-1}	ppm	ppm	2π/rad	2π/rad	1 d^{-1}	3 d^{-1}	Full	
f_{454}	14.7090	0.0001	18.0	6.0	0.278	0.332	12.5	11.8	5.0	$f_4 + f_{14}$
f_{455}	14.8642	0.0001	18.0	6.0	−0.308	0.332	12.4	12.0	5.0	$f_4 + f_{11}$
f_{456}	14.9555	0.0001	17.9	6.0	0.056	0.335	12.5	12.0	5.0	$f_4 + f_{12}$
f_{457}	12.9976	0.0001	17.6	6.0	−0.013	0.342	8.4	7.2	4.9	$f_4 + f_{19}$
f_{458}	16.6948	0.0001	17.2	6.0	0.423	0.348	12.6	12.3	4.8	
f_{459}	12.0614	0.0001	17.2	6.0	−0.298	0.348	4.9	4.4	4.8	
f_{460}	14.9256	0.0001	17.2	6.0	0.039	0.349	12.0	11.5	4.8	$f_4 + f_{16}$
f_{461}	16.1643	0.0001	16.9	6.0	−0.213	0.355	11.8	11.6	4.7	
f_{462}	12.8253	0.0001	16.5	6.0	0.182	0.364	7.4	6.2	4.6	
f_{463}	12.9558	0.0001	16.4	6.0	−0.220	0.366	7.7	6.6	4.6	
f_{464}	17.0363	0.0001	16.2	6.0	−0.378	0.371	11.0	11.8	4.5	
f_{465}	15.4997	0.0001	16.1	6.0	−0.234	0.373	10.6	11.2	4.5	
f_{466}	12.7522	0.0001	16.0	6.0	0.263	0.374	7.0	5.9	4.5	$f_4 - f_{22}$
f_{467}	23.1808	0.0001	16.0	6.0	−0.100	0.373	16.1	16.2	4.5	
f_{468}	15.6513	0.0001	15.9	6.0	0.308	0.378	10.4	11.0	4.4	
f_{469}	12.5645	0.0001	15.8	6.0	0.317	0.380	6.2	5.3	4.4	
f_{470}	14.8464	0.0001	15.7	6.0	−0.345	0.382	10.9	10.4	4.4	
f_{471}	19.3378	0.0001	15.7	6.0	0.122	0.382	13.2	13.6	4.4	
f_{472}	16.1943	0.0001	15.6	6.0	0.156	0.384	11.3	10.8	4.4	
f_{473}	20.9491	0.0001	15.6	6.0	−0.483	0.384	13.8	14.4	4.4	
f_{474}	12.1746	0.0001	15.4	6.0	0.478	0.391	4.8	4.2	4.3	
f_{475}	19.7423	0.0001	15.2	6.0	0.145	0.392	13.3	13.0	4.3	
f_{476}	12.5178	0.0001	15.1	6.0	−0.421	0.399	5.8	4.9	4.2	
f_{477}	13.3910	0.0002	14.8	6.0	0.221	0.406	8.2	7.3	4.1	

Table 3.9: continued.

	f d^{-1}	ϵ_f d^{-1}	A ppm	ϵ_A ppm	ϕ 2π/rad	ϵ_ϕ 2π/rad	S/N 1 d^{-1}	3 d^{-1}	Full	Comment
f_{478}	12.4885	0.0002	14.8	6.0	−0.148	0.407	5.6	4.8	4.1	
f_{479}	12.2083	0.0002	14.7	6.0	−0.313	0.409	4.7	4.1	4.1	
f_{480}	17.0459	0.0002	14.4	6.0	0.299	0.417	9.9	10.5	4.0	
f_{481}	21.0439	0.0002	14.3	6.0	0.238	0.421	12.7	13.3	4.0	
f_{482}	14.7307	0.0002	14.2	6.0	0.184	0.422	9.8	9.3	4.0	$f_4 + f_{17}$
f_{483}	21.1916	0.0002	14.2	6.0	0.276	0.422	12.7	13.3	4.0	
f_{484}	13.2617	0.0002	14.1	6.0	0.219	0.425	7.4	6.6	4.0	
f_{485}	22.9637	0.0002	13.7	6.0	0.239	0.439	13.5	13.9	3.8	
f_{486}	14.8705	0.0002	13.7	6.0	0.039	0.439	9.4	9.1	3.8	$f_4 + f_9$
f_{487}	19.8570	0.0002	13.5	6.0	0.095	0.445	11.8	11.6	3.8	
f_{488}	16.3605	0.0002	13.4	6.0	−0.010	0.447	9.9	9.4	3.8	
f_{489}	14.8975	0.0002	13.4	6.0	0.202	0.448	9.3	8.9	3.7	$f_4 + f_{19}$
f_{490}	15.6815	0.0002	12.9	6.0	0.050	0.467	8.4	8.9	3.6	
f_{491}	13.3899	0.0002	12.4	6.0	−0.218	0.483	6.9	6.2	3.5	
f_{492}	15.9821	0.0002	12.2	6.0	0.144	0.493	8.5	8.4	3.4	
f_{493}	17.5836	0.0002	12.2	6.0	−0.233	0.493	9.0	9.3	3.4	
f_{494}	12.8220	0.0002	12.2	6.0	−0.125	0.495	5.4	4.6	3.4	
f_{495}	14.0685	0.0002	12.1	6.0	−0.291	0.496	7.8	7.2	3.4	
f_{496}	14.2715	0.0002	12.1	6.0	−0.236	0.496	8.0	7.4	3.4	
f_{497}	19.4592	0.0002	12.0	6.0	−0.391	0.498	10.2	10.4	3.4	
f_{498}	13.0735	0.0002	12.0	6.0	−0.014	0.501	5.9	5.1	3.4	$f_4 - f_{23}$
f_{499}	14.8217	0.0002	12.0	6.0	0.124	0.501	8.3	7.9	3.3	$f_4 + f_{23}$
f_{500}	12.6949	0.0002	11.9	6.0	0.049	0.506	5.1	4.2	3.3	
f_{501}	14.0780	0.0002	11.9	6.0	0.351	0.506	7.6	7.1	3.3	

Table 3.9: continued.

	f	ϵ_f	A	ϵ_A	ϕ	ϵ_ϕ	S/N			Comment
	d^{-1}	d^{-1}	ppm	ppm	2π/rad	2π/rad	1 d^{-1}	3 d^{-1}	Full	
f_{502}	12.3954	0.0002	11.7	6.0	−0.327	0.514	4.3	3.6	3.3	
f_{503}	20.8294	0.0002	11.5	6.0	−0.347	0.523	10.1	10.6	3.2	
f_{504}	19.5909	0.0002	11.4	6.0	−0.417	0.525	9.9	9.8	3.2	
f_{505}	16.1093	0.0002	11.4	6.0	0.227	0.528	8.0	7.8	3.2	
f_{506}	16.5448	0.0002	11.0	6.0	−0.091	0.548	8.0	7.7	3.1	
f_{507}	15.8904	0.0002	10.8	6.0	0.420	0.556	7.5	7.5	3.0	
f_{508}	15.6360	0.0002	10.8	6.0	−0.180	0.557	7.1	7.5	3.0	
f_{509}	15.1430	0.0002	10.6	6.0	−0.155	0.568	7.3	7.2	3.0	$f_4 + f_{22}$
f_{510}	20.8348	0.0002	10.5	6.0	0.460	0.574	9.2	9.6	2.9	
f_{511}	14.9870	0.0002	10.4	6.0	0.178	0.578	7.3	7.0	2.9	$f_4 + f_{25}$
f_{512}	17.2399	0.0002	10.2	6.0	0.377	0.590	6.9	7.6	2.8	
f_{513}	13.8172	0.0002	10.2	6.0	−0.350	0.593	6.3	5.8	2.8	
f_{514}	15.3975	0.0002	10.1	6.0	0.244	0.595	6.8	7.0	2.8	
f_{515}	20.9933	0.0002	9.8	6.0	0.209	0.612	8.7	9.1	2.8	
f_{516}	16.0626	0.0002	9.7	6.0	−0.357	0.619	6.7	6.7	2.7	
f_{517}	16.6232	0.0002	9.7	6.0	−0.090	0.618	7.1	6.9	2.7	
f_{518}	20.9057	0.0002	9.6	6.0	−0.199	0.626	8.5	8.8	2.7	
f_{519}	23.2154	0.0002	9.5	6.0	−0.176	0.631	9.6	9.7	2.7	
f_{520}	18.5167	0.0002	9.3	6.0	−0.421	0.648	7.8	7.4	2.6	
f_{521}	19.3485	0.0002	9.2	6.0	0.167	0.652	7.8	8.0	2.6	
f_{522}	17.3062	0.0003	7.8	6.0	0.136	0.763	5.3	5.9	2.2	

Chapter 4

Asteroseismic modelling of KIC 10080943A and KIC 10080943B

This chapter was originally published as

Asteroseismic modelling of the two F-type hybrid pulsators KIC 10080943A and KIC 10080943B

V. S. Schmid & C. Aerts

Astronomy & Astrophysics, vol. 592, A116, 15 pages (2016)

Abstract

Context. Pulsating binary stars are ideal targets for testing the theory of stellar structure and evolution. Fundamental parameters can be derived to high precision from binary modelling and provide crucial constraints for seismic modelling. High-order gravity modes are sensitive to the conditions near the convective core and therefore allow for a determination of parameters describing interior physics, especially the convective-core overshooting parameter. KIC 10080943 is a binary system that contains two gravity and pressure hybrid pulsators. A detailed observational study has provided fundamental and seismic parameters for both components.

Aims. We aim to find a model that is able to predict the observed g-mode period spacings and stellar parameters of both components of KIC 10080943.
Methods. By calculating model grids with the stellar evolution code MESA and the seismic code GYRE, we can compare theoretical properties to the observed mean period spacing and position in the Hertzsprung-Russell diagram.
Results. The masses of our best models are somewhat below the values estimated from binarity, which is a consequence of the low observed mean g-mode period spacing. We find that the amount of core overshooting and diffusive mixing can be well constrained by the equal-age requirement for the two stars, however, we find no significant difference for different shapes of the core overshooting. The measured rotation rates are within the limit of validity for the first-order perturbation approximation. We can find a good fit by using the traditional approximation for the pulsations, when taking slightly younger models with a higher asymptotic period spacing. This is because the zonal modes experience a slight shift due to the Coriolis force, which the first-order perturbation approximation ignores.

4.1 Introduction

Stellar models play an important role in aiding astrophysical research in a wide variety of contexts, despite several shortcomings and uncertainties in the input physics. Fortunately, we can test and improve these models by comparing observed stellar pulsations, that is the asteroseismic fingerprints of the stellar interior, to theoretical predictions. It is imperative to choose the test cases wisely by the amount of observational constraints they hold. As such, gravity (g) and pressure (p) mode hybrid pulsators have a high potential for testing theories of stellar structure and evolution.

The periods of high-order g modes of a non-rotating, unevolved star with a convective core and a radiative envelope are predicted to be equally spaced (Tassoul 1980). Yet, deviations from this equidistant spacing are expected as the star evolves or rotates (Miglio et al. 2008; Bouabid et al. 2013). The extent of the convective core and chemical composition gradients at the boundary of that core influence the mean value and structure of the period spacing, while rotation introduces a tilt in the period spacing pattern. This is of particular interest for stars of intermediate mass ($1.5 \leq M\ (M_\odot) \leq 2.2$) that inhabit the transition region, where a radiative central region gives way to a convective core and the convective envelope becomes increasingly thinner. For these types of stars the g modes are thought to be excited by the convective flux blocking mechanism (Guzik et al. 2000; Dupret et al. 2005). The heat-driven p modes of hybrid pulsators can then provide an additional selection criterion based on the predictions of mode excitation. Very recently, there have been several studies exploiting the seismic potential of g-mode pulsators with carefully identified modes from four years of *Kepler* (Borucki et al. 2010) data (e.g. Kurtz et al. 2014; Moravveji et al. 2015; Pápics et al. 2015; Saio et al. 2015; Van Reeth et al. 2015a,b).

The main caveat of these studies is that they only concern single stars. Their derived fundamental parameters and ages are therefore still dependent on the accuracy of stellar models on which the seismic properties are based. An additional and independent test can be provided by pulsating binary stars, whose measurements of fundamental parameters rely only on Kepler's laws and geometry. Double-lined spectroscopic binaries, where radial velocities of both components are measured, yield a mass ratio, while eclipsing binaries allow for the determination of absolute masses and radii. Such systems are rare and require a dedicated, detailed study to recover the seismic properties of the pulsating star and precise stellar parameters. There have only been a handful of published analyses so far (e.g. Maceroni et al. 2009, 2014; Welsh et al. 2011; Hambleton et al. 2013).

In this chapter we present the seismic modelling of two hybrid pulsators; KIC 10080943A and KIC 10080943B. They reside in a double-lined spectroscopic binary system and have very similar seismic properties and stellar parameters, which are described in Sect. 4.2 and whose analysis has been published by Schmid et al. (2015). We use the one-dimensional (1D) stellar evolution code MESA (Paxton et al. 2011, 2013, 2015) and the stellar pulsation code GYRE (Townsend & Teitler 2013) to find the best representation of both stars, assuming two coeval single stars and neglecting their tidal influence. The modelling process is explained in detail in Sect. 4.3. Finally, we present a discussion of our results in Sect. 4.4.

4.2 Observational constraints on KIC 10080943

KIC 10080943 is an eccentric, double-lined binary system, containing two γ Dor/δ Sct hybrid pulsators (Fig. 1.5). Keen et al. (2015) published the analysis of the period spacings of the g modes from *Kepler* photometry. In Chapter 3 we have performed a detailed analysis of the system; we derived fundamental parameters of both components from modelling the binary signals of ellipsoidal variation and reflection in the *Kepler* light curve in addition to the radial velocity curves and disentangled component spectra from high-resolution follow-up spectroscopy covering the orbit. We were able to assign most period spacing series and high-amplitude p modes to either the primary or the secondary. This was achieved by analysing the phase modulations of the p modes that arise from the binary motion. Modes of the primary have a time delay of 36.2 ± 4.8 s, while those of the secondary are delayed by 44.0 ± 3.5 s. Combination frequencies between the p modes and two period spacing series, which form a series of rotationally split doublets, helped to determine that these belong to the secondary. Three other

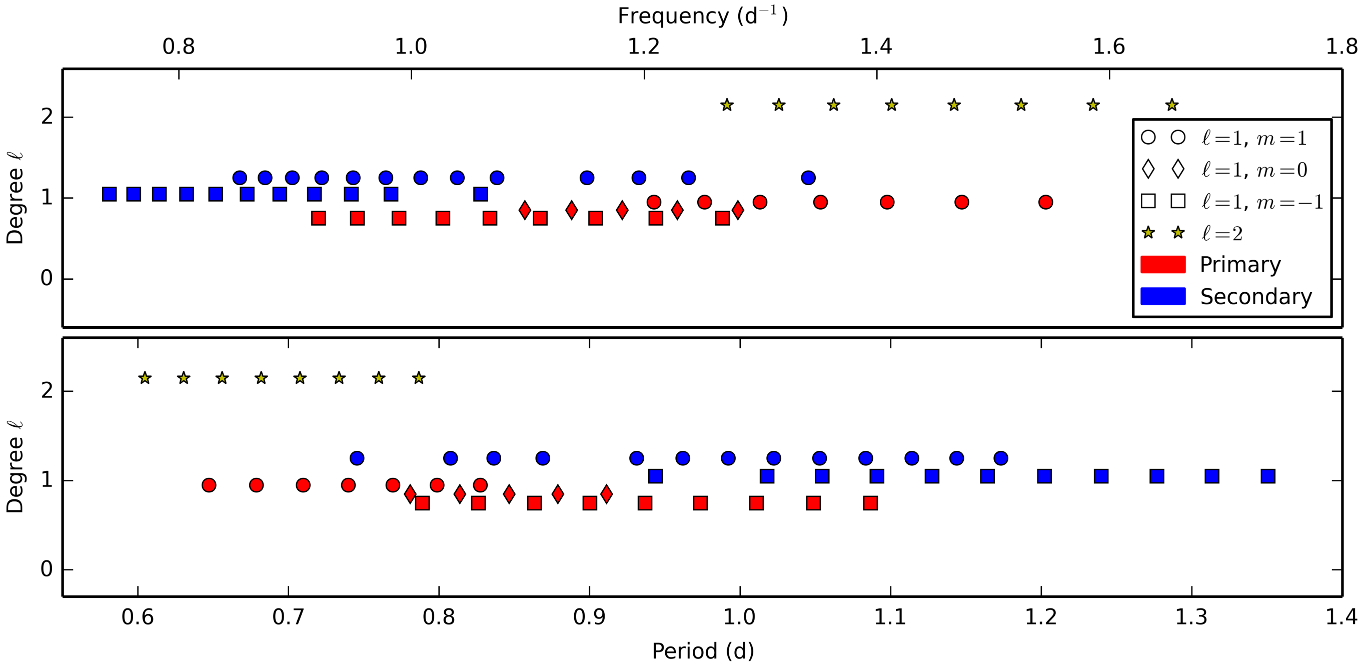

Figure 4.1: Observed g modes in frequency (*top*) and period (*bottom*) with the degree ℓ plotted on the y-axis. Modes of the primary are shown in red and modes of the secondary are shown in blue. The m values are distinguished by the different symbols. The yellow stars denote the $\ell = 2$ modes, which could not be assigned to either component.

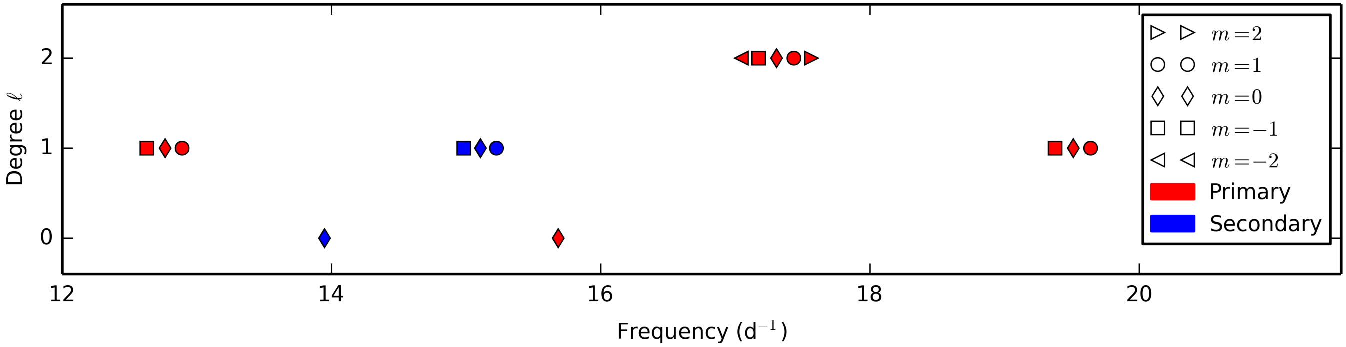

Figure 4.2: Observed p-mode frequencies with the degree ℓ plotted on the y-axis. The ℓ value was estimated, assuming that all observed multiplets are complete. Modes of the primary are shown in red and those of the secondary are shown in blue. The m values are distinguished by the different symbols.

Table 4.1: Fundamental and seismic parameters of the primary and secondary component of KIC 10080943.

	Primary	Secondary
$q = M_2/M_1$	0.96 ± 0.01	
M ($M_\odot$)	2.0 ± 0.1	1.9 ± 0.1
R ($R_\odot$)	2.9 ± 0.1	2.1 ± 0.2
$T_{\rm eff}$ (K)	7100 ± 200	7480^{+180}_{-200}
$\log g$ (cgs)	3.81 ± 0.03	4.1 ± 0.1
[M/H]	-0.05 ± 0.17	-0.09 ± 0.30
$\log(L/L_\odot)$	1.28 ± 0.06	1.1 ± 0.1
ΔP (s)	2817 ± 26	2905 ± 36

period spacing series form series of triplets with a different rotational splitting value and thus originate in the primary. Figure 4.1 shows the six period spacing series and which star they originate in. The series of $\ell = 2$ modes could not be assigned to either star, as it does not show combination frequencies or rotational splitting. In Fig. 4.2 the p modes that can be connected to one star or the other are shown.

All derived stellar parameters including the mean period spacing values are listed in Table 4.1 and are used to place both stars in an Hertzsprung-Russell diagram (HRD) inside a 1-σ error box in Fig. 4.3. It is obvious that the parameters lack the precision typical for double-lined eclipsing binaries (Southworth 2012), as no eclipses can be observed for KIC 10080943. The radii are then derived from the equipotential surfaces in Roche geometry, as opposed to the width of the eclipses. The ratio of the effective temperatures is somewhat constrained by the ellipsoidal variation and the reflection effect, while these effects are largely independent of the orbital inclination (for more information on the binary and a description of the modelling process, see Chapter 3 or Schmid et al. 2015). This high uncertainty of the orbital inclination propagates into the precision of the absolute masses. The mass ratio of the two components, however, was derived with great confidence from the ratio of the radial velocity amplitudes. Hence, the binarity of the system still yields crucial additional constraints for the theoretical stellar models compared to single star pulsators, as is discussed below.

The main diagnostic for finding a model representative of KIC 10080943A and KIC 10080943B is the period spacing of the high-order g modes. For both components, the mean period spacing value is rather low at $\Delta P < 3000$ seconds for stars near 2 $M_\odot$. Indeed, comparing with the sample of γ Dor stars in Van Reeth et al. (2015b), the measured ΔP values of both components hints at masses < 2 $M_\odot$. Furthermore, the observed period spacing series show a significant wavy structure without clear dips and a slight tilt, which is caused by rotation. This points towards evolved stars with a low central hydrogen mass fraction, where the receding convective hydrogen-burning core has left behind a chemical composition gradient ∇_μ leading to a peak in the Brunt-Väisälä frequency N and therefore a decrease in the asymptotic period spacing (e.g. Miglio et al. 2008).

In addition to the g modes, two p modes were identified as candidate radial modes and can help distinguish between possible models. To estimate their radial overtone, we calculate the pulsation constant Q (Breger 1990) as

$$Q = P\sqrt{\frac{\bar{\rho}}{\bar{\rho_\odot}}}, \tag{4.1}$$

or, expressed in observable parameters

$$\log Q = -6.454 + \log P + 0.5 \log g + 0.1 M_{\text{bol}} + \log T_{\text{eff}}. \tag{4.2}$$

For the highest amplitude p mode ($f_{s,2}$ = 13.947586 d^{-1}) and for the parameters of the secondary, we find $Q = 0.0332 \pm 0.0045$, which is indicative of the radial fundamental mode. The p mode with frequency $f_{s,1}$ = 15.68333 d^{-1} belongs to the primary and has $Q = 0.018 \pm 0.001$, which is consistent with $3 \leq n \leq 5$ (Stellingwerf 1979).

In addition to these seismic diagnostics, the main constraint from the binarity is the requirement of equal age, equal composition, and the mass ratio. This means that the seismic properties of both models have to match the observations at the same age, while the ratio of their masses also has to be in agreement with the observational measurement.

4.3 Searching for the best seismic models

We used MESA (Paxton et al. 2011, 2013, 2015, version 7385) to calculate evolutionary tracks for different parameters, which are specified in the following sections. For all tracks we used OPAL opacity tables (Iglesias & Rogers 1993, 1996) constructed for the solar metal mixture provided by Asplund et al. (2009). Stellar layers are dynamically unstable against convection according to the Schwarzschild criterion and are modelled with the mixing length theory (MLT) by Cox & Giuli (1968, chap. 14), using $\alpha_{\text{MLT}} = 1.8$. All equilibrium models along the evolutionary tracks are non-rotating, as both components are slow rotators (rotational period near the core $P_{c,1} \approx 7$ d and $P_{c,2} \approx 11$ d, see Sect. 3.5.2). Our MESA inlist is provided in Appendix A and is available for further choices of input physics.

As already mentioned in Sect. 4.2, the Brunt-Väisälä frequency N increases with the steepness of the chemical composition gradient ∇_μ. The shape and strength of the mixing of the stellar material therefore influence the shape of N and hence the periods and period spacings of high-order g modes. This can be illustrated by the asymptotic period spacing, which is defined by Tassoul (1980) as

$$\Delta P_c = \frac{2\pi^2}{L\int_{x_0}^{1} \frac{|N|}{x}\mathrm{d}x}, \tag{4.3}$$

where $L = \sqrt{\ell(\ell+1)}$, $x = r/R$, and x_0 the convective-core boundary. To probe the strength of mixing beyond the convective regions, we included convective-core overshooting and diffusive mixing as free parameters into our models. Convective-core overshooting mainly increases the size of the convective core, thus decreasing the integral $\int |N|/x\mathrm{d}x$. It is implemented in MESA using two different definitions that both depend on the MLT diffusion coefficient ($D_{\rm conv}$) and an adjustable parameter. In the exponential description, the region immediately outside the core has a diffusion coefficient determined by

$$D_{\rm ov} = D_{\rm conv}\exp\left(-\frac{2z}{f_{\rm ov}H_P}\right), \tag{4.4}$$

where H_P is the local pressure scale height, z is the distance from the convective-core boundary, and $f_{\rm ov}$ is a free parameter (Herwig 2000). This definition results in an exponentially decaying $D_{\rm ov}$. Alternatively, overshooting can also be defined as a step function, where the extent of the overshooting layer is $d_{\rm ov} = \alpha_{\rm ov}H_P$ with the adjustable parameter $\alpha_{\rm ov}$. Typically $\alpha_{\rm ov} \simeq 10 f_{\rm ov}$ and increasing either parameter leads to a wider mixed region beyond the core. In the radiative parts of the model, where neither convection nor overshooting is active, we set a minimum diffusion coefficient $D_{\rm mix}$ of 1 $\mathrm{cm}^2\,\mathrm{s}^{-1}$. It is implemented such that the diffusion coefficient throughout the star does not fall below this value. The higher it is, the more the chemical composition gradient is washed out in the radial direction, leading to fewer dips in the period spacing pattern. Apart from affecting ∇_μ, both overshooting and diffusion also have the consequence of mixing more hydrogen into the central region and therefore extending the time the stars spend on the main sequence. In other words, otherwise equal stars have a higher X_c at a given age when only the mixing strength is increased.

Based on these stellar models, we calculate theoretical pulsation modes, using the stellar pulsation code GYRE (Townsend & Teitler 2013, version 4.3). To take the effect rotation has on the observed frequencies into account, we perturbed the frequencies of the calculated zonal modes. In a first step we apply the first order perturbative approach $\Delta f = m\beta_{n,\ell}\Omega$ (Ledoux 1951), where $\beta_{n,\ell} = 1 - C_{n,\ell}$ and $C_{n,\ell}$ is the Ledoux constant. We use $\beta_{n,\ell}$ as calculated by GYRE and the observed frequency splitting Δf as a first guess for the rotational frequency Ω. The validity of the perturbative approach for γ Dor stars was tested by Ballot et al. (2010) for different rotation rates. For both stars and the observational estimates of the rotation rates (Schmid et al. 2015) $0.14 < 2\Omega_c/f_{\rm co} < 0.27$, where Ω_c is the rotation rate near the core and $f_{\rm co}$ are the

Table 4.2: Extents of the grid parameters.

	begin	end	step	N
coarse grid				704
M ($M_\odot$)	1.7	2.2	0.05	11
Z	0.012	0.018	0.002	4
f_ov	0.0	0.03	0.01	4
$\log D_\mathrm{mix}$	0	3	1	4
fine grid (exponential overshooting)				3267
M ($M_\odot$)	1.76	1.86	0.01	11
Z	0.0105	0.0125	0.001	3
f_ov	0.005	0.015	0.001	11
$\log D_\mathrm{mix}$	0	2	0.25	9
fine grid (step overshooting)				3267
M ($M_\odot$)	1.76	1.86	0.01	11
Z	0.0105	0.0125	0.001	3
α_ov	0.05	0.15	0.01	11
$\log D_\mathrm{mix}$	0	2	0.25	9

Notes. The overshooting parameters f_ov and α_ov are expressed in terms of local pressure scale height (H_P) and the diffusion coefficient D_mix has the unit cm^2 s^{-1}.

g-mode frequencies in the co-rotating frame of reference. This means that they are in the validity range of the perturbative approach to first order.

An alternative method to treat the coupling between rotation and pulsation is the traditional approximation of rotation (TAR; e.g. Townsend 2003), which is also implemented in GYRE. This method is based on neglecting the horizontal component of the rotation vector and is valid when the horizontal displacement is larger than the radial displacement, which is the case for g modes in γ Dor stars. Bouabid et al. (2013) studied the influence of the Coriolis force on high-order g modes, using the TAR, and compared their computations to predictions by the first-order perturbative approach. These authors showed that, even for slow rotation rates, the Coriolis force has an influence on the mode periods, which is stronger at higher radial orders. This force causes a departure from linearity in rotational splitting and also effects the zonal modes, which are unperturbed in the perturbative approach.

Table 4.3: Parameters of the best combination of primary and secondary models for each grid of Table 4.2.

	Model 1	Model 2	Model 3	Model 4	Model 5	Model 6
grid	*coarse*	*exp. ov. (Ledoux)*	*step ov. (Ledoux)*	*exp. ov. (TAR)*	*step ov. (TAR)*	*morphology*
M_1 ($M_\odot$)	1.85	1.82	1.81	1.82	1.81	1.67
M_2 ($M_\odot$)	1.75	1.76	1.76	1.76	1.76	1.60
Z	0.012	0.0125	0.0125	0.0125	0.0125	0.010
$f_{\rm ov,1}$ or $\alpha_{\rm ov,1}$	0.01	0.008	0.11	0.008	0.11	0.007
$f_{\rm ov,2}$ or $\alpha_{\rm ov,2}$	0.0	0.005	0.05	0.005	0.05	0.006
$\log(D_{\rm mix,1})$	0	0.25	0.25	0.25	0.25	0.5
$\log(D_{\rm mix,2})$	2	1.5	1.75	1.5	1.75	0.75
a_1 (Gyr)	1.087	1.123	1.110	1.102	1.089	1.082
a_2 (Gyr)	1.082	1.127	1.110	1.100	1.081	1.085
$X_{c,1}$	0.09	0.1	0.11	0.12	0.13	0.22
$X_{c,2}$	0.24	0.19	0.21	0.22	0.23	0.29
$\Delta P_{c,1}$ (s)	2832	2806	2816	2873	2877	2829
$\Delta P_{c,2}$ (s)	2909	2905	2904	2939	2942	2851
$T_{\rm eff,1}$ (K)	7131	7074	7110	7157	7189	7583
$T_{\rm eff,2}$ (K)	7526	7308	7372	7387	7452	7597
R_1 ($R_\odot$)	2.92	2.81	2.72	2.74	2.66	2.12
R_2 ($R_\odot$)	2.29	2.43	2.39	2.38	2.33	1.90
$\log(L_1/L_\odot)$	1.30	1.25	1.23	1.25	1.23	1.13
$\log(L_2/L_\odot)$	1.18	1.18	1.18	1.18	1.18	1.04

Notes. The overshooting parameters $f_{\rm ov}$ and $\alpha_{\rm ov}$ are expressed in terms of local pressure scale height (H_P) and the diffusion coefficient $D_{\rm mix}$ has the unit cm^2 s^{-1}.

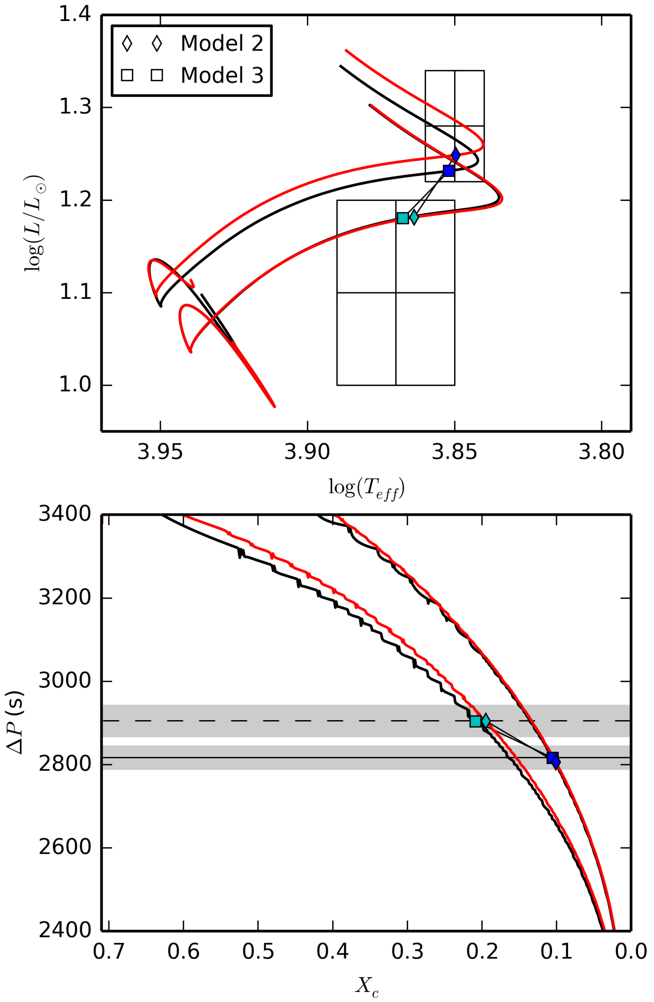

Figure 4.3: *Top panel:* Hertzsprung-Russell diagram with the observed positions and 1σ areas of both components of KIC 10080943, marked by the boxes (the primary is the cooler, more luminous star). The positions of the components in Model 2 are given by the diamonds and for Model 3 by the squares, while the respective evolutionary tracks are given by the red and black solid lines. Dark blue symbols mark the primary, while the light blue symbols indicate the secondary models. Parameters of these models are given in Table 4.3. *Bottom panel:* The asymptotic period spacing ΔP as a function of central hydrogen mass fraction X_c. The observed mean period spacing of the primary (secondary) is given as the horizontal solid (dashed) line and the 1σ areas are shown as the grey patch.

4.3.1 MESA model grids

From the results of the binary modelling in Chapter 3, we can draw an error box on the HRD, within which our best models should reside. We calculated a grid of models over the following parameters that influence the position of the model on the HRD: mass M, metallicity Z, convective-core overshooting f_{ov} in the exponential description, and diffusive mixing $D_{\rm mix}$ (the extent of the grid is given in Table 4.2), while the initial hydrogen mass fraction was fixed at the solar value $X_i = 0.71$.

At every time step of each track, we calculated the asymptotic period spacing ΔP_c (Eq. 4.3). This parameter, as well as the fundamental model parameters $\log(L/L_\odot)$, $\log(R/R_\odot)$, $\log T_{\rm eff}$, and X_c were then interpolated on an equidistant age scale with steps of $\Delta a = 10^7$ years. At every age step we evaluated models for the primary and the secondary simultaneously by comparing the observed to the asymptotic period spacing, allowing only combinations with equal composition at the ZAMS ($Z_1 = Z_2$) and which fulfil the observed mass ratio $M_2/M_1 = q = 0.96 \pm 0.01$ within 2σ. We calculated the $\chi^2_{\rm tot}$ as

$$\chi^2_{\rm tot} = \chi^2_1 + \chi^2_2 = \left(\frac{\Delta P_c - \Delta P_{o,1}}{\sigma(\Delta P_{o,1})}\right)^2 + \left(\frac{\Delta P_c - \Delta P_{o,2}}{\sigma(\Delta P_{o,2})}\right)^2, \tag{4.5}$$

where $\Delta P_{o,1}$ and $\Delta P_{o,2}$ refer to the mean of the observed period spacing of the zonal dipole modes for the primary and the secondary, respectively. For about 4.1% of all 19 456 valid combinations $\chi^2_1 < 4$ and $\chi^2_2 < 4$ at the same age, meaning that the asymptotic period spacing of the model is within 2σ of the observations. When we compare the model tracks to the observations it becomes obvious that those with high diffusion ($\log D_{\rm mix} = 3$) are too luminous and too old. Thus, we can limit the number of good models even further, when only considering those whose $\log T_{\rm eff}$ and $\log(R/R_\odot)$ lie within 2σ of the observed values, leaving 60 combinations of primary and secondary models fulfilling all observational constraints derived from the g-mode period spacings and the binarity of our target.

We find that the remaining 60 models have common characteristics. They have low masses (the highest primary mass $M_1 = 1.9\ M_\odot$; the best models have $M_1 = 1.8 - 1.85\ M_\odot$ and $M_2 = 1.7 - 1.75\ M_\odot$) and low metallicity, with the majority having $Z = 0.012$. While the core overshooting is limited to small values $f_{\rm ov} = 0.0 - 0.1$, diffusion with values $\log D_{\rm mix} = 1 - 2$ are possible. As already predicted by the mean value and structure of the observed period spacing, both stars are old with $a \approx 1$ Gyr and low central hydrogen mass fractions $X_{c,1} = 0.05 - 0.15$ and $X_{c,2} = 0.15 - 0.3$. The parameters of the best model are given in Table 4.3.

Based on these common characteristics, we computed two denser grids with refined steps in mass and the mixing parameters (see Table 4.2). The difference between those grids is the definition of core overshooting, where one grid uses the exponential description and the other uses step overshooting. We analysed them using the same

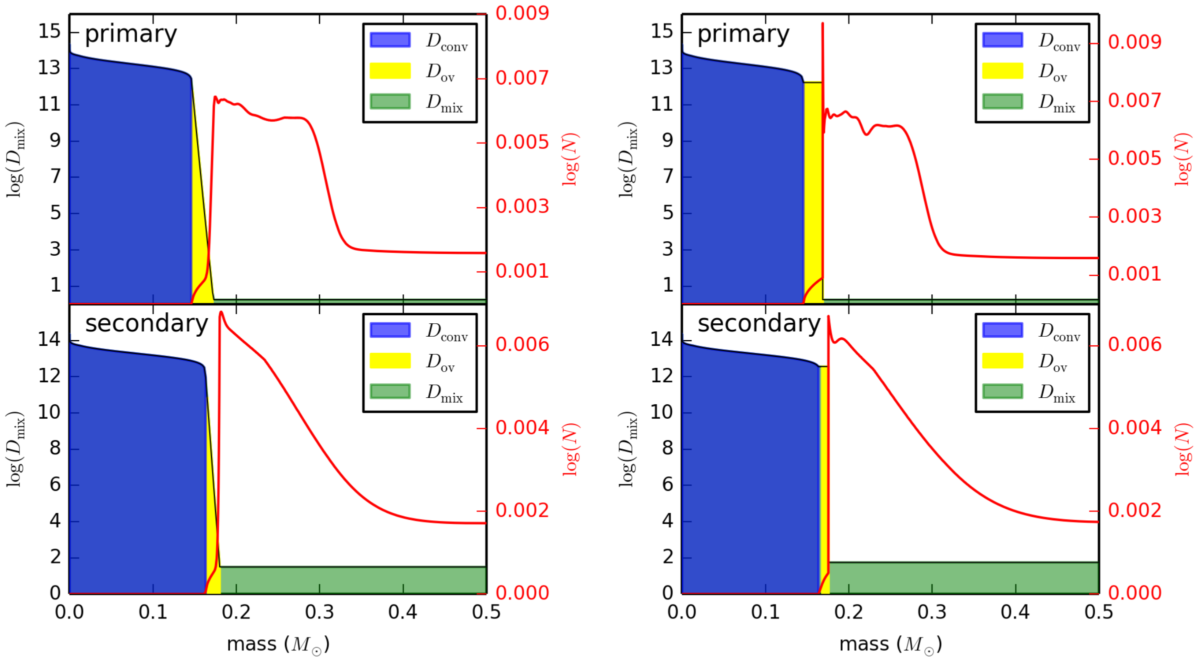

(a) Interior structure of Model 2.

(b) Interior structure of Model 3.

Figure 4.4: Diffusion coefficient $\log D$ for the inner $0.5M_\odot$ of the primary (*top panels*) and the secondary (*bottom panel*) as a function of enclosed mass. Blue shaded regions are convective, yellow shaded parts denote the overshooting-layer at the edge of the convective core, and green shaded parts are radiative regions with a minimum diffusion coefficient $\log D_{\rm mix}$. The log of the Brunt-Väisälä frequency $\log N$ is shown as the red solid line.

method as described above and found 97 880 and 170 449 models fulfilling the requirements for the exponential-overshoot and step-overshoot grids, respectively. Their parameters agree well with the results of the coarse grid analysis and can be compared in Table 4.3 for the models of lowest χ^2. Figure 4.3 shows their position and evolutionary tracks in the HRD and Fig. 4.4 illustrates their interior structure by showing $\log D$ and $\log N$ as a function of enclosed mass. In accordance with results from the previous grid, we find that higher values of overshooting combined with low values in envelope diffusion are favoured for the primary, while we find the opposite for the secondary (see Sect. 4.4 for a discussion on the relevance of these values). Furthermore, we again find that, based on this χ^2 approach, the best models are old at around 1.1 Gyr and have a low X_c (see Figs 4.5 and 4.6).

So far, we have only taken into account the mean of the observed g-mode period spacing, neglecting the effect of rotation and the information that is held in the spacing morphology. In the next step, we therefore calculate the adiabatic frequencies of our models with GYRE and compare their seismic properties to the observations.

4.3.2 Period spacing with GYRE

We calculated the zonal dipole and quadrupole modes with GYRE for the coeval models with the lowest χ^2. As we clearly see the effect of rotation in the observed frequency spectrum (see Fig. 4.1), we apply Ledoux splitting to the zonal modes to obtain the theoretical prograde and retrograde modes and the rotational frequencies Ω_c near the core for both components. We derive $\Omega_{c,1} = 0.13963 \pm 0.00007\ \mathrm{d}^{-1}$ and $\Omega_{c,2} = 0.09034 \pm 0.00002\ \mathrm{d}^{-1}$ and a negligible difference between the models with exponential and those with step overshooting. For these rotation rates and the co-rotating dipole-mode frequencies we find $0.198 < 2\Omega_{c,1}/f_{\mathrm{co}} < 0.264$ and $0.144 < 2\Omega_{c,2}/f_{\mathrm{co}} < 0.237$. The comparison between the calculated modes of Models 2 and 3 and the observed period spacings is illustrated in Fig. 4.7, while Fig. 4.8 shows the comparison of the p modes. Our main focus lies in comparing the mean period spacing values and the structure of the period spacing pattern, rather than individual frequencies. We find a satisfactory fit for both models and cannot distinguish between exponential or step overshooting. Furthermore, we are able to assign the $\ell = 2$ series (yellow stars in Fig. 4.1) to the primary, as there is a clear overlap with the retrograde sectoral modes of both models, while there is a gap for the models of the secondary. From Eq. (4.3), we expect that the ratio of the asymptotic period spacing of the quadrupole modes to the asymptotic period spacing of the dipole modes is $\Delta P_c(\ell = 2)/\Delta P_c(\ell = 1) = 0.577$. We use the derived $\Omega_{c,1}$ to shift the observed quadrupole sectoral modes to their zonal counterparts, and find $\Delta P_o(\ell = 2) = 1664 \pm 21$ s and $\Delta P_o(\ell = 2)/\Delta P_{o,1}(\ell = 1) = 0.591 \pm 0.009$. For the secondary and $\Omega_{c,2}$ we find $\Delta P_o(\ell = 2) = 1840 \pm 14$ s and $\Delta P_o(\ell = 2)/\Delta P_{o,2}(\ell = 1) = 0.633 \pm 0.009$. These results support that the $\ell = 2$ series originates in the primary.

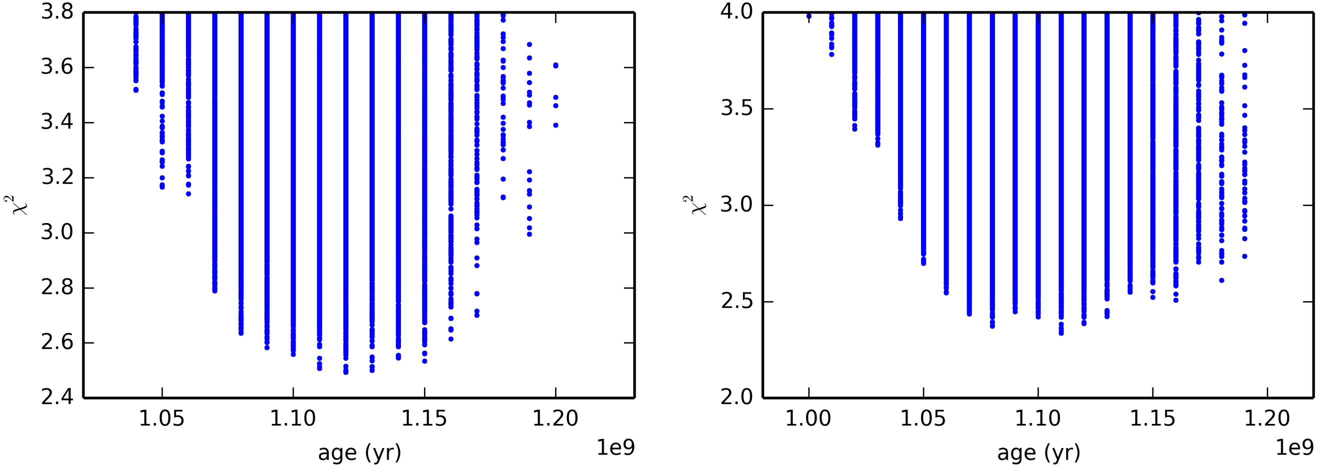

(a) Fine grid – exponential overshoot

(b) Fine grid – step overshoot

Figure 4.5: Chi-squared distribution of age for all coeval models in the two denser grids, which fall within 2σ of the HRD position of both stars and have equal composition.

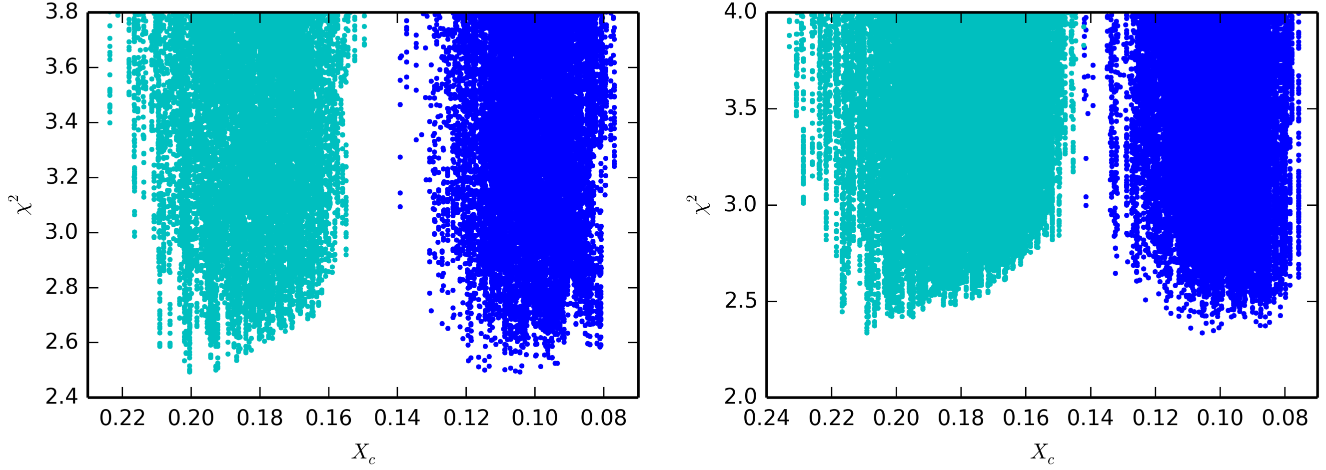

(a) Fine grid – exponential overshoot

(b) Fine grid – step overshoot

Figure 4.6: Chi-squared distribution of central hydrogen mass fraction X_c for the same models as in Fig. 4.5. The models for the primary are indicated by the dark blue points, while the models for the secondary are indicated by the light blue points.

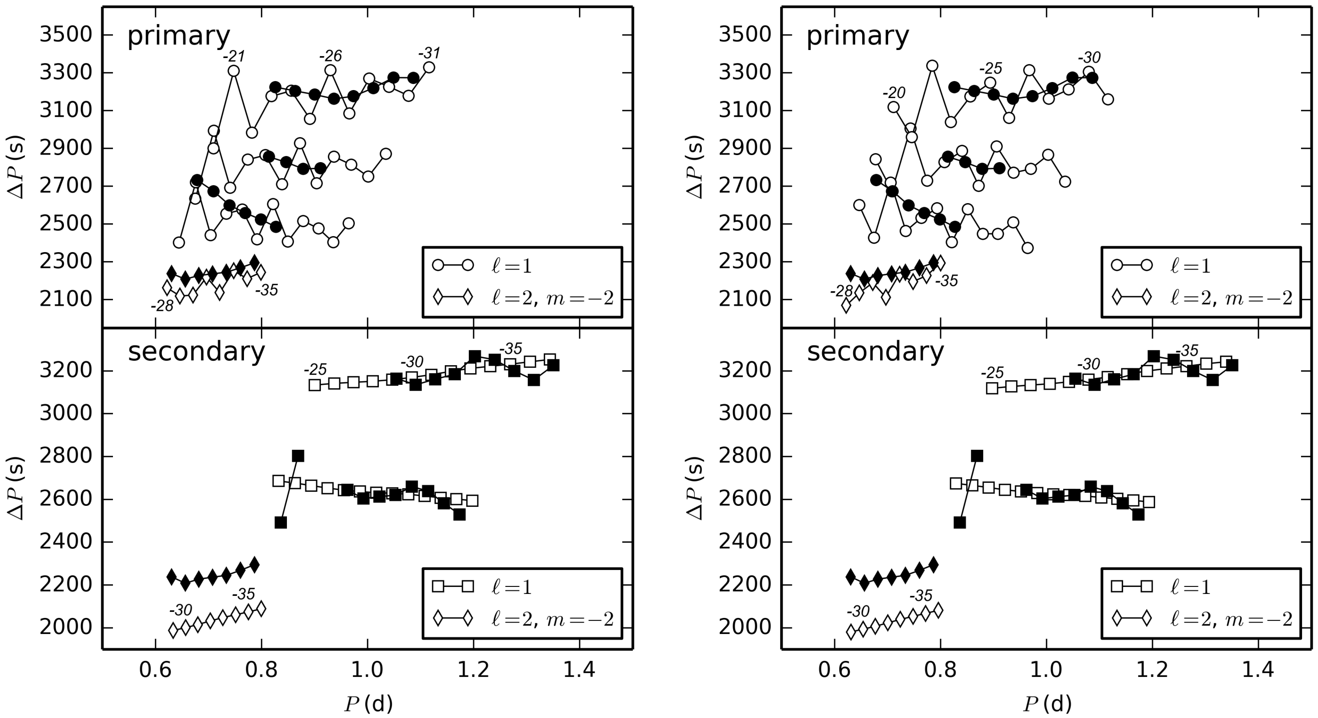

(a) Gravity modes of Model 2.

(b) Gravity modes of Model 3.

Figure 4.7: Comparison of theoretical (empty symbols) to observed (filled symbols) period spacing for the primary *(top panels)* and the secondary *(bottom panels)*. Ledoux splitting has been applied to the theoretical zonal modes to fit the retrograde and prograde modes. The uncertainties of the observed period spacings are smaller than the symbols. The radial orders *k* are indicated near selected modes.

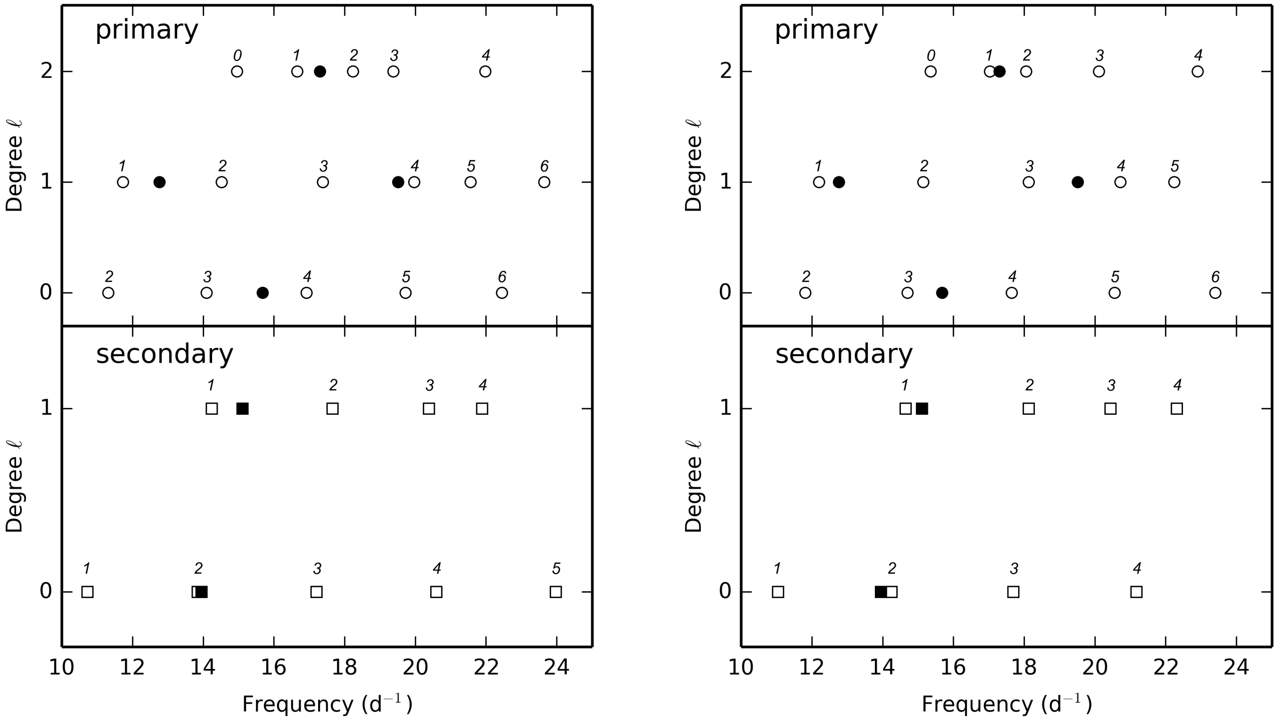

(a) Pressure modes of Model 2.

(b) Pressure modes of Model 3.

Figure 4.8: Comparison of the theoretical zonal p modes (empty symbols) to the observed modes (filled symbols) as a function of degree ℓ. Modes of the primary are shown in the *top panels* and for the secondary in the *bottom panels*. The radial orders are given above the respective modes.

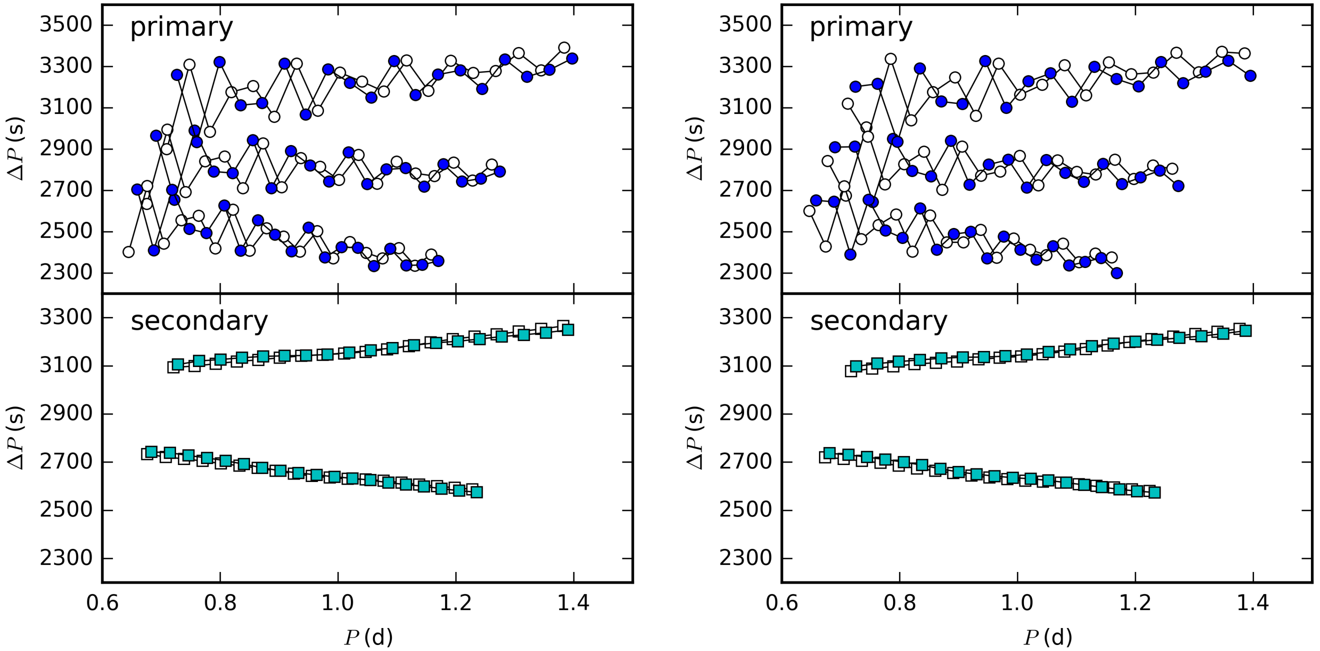

(a) Period spacing for Model 2 and Model 4.

(b) Period spacing for Model 3 and Model 5.

Figure 4.9: Difference between first-order perturbation approximation and TAR for the rotation rates $\Omega_{c,1} = 0.13963$ d^{-1} and $\Omega_{c,2} = 0.09034$ d^{-1}. GYRE zonal modes with a Ledoux shift applied are shown as the empty symbols and GYRE modes calculated using the TAR are shown as the filled symbols, where the primary is in dark blue and the secondary in light blue.

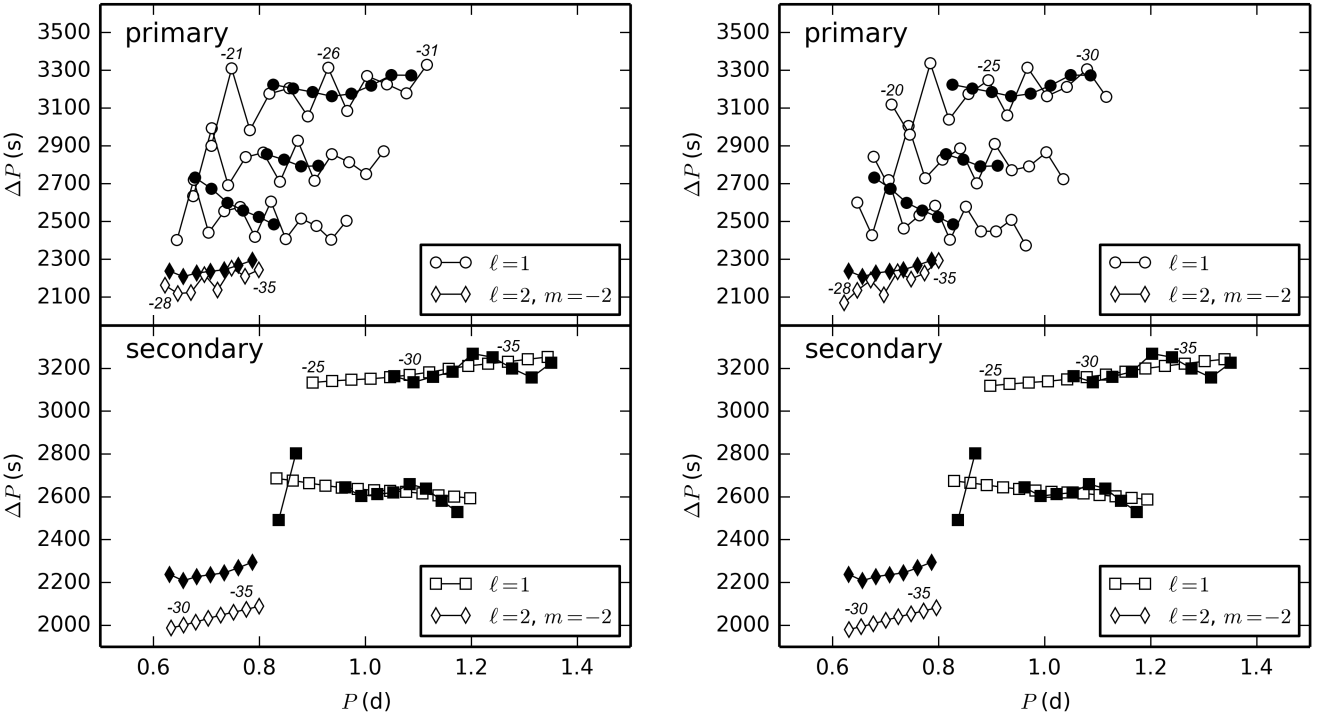

(a) Gravity modes of Model 4.

(b) Gravity modes of Model 5.

Figure 4.10: Same as Fig. 4.7, but using the TAR instead of the Ledoux splitting to estimate the influence of rotation.

To test the accuracy of the rotation rates derived with the Ledoux splitting, i.e. $\Omega_{c,1} = 0.13963$ and $\Omega_{c,2} = 0.09034$, we recompute all modes using the TAR. At the rotation rates that were found from the first order perturbations, we find a disagreement between the GYRE modes and the observations. However, we find that by altering the rotation rates, we cannot obtain a better fit. Rather, we find that the observed shift is due to a difference in the mean period spacing values. We selected Models 2 and 3 as having the lowest χ^2 for the asymptotic period spacing, which is only valid for zonal modes in a non-rotating case. As the Coriolis force shifts the zonal modes to higher frequencies, we find a decreased period spacing. Therefore, we find a better fit, when selecting younger models (Models 4 and 5; see Table 4.3) where $\Delta P_{c,1}$ is about 64 s higher and $\Delta P_{c,2}$ is about 36 s higher, for both the exponential and step overshooting grids. Figure 4.9 shows how the period spacings of the best models from the grid search and these younger models compare, using the two different approximations (Ledoux versus TAR) for the puslations. We compare the period spacings of these younger models to the observations in Fig. 4.10. As can be seen there is only a slight difference between Fig. 4.10 and Fig. 4.7, which mainly results from adopting younger models.

4.4 Disucssion

4.4.1 On the mixing parameters of the coeval models

During the analysis of all three grids of coeval models based on ΔP_c, T_{eff}, and R, we found a clear trend for high overshooting and low diffusive mixing for the primary, and low overshooting and high diffusive mixing for the secondary. The main reasons why these parameters influence our model selection, is that stronger mixing increases the main sequence lifetime of a star by providing fresh hydrogen to the nuclear-burning core. By directly affecting the stellar structure they also alter the Brunt-Väisälä frequency N (see Fig. 4.4) and thus ΔP_c. Both effects are illustrated in Fig. 4.11. In this figure it can also be seen that higher mass models have a higher period spacing at a given X_c. Yet, the evolution of ΔP_c is faster for the primary and drops to the observed value in shorter time than for the secondary, when the strength of mixing is equal in both components. Thus, a higher value of f_{ov} for the primary is needed to slow the evolution of ΔP_c down. Additionally, it extends the evolutionary track to reach the observed $T_{\text{eff},1}$, when it would otherwise turn off before the observed error box. For the secondary, additional mixing is mainly required to adjust the evolution of ΔP_c with that of the primary. As models with $f_{\text{ov}} = 0.0$ and $\log(D_{\text{mix}}) = 0.0$ already cross the observational error box on the HRD, increasing f_{ov} would result in a too cool and too big star. Diffusive mixing on the other hand, has a weaker influence on the main sequence lifetime than overshooting and is thus the preferred mixing mechanism for the secondary. In summary we state that the equal age requirement and the stellar parameters from binary modelling, serve as a

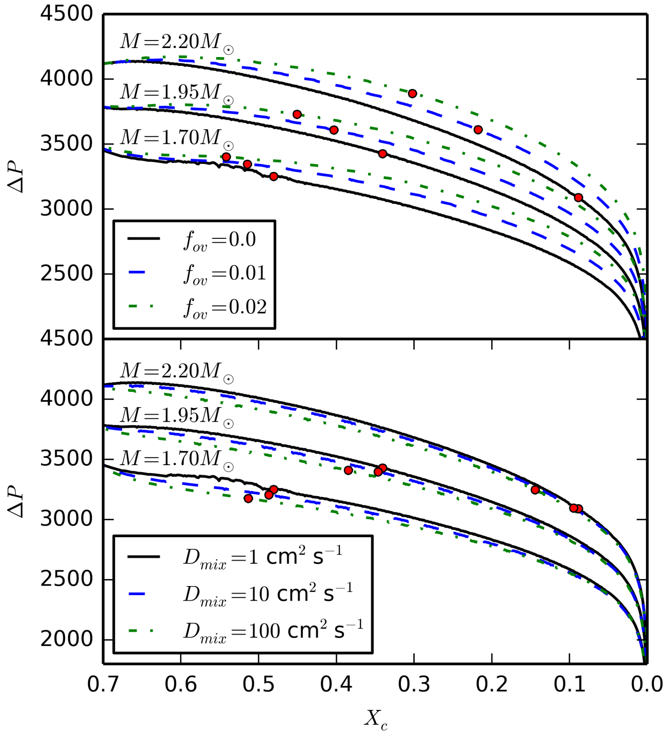

Figure 4.11: Asymptotic period spacing ΔP as a function of central hydrogen mass fraction X_c for different masses and with different values of $f_{\rm ov}$ (*top panel*) and $D_{\rm mix}$ (*bottom panel*). The red points denote ages of 0.6 Gyr.

stringent constraint to derive the width of the core-overshooting region and the strength of radial envelope mixing in both stars at the current evolutionary stage. Variations throughout the stellar evolution of these parameters are likely to occur. Both stars could thus have had similar values near the ZAMS or started off with different values at birth.

4.4.2 The period spacing morphology

When focusing only on the morphology of the period spacing we find Models 2 and 3 to be less satisfying fits to the observations than suggested by the mean period spacing values. While the computed period spacing for the primary has variations that are too strong and too short, the structure of the secondary model is too smooth (see Figs. 4.7 and 4.10). Miglio et al. (2008) showed that the interval of the dips in period spacing depends on the steepness of the chemical composition gradient near the core, which grows with increasing age or decreasing X_c as more and more hydrogen is burned into helium. In Figs 4.12 and 4.13 we show how the period spacing evolves for different values of X_c for a model of $M = 1.81\ M_\odot$ with exponential overshooting and step overshooting, respectively. For the secondary, the lack of structure in the computed period spacing can be explained by high diffusion, which diminishes ∇_μ near the core. In Figs 4.14 and 4.15 it is clearly visible how the dips in period spacing disappear with increasing $\log(D_{\rm mix})$. Hence, the period spacing morphology points to stars with a higher X_c than we found with the grid search, explained in Sect. 4.3. Indeed, we find a better fit with models where $X_c \approx 0.35$ and $0.5 \leq \log(D_{\rm mix}) \leq 0.75$, while we find that overshooting only has weak influence. The similarity of these values for both stars is a direct consequence of the similar morphology in the observed period spacings of both components, however, they are in contradiction to the other observational constraints. By increasing X_c the stars move closer to the ZAMS and outside the error box defined by $T_{\rm eff}$ and R from binary modelling. In even stronger disagreement, however, are the asymptotic period spacings, as they are several σ above the observed values.

To obtain better agreement between the period spacing morphology and the mean period spacing values, as well as the stellar parameters, we exploit correlations between mass, metallicity, and ΔP_c. For a given X_c, the asymptotic period spacing decreases with decreasing mass and decreasing metallicity. However, models with low metal content are more luminous than those with high metal content and, therefore, mimic higher mass models with high metallicity in the HRD. To decrease ΔP_c as much as possible, we use a secondary mass of $M_2 - 3\sigma_{M_2} = 1.6\ M_\odot$ and determine the primary mass via the mass ratio as $M_1 = M_2/q = 1.67\ M_\odot$. We choose a metallicity of $Z = 0.01$, which is still in agreement with the slightly sub-solar metallicity found in Chapter 3. The mixing parameters were chosen to conform with the observed structure in the measured period spacing pattern. From the computed evolutionary tracks we determine the coeval Model 6, where $\chi^2_{\rm tot}$ is at a minimum (all grid and global parameters of Model 6 can be found in Table 4.3). For this model, we compute the zonal dipole and quadrupole modes with GYRE and apply the Ledoux splitting for the prograde and retrograde modes. The derived rotation rates for this model, are $\Omega_{c,1} = 0.13969 \pm 0.00003$ d^{-1} and $\Omega_{c,2} = 0.09047 \pm 0.00004$ d^{-1}. We show the result for this test in Fig. 4.16, where the computed g and p modes are compared to the observed modes. We find a much better fit of the period spacing morphology and even the asymptotic period spacing values lie within 2σ of the observed mean values (Fig. 4.16a). Some room for improvement exists for the global parameters of the primary model, as can be seen in Fig. 4.17. The $T_{\rm eff}$ and $\log(L/L_\odot)$ of the model still lie within 3σ of the observed values, but its radius $R = 2.12\ R_\odot$ lies outside this range.

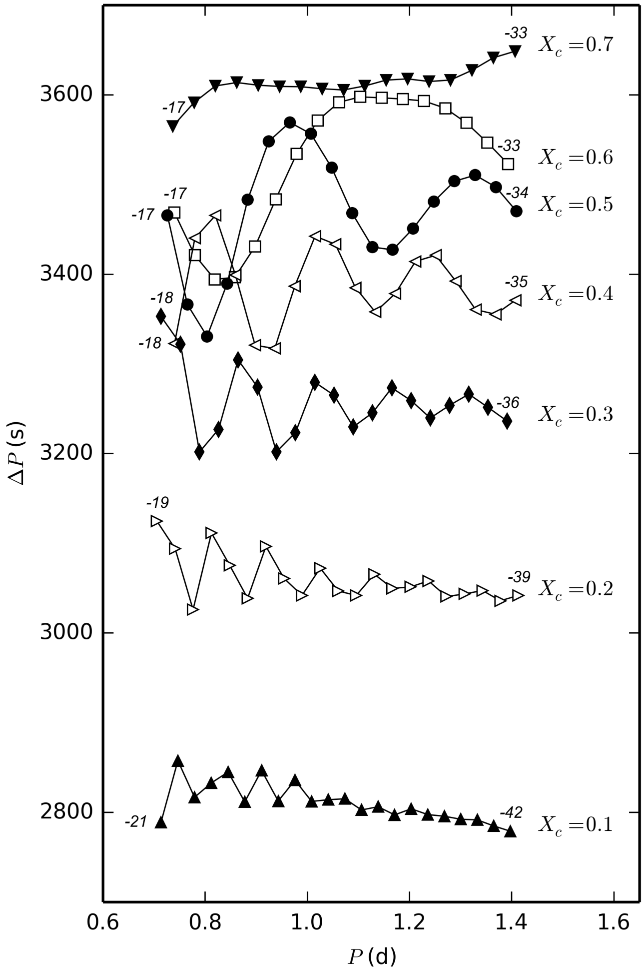

Figure 4.12: Period spacing for different values of X_c for models with M = 1.81 $M_\odot$, Z = 0.0125, exponential core-overshooting $f_{\rm ov}$ = 0.011, and $\log(D_{\rm mix})$ = 0.75. The radial orders of the first and last mode in the period spacing is given. The filling of the symbols is alternated to enhance visibility.

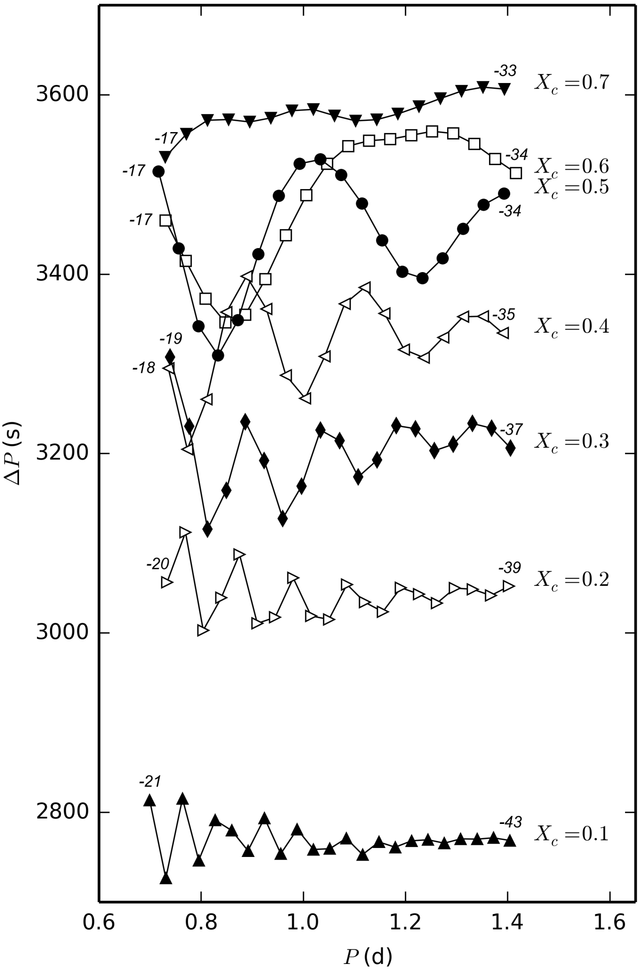

Figure 4.13: Period spacing for different values of X_c for models with $M = 1.81\ M_\odot$, $Z = 0.0125$, step overshooting $\alpha_{\rm ov} = 0.11$, and $\log(D_{\rm mix}) = 0.75$. The radial orders of the first and last mode in the period spacing is given. The filling of the symbols is alternated to enhance visibility.

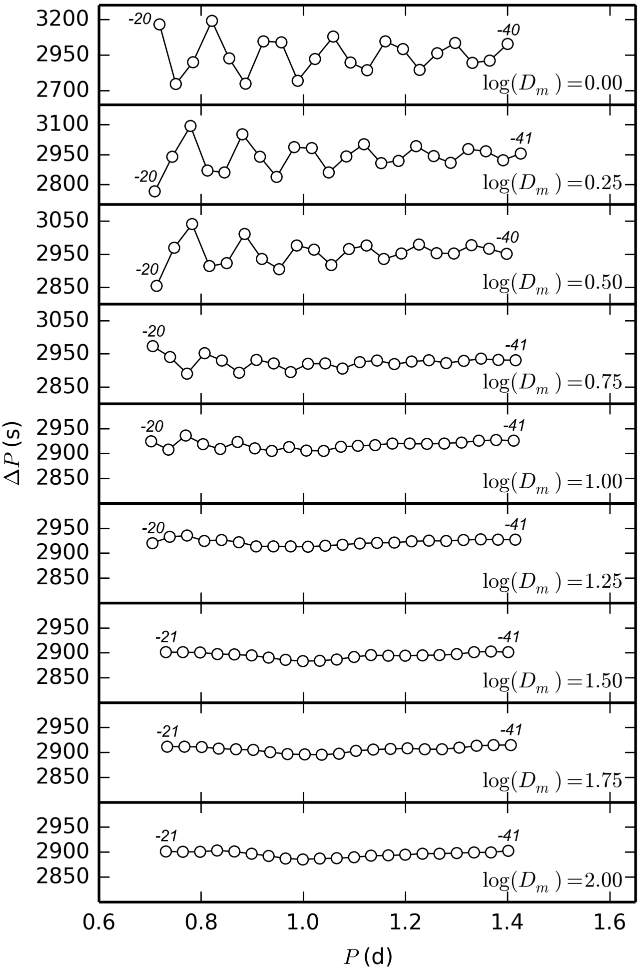

Figure 4.14: Period spacing for different values of $\log(D_{\mathrm{mix}})$ for models with $M = 1.76\ M_{\odot}$, $Z = 0.0125$, exponential overshooting $f_{\mathrm{ov}} = 0.005$, and $X_c = 0.20$. The radial orders of the first and last mode in the period spacing is given.

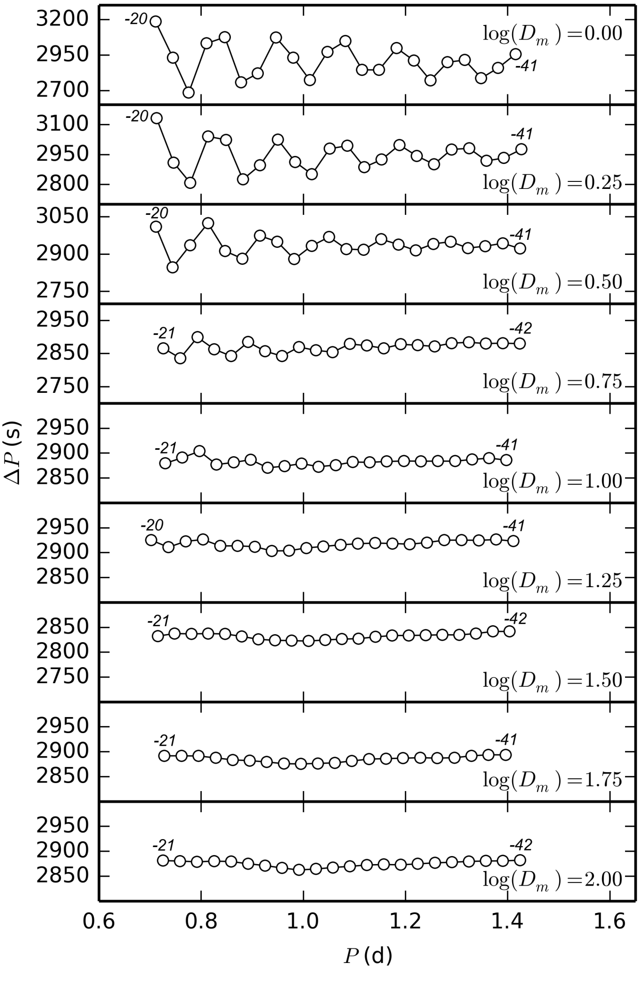

Figure 4.15: Period spacing for different values of log($D_{\rm mix}$) for models with M = 1.76 $M_\odot$, Z = 0.0125, step overshooting $\alpha_{\rm ov}$ = 0.05, and X_c = 0.20. The radial orders of the first and last mode in the period spacing is given.

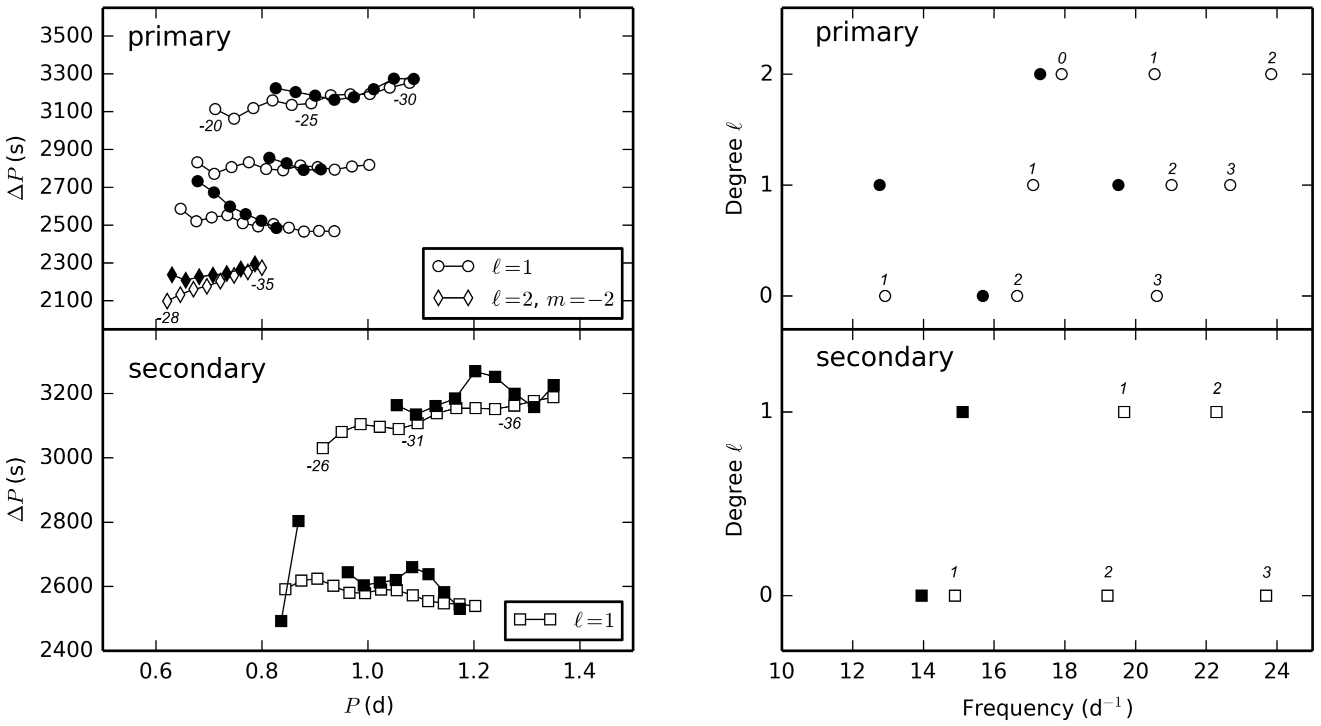

(a) Gravity modes of Model 6.

(b) Pressure modes of Model 6.

Figure 4.16: Comparison of theoretical modes (empty symbols) to observed modes (filled symbols) for the primary (*top panels*) and the secondary (*bottom panels*). The radial orders are given near selected modes.

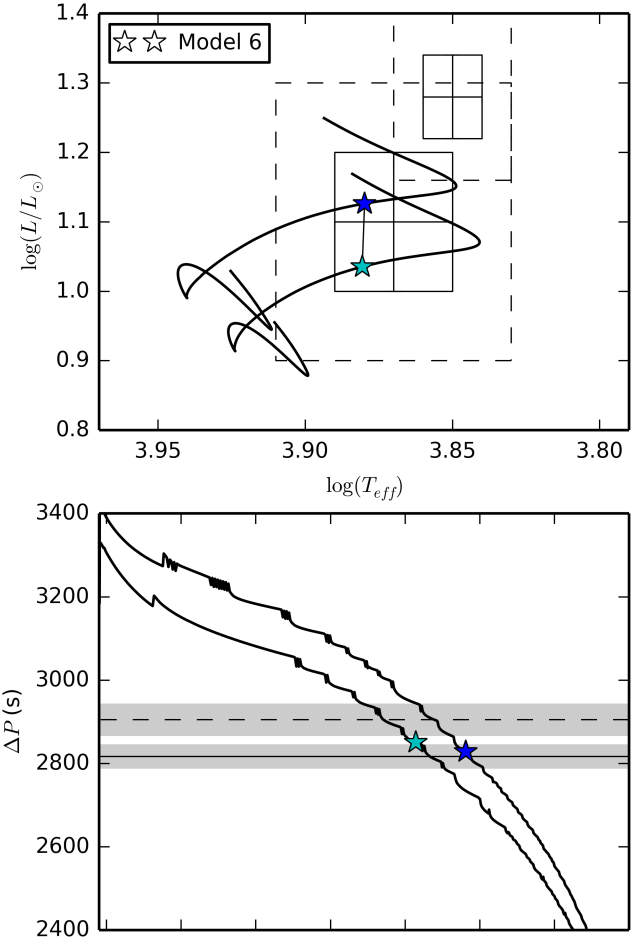

Figure 4.17: Same as Fig. 4.3 but for Model 6, indicated by stars and its evolutionary track as the black solid line. Here the 2σ areas for $T_{\mathrm{eff},1,2}$ and $\log(L_{1,2}/L_\odot)$ are also shown as dashed boxes.

4.4.3 Varying the He mass fraction

In the model grids discussed above, we have assumed an initial hydrogen mass fraction $X_i = 0.71$. Varying X_i and thereby adapting the initial helium mass fraction Y_i influences the positions of the tracks on the HRD and the asymptotic period spacing. Increasing Y_i, while decreasing X_i causes a star of the same mass and Z to become more luminous. Furthermore, for a given X_c, ΔP_c increases. We therefore tested whether changing the helium mass fraction would lead to higher masses that are in better agreement with the values from binary modelling, following the same modelling procedure as carried out for fixed $X_i = 0.71$. We computed two additional small grids of models for $X_i = 0.7$ and $X_i = 0.72$, using exponential overshooting. The best fitting model with $X_i = 0.72$ has a primary mass of $M_1 = 1.83\ M_\odot$, which is slightly higher than the mass of Model 2. However, this increase in mass is accompanied with a lower metallicity of $Z = 0.0115$. The secondary mass is the same as for Model 2, while the overshooting and diffusion parameters only change slightly ($f_{\mathrm{ov},1} = 0.01$, $\log D_{\mathrm{mix},1} = 0$, $f_{\mathrm{ov},2} = 0.005$, and $\log D_{\mathrm{mix},2} = 1.75$).

4.4.4 The p modes

The observed p modes provide weaker constraints for both components than the g modes because of their uncertain mode identification, which is based on the assumption that all observed multiplets are complete. Models 2 and 3, which best fit the observed mean period spacing and binary parameters, confirm the mode identification for the secondary (Fig. 4.8). The singlet and highest amplitude p mode $f_{s,2}$ fits the first overtone mode better than the radial fundamental. For the primary, the situation is somewhat more ambiguous. For the singlet $f_{s,1}$ and the triplet centre frequency $f = 19.51028\ \mathrm{d}^{-1}$, neither ℓ nor k can be assigned without doubt. As for the g modes, it is not possible to distinguish between exponential and step overshooting using the p modes.

In Chapter 3 we used the rotational splittings observed in the p modes and the g modes to provide an estimate of the core-to-surface rotation rates. They showed that both stars might have a slight differential rotation in the radial direction. We now use our best models to compute the Ledoux constant $C_{n,\ell}$ and derive the envelope rotation rates based on the p-mode splittings. Since the splittings detected in Chapter 3 show a significant asymmetry, which cannot be reproduced by the first order Ledoux approximation, we use the average Δf per multiplet.

For the triplet associated with the secondary (see Fig. 4.2) we find that $\beta_{n,\ell} = (1 - C_{n,\ell})$ is close to 1, which is the expected value for pure p modes. This yields an envelope rotation rate of $\Omega_{e,2} = 0.122 \pm 0.002\ \mathrm{d}^{-1}$ for the secondary. Thus, we observe differential rotation in the radial direction with a slower core than envelope, given the ratio of surface-to-core rotation rate $\Omega_{e,2}/\Omega_{c,2} = 1.35 \pm 0.02$. This value is equal for Models 2 and 3.

For the primary, the situation is slightly more complicated. Using $\beta_{n,\ell}$ for the modes of radial orders $n = 1$ and $n = 4$ for the dipole modes and $n = 1$ for the quadrupole mode, we derive rotation rates in the range $0.137 \leq \Omega_{e,1}$ (d^{-1}) ≤ 0.173. The envelope of the primary can thus be either faster or slower than its core, depending on the p-mode multiplet. When we examine the $\beta_{n,\ell}$ values of the individual modes more closely, we find that some have values below 0.9. For the mode near $f = 19.51$ d^{-1} we find $\beta_{4,1} \approx 0.8$ and a rotation rate of $0.16 - 0.17$ d^{-1}, while $\beta_{3,1} \approx 0.97$ and hence $\Omega_{e,1} \approx 0.135$ d^{-1}. This is because the $n = 4$ mode has a mixed mode character and not only probes the envelope (like pure p modes) but also has a high amplitude near the convective core (like pure g modes). This is also the case for the quadrupole mode, where we find envelope rotation rates of $0.14 - 0.15$ d^{-1}. Examples of rotational kernels $K_{n,\ell}$ are shown in Fig. 4.18. The mixed dipole modes of orders $n = 4$ and $n = 5$ (top panels) have a high amplitude close to the convective core, as well as near the surface. Rotational kernels of the quadrupole modes are shown in the bottom panels of Fig. 4.18. To obtain a better estimate of the surface-to-core rotation rate, we only use the rotation rates derived from the pure p-mode triplet near $f = 12.76$ d^{-1}. For this triplet $\Omega_{e,1}$ ranges from 0.131 ± 0.003 d^{-1} to 0.137 ± 0.003 d^{-1}, using either modes of $n = 1$ or $n = 2$ of both Models 2 and 3. Thus, we find almost uniform rotation with a slightly faster core than envelope, with $\Omega_{e,1}/\Omega_{c,1} = 0.94 \pm 0.2$ up to 0.98 ± 0.2.

Moreover, we use the p modes to compare the scenario that predicts the mean period spacing and the binary parameters (Models 2 and 3), to the scenario that predicts the period spacing morphology (Model 6). We find that the p modes of Model 6 have frequencies that are too high and therefore do not agree with the observations. Aside from the binary parameters, the p-mode frequencies are thus another indication that Models 2 and 3 are indeed better representations for the two stars of KIC 10080943 than Model 6.

4.4.5 Orbital evolution

As a consequence of tidal interaction, we expect binary systems to synchronise the rotation rates of their components with the orbital period and to circularise their orbits over time (Sect. 1.4.3 or Zahn 1977). In Chapter 3 we found an eccentricity $e = 0.4535 \pm 0.0004$ for the orbit of KIC 10080943 and in Sect. 4.4.4 we find envelope rotation rates that are different from the orbital frequency $f_{\mathrm{orb}} = 0.06520 \pm 0.00004$ d^{-1}. Hence, both components rotate asynchronously with the orbit. At an age of ~ 1.1 Gyr, however, the tidal forces have had a long time to influence the system. We can estimate the timescales on which synchronisation and circularisation is expected for a system like KIC 10080943, using the formulae presented in Sec. 1.4.3 and assuming

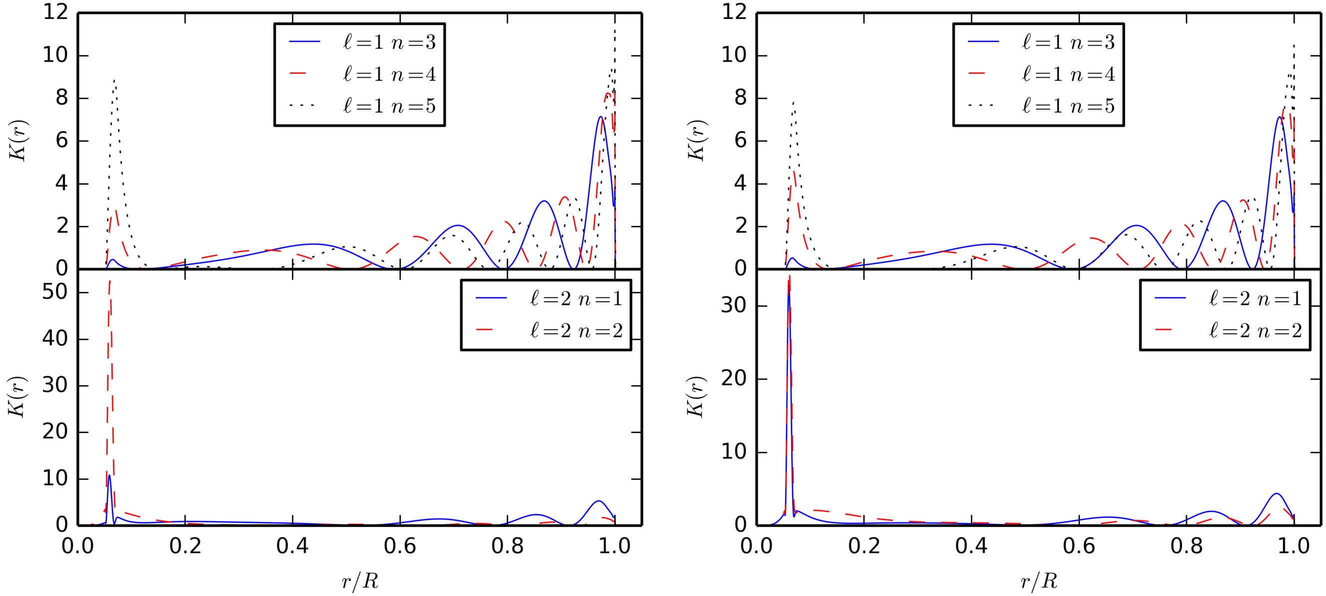

(a) Kernels of the primary of Model 2.

(b) Kernels of the primary of Model 3.

Figure 4.18: Rotation kernels (see Eq. (3.356) in Aerts et al. 2010) as a function of fractional radius for the dipole and quadrupole modes of mixed-mode character. As a comparison the dipole mode of order $n = 3$ is shown, which is a pure p mode.

$I/MR^2 \sim 10^{-2}$ and $E_2 \sim 10^{-8}$ (Zahn 1975). Circularisation is expected to occur only after $\sim 10^{12}$ years for stars with a deep convective envelope or after $\sim 10^{14}$ years and $\sim 10^{16}$ years for a primary and secondary component with a radiative envelope, respectively. The seismic age is thus in good agreement with the eccentric orbit of the system. Synchronisation happens on a shorter timescale than circularisation. For stars with a convective envelope, synchronous rotation is predicted to occur at an age of $\sim 5 \times 10^8$ years. This is seemingly in contradiction with the age and the rotation rates that we derived for KIC 10080943. However, our models have shallow convective envelopes with a depth of $\sim 0.03\ R_\odot$ and $\sim 0.025\ R_\odot$ for the primary and the secondary, respectively. These envelopes contain only a mass of $\sim 3 \times 10^{-8}\ M_\odot$ and $\sim 2 \times 10^{-8}\ M_\odot$ for the primary and secondary, respectively. It is thus questionable whether these are efficient in dissipating the tides. For stars with radiative envelopes the synchronisation timescales for the primary and the secondary are $\sim 4 \times 10^{10}$ years and $\sim 4 \times 10^{11}$ years, respectively. Hence, long enough to be consistent with the seismic age.

4.5 Summary

In this chapter we have presented detailed seismic modelling for two F-type g and p mode hybrid pulsators that reside in the binary system KIC 10080943 (Chapter 3; Keen et al. 2015; Schmid et al. 2015). We calculated stellar model grids with MESA, covering the observed range of stellar parameters, and compared the observed pulsation modes to predictions by the stellar pulsation code GYRE. For the analysis, we were able to exploit observational constraints from the binarity and the pulsations. This was implemented by requiring an equal age and composition, the mass ratio, and the position in the HRD within 2σ of the binary solution, together with asymptotic period spacing values within 2σ of the observed mean period spacing. With this approach, we provide the first such consistent seismic modelling of a binary F-type g-mode pulsator. We find that the stars have an age of $\simeq 1.1$ Gyr and have a low central hydrogen mass fraction of $X_{c,1} \simeq 0.1$ and $X_{c,2} \simeq 0.2$. This is a consequence of the observed mean period spacing values, which are below 3000 s and, thus, rather low for $2\ M_\odot$ stars. In fact, our best models have masses 2σ below the binary values. However, the age is in good agreement with the observed HRD positions of both stars with cool temperatures and big radii. Furthermore, we were able to determine the rotation rates of the regions near the core to be $\Omega_{c,1} = 0.13963 \pm 0.00007\ \mathrm{d}^{-1}$ and $\Omega_{c,2} = 0.09034 \pm 0.00002\ \mathrm{d}^{-1}$. When the traditional approximation of rotation is used at these rotation rates instead of the first-order perturbative Ledoux approximation, a lower asymptotic period spacing is required for both stars. This is because the zonal modes are influenced by the Coriolis force and shifted to higher frequencies.

To test the shape of the convective-core overshooting we computed two grids that differ only in the overshooting prescription. One grid uses exponential core overshooting, while the other uses step overshooting. We could not find a significant difference between these two grids, in the sense that the difference in morphology of the period spacing pattern between these two descriptions is by far inferior to the discrepancy between the observed and theoretical morphology. We could show, however, that the stellar parameters derived from binary modelling and the requirement of equal age and composition for both stars, can constrain the amount of overshooting and diffusive mixing. For the primary, we find high values of overshooting and low values of diffusion and for the secondary we find the opposite. The best model for the exponential overshooting grid is $M_1 = 1.82\ M_\odot$, $M_2 = 1.76\ M_\odot$, $Z = 0.0125$, $f_{\rm ov,1} = 0.008$, $f_{\rm ov,2} = 0.005$, $\log(D_{\rm mix,1}) = 0.25$, and $\log(D_{\rm mix,2}) = 1.5$; $f_{\rm ov}$ is expressed in local pressure scale height H_P and $D_{\rm mix}$ has a unit of cm^2 s^{-1}. For the step overshooting grid, the best model is similar at $M_1 = 1.81\ M_\odot$, $M_2 = 1.76\ M_\odot$, $Z = 0.0125$, $\alpha_{\rm ov,1} = 0.11$, $\alpha_{\rm ov,2} = 0.05$, $\log(D_{\rm mix,1}) = 0.25$, and $\log(D_{\rm mix,2}) = 1.75$.

These best models fail to predict the detailed period spacing structure, which points to the limitations of 1D stellar models in terms of chemical mixing in the radial direction only. For these 1D stellar models, we find a better agreement with the observed structures for stars that have a higher X_c and more similar mixing parameters, which contradicts the observed mean period spacing and stellar parameters. We are able to find a coeval model with low masses and metallicity that fits both the morphology and mean value of the period spacing. Yet, the p-mode frequencies of this model are too high to reproduce the observed frequencies. This points mean densities that are too high or radii that are too small. This model, indeed, has a discrepancy with the binary modelling at $+3\sigma$ level. Especially, the primary radius of the model is 4σ below the observed value. An independent measurement of the radius, for example through a precise distance provided by the ESA Gaia mission (Perryman et al. 2001), could help to firmly exclude such younger models. The fact that the variations of the period spacing of the primary are too strong clearly points towards missing extra mixing in the transversal direction, which is perhaps of rotational origin.

During our analysis, we ignored the influence both stars have on each other and modelled them as coeval single stars. This approach is justified, as the observed interaction is weak and we relied on the g modes, whose probing power is situated near the core. We can estimate the tidal influence by the tide-generating potential, which depends on the small parameter $\varepsilon_T = (R_1/a)^3(M_2/M_1)$ (e.g. Willems & Aerts 2002) and find $\varepsilon_T \approx 3.7 \times 10^{-4}$ for KIC 10080943. The influence of the centrifugal force due to the rotation on the pulsations can be estimated by $(\Omega/f_{\rm co})^2$, which lies between 0.01 and 0.017 for the primary and between 0.005 and 0.014 for the secondary (see e.g. Aerts et al. 2002). Thus, the centrifugal force has a much stronger influence on the pulsations than the tides, but is so small that our approach based on the Coriolis force above is fully justified. Also, the brightening signal, which is detected in the high-precision *Kepler* light curve, has a small amplitude and the reflection effect outweighs the contribution of the tidal distortion. Some evidence of the tidal forces, however, could be detected in one $\ell = 1$ g mode, which has a frequency of exactly $15f_{\mathrm{orb}}$, and in the rotational splitting of the p modes (Schmid et al. 2015). The next step towards improving the modelling of this binary would be to create a binary model that takes these interactions into account. Such models could also help gauge the effect the tidal forces have on the level of mixing or the convective-core size. The best models we obtained so far constitute a fruitful starting point for more detailed studies such as these. Other future work could include mode excitation. As of now, GYRE does not include a pulsation-convection interaction, which would be necessary to study the mode excitation by convective flux blocking (Guzik et al. 2000; Dupret et al. 2005). Therefore, KIC 10080943 is a rich target, which still holds potential for improving stellar and seismic models.

Appendix A: MESA inlist

```
! MESA inlist for KIC10080943 grid calculations
! Parameters input via run_star_extras.f not in inlist
! evolve main sequence model starting from ZAMS

&star_job

!!! start from ZAMS
    relax_Z = .true.
    change_Z = .true.
    relax_initial_Z = .true.
    change_initial_Z = .true.
    ! new_Z set via run_star_extras.f

    relax_Y = .true.
    change_Y = .true.
    relax_initial_Y = .true.
    change_initial_Y = .true.
    ! new_Y set via run_star_extras.f

!!! Composition and opacities (Asplund09+OPAL)
    kappa_file_prefix = 'a09'
    kappa_lowT_prefix =  'lowT_fa05_a09p'
    initial_zfracs = 6

    change_lnPgas_flag = .true.
    change_initial_lnPgas_flag = .true.
    new_lnPgas_flag = .true.
```

```
    change_net = .true.
    new_net_name = 'pp_cno_extras_o18_ne22.net'
    change_initial_net = .true.

  ! display on-screen plots
    pgstar_flag = .false.

/ !end of star_job namelist



&controls

!!! Starting specifications
    ! initial_mass set via run_star_extras.f

!!! Atmosphere
    which_atm_option = 'photosphere_tables'

!!! Mixing
  ! Diffusive mixing
    set_min_D_mix = .true.
    !min_D_mix set via run_star_extras.f
    remove_small_D_limit = 0

  ! Convection MLT
    mixing_length_alpha = 1.8

  ! Over- and undershooting
    D_mix_ov_limit = 5d-2

    ! for coarse and exponential overshoot grid
    ! overshoot_f_above_burn_h set via run_star_extras

    ! for step overshoot grid
    ! step_overshoot_f_above_burn_h set via run_star_extras

    overshoot_f0_above_burn_h = 0.001

    step_overshoot_D = 0
    step_overshoot_D0_coeff = 1
```

```
    num_cells_for_smooth_brunt_B = 0
    num_cells_for_smooth_gradL_composition_term = 0

!!! Time step control
    varcontrol_target = 2.5d-5

    max_age = 2d10
    max_years_for_timestep = 1d7

  ! Stop condition
    xa_central_lower_limit_species(1) = 'h1'
    xa_central_lower_limit(1) = 1d-3
    when_to_stop_rtol = 1d-3
    when_to_stop_atol = 1d-3

!!! Mesh grid
    max_allowed_nz = 10000
    mesh_delta_coeff = 0.5
    cubic_interpolation_in_Z = .true.

    xa_function_species(1) = 'he4'
    xa_function_weight(1) = 100
    xa_function_param(1) = 1d-2

    xa_function_species(2) = 'he3'
    xa_function_weight(2) = 100
    xa_function_param(2) = 1d-5

    mesh_dlogX_dlogP_extra(:) = 0.1
    mesh_dlogX_dlogP_full_on(:) = 2
    mesh_dlogX_dlogP_full_off(:) = 1

    mesh_logX_species(1) = 'he4'
    mesh_logX_min_for_extra(1) = -6
    mesh_logX_species(2) = 'n14'
    mesh_logX_min_for_extra(2) = -6
    mesh_logX_species(3) = 'c12'
    mesh_logX_min_for_extra(3) = -6

    xtra_coef_czb_full_on = 1.0
    xtra_coef_czb_full_off = 1.0
```

```
    xtra_coef_a_l_nb_czb = 0.1
    xtra_dist_a_l_nb_czb = 10.0
    xtra_coef_b_l_nb_czb = 0.1
    xtra_dist_b_l_nb_czb = 3.0

    okay_to_remesh = .true.

!!! GYRE output
    write_pulse_info_with_profile = .true.
    pulse_info_format = 'GYRE'
    add_atmosphere_to_pulse_info = .true.

/ ! end of controls namelist
```

Chapter 5

Conclusions and future prospects

Detailed asteroseismic studies can highlight discrepancies in the current theory of stellar structure and can point into the direction of improvement. Additional input can be provided by binary stars, which enable us to derive stellar parameters independent of stellar models. In this thesis we presented two case studies of intermediate-mass pulsating stars residing in binary systems. We showed short-comings of stellar models and the importance of binary stars.

In Chapter 2 we attempted mode identification for the δ Sct star 4 CVn. For this analysis we used a highly resolved spectroscopic data set, spanning over four years from January 2008 until June 2011. The variations in the absorption-line profiles can be used to derive the pulsation mode frequencies and the quantum numbers ℓ and m. Based on the variations of the radial velocities derived from the spectra, we discovered that 4 CVn is the primary component of a wide eccentric binary ($P = 124.44$ d, $e = 0.311$). After correcting for the binary motion, we detected 20 pulsation frequencies, including 9 that were not found in photometric data before. Yet, we were not able to obtain distinct results from the mode identification for the two dominating modes, owing mainly to the fast rotation of 4 CVn. For this mode-identification technique it is crucial to use unblended absorption lines that are deep and sharp. However, the fast rotation leads to rotational broadening of each line of $v \sin i \simeq 106.7\ \mathrm{km\,s^{-1}}$, which means that most lines in the already dense F-type spectrum are blended. In the observed range from 4200 Å to 4700 Å, we only found one suitable line: Fe II at 4508.288 Å. We attempted to solve this problem by computing an average line profile, using the least-squares deconvolution technique (LSD, Donati et al. 1997; Kochukhov et al. 2010). We found that the pulsation signal was smeared out in the LSD profiles, as we detected fewer frequencies than in the single Fe II line, yet with a lower S/N. Furthermore, fast rotation alters the geometry of the modes (Reese et al. 2009). As 4 CVn rotates at a third of its critical break-up velocity or even faster, this could be an explanation why we obtained such poor fits to the variable line profiles. The current methodology for spectroscopic mode identification is based on one-dimensional spherical equilibrium models, which excludes a description of rotational deformation. We were not able to constrain the inclination angle of the rotation axis, which means that the rotation could be even faster than the measured $v \sin i$. In addition to the asteroseismic analysis, we presented an abundance analysis and revision of the fundamental atmospheric parameters. We used these results to define two sets of stellar input parameters, in addition to the model by Breger & Pamyatnykh (2002), for mode identification. It was not possible to distinguish between these three sets of stellar parameters, based on our results and the χ^2 statistics. Unfortunately, we could not use the binarity to obtain more precise stellar parameters, as we did not detect any signal of the secondary. The primary star is a sub-giant and is far more luminous than the likely low-mass companion.

When a complete description of rotation, including higher-order effects and the centrifugal force, is incorporated into stellar pulsation codes, the present data could be revisited, as a better interpretation of the observations can be obtained. Moreover, an extension of the mode-identification technique to include blended lines would allow us to use a larger part of the spectra. Repeating this extensive observing campaign for 4 CVn, to obtain spectra in a wider wavelength range would require a huge amount of time and effort. Rather, it would be better to set up such a campaign for a known moderately-rotating δ Sct pulsator in a double-lined, eclipsing binary system. For such a system, accurate masses and radii can be derived and the inclination angle of the rotation axis can be approximated by the orbital inclination. This provides useful constraints for mode identification from line-profile variations, which in turn would be a crucial input for seismic modelling.

For four years, the *Kepler* satellite observed about 150 000 stars almost continuously with sub-mmag precision. These are ideal prerequisites for characterising pulsating stars in double-lined binary systems. One such system is KIC 10080943. Tkachenko et al. (2013a) discovered that it is a double-lined binary system showing γ Dor and δ Sct-like pulsations. The periodogram of KIC 10080943 shows regular patterns from the longest to the shortest periods. In the long-period regime, we found several frequencies that are exact multiples of the orbital frequency, i.e. orbital harmonics. These originate from a non-sinusoidal brightening signal that is recurrent with the orbital period at the phase of periastron passage and is consistent with reflection or ellipsoidal variation in an eccentric orbit. In the short ($P = 15.3364$ d) and eccentric ($e = 0.454$) orbit, the stars approach close enough at periastron to become deformed and to mutually heat the hemispheres facing each other. We derived the masses and radii of both components, as well as the system parameters from modelling the brightness and radial velocity variations, taking into account degeneracies found between the equipotential surfaces and the surface albedos and gravity darkening exponents. Unfortunately, we found that the orbital inclination is only weakly constrained from the observed effects.

There is remarkable regularity among the pulsation modes of KIC 10080943. In the g-mode regime, we detected six series of modes equally spaced in period. Three of these form rotationally split triplets of retrograde, zonal, and prograde dipole modes, associated with the primary. Two series form rotationally split doublets of prograde and retrograde dipole modes that belong to the secondary. We found evidence for equally spaced quadrupole modes as well that could not be attributed with certainty to either of the stars. In the p mode range we detected four rotationally split multiplets with two different splitting values. This is evidence that both stars pulsate as γ Dor/δ Sct hybrids. From phase variations of the high-amplitude p modes that are due to the light-travel time effect in the binary orbit, we could distinguish between pulsations arising in the primary or in the secondary component. Using the observed phase modulation and non-linear coupling between the g and the p modes, we could unravel which g mode period-spacing series and which p-mode multiplets belong to which star. We derived preliminary core-to-surface rotation rates and found slight differential rotation in the radial direction for both components.

In Chapter 4 we used these stringent observational constraints to perform seismic modelling of both KIC 10080943A and KIC 10080943B. To this end, we computed the zonal dipole and quadrupole modes of non-rotating stellar models and ignored the tidal influence the two stars have on each other, which is justified given the weak tide-generating potential of $\varepsilon_T \approx 3.7 \times 10^{-4}$. The g modes are sensitive to the conditions near the stellar core. Chemical composition gradients, as well as rotation, lead to departure from equidistant spacings in periods of the g modes (Miglio et al. 2008; Bouabid et al. 2013). The asymptotic period spacing is furthermore dependent on the mass and metallicity of the models. Therefore, we calculated grids of stellar models, where mass, metallicity and the mixing mechanisms of convective-core overshooting and diffusive mixing are described by free parameters in the MESA stellar evolution code. Since these two stars form a binary system, we knew their precise mass, radii, and temperature ratios and could assume that they have an equal age and composition. These requirements, as well as the observed period spacings, served as observational constraints. We found that both stars are close to the terminal-age main sequence with low central-hydrogen mass fractions and an age of some 1.1 Gyr. The masses of our best seismic models occur at 2σ below the values determined from binary modelling. We tested two different descriptions of core overshooting, exponential overshooting and step overshooting, and could not distinguish between the two. The observed and calculated period spacing morphologies show too large discrepancies to find a significant difference between the two shapes of overshooting. When we aimed at explaining the period spacing morphology better, we lost the agreement with the stellar parameters derived from binarity at $+3\sigma$ level and failed to predict the observed p modes. The diffusive mixing in the radial direction of the one-dimensional stellar models, which serves as a fudge factor for the missing rotational mixing and other unknown mixing mechanisms, is clearly insufficient as a physical description to explain the structure of the Brunt-Väisälä frequency. However, a solid conclusion is that it is necessary to include a certain level of chemical mixing to explain the positions in the HRD and the observed mean period spacing values of the two stars at equal age. Moreover, we used the computed p modes to derive accurate values for the core-to-surface rotation rates. For the primary, we found almost uniform rotation with a slightly faster core. For the secondary, we found that it is rotating differentially with a faster envelope than core. Such different core-to-envelope rotation was also found for two single hybrid F-type pulsators from *Kepler* data recently and is well explained by the phenomenon of internal gravity waves (Rogers 2015). In a binary system the rotation rates of the components are influenced by the tidal forces, which ultimately lead to synchronised rotation with the orbital period and a circular orbit. We estimated the timescales on which synchronisation and circularisation are expected to happen for KIC 10080943 and compared them to the seismic age. Given the extremely narrow convective envelopes of the stars, these timescales are longer than the derived age and are thus in agreement with the observed asynchronous rotation and high eccentricity of the orbit.

As already mentioned, we ignored tidal forces among these two stars and modelled them as single stars. While the influence is indeed weak it is still present, as we observe one dipole g mode of the secondary with a frequency of $15f_{\mathrm{orb}}$. The tidal influence can also be observed in the splittings of the p modes. A more accurate model can therefore be obtained, by treating KIC 10080943A and KIC 10080943B as binary stars subject to tides. Tidal forces could also be a possible origin of chemical mixing, which is currently insufficiently explained by the one-dimensional models. For this endeavour, the models we presented in this thesis can serve as a valuable starting point. Furthermore, we only made limited use of the p modes. This is due to insufficient mode identification, which was based on the assumption that all observed multiplets are complete. The white-light photometry by *Kepler* does not allow to identify the degree of the observed modes. For this, ground-based multi-colour photometry or high-resolution spectroscopy would have to be obtained (as was done for 4 CVn in Chapter 2). Once the mode degrees of the p modes are known, mode excitation can be included into the modelling process as well. Additionally, mode excitation could also be computed for the g modes, with a seismic code that includes the pulsation-convection interaction. Obviously, KIC 10080943 has the potential for many follow-up analyses.

Table 5.1: Orbital parameters of the single-lined binaries.

	KIC 5790807	KIC 10001167
Photometric solution		
$P_{\mathrm{orb,Kp}}$ (d)	79.9962 ± 0.0005	120.39097 ± 0.00094
$T_{0,\mathrm{Kp}}$ (BJD)	54960.13	54957.6 ± 0.8
Radial velocity solution		
$P_{\mathrm{orb,RV}}$ (d)	79.961 ± 0.025	120.35 ± 0.12
$T_{0,\mathrm{RV}}$ (BJD)	2 456 480.94 ± 0.06	2 456 508.7 ± 0.4
e	0.852 ± 0.006	0.160 ± 0.002
ω (deg)	162.7 ± 1.1	214 ± 1.3
K (km s^{-1})	23.4 ± 0.8	24.97 ± 0.04
γ (km s^{-1})	−27.97 ± 0.098	−103.5 ± 0.02
$a_1 \sin i$ ($R_{\odot}$)	19.3 ± 0.8	58.6 ± 0.1

5.1 Towards extending the sample of known binary pulsators

The two case-studies, 4 CVn and KIC 10080943, presented here show what pulsating stars in binary systems can add to seismic modelling. The lack of constraints we can achieve for 4 CVn and the modest accuracy obtained for the stellar parameters of KIC 10080943 highlight that double-lined eclipsing binaries deliver the most stringent constraints. It would thus be interesting to repeat such analyses as presented in this thesis, but for double-lined eclipsing binaries containing multiperiodic pulsating stars. Furthermore, it is also crucial to analyse systems that exhibit period spacings in the g modes, as these hold the most information on the stellar interior. Many of the *Kepler* targets have not been studied in detail yet. Van Reeth et al. (2015b) have presented a sample of 67 γ Dor stars and found period spacing for 50 of these stars. However, most are single stars and the binaries among them are non-eclipsing. Several such pulsating stars are thus, undoubtedly present in the *Kepler* data. A dedicated search for double-lined eclipsing *Kepler* targets of intermediate mass with a highly structured periodogram could lead to many new avenues for the theory of stellar structure. It would furthermore extend the number of stars with known overshooting parameters, which would enable a statistical analysis of this phenomenon as a function of stellar characteristics, as in Aerts et al. (2014) for massive OB stars.

To provide a starting point for more such detailed studies, we have selected a sample of five targets from the *Kepler* Eclipsing Binary Catalogue and obtained follow-up spectroscopy with the HERMES spectrograph. All targets have $Kp < 12$ mag, detached components, and clear signs of variation or pulsations in the phases outside eclipse. We extracted the radial velocities from the spectra as explained in Sect. 1.5.2, using

Table 5.2: Orbital parameters of the double-lined binaries.

	KIC 6117415	KIC 10031808
Photometric solution		
$P_{\mathrm{orb,Kp}}$ (d)	19.741625 ± 0.000077	8.58964 ± 0.00002
$T_{0,\mathrm{Kp}}$ (BJD)	54969.45	54956.43 ± 0.06
Radial velocity solution		
$P_{\mathrm{orb,RV}}$ (d)	19.73 ± 0.01	8.590 ± 0.007
$T_{0,\mathrm{RV}}$ (BJD)	$2\,456\,410.31 \pm 0.03$	$2\,455\,300.10 \pm 0.03$
e	0.754 ± 0.005	0.273 ± 0.006
ω (deg)	211.7 ± 0.2	275 ± 1
q	0.94 ± 0.02	0.970 ± 0.009
K_1 (km s^{-1})	81 ± 1	80.3 ± 0.5
K_2 (km s^{-1})	86 ± 2	82.8 ± 0.6
γ (km s^{-1})	-21.7 ± 0.8	12.0 ± 0.3
$a \sin i$ ($R_\odot$)	42.8 ± 0.7	26.6 ± 0.1

F0 or G2 line masks, and obtained orbital parameters. In the following, we introduce these five systems in order to trigger follow-up studies.

KIC 8823868 or *Kepler* Object of Interest KOI-81 is an A-type star in orbit with a less-luminous, yet hotter object, presumably a white dwarf (Rowe et al. 2010; van Kerkwijk et al. 2010). This configuration implies a history of mass exchange in the system. A similar object, also discovered by Rowe et al. (2010) is the Doppler-beaming system KOI-74 (van Kerkwijk et al. 2010; Bloemen et al. 2012). Evidence for Doppler beaming was also detected for KOI-81, however, with a much weaker signal and entangled with pulsations. In Fig. 5.1 we show the phase-folded light curve, a zoom to show the pulsations and a frequency spectrum. The frequency spectrum was computed after the eclipses were cut from the light curve. While an interesting target for A-star g-mode asteroseismology, this star was not the main focus of our attention so far, due to more suitable targets for our PhD research.

From the four eclipsing binaries for which radial velocities could be extracted, two are single-lined systems: **KIC 5790807** and **KIC 10001167**. We fitted a Keplerian orbit to the radial-velocity curves, to obtain the orbital parameters: period P_{orb}, time of periastron passage T_0, eccentricity e, longitude of periastron passage ω, semi-amplitude of the radial-velocity curve K, and systemic velocity γ. From these orbits, we computed the semi-major axis of the primary orbit $a_1 \sin i$. Table 5.1 lists these values for KIC 5790807 and KIC 10001167 along with the orbital period and time of superior conjunction obtained from the *Kepler* photometry (for some systems and parameters no uncertainties are reported). The former, illustrated in Fig. 5.2, is an eccentric ($e = 0.852$) system, which only displays one eclipse and a brightening

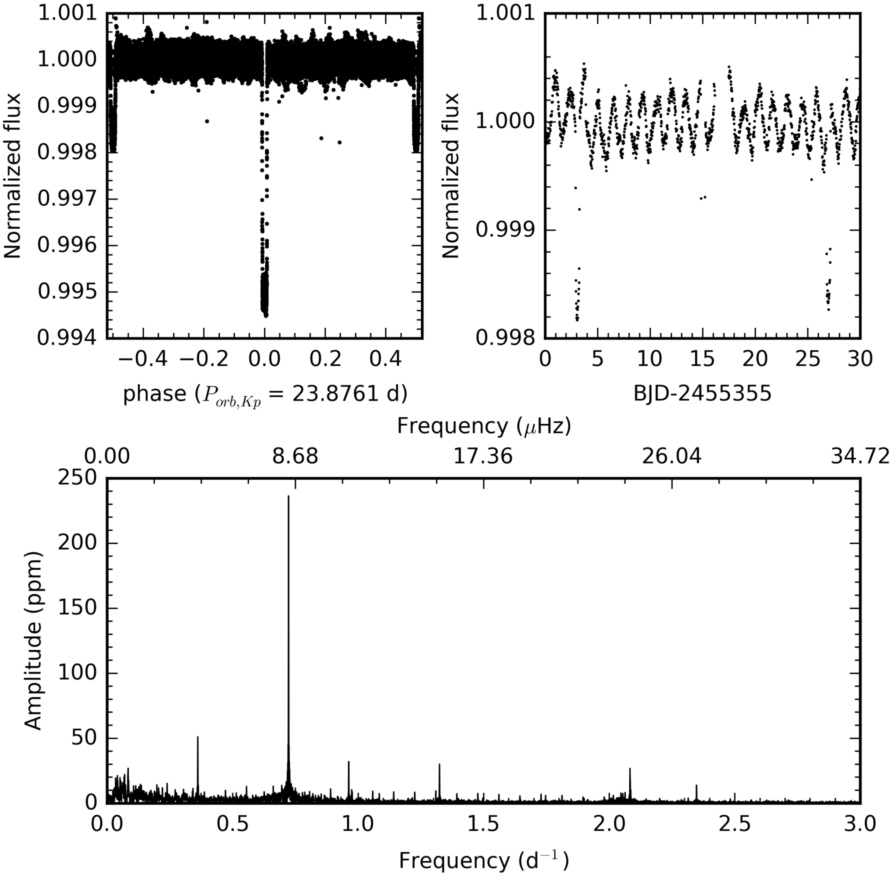

Figure 5.1: *Top-left panel:* Phase-folded *Kepler* light curve of KIC 8823868 or KOI-81 using the ephemeris BJD = 54988.01(9) + 23.8761(1) × E. *Top-right panel:* A zoom onto the light curve to show the pulsations. *Bottom panel:* A frequency spectrum of the light curve without eclipses. No variability beyond 3 d^{-1} was detected.

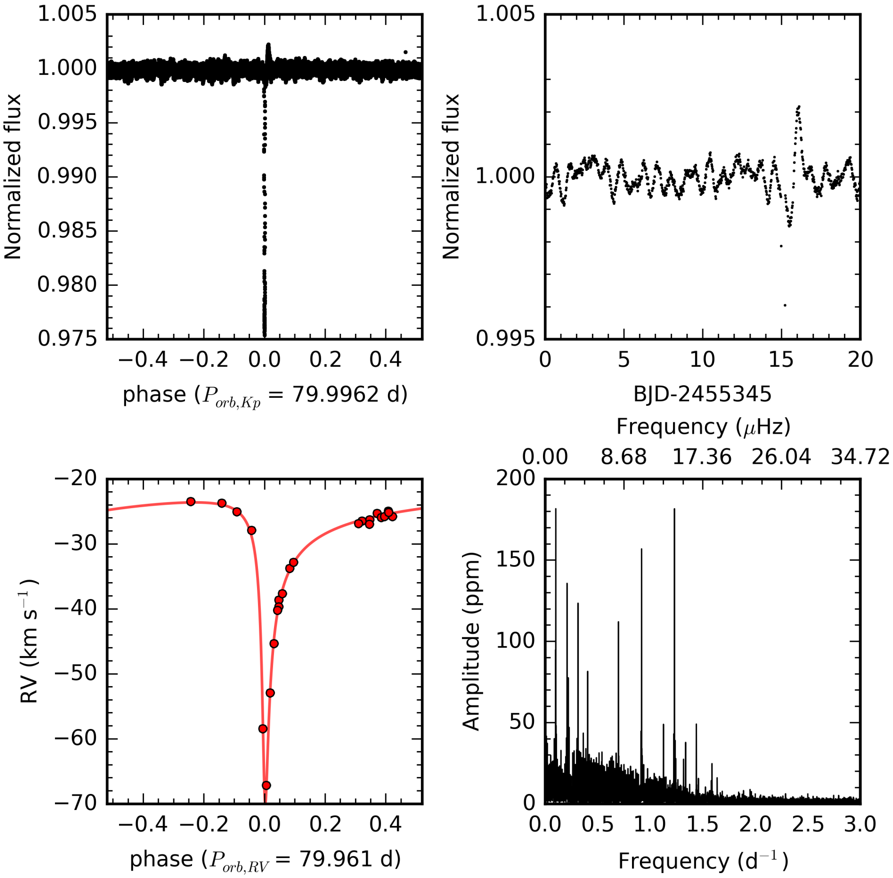

Figure 5.2: *Top-left panel: Kepler* light curve of KIC 5790807 phase-folded onto the period of the eclipses. *Top-right panel:* A 20-d zoom of the light curve. *Bottom-left panel:* HERMES radial velocities (red dots) with the orbital fit shown as the red solid line, phase-folded onto the period of the radial velocities. *Bottom-right panel:* Fourier transform of the light curve after the eclipses have been cut out.

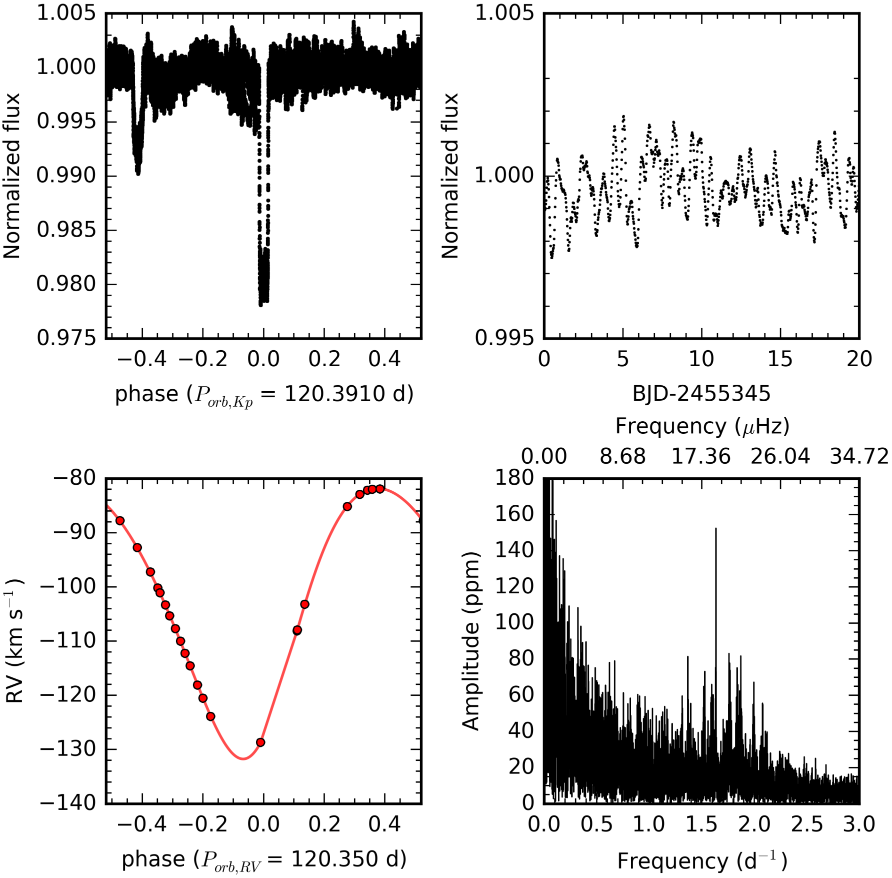

Figure 5.3: Same as Fig. 5.2 but for the eclipsing red giant KIC 10001167.

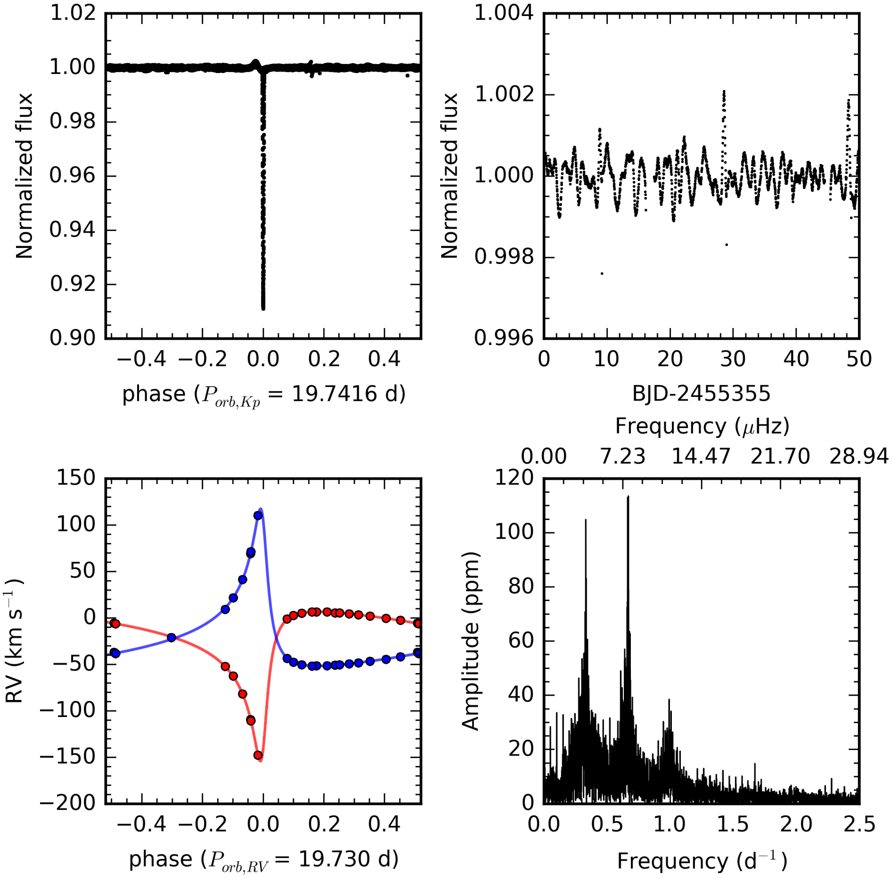

Figure 5.4: *Top-left panel: Kepler* light curve of KIC 6117415 phase-folded by the ephemeris obtained from the EB Catalogue. *Top-left panel:* A zoom onto the *Kepler* light curve to show the pulsation signal. *Bottom-left panel:* HERMES radial velocities of the more massive primary (red dots) of the secondary (blue dots). Orbital fits, with the parameters of Table 5.2 are shown as the red and blue solid line for the primary and secondary, respectively. *Bottom-right panel:* A Fourier transform after the eclipses and brightening signal have been cut from the light curve.

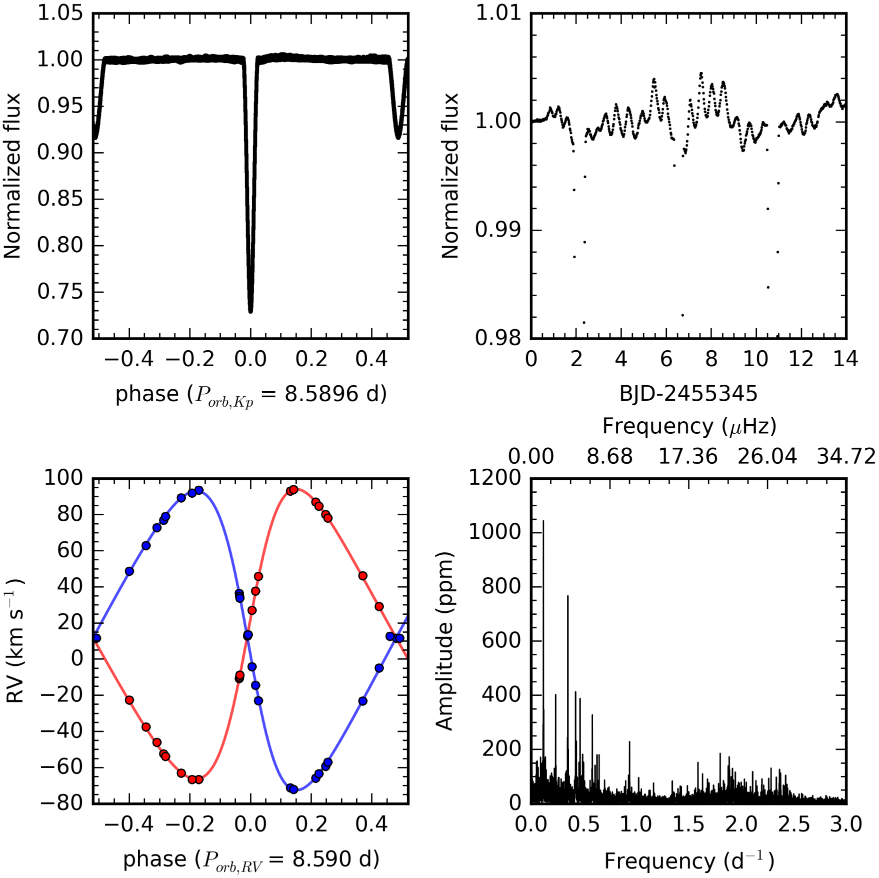

Figure 5.5: Same as Fig. 5.4, but for KIC 10031808.

signal. This system is a good candidate for tidally-induced pulsations, given its high eccentricity. Indeed, there are clear peaks of low frequency with significant amplitude in the Fourier transform when calculated after cutting the eclipses from the light curve but keeping the brightening signal (bottom-right panel of Fig. 5.2). The data of KIC 10001167 are shown in Fig. 5.3. It has a much lower eccentricity and a flat-bottomed primary eclipse. We have used an Arcturus line mask to extract the radial velocities, as this system is one of 19 eclipsing red-giants with solar-like oscillations, observed by *Kepler* and meanwhile studied by another research team (Gaulme et al. 2013, 2014). In the periodogram (bottom-right panel of Fig. 5.3), we detect a power excess due to oscillations.

Two of the eclipsing binary systems are double-lined, those are **KIC 6117415** and **KIC 10031808**. For these systems we obtain two sets of radial velocities, one for the primary and one for the secondary, which were both fitted with Keplerian orbits. Their orbital parameters from radial velocities are compared to the parameters derived from *Kepler* photometry in Table 5.2. Here, we can also obtain the mass ratio of the system $q = K_1/K_2 = M_2/M_1$ and the semi-major axis of the relative orbit $a \sin i$. In Fig. 5.4 we show the light curve and radial velocity curves of KIC 6117415 and Fig. 5.5 displays the data for KIC 10031808.

5.2 Other current and future space missions

After two of the four reaction wheels that keep the pointing of *Kepler* stable failed, the mission was repurposed to observe the ecliptic plane as K2 (Howell et al. 2014). By observing in the ecliptic plane, the solar pressure is minimised but the spacecraft has to correct its pointing for the drift every $\sim$ 12 h. Different fields-of-view are observed for about 85 days each, after which the satellite has to point to a different field to avoid sunlight from entering the apertures. The advantage of this mission, is that many different targets can now be observed with K2. However, the short duration of each campaign leads to a much lower frequency resolution, which makes the detection of g mode period spacings and rotational splittings harder.

There are two more upcoming space missions that could bring about new advances in the fields of asteroseismology and binary stars. The Transiting Exoplanet Survey Satellite (TESS; Ricker et al. 2015) is a NASA mission, to be launched end 2017. It is the follow-up mission of *Kepler* and its main purpose is to search for planets around bright stars, using the transit method like its precursor. To this end, it will conduct an all-sky survey for two years, spending one year per hemisphere. The array of four lenses covers an area of $96^\circ \times 24^\circ$, extending from the poles to 6° above the ecliptic in length. It will sweep the sky and produce light curves of 27-d length in the tile closest to the ecliptic and of 351-d length on the poles. One clear advantage this mission has over *Kepler* is that it surveys bright and nearby stars, making ground-based follow-up easier. However, the longest light curves that it will produce are of one year duration and therefore cannot compete with the frequency resolution produced by four year *Kepler* data.

The second mission is ESA's PLAnetary Transits and Oscillations of stars (PLATO; Rauer et al. 2014). It was chosen as the third medium-class mission by ESA on 19 February 2014 and launch is targeted for 2024. The goal of this mission is to find and classify transiting planetary systems around bright solar-type stars and to use asteroseismology to characterise the planet host star. For this it will use a novel multi-telescope design with 32 cameras, having a 25 s read-out cadence and 2 fast cameras operating at a 2.5 s cadence. This results in a large dynamic range, as it will observe stars from $m_V = 4 - 16$ mag, and a large field-of-view of $\sim$ 2250 sq. deg. This leads to stellar samples of hundreds of thousands. Among these, some 40 000 stars per pointing will be reserved for a rich complementary science programme that is open to anyone as Guest Observer. Observations are planned in three phases, where the first two phases are dedicated to two target fields that will be observed for two to three years each. After these two long-term fields the mission will conduct a step-and-stare phase, where numerous target fields will be observed for up to five months. The mission is planned for a six years life time. The advantage of this mission is obvious; the main focus again lies on bright stars, which are easy to follow up with ground-based facilities and light curves of a long time base will be produced for numerous stars, which is ideal for asteroseismology.

The future for asteroseismology of single or binary stars is therefore bright. Enormous amounts of data of unprecedented precision have been and will be produced by space missions in the future. The current bottleneck for interpretation is thus not on the observational side, but lies in the effort that has to be done for analysing one target to great detail. Furthermore, some puzzles in the theory of stellar structure and evolution that were highlighted by observations remain unsolved, such as the angular momentum transport within stars and internal mixing processes. Going toward more realistic two-dimensional or even three-dimensional stellar models could help and is probably necessary to solve these current shortcomings in the theory. Future computational advances will therefore greatly help stellar physics.

Bibliography

Abdul-Masih, M., Prša, A., Conroy, K., et al. 2016, AJ, 151, 101

Aerts, C. 2007, in IAU Symposium, Vol. 240, Binary Stars as Critical Tools & Tests in Contemporary Astrophysics, ed. W. I. Hartkopf, P. Harmanec, & E. F. Guinan, 432–441

Aerts, C. 2015, Astronomische Nachrichten, 336, 477

Aerts, C., Christensen-Dalsgaard, J., & Kurtz, D. W. 2010, Asteroseismology, 1st edn. (Springer), 866

Aerts, C., de Pauw, M., & Waelkens, C. 1992, A&A, 266, 294

Aerts, C., Eyer, L., & Kestens, E. 1998, A&A, 337, 790

Aerts, C., Handler, G., Arentoft, T., et al. 2002, MNRAS, 333, L35

Aerts, C., Molenberghs, G., Kenward, M. G., & Neiner, C. 2014, ApJ, 781, 88

Asplund, M., Grevesse, N., Sauval, A. J., & Scott, P. 2009, ARA&A, 47, 481

Auvergne, M., Bodin, P., Boisnard, L., et al. 2009, A&A, 506, 411

Ballot, J., Lignières, F., Reese, D. R., & Rieutord, M. 2010, A&A, 518, A30

Balona, L. A. 2014, MNRAS, 437, 1476

Balona, L. A. & Dziembowski, W. A. 2011, MNRAS, 417, 591

Balona, L. A., Guzik, J. A., Uytterhoeven, K., et al. 2011, MNRAS, 415, 3531

Balona, L. A., Krisciunas, K., & Cousins, A. W. J. 1994, MNRAS, 270, 905

Beck, P. G., Bedding, T. R., Mosser, B., et al. 2011, Science, 332, 205

Beck, P. G., Hambleton, K., Vos, J., et al. 2014, A&A, 564, A36

Beck, P. G., Montalban, J., Kallinger, T., et al. 2012, Nature, 481, 55

Bedding, T. R., Murphy, S. J., Colman, I. L., & Kurtz, D. W. 2015, in European Physical Journal Web of Conferences, Vol. 101, The Space Photometry Revolution - CoRoT Symposium 3, Kepler KASC-7 Joint Meeting, ed. R. A. García & J. Ballot, 01005

Bloemen, S., Degroote, P., Conroy, K., et al. 2013, in EAS Publications Series, Vol. 64, Setting a New Standard in the Analysis of Binary Stars, ed. K. Pavlovski, A. Tkachenko, & G. Torres, 269–276

Bloemen, S., Marsh, T. R., Degroote, P., et al. 2012, MNRAS, 422, 2600

Borucki, W. J., Koch, D., Basri, G., et al. 2010, Science, 327, 977

Bouabid, M.-P., Dupret, M.-A., Salmon, S., et al. 2013, MNRAS, 429, 2500

Bradley, P. A., Guzik, J. A., Miles, L. F., et al. 2015, AJ, 149, 68

Breger, M. 1990, Delta Scuti Star Newsletter, 2, 13

Breger, M. 2000a, in Astronomical Society of the Pacific Conference Series, Vol. 210, Delta Scuti and Related Stars, ed. M. Breger & M. Montgomery, 3

Breger, M. 2000b, MNRAS, 313, 129

Breger, M. 2010, in Variable Stars, the Galactic halo and Galaxy Formation, ed. C. Sterken, N. Samus, & L. Szabados, 95

Breger, M. 2016, A&A, 592, A97

Breger, M. & Bischof, K. M. 2002, A&A, 385, 537

Breger, M., Davis, K. A., & Dukes, R. J. 2008, Communications in Asteroseismology, 153, 63

Breger, M., Handler, G., Garrido, R., et al. 1999, A&A, 349, 225

Breger, M., Lenz, P., Antoci, V., et al. 2005, A&A, 435, 955

Breger, M. & Pamyatnykh, A. A. 2002, in Astronomical Society of the Pacific Conference Series, Vol. 259, IAU Colloq. 185: Radial and Nonradial Pulsations as Probes of Stellar Physics, ed. C. Aerts, T. R. Bedding, & J. Christensen-Dalsgaard, 388

Breger, M. & Pamyatnykh, A. A. 2006, MNRAS, 368, 571

Breger, M., Stich, J., Garrido, R., et al. 1993, A&A, 271, 482

Cantiello, M., Mankovich, C., Bildsten, L., Christensen-Dalsgaard, J., & Paxton, B. 2014, ApJ, 788, 93

Carroll, B. W. & Ostlie, D. A. 2006, An Introduction to Modern Astrophysics, 2nd edn. (Addison-Wesley), 1400

Castanheira, B. G., Breger, M., Beck, P. G., et al. 2008, Communications in Asteroseismology, 157, 124

Chaplin, W. J. & Miglio, A. 2013, ARA&A, 51, 353

Christensen-Dalsgaard, J. 2002, Reviews of Modern Physics, 74, 1073

Christensen-Dalsgaard, J., Dappen, W., Ajukov, S. V., et al. 1996, Science, 272, 1286

Claret, A. 2003, A&A, 406, 623

Claret, A. 2007, A&A, 475, 1019

Claret, A. & Bloemen, S. 2011, A&A, 529, A75

Conroy, K. E., Prša, A., Stassun, K. G., et al. 2014, AJ, 147, 45

Cousins, A. W. J. 1992, The Observatory, 112, 53

Cousins, A. W. J., Caldwell, J. A. R., & Menzies, J. W. 1989, Information Bulletin on Variable Stars, 3412

Cox, J. P. & Giuli, R. T. 1968, Principles of stellar structure (New York: Gordon and Breach)

Cunha, M. S., Aerts, C., Christensen-Dalsgaard, J., et al. 2007, A&A Rev., 14, 217

Cuypers, J., Aerts, C., De Cat, P., et al. 2009, A&A, 499, 967

De Ridder, J., Barban, C., Baudin, F., et al. 2009, Nature, 459, 398

Debosscher, J., Aerts, C., Tkachenko, A., et al. 2013, A&A, 556, A56

Degroote, P., Acke, B., Samadi, R., et al. 2011, A&A, 536, A82

Degroote, P., Aerts, C., Ollivier, M., et al. 2009, A&A, 506, 471

Degroote, P., Conroy, K., Hambleton, K., et al. 2013, in EAS Publications Series, Vol. 64, Setting a New Standard in the Analysis of Binary Stars, ed. K. Pavlovski, A. Tkachenko, & G. Torres, 277–284

Deheuvels, S., Ballot, J., Beck, P. G., et al. 2015, A&A, 580, A96

Deheuvels, S., Doğan, G., Goupil, M. J., et al. 2014, A&A, 564, A27

Deheuvels, S., García, R. A., Chaplin, W. J., et al. 2012, ApJ, 756, 19

Donati, J.-F., Semel, M., Carter, B. D., Rees, D. E., & Collier Cameron, A. 1997, MNRAS, 291, 658

Doyle, L. R., Carter, J. A., Fabrycky, D. C., et al. 2011, Science, 333, 1602

Driebe, T., Schoenberner, D., Bloecker, T., & Herwig, F. 1998, A&A, 339, 123

Duchêne, G. & Kraus, A. 2013, ARA&A, 51, 269

Dupret, M.-A., Grigahcène, A., Garrido, R., Gabriel, M., & Scuflaire, R. 2005, A&A, 435, 927

Foreman-Mackey, D., Hogg, D. W., Lang, D., & Goodman, J. 2013, PASP, 125, 306

Foreman-Mackey, D., Price-Whelan, A., Ryan, G., et al. 2014, triangle.py v0.1.1

Fuller, J., Cantiello, M., Lecoanet, D., & Quataert, E. 2015, ApJ, 810, 101

Fuller, J. & Lai, D. 2012, MNRAS, 420, 3126

Gaulme, P., Jackiewicz, J., Appourchaux, T., & Mosser, B. 2014, ApJ, 785, 5

Gaulme, P., McKeever, J., Rawls, M. L., et al. 2013, ApJ, 767, 82

Gilliland, R. L., Jenkins, J. M., Borucki, W. J., et al. 2010, ApJ, 713, L160

Goode, P. R. & Thompson, M. J. 1992, ApJ, 395, 307

Grevesse, N., Asplund, M., & Sauval, A. J. 2007, Space Sci. Rev., 130, 105

Grigahcène, A., Antoci, V., Balona, L., et al. 2010, ApJ, 713, L192

Grigahcène, A., Dupret, M.-A., Gabriel, M., Garrido, R., & Scuflaire, R. 2005, A&A, 434, 1055

Guzik, J. A., Kaye, A. B., Bradley, P. A., Cox, A. N., & Neuforge, C. 2000, ApJ, 542, L57

Hadrava, P. 1995, A&AS, 114, 393

Hambleton, K. M., Kurtz, D. W., Prša, A., et al. 2013, MNRAS, 434, 925

Handler, G. 1999, MNRAS, 309, L19

Hareter, M. 2012, Astronomische Nachrichten, 333, 1048

Heber, U. 2009, ARA&A, 47, 211

Henry, G. W., Fekel, F. C., & Henry, S. M. 2007, AJ, 133, 1421

Herwig, F. 2000, A&A, 360, 952

Hilditch, R. W. 2001, An Introduction to Close Binary Stars, 1st edn. (Cambridge University Press), 392

Howell, S. B., Sobeck, C., Haas, M., et al. 2014, PASP, 126, 398

Huber, D., Silva Aguirre, V., Matthews, J. M., et al. 2014, ApJS, 211, 2

Iglesias, C. A. & Rogers, F. J. 1993, ApJ, 412, 752

Iglesias, C. A. & Rogers, F. J. 1996, ApJ, 464, 943

Ilijic, S., Hensberge, H., Pavlovski, K., & Freyhammer, L. M. 2004, in Astronomical Society of the Pacific Conference Series, Vol. 318, Spectroscopically and Spatially Resolving the Components of the Close Binary Stars, ed. R. W. Hilditch, H. Hensberge, & K. Pavlovski, 111–113

Jenkins, J. M., Caldwell, D. A., Chandrasekaran, H., et al. 2010, ApJ, 713, L120

Jorissen, A. 2003, in Asymptotic giant branch stars, by Harm J. Habing and Hans Olofsson. Astronomy and astrophysics library, New York, Berlin: Springer, 2003, p. 461, ed. H. J. Habing & H. Olofsson, 461

Kaye, A. B., Handler, G., Krisciunas, K., Poretti, E., & Zerbi, F. M. 1999, PASP, 111, 840

Keen, M. A., Bedding, T. R., Murphy, S. J., et al. 2015, MNRAS, 454, 1792

Kippenhahn, R., Weigert, A., & Weiss, A. 2012, Stellar Structure and Evolution, 2nd edn. (Springer)

Kirk, B., Conroy, K., Prša, A., et al. 2016, AJ, 151, 68

Koch, D. G., Borucki, W. J., Basri, G., et al. 2010, ApJ, 713, L79

Kochukhov, O., Makaganiuk, V., & Piskunov, N. 2010, A&A, 524, A5

Krisciunas, K., Griffin, R. F., Guinan, E. F., Luedeke, K. D., & McCook, G. P. 1995, MNRAS, 273, 662

Kupka, F. G., Ryabchikova, T. A., Piskunov, N. E., Stempels, H. C., & Weiss, W. W. 2000, Baltic Astronomy, 9, 590

Kurtz, D. W., Saio, H., Takata, M., et al. 2014, MNRAS, 444, 102

Kurtz, D. W., Shibahashi, H., Murphy, S. J., Bedding, T. R., & Bowman, D. M. 2015, MNRAS, 450, 3015

Ledoux, P. 1951, ApJ, 114, 373

Lehmann, H., Tkachenko, A., Semaan, T., et al. 2011, A&A, 526, A124

Lenz, P., Pamyatnykh, A. A., & Breger, M. 2010, in Variable Stars, the Galactic halo and Galaxy Formation, ed. C. Sterken, N. Samus, & L. Szabados, 83

Lomb, N. R. 1976, Ap&SS, 39, 447

Loumos, G. L. & Deeming, T. J. 1978, Ap&SS, 56, 285

Lucy, L. B. 1967, ZAp, 65, 89

Maceroni, C., Lehmann, H., da Silva, R., et al. 2014, A&A, 563, A59

Maceroni, C., Montalbán, J., Gandolfi, D., Pavlovski, K., & Rainer, M. 2013, A&A, 552, A60

Maceroni, C., Montalbán, J., Michel, E., et al. 2009, A&A, 508, 1375

Maeder, A. 2009, Physics, Formation and Evolution of Rotating Stars (Springer)

Maeder, A. & Meynet, G. 2012, Reviews of Modern Physics, 84, 25

Mantegazza, L. 2000, in Astronomical Society of the Pacific Conference Series, Vol. 210, Delta Scuti and Related Stars, ed. M. Breger & M. Montgomery, 138

McCarthy, J. K., Sandiford, B. A., Boyd, D., & Booth, J. 1993, PASP, 105, 881

Miglio, A., Montalbán, J., Noels, A., & Eggenberger, P. 2008, MNRAS, 386, 1487

Montgomery, M. H. & O'Donoghue, D. 1999, Delta Scuti Star Newsletter, 13, 28

Moravveji, E., Aerts, C., Papics, P. I., Andres Triana, S., & Vandoren, B. 2015, A&A, 580, A27

Moravveji, E., Townsend, R. H. D., Aerts, C., & Mathis, S. 2016, ApJ, 823, 130

Mosser, B., Goupil, M. J., Belkacem, K., et al. 2012, A&A, 548, A10

Murphy, S. J., Bedding, T. R., Shibahashi, H., Kurtz, D. W., & Kjeldsen, H. 2014, MNRAS, 441, 2515

Murphy, S. J., Pigulski, A., Kurtz, D. W., et al. 2013, MNRAS, 432, 2284

Murphy, S. J. & Shibahashi, H. 2015, MNRAS, 450, 4475

Nelder, J. A. & Mead, R. 1965, Comput. J., 7, 308

Pápics, P. I. 2012, Astronomische Nachrichten, 333, 1053

Pápics, P. I., Briquet, M., Baglin, A., et al. 2012, A&A, 542, A55

Pápics, P. I., Moravveji, E., Aerts, C., et al. 2014, A&A, 570, A8

Pápics, P. I., Tkachenko, A., Aerts, C., et al. 2013, A&A, 553, A127

Pápics, P. I., Tkachenko, A., Aerts, C., et al. 2015, ApJ, 803, L25

Paxton, B., Bildsten, L., Dotter, A., et al. 2011, ApJS, 192, 3

Paxton, B., Cantiello, M., Arras, P., et al. 2013, ApJS, 208, 4

Paxton, B., Marchant, P., Schwab, J., et al. 2015, ApJS, 220, 15

Perryman, M. A. C., de Boer, K. S., Gilmore, G., et al. 2001, A&A, 369, 339

Prša, A., Batalha, N., Slawson, R. W., et al. 2011, AJ, 141, 83

Prša, A., Degroote, P., Conroy, K., et al. 2013, in EAS Publications Series, Vol. 64, Setting a New Standard in the Analysis of Binary Stars, ed. K. Pavlovski, A. Tkachenko, & G. Torres, 259–268

Prša, A. & Zwitter, T. 2005, ApJ, 628, 426

Raskin, G., van Winckel, H., Hensberge, H., et al. 2011, A&A, 526, A69

Rauer, H., Catala, C., Aerts, C., et al. 2014, Experimental Astronomy, 38, 249

Reese, D. R., MacGregor, K. B., Jackson, S., Skumanich, A., & Metcalfe, T. S. 2009, A&A, 506, 189

Reese, D. R., Prat, V., Barban, C., van 't Veer-Menneret, C., & MacGregor, K. B. 2013, A&A, 550, A77

Ricker, G. R., Winn, J. N., Vanderspek, R., et al. 2015, Journal of Astronomical Telescopes, Instruments, and Systems, 1, 014003

Rogers, T. M. 2015, ApJ, 815, L30

Rowe, J. F., Borucki, W. J., Koch, D., et al. 2010, ApJ, 713, L150

Rucinski, S. M. 1989, Comments on Astrophysics, 14, 79

Saio, H. 1981, ApJ, 244, 299

Saio, H., Kurtz, D. W., Takata, M., et al. 2015, MNRAS, 447, 3264

Scargle, J. D. 1982, ApJ, 263, 835

Schaller, G., Schaerer, D., Meynet, G., & Maeder, A. 1992, A&AS, 96, 269

Schmid, V. S., Themeßl, N., Breger, M., et al. 2014, A&A, 570, A33

Schmid, V. S., Tkachenko, A., Aerts, C., et al. 2015, A&A, 584, A35

Schwarzenberg-Czerny, A. 2003, in Astronomical Society of the Pacific Conference Series, Vol. 292, Interplay of Periodic, Cyclic and Stochastic Variability in Selected Areas of the H-R Diagram, ed. C. Sterken, 383

Seaton, M. J. 2005, MNRAS, 362, L1

Shibahashi, H. & Kurtz, D. W. 2012, MNRAS, 422, 738

Shibahashi, H., Kurtz, D. W., & Murphy, S. J. 2015, MNRAS, 450, 3999

Shulyak, D., Tsymbal, V., Ryabchikova, T., Stütz, C., & Weiss, W. W. 2004, A&A, 428, 993

Simon, K. P. & Sturm, E. 1994, A&A, 281, 286

Slawson, R. W., Prša, A., Welsh, W. F., et al. 2011, AJ, 142, 160

Southworth, J. 2012, in Orbital Couples: Pas de Deux in the Solar System and the Milky Way, ed. F. Arenou & D. Hestroffer, 51–58

Stancliffe, R. J., Fossati, L., Passy, J.-C., & Schneider, F. R. N. 2015, A&A, 575, A117

Stellingwerf, R. F. 1979, ApJ, 227, 935

Tassoul, M. 1980, ApJS, 43, 469

Tayar, J. & Pinsonneault, M. H. 2013, ApJ, 775, L1

Telting, J. H., Baran, A. S., Nemeth, P., et al. 2014, A&A, 570, A129

Thompson, S. E., Everett, M., Mullally, F., et al. 2012, ApJ, 753, 86

Tkachenko, A. 2015, A&A, 581, A129

Tkachenko, A., Aerts, C., Yakushechkin, A., et al. 2013a, A&A, 556, A52

Tkachenko, A., Lehmann, H., Smalley, B., Debosscher, J., & Aerts, C. 2012, MNRAS, 422, 2960

Tkachenko, A., Lehmann, H., Smalley, B., & Uytterhoeven, K. 2013b, MNRAS, 431, 3685

Tkachenko, A., Van Reeth, T., Tsymbal, V., et al. 2013c, A&A, 560, A37

Torres, G., Andersen, J., & Giménez, A. 2010, A&A Rev., 18, 67

Townsend, R. H. D. 2003, MNRAS, 343, 125

Townsend, R. H. D., Owocki, S. P., & Howarth, I. D. 2004, MNRAS, 350, 189

Townsend, R. H. D. & Teitler, S. A. 2013, MNRAS, 435, 3406

Triana, S. A., Moravveji, E., Pápics, P. I., et al. 2015, ApJ, 810, 16

Tsymbal, V. 1996, in Astronomical Society of the Pacific Conference Series, Vol. 108, M.A.S.S., Model Atmospheres and Spectrum Synthesis, ed. S. J. Adelman, F. Kupka, & W. W. Weiss, 198

Uytterhoeven, K., Moya, A., Grigahcène, A., et al. 2011, A&A, 534, A125

van Kerkwijk, M. H., Rappaport, S. A., Breton, R. P., et al. 2010, ApJ, 715, 51

van Leeuwen, F. 2007, A&A, 474, 653

Van Reeth, T., Tkachenko, A., Aerts, C., et al. 2015a, A&A, 574, A17

Van Reeth, T., Tkachenko, A., Aerts, C., et al. 2015b, ApJS, 218, 27

van Winckel, H. 2003, ARA&A, 41, 391

Walker, G., Matthews, J., Kuschnig, R., et al. 2003, PASP, 115, 1023

Welsh, W. F., Orosz, J. A., Aerts, C., et al. 2011, ApJS, 197, 4

Willems, B. & Aerts, C. 2002, A&A, 384, 441

Wilson, R. E. 1979, ApJ, 234, 1054

Wilson, R. E. 1990, ApJ, 356, 613

Wilson, R. E. 1993, in Astronomical Society of the Pacific Conference Series, Vol. 38, New Frontiers in Binary Star Research, ed. K.-C. Leung & I.-S. Nha, 91

Wilson, R. E. & Devinney, E. J. 1971, ApJ, 166, 605

Zahn, J.-P. 1975, A&A, 41, 329

Zahn, J.-P. 1977, A&A, 57, 383

Zahn, J.-P. 1992, in Binaries as Tracers of Star Formation, ed. A. Duquennoy & M. Mayor, 253–268

Zima, W. 2006, A&A, 455, 227

Zima, W. 2008, Communications in Asteroseismology, 155, 17

Zima, W., Wright, D., Bentley, J., et al. 2006, A&A, 455, 235

Zwintz, K., Fossati, L., Ryabchikova, T., et al. 2014, Science, 345, 550

Curriculum Vitae

Valentina Susanne Schmid was born on the 25th of July, 1987 in Vienna, Austria. There she attended the technical high school HTBLVA Spengergasse, where early on she came in touch with computing and programming. Afterwards, she studied astronomy at the University of Vienna, while simultaneously working as a software developer for Ing. Martin Beofsich. She also spent five months abroad as an Erasmus student at KU Leuven, where she met Prof. Dr. Conny Aerts and conducted research for her master thesis. In September 2012, Valentina graduated with honours and obtained the degree of Master of Science. As a PhD fellow of the Research Foundation Flanders (FWO) Valentina studied pulsating stars in binary systems under the supervision of Conny Aerts. She successfully defended her PhD on the 29th of August, 2016.

List of publications

Articles in refereed international journals

Journal abbreviations and impact factors (ISI JCR 2015):

A&A: Astronomy & Astrophysics (4.4)
AN: Astronomische Nachrichten (0.9)
ApJS: Astrophysical Journal Supplement Series (11.2)
MNRAS: Monthly Notices of the Royal Astronomical Society (5.1)

V. S. Schmid and C. Aerts: *Asteroseismic modelling of the two F-type hybrid pulsators KIC 10080943A and KIC 10080943B* in A&A vol. 592, A116 (2016)

V. S. Schmid, A. Tkachenko, C. Aerts, P. Degroote, S. Bloemen, S. J. Murphy, T. Van Reeth, P. I. Pápics, T. R. Bedding, M. A. Keen, A. Prša, J. Menu, J. Debosscher, M. Hrudková, K. De Smedt, R. Lombaert, and P. Nemeth: *KIC 10080943: An eccentric binary system containing two pressure- and gravity-mode hybrid pulsators* in A&A vol. 584, A35 (2015)

M. A. Keen, T. R. Bedding, S. J. Murphy, **V. S. Schmid**, C. Aerts, A. Tkachenko, R.-M. Ouazzani, and D. W. Kurtz: *KIC 10080943: a binary star with two γ Doradus/δ Scuti hybrid pulsators. Analysis of the g modes* in MNRAS vol. 454, Issue 2, pp. 1792-1797 (2015)

B. Buysschaert, C. Aerts, S. Bloemen, J. Debosscher, C. Neiner, M. Briquet, J. Vos, P. I. Pápics, R. Manick, **V. S. Schmid**, H. Van Winckel, and A. Tkachenko: *Kepler's first view of O-star variability: K2 data of five O stars in Campaign 0 as a proof of concept for O-star asteroseismology* in MNRAS vol. 453, Issue 1, pp. 89-100 (2015)

T. Van Reeth, A. Tkachenko, C. Aerts, P. I. Pápics, S. A. Triana, K. Zwintz, P. Degroote, J. Debosscher, S. Bloemen, **V. S. Schmid**, K. De Smedt, Y. Frémat, A. S. Fuentes, W. Homan, M. Hrudková, R. Karjalainen, R. Lombaert, P. Nemeth, R. Østensen, G. Van De Steene, J. Vos, G. Raskin, and H. Van Winckel: *Gravity-mode period spacings as a seismic diagnostic for a sample of γ Doradus stars from Kepler space photometry and high-resolution ground-based spectroscopy* in ApJS vol. 218, 27 (2015)

M. Breger, P. Lenz, A. A. Pamyatnykh, **V. S. Schmid**, and P. G. Beck: *Frequencies and mode identifications of the δ Scuti star EE Camelopardalis* in A&A vol. 575, A46 (2015)

P. G. Beck, E. Kambe, M. Hillen, E. Corsaro, H. Van Winckel, E. Moravveji, J. De Ridder, S. Bloemen, S. Saesen, P. Mathias, P. Degroote, T. Kallinger, T. Verhoelst, H. Ando, F. Carrier, B. Acke, R. Oreiro, A. Miglio, P. Eggenberger, B. Sato, K. Zwintz, P. I. Pápics, P. Marcos-Arenal, S. A. Sans Fuentes, **V. S. Schmid**, C. Waelkens, R. Østensen, J. M. Matthews, M. Yoshida, H. Izumiura, H. Koyano, S. Nagayama, Y. Shimizu, N. Okada, K. Okita, A. Sakamoto, T. Yamamuro, and C. Aerts: *Detection of solar-like oscillations in the bright red giant stars γ Piscium and θ^1 Tauri from a 190-day high-precision spectroscopic multi-site campaign* in A&A vol. 573, A138 (2015)

V. S. Schmid, N. Themeßl, M. Breger, P. Degroote, C. Aerts, P. G. Beck, A. Tkachenko, T. Van Reeth, S. Bloemen, J. Debosscher, B. G. Castanheira, B. E. McArthur, P. I. Pápics, V. Fritz, and R. E. Falcon: *Discovery of binarity, spectroscopic frequency analysis, and mode identification of the δ Scuti star 4 CVn* in A&A vol. 570, A33 (2014)

P. G. Beck, K. Hambleton, J. Vos, T. Kallinger, S. Bloemen, A. Tkachenko, R. A.García, R. H. Østensen, C. Aerts, D. W. Kurtz, J. De Ridder, S. Hekker, K. Pavlovski, S. Mathur, K. De Smedt, A. Derekas, E. Corsaro, B. Mosser, H. Van Winckel, D. Huber, P. Degroote, G. R. Davies, A. Prša, J. Debosscher, Y. Elsworth, P. Nemeth, L. Siess, **V. S. Schmid**, P. I. Pápics, B. L. de Vries, A. J. van Marle, P. Marcos-Arenal, and A. Lobel: *Pulsating red giant stars in eccentric binary systems discovered from Kepler space-based photometry. A sample study and the analysis of KIC 5006817* in A&A vol. 564, A36 (2014)

N. Nardetto, E. Poretti, M. Rainer, G. Guiglion, M. Scardia, **V. S. Schmid**, and P. Mathias: *Understanding the dynamical structure of pulsating stars. HARPS spectroscopy of the δ Scuti stars ρ Puppis and DX Ceti* in A&A vol. 561, A151 (2014)

T. Morel, M. Briquet, M. Auvergne, G. Alecian, S. Ghazaryan, E. Niemczura, L. Fossati, H. Lehmann, S. Hubrig, C. Ulusoy, Y. Damerdji, M. Rainer, E. Poretti, F. Borsa, M. Scardia, **V. S. Schmid**, H. Van Winckel, K. De Smedt, P. I. Pápics, J. F. Gameiro, C. Waelkens, M. Fagas, K. Kamiński, W. Dimitrov, A. Baglin, E. Michel, L. Dumortier,

Y. Frémat, H. Hensberge, A. Jorissen, and S. Van Eck: *A search for pulsations in the HgMn star HD 45975 with CoRoT photometry and ground-based spectroscopy* in A&A vol. 561, A35 (2014)

C. Aerts, S. Simón-Díaz, C. Catala, C. Neiner, M. Briquet, N. Castro, **V. S. Schmid**, M. Scardia, M. Rainer, E. Poretti, P. I. Pápics, P. Degroote, S. Bloemen, R. H. Østensen, M. Auvergne, A. Baglin, F. Baudin, E. Michel, and R. Samadi: *Low-amplitude rotational modulation rather than pulsations in the CoRoT B-type supergiant HD 46769* in A&A vol. 557, A114 (2013)

S. Desidera, A. Sozzetti, A. S. Bonomo, R. Gratton, E. Poretti, R. Claudi, D. W. Latham, L. Affer, R. Cosentino, M. Damasso, M. Esposito, P. Giacobbe, L. Malavolta, V. Nascimbeni, G. Piotto, M. Rainer, M. Scardia, **V. S. Schmid**, A. F. Lanza, G. Micela, I. Pagano, L. R. Bedin, K. Biazzo, F. Borsa, E. Carolo, E. Covino, F. Faedi, G. Hébrard, C. Lovis, A. Maggio, L. Mancini, F. Marzari, S. Messina, E. Molinari, U. Munari, F. Pepe, N. Santos, G. Scandariato, E. Shkolnik, and J. Southworth: *The GAPS programme with HARPS-N at TNG. II. No giant planets around the metal-poor star HIP 11952* in A&A vol. 554, A29 (2013)

V. S. Schmid, N. Themeßl, M. Breger, C. Aerts, P. G. Beck, B. G. Castanheira, V. Fritz, P. I. Pápics, J. Debosscher, and R. E. Falcon: *Spectroscopic frequencies of 4 CVn in 2010 and 2011* in AN vol. 333, Issue 10, pp. 1080-1082 (2012)

Articles in conference proceedings

V. S. Schmid, J. Debosscher, P. Degroote, and C. Aerts: *Asteroseismology of eclipsing binary stars using Kepler and the HERMES spectrograph* in Setting a New Standard in the Analysis of Binary Stars, ed. K. Pavlovski, A. Tkachenko, and G. Torres., EAS Publication Series vol. 64, pp. 421-422 (2013)